

**Cardiff University**

**Cardiff School of Biosciences**

---

**Craig McPhee BSc MSc**

---

**Development and  
characterisation of synthetic  
model lipid membranes under  
linear and non-linear  
microscopy**

---

A thesis submitted to Cardiff University for the degree of

Doctor of Philosophy

December 2016



## Declaration and Statements

### Declaration

This work has not been submitted in substance for any other degree or award at this or any other university or place of learning, nor is being submitted concurrently in candidature for any degree or other award.

Signed Craig McPhee (Candidate) Date 29/12/2016

### Statement 1

This thesis is being submitted in partial fulfillment of the requirements for the degree of PhD.

Signed Craig McPhee (Candidate) Date 29/12/2016

### Statement 2

This thesis is the result of my own independent work/investigation, except where otherwise stated, and the thesis has not been edited by a third party beyond what is permitted by Cardiff Universitys Policy on the Use of Third Party Editors by Research Degree Students. Other sources are acknowledged by explicit references. The views expressed are my own.

Signed Craig McPhee (Candidate) Date 29/12/2016

### Statement 3

I hereby give consent for my thesis, if accepted, to be available online in the Universitys Open Access repository and for inter-library loan, and for the title and summary to be made available to outside organisations.

Signed Craig McPhee (Candidate) Date 29/12/2016

Dedicated to my family, without whose help, this would never have  
happened...

## Abstract

Lipid domains provide a framework for localised functionality of the cellular membrane through transient coordination of certain lipids and membrane proteins into structurally distinct, stabilised heterogeneous membrane regions. Present experimental studies fall short of conclusively proving lipid domain existence within the plasma membrane due to the lack of label-free, chemically sensitive nanoscale detection. Herein, I present my progress towards developing novel, label-free optical microscopy techniques to overcome these limitations.

Giant unilamellar vesicles (GUVs) represent a simple model of cellular membranes and are well suited for the study of lipid domains. In this thesis, I discuss the demonstration of a novel, label free method to directly assess GUV lamellarity: Quantitative differential interference contrast microscopy (qDIC). Under qDIC, a contrast image is produced which encodes the difference in optical phase (hence optical path length) after propagation through two adjacent points of the sample. I show that, with appropriate data analysis applied to qDIC contrast images, we are able to measure membrane lamellarity directly with sub-nm precision. I then demonstrate the application of this method to static synthetic membranes exhibiting lipid domains: Planar Lipid Bilayer Patches (PLBPs). Sub-nm thickness differences ( $\sim 9\text{\AA}$ ) attributable to coexisting lipid domains are resolved and quantified. Overall, these results demonstrate that label free qDIC is a rapid, non-perturbing, sensitive and accurate method, providing an alternative to fluorescence microscopy, for quantitative studies of lipid domains in model membranes.

Furthermore, I discuss correlative qDIC and Coherent Anti-Stokes Raman scattering microscopy (CARS) of PLBPs with lipid domains. CARS

microscopy has emerged in the last decade as a powerful, chemically-specific multi-photon imaging method which overcomes the sensitivity and speed limitations of spontaneous Raman scattering, and enables rapid quantitative analysis of lipids label-free. I demonstrate application of broad-band hyper-spectral CARS imaging over the  $\text{CH}_{2,3}$  stretching vibrational resonances, combined with in-house developed phase-corrected Kramers Krönig (PCKK) analysis, which allowed us to resolve and quantify the chemical components of lipid domains at the single bilayer level.

Stimulated Raman loss (SRL) microscopy is an alternative, chemically specific, non-linear imaging modality recently implemented within our research group. In contrast to CARS microscopy, SRL rejects non-resonant background providing high contrast imaging of single lipid bilayers comparable to fluorescence imaging. I demonstrate early application of SRL at the single bilayer level across the  $\text{CH}_{2,3}$  stretch region.

During this project a number of notable achievements have been made. A novel qDIC method has been developed and utilised. CARS microscopy has been applied to determine lipid liquid phase at both single frequency and hyper-spectral imaging modalities. SRL microscopy has then been applied, demonstrating superior contrast to that seen under CARS. These studies form the foundation for further chemically specific investigation.

## Acknowledgements

I would like to take this opportunity to thank the many people, without whom this PhD would simply not have been possible. I begin with my supervisors: Prof Paola Borri, Prof Wolfgang Langbein and Prof John Harwood.

Paola has long maintained an open door policy which I (and others) have found to be crucial during the course of a PhD. Paola has always been open and supportive, able to offer timely advice and answer difficult questions, saving the poor PhD student many hours of toil. In addition, Paola has been of great help over the past year, which has been a very difficult time for both myself and my family.

Secondly, I wish to thank Prof Langbein. His ability to develop new theories or find new angles to look at existing problems has never ceased to amaze me. Not only has he developed the theories behind the qDIC that I have implemented, but he has also single handedly designed and built all of the equipment on which my CARS, TPE and SRL data has been taken. It is fair to say that without Wolfgang, there would be no group or thesis.

Thirdly, I wish to thank Prof John Harwood for his helpful and timely advice regarding lipids and choices of lipids (for which he is a world renowned expert). Several potential problems were avoided thanks to his intervention.

I would also like to thank Oliver Castell who helped me to develop the droplet interface bilayer model (which sad to say I decided not to include within the thesis). Although the model has continued with subsequent PhD students!

A great, great many thanks must also go to Dr Pete Watson. Pete and I were only tangentially connected during my studies, however whenever I needed to borrow (steal) crucial equipment / chemicals: Pete was always

generous and forthcoming. I would especially like to thank Pete for all that he did for me when I was diagnosed with a long term illness: without asking, and when I needed him, he was there! For that he will always have my gratitude.

Special thanks are also due to Dr Iyestyn Pope who spent many hours showing me how to use the equipment and then subsequently extract the data from it. He has also been a great support throughout the PhD and has made my time here much the better!

Finally, I would like to thank my friend Dr George Zorinyants, not only has his deep knowledge of Physics, Maths and programming been generously shared. He has almost single handedly pulled me through many difficult times when I had thought things to be impossible. In addition: he introduced me to my wife!

Thanks also go to all those I have not named, principally my fellow PhD students and post-docs, whose constant banter and positive outlook have made the working environment much the richer for having them!

## Contents

<b>Declaration and Statements</b>	<b>ii</b>
<b>Abstract</b>	<b>iv</b>
<b>Acknowledgements</b>	<b>vi</b>
<b>List of Figures</b>	<b>xiii</b>
<b>List of Tables</b>	<b>xvii</b>
<b>1 Introduction</b>	<b>1</b>
1.1 Theoretical introduction to lipids . . . . .	1
1.2 Theoretical introduction to biological membranes . . . . .	11
1.3 Synthetic Model Membranes . . . . .	19
1.4 Lipid Rafts . . . . .	22
1.5 Common techniques for lipid analysis . . . . .	26
1.5.1 Fluorescence Microscopy . . . . .	26
1.5.2 Cold Detergent extraction . . . . .	27
1.5.3 Metallic nano-particle tracking . . . . .	28
1.6 Imaging Modalities . . . . .	29
1.6.1 Historical development . . . . .	29
1.6.1.1 Quantitative differential interference contrast microscopy . . . . .	29
1.6.1.2 CARS Microscopy . . . . .	33

1.6.1.3	Stimulated Raman Loss Microscopy . . . . .	36
1.6.2	Theoretical development . . . . .	38
1.6.2.1	Induced Polarisation . . . . .	39
1.6.2.2	Quantitative differential interference microscopy	41
1.6.2.3	Raman Microscopy . . . . .	43
1.6.2.4	CARS Microscopy . . . . .	46
1.6.2.5	Momentum and propagation considerations .	51
1.6.2.6	Stimulated Raman Loss Microscopy . . . . .	53
1.7	Motivation . . . . .	56
<b>2</b>	<b>Materials and Methods</b>	<b>58</b>
2.1	Synthetic membrane Methods . . . . .	58
2.1.1	Stock Lipid Handling and preparation . . . . .	58
2.1.2	Free in solution bilayer formation . . . . .	61
2.1.2.1	Lipid Concentrations . . . . .	61
2.1.2.2	Electroformation in H <sub>2</sub> O . . . . .	61
2.1.2.3	Electroformation in Sugar Solutions . . . . .	64
2.1.2.4	GUV formation by gentle hydration . . . . .	66
2.1.3	Surface Constrained Bilayer formation . . . . .	69
2.1.3.1	sGUV electroformation - Lipid preparation and deposition . . . . .	69
2.1.3.2	sGUV Electroformation from ITO coated sur- faces . . . . .	72
2.1.3.3	sGUV electroformation from dielectric sub- strates . . . . .	74
2.1.3.4	Biotinylated GUV Formation and surface prepa- ration . . . . .	76
2.1.3.5	PLBP deposition . . . . .	76
2.1.4	Thin Layer Chromatography . . . . .	79
2.2	CARS Experimental Setup . . . . .	79
2.2.1	CARS Image acquisition . . . . .	84
<b>3</b>	<b>Giant Unilamellar Vesicles</b>	<b>87</b>
3.1	Introduction . . . . .	87
3.2	Fluorescence quantisation . . . . .	90
3.3	Fluorescence and qDIC assessment of vesicle lamellarity . .	97

3.3.1	qDIC Image acquisition and analysis . . . . .	97
3.3.2	qDIC object phase extraction techniques . . . . .	102
3.3.3	Correlative Fluorescence to qDIC . . . . .	103
3.4	Two photon microscopy of Atto-488 DOPE in giant unilamellar vesicles . . . . .	110
3.4.1	DOPC giant unilamellar vesicles . . . . .	111
3.4.2	Porcine Sphingomyelin vesicles . . . . .	114
3.4.3	Sphingomyelin and Cholesterol vesicles . . . . .	116
3.4.4	DOPC and Cholesterol vesicles . . . . .	117
3.4.5	DOPC and Sphingomyelin vesicles . . . . .	119
3.4.6	Ternary giant unilamellar vesicles . . . . .	120
3.5	Fluorescence microscopy of coexisting lipid liquid domains . . . . .	122
3.5.1	Introduction . . . . .	122
3.5.2	Co-existing Lipid liquid phases visualised by NBD-DOPE fluorescence . . . . .	124
3.5.3	Co-existing lipid liquid phases visualised by Naptho[2,3-a]pyrene fluorescence . . . . .	127
3.5.4	Co-existing Lipid liquid phases visualised by Atto-488 DOPE fluorescence . . . . .	129
3.6	CARS microscopy of Giant Unilamellar vesicles . . . . .	131
3.6.1	Hyperspectral CARS of DOPC unilamellar vesicles . . . . .	138
3.6.2	Hyperspectral imaging of multilamellar Sphingomyelin vesicles . . . . .	140
3.6.3	Discussion . . . . .	142
3.7	Background reduction with D <sub>2</sub> O . . . . .	142
3.8	Biotinylated GUV . . . . .	146
3.9	Deuterated Sphingomyelin GUV . . . . .	149
3.10	Summary . . . . .	151
<b>4</b>	<b>Planar Lipid Bilayer Patches</b>	<b>153</b>
4.1	Introduction . . . . .	153
4.2	Quantitative DIC microscopy of Bilayer Patches . . . . .	155
4.3	Optimisation of CARS imaging for PLBPs . . . . .	165
4.4	Correlative CARS and Two Photon microscopy of PLBPs . . . . .	168

4.4.1	Correlative CARS and two photon imaging of non partitioned PLBPs . . . . .	168
4.4.2	Correlative CARS and two photon microscopy of partitioned PLBPs . . . . .	171
4.5	Hyperspectral CARS imaging of PLBPs . . . . .	174
4.5.1	Hyperspectral CARS of homogeneous PLBPs . . . . .	174
4.6	Hyperspectral CARS, qDIC and Fluorescence of labelled PLBPs	181
4.7	Hyperspectral CARS, qDIC and Fluorescence of label-free PLBPs . . . . .	185
4.8	Stimulated Raman loss of PLBPs . . . . .	188
4.9	Summary . . . . .	192
<b>5</b>	<b>Conclusions</b>	<b>194</b>
5.1	Thesis Summary . . . . .	194
	<b>APPENDICES</b>	<b>200</b>
<b>A</b>	<b>Raman analysis of bulk lipids</b>	<b>201</b>
A.1	Introduction . . . . .	201
A.2	Raman microscopy . . . . .	202
A.2.1	Spectral Analysis of DOPC . . . . .	203
A.2.2	Spectral Analysis of Sphingomyelin . . . . .	206
A.2.3	Spectral Analysis of Cholesterol . . . . .	208
A.2.4	Spectral basis for chemically sensitive imaging . . . . .	210
<b>B</b>	<b>Neutravidin binding protocol</b>	<b>212</b>
<b>C</b>	<b>Piranha Protocol</b>	<b>214</b>
<b>D</b>	<b>Atto-488 and NBD-DOPE Photobleaching</b>	<b>218</b>
	<b>Bibliography</b>	<b>220</b>
	<b>List of Abbreviations</b>	<b>248</b>
	<b>GNU Free Documentation License</b>	<b>250</b>
1.	APPLICABILITY AND DEFINITIONS . . . . .	251
2.	VERBATIM COPYING . . . . .	253

3. COPYING IN QUANTITY . . . . . 253  
4. MODIFICATIONS . . . . . 254  
5. COMBINING DOCUMENTS . . . . . 256  
6. COLLECTIONS OF DOCUMENTS . . . . . 257  
7. AGGREGATION WITH INDEPENDENT WORKS . . . . . 257  
8. TRANSLATION . . . . . 258  
9. TERMINATION . . . . . 258  
10. FUTURE REVISIONS OF THIS LICENSE . . . . . 259  
11. RELICENSING . . . . . 259  
ADDENDUM: How to use this License for your documents . . . . . 260

**Publications, achievements and conference proceedings** 262

## List of Figures

1.1	Structure of DOPC, Sphingomyelin and Cholesterol . . . . .	2
1.2	Structure of Glycerol and Sphingosine . . . . .	3
1.3	Structure of common phospholipid headgroups . . . . .	5
1.4	Saturated, trans-mono-unsaturated and cis mono-unsaturated free fatty acids . . . . .	7
1.5	Molecular dynamics simulations of sphingomyelin and choles- terol packing . . . . .	10
1.6	Relation of acyl chain density and shape to macroscopic lipid phase . . . . .	12
1.7	Modern fluid mosaic model for the lipid bilayer . . . . .	14
1.8	Lipid raft model for the plasma membrane . . . . .	16
1.9	Mattress model of the cell membrane . . . . .	18
1.10	Cutaway representations of primary synthetic lipid models . .	20
1.11	Schematic representation of lipid raft and caveolae . . . . .	24
1.12	Preferential phase partitioning of fluorescent lipid analogues into $L_o$ and $L_d$ domains of model and native membranes . . .	27
1.13	Schematic representation of a DIC microscope . . . . .	31
1.14	Real and imaginary contributions to the observed CARS signal	51
1.15	CARS Anti-Stokes radiation patterns from single and ensem- ble Hertzian dipoles . . . . .	53
2.1	Schematic representation a GUV Formation chamber . . . . .	63

2.2	Schematic representation of a typical imaging chamber . . . . .	65
2.3	Gentle Hydration formation setup . . . . .	68
2.4	Surface attached GUV formation from ITO coated glass substrates . . . . .	73
2.5	Surface attached GUV formation on dielectric substrate . . . . .	75
2.6	Schematic representation of PLBP formation . . . . .	78
2.7	CARS and TPE microscope schematic . . . . .	80
2.8	Resonant and non-resonant signal intensities as a function of pulse spectral width. . . . .	82
3.1	Example analysis of Atto-488 stained DOPC vesicles . . . . .	92
3.2	Measured equatorial fluorescence from a large population (n=466) of thin walled DOPC vesicles stained with Atto-488 DOPE. . . . .	95
3.3	Characterisation of DOPC vesicle lamellarity under fluorescence. . . . .	96
3.4	Correlative fluorescence and qDIC response for a single DOPC GUV. . . . .	100
3.5	Comparison and optimisation of measured to model qDIC signals . . . . .	101
3.6	Examples of passing and rejected GUV from qDIC analysis . . . . .	104
3.7	Characterisation of fluorescent DOPC vesicles under defocused conditions. . . . .	106
3.8	qDIC assessment of thin walled vesicle lamellarity. . . . .	107
3.9	Correlative fluorescence and qDIC analysis of thin walled vesicle lamellarity. . . . .	109
3.10	Spherical projections of DOPC giant unilamellar vesicles visualised with two photon fluorescence microscopy . . . . .	113
3.11	Spherical projections of Porcine Sphingomyelin (PSM) vesicles visualised with two photon fluorescence microscopy. . . . .	115
3.12	Spherical projections of Porcine Sphingomyelin (PSM) and Cholesterol vesicles visualised with two photon fluorescence microscopy . . . . .	116
3.13	Spherical projections of DOPC and Cholesterol vesicles visualised with two photon fluorescence microscopy . . . . .	117

3.14	3d Reconstruction of DOPC and Cholesterol vesicle . . . . .	118
3.15	Spherical projections of DOPC and Sphingomyelin vesicles visualised with two photon fluorescence microscopy . . . . .	119
3.16	Spherical projections of DOPC, Sphingomyelin and Cholesterol vesicles visualised with two photon fluorescence microscopy . . . . .	121
3.17	Structure of Naphthopyrene . . . . .	123
3.18	False colour images of coexisting lipid liquid phases in DOPC:PSM:Cholesterol vesicles . . . . .	125
3.19	False colour images of coexisting lipid liquid phases in DOPC:PSM:Cholesterol vesicles . . . . .	126
3.20	False colour images of coexisting lipid liquid phases in DOPC:PSM:Cholesterol vesicles with Naphthopyrene . . . . .	128
3.21	False colour images of coexisting lipid liquid phases in DOPC:PSM:Cholesterol vesicles . . . . .	130
3.22	Label Free CARS Microscopy of free in solution GUV. . . . .	134
3.23	Correlative DIC and CARS microscopy of ternary vesicles . . . . .	136
3.24	Label free CARS microscopy of thin walled DOPC vesicles. . . . .	139
3.25	Hyperspectral CARS analysis of multilamellar Porcine sphingomyelin vesicles. . . . .	141
3.26	CARS spectra of deuterium and hydrogen oxide. . . . .	145
3.27	Surface bound GUV incorporating 0.1mol% Biotin-DOPE . . . . .	148
3.28	Deuterated, d31 (16:0) sphingomyelin vesicles imaged under CARS microscopy at $2090\text{cm}^{-1}$ . . . . .	150
4.1	Imaging and assessment of a single lipid bilayer under two photon fluorescence, DIC and qDIC microscopy. . . . .	157
4.2	Mapping phase and axial thickness under qDIC . . . . .	159
4.3	Integrated qDIC and correlative fluorescence imaging of lipid phase domains in PLBPs. . . . .	162
4.4	Quantitative DIC microscopy assessment of the thickness of a statistically significant population of planar lipid bilayer patches . . . . .	164
4.5	Comparison of CARS imaging of a single PLBP at the $\text{CH}_{2,3}$ stretch peak at $2850\text{cm}^{-1}$ . . . . .	166

4.6	Comparison of two photon imaging of single component (DOPC) PLBPs with chemically specific CARS imaging of the same patches . . . . .	170
4.7	Comparative analysis of phase separated PLBPs under CARS and Two Photon fluorescence imaging. . . . .	173
4.8	CARS and TPE microscopy applied to DOPC PLBPs. . . . .	177
4.9	Hyperspectral CARS and nNMF applied to uniform PSM enriched PLBPs. . . . .	180
4.10	CARS, TPE and qDIC applied to labelled phase separated PLBPs. . . . .	183
4.11	Hyperspectral CARS and qDIC applied to label free PLBPs. . . . .	187
4.12	Simultaneously acquired label free images of ternary (DOPC:PSM:Cholesterol, 2:1:1 molar ratio) PLBPs and vesicles under SRL. . . . .	191
A.1	Raman spectra of drop cast, bulk phase DOPC lipid. . . . .	205
A.2	Raman Spectra of drop cast PSM . . . . .	207
A.3	Raman Spectra of Cholesterol . . . . .	209
A.4	Comparison of Raman spectra for model lipids . . . . .	211
D.1	Comparison of photobleaching between Atto-488 and NBD . . . . .	219

## List of Tables

1.1	Headgroups and net charges of common Phospholipids at neutral pH, adapted from (Nelson et al., 2008) . . . . .	5
2.1	Miscibility temperature, structure and headgroup structure for primary lipids, Sterols and synthetic lipid analogues used in this study. . . . .	59
3.1	Relative concentrations of model lipid species used to characterise the partitioning behaviour of NBD-DOPE within Giant Unilamellar Vesicles. . . . .	112
4.1	Analysis of acquisition times and signal to noise ratio for different dwell times for imaging PLBPs at the CH <sub>2</sub> peak at 2850cm <sup>-1</sup> . It should be noted that at the time our setup could not perform arbitrary dwell times, the ones presented were the only possible. . . . .	167

## 1.1 Theoretical introduction to lipids

In this study, we address the physical and chemical observables of phase separated lipid domains (lipid rafts). Herein, we briefly review the structure and properties of fundamental lipid molecules, specifically with relation to macroscopic properties arising from molecular ones.

Lipid molecules of relevance to Biology present in a variety of forms. The defining characteristic of lipids is based upon solubility, lipids are inherently insoluble in water. A more precise definition is: 'lipid molecules are soluble in low polarity solvents and insoluble in high-polarity solvents' (Gunstone et al., 2007). In this study, of primary concern are the lipids 1,2 Dioleoyl-sn-glycero-3-phosphatidylcholine (DOPC), sphingomyelin and cholesterol. As shown in figure 1.1 sphingomyelin and DOPC both contain the zwitterionic headgroup (choline) which possesses both a positive charge upon its nitrogen moiety and a negative charge on the phosphate group. In addition, both molecules possess apolar (uncharged) acyl chains. In contrast, cholesterol possesses no net charge and exhibits a planar conformation. Charge distribution and location within lipid molecules has important implications for both molecular packing within specific lipid phases and for the nature of the lipid phases formed. The charged headgroups of both DOPC and sphingomyelin permit coordination with the hydrogen bonding structure of water, whilst their uncharged acyl chains are hydrophobic. This leads to the formation of bilayer structures with the uncharged acyl region sequestered toward the interior. Cholesterol by comparison is

unable to form bilayers in isolation and will tend to aggregate in bulk when exposed to water (Nelson, 1967a). Charge is however not the only consideration. The conformation of the molecule, head-group volume, length of the acyl chains and the presence and location of unsaturated bonds also effect molecular packing and have implications for the possible lipid structures formed.

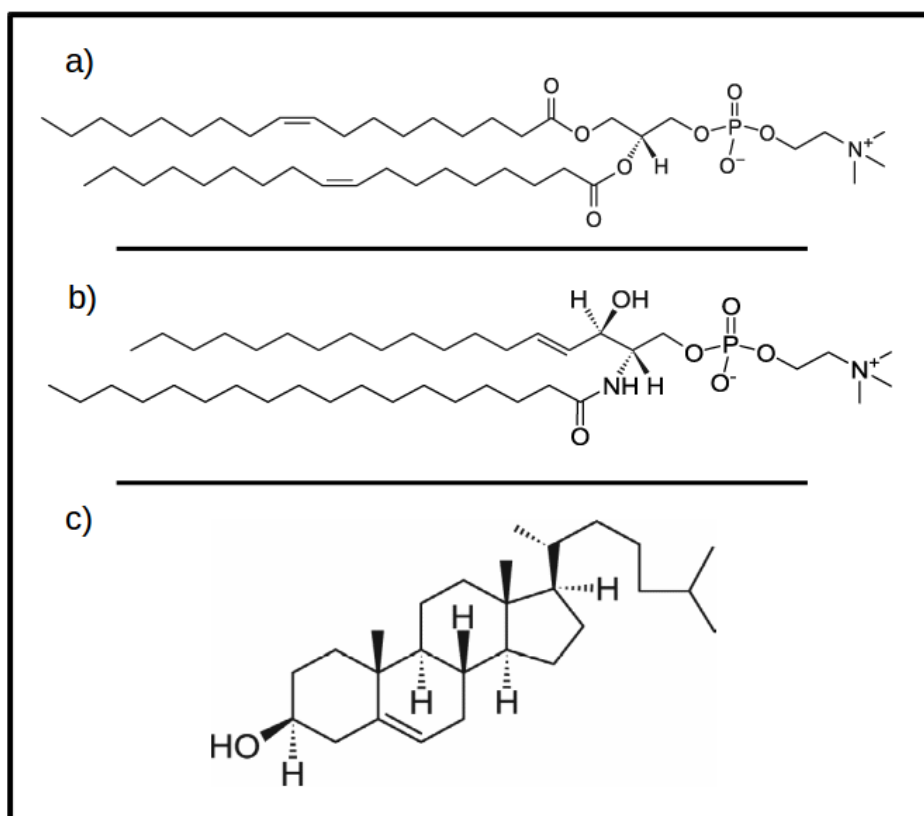


Figure 1.1: Molecular structure including net charge location(s) for a) DOPC, b) Sphingomyelin and c) Cholesterol. Both DOPC and sphingomyelin possess the same zwitterionic headgroup, choline. Chemical images provided by the supplier: Avanti-Polar Lipids Inc.

In further consideration of lipid molecular structure, we examine the backbone molecules present in lipids relevant to mammalian cell lines. Shown in figure 1.2 there are two molecular bases which can form the backbone of polar lipids: Sphingosine and Glycerol groups. Characteristic to both is a 3 Carbon backbone permitting attachment of differing functional groups. Glycerol is hydrophilic in nature and capable of monomeric insertion within the hydrogen bonding network of liquid water (Towey and Dougan, 2011). By contrast to glycerol, sphingosine possesses an unsaturated (C15) carbon chain already present at the (1,3) carbon location. The backbone molecules act as a linker separating the polar and apolar moieties of the lipid, presenting a barrier to water ingress into the bilayer interior (Hubner and Blume, 1998). This reinforces the amphiphilic nature of the molecule taken as a whole, contributing toward the tendency for bilayer formation. In all eukaryotic cells, fatty acids are attached to the backbone at the 1st and 2nd positions. The headgroup is attached at the third position. Certain archaea have the headgroup present in the first position.

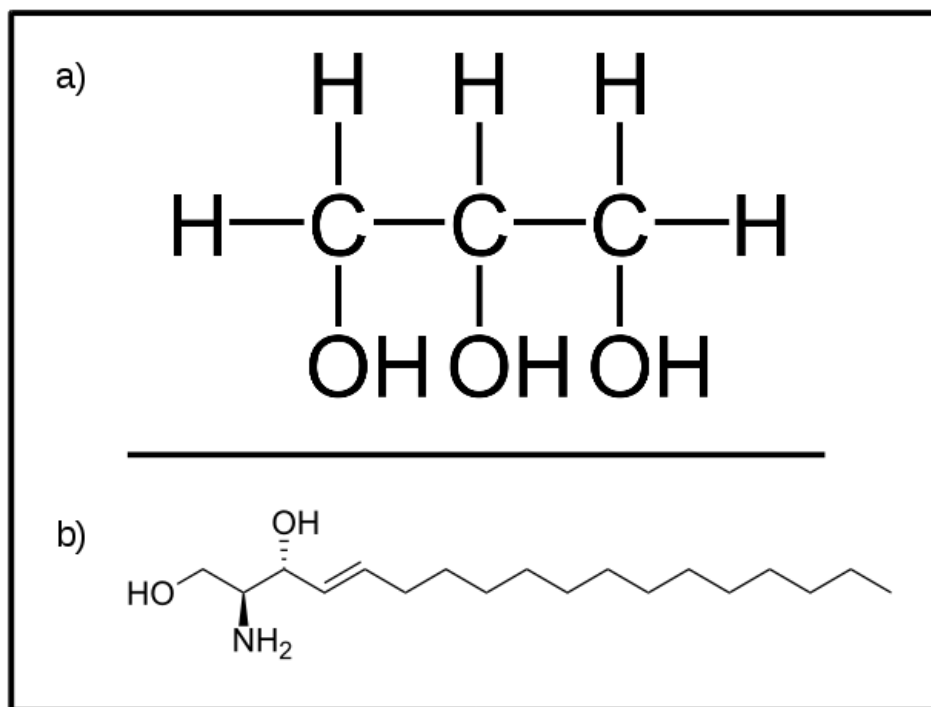


Figure 1.2: Molecular structure of (a) Glycerol and (b) Sphingosine. Figure based on public domain works.

In order to attach a headgroup molecule with the backbone, a linker molecule must be present. Within this study, lipids of interest have their headgroups attached through a phosphodiester bond linkage as shown in figure 1.1 (a and b) and figure 1.3 i.e. the phospholipids. In addition to linking the molecules, the phosphate group also carries a negative charge at physiological pH. This has a bearing upon the interaction between neighbouring lipids within a bilayer structure and upon the conductivity of biological membranes (McLaughlin et al., 1970). To this phospho-group there are a number of attached headgroups of biological significance. These are shown in table 1.1 and figure 1.3. Crucially, the headgroup can have negative, neutral or positive charges. Combined with the negative charge present upon the phosphate, this leads to the formation of lipids with either positive, negative or neutral (Zwitterionic) characteristics. In this study the phospholipids sphingomyelin and phosphatidylcholine are used primarily. These carry zero overall charge at pH 7 (Miller et al., 1998). For some experiments, to facilitate formation of synthetic membranes, phosphatidylglycerol is used, which carries a negative charge. This is a requirement for formation of giant liposomes in physiological strength buffers due to charge interactions with the ions in solution (Akashi et al., 1996). At low strengths or in deionised water, formation by electroformation can proceed without any charged lipid component.



In order to understand the nature of lipid packing into bilayer structures, both charge repulsion / attraction between headgroups and the overall headgroup size must be accounted for. Different headgroup structures have been linked with effects such as changes in membrane curvature (Cooke and Deserno, 2006) and therefore recruitment of specific lipid types to membrane domains with constrained geometries.

In consideration of the nature of the fatty acid chains attached to the lipids, long chain acids do not tend to carry an overall charge at physiological pH. Therefore the primary consideration with regards to packing of internal bilayer regions is the conformation adopted by the acyl chains (Barton and Gunstone, 1975). It should be noted that these chains are in general highly flexible and can exhibit a variety of equilibrium conformations. Shown in figure 1.4 (a) saturated acyl chains such as palmitic acid, possess only C-C single bonds, about which the chains are free to rotate. Chains of this type adopt a straight conformation (on the average) within the bilayer. This permits close packing between neighbouring lipids (Small, 1984). Van de Waals and London type forces between chains in close proximity tend to reinforce packing (Lis et al., 1982) and produce a lipid phase in which lipid mobility is reduced. Sphingomyelin is employed in this study and exhibits this type of packing geometry (Ramstedt and Slotte, 1999). Unsaturated and polyunsaturated fatty acids possess rigid carbon-carbon double and / or triple bonds. Double bonds are present in two forms: cis and trans conformations depending upon the directionality with which the Carbon chain extends upon either side of the bond. As shown in figure 1.4 (c) in the cis conformation the carbon chain orients spatially, either side of the double bond, toward the same direction. In trans conformation (figure 1.4, b) the carbon chain extends in opposing directions about the double bond. Since rotation about a double bond is not possible, long chain hydrocarbons with cis double bonds possess a permanent kink. Those with trans configurations tend to exhibit straight chain geometry.

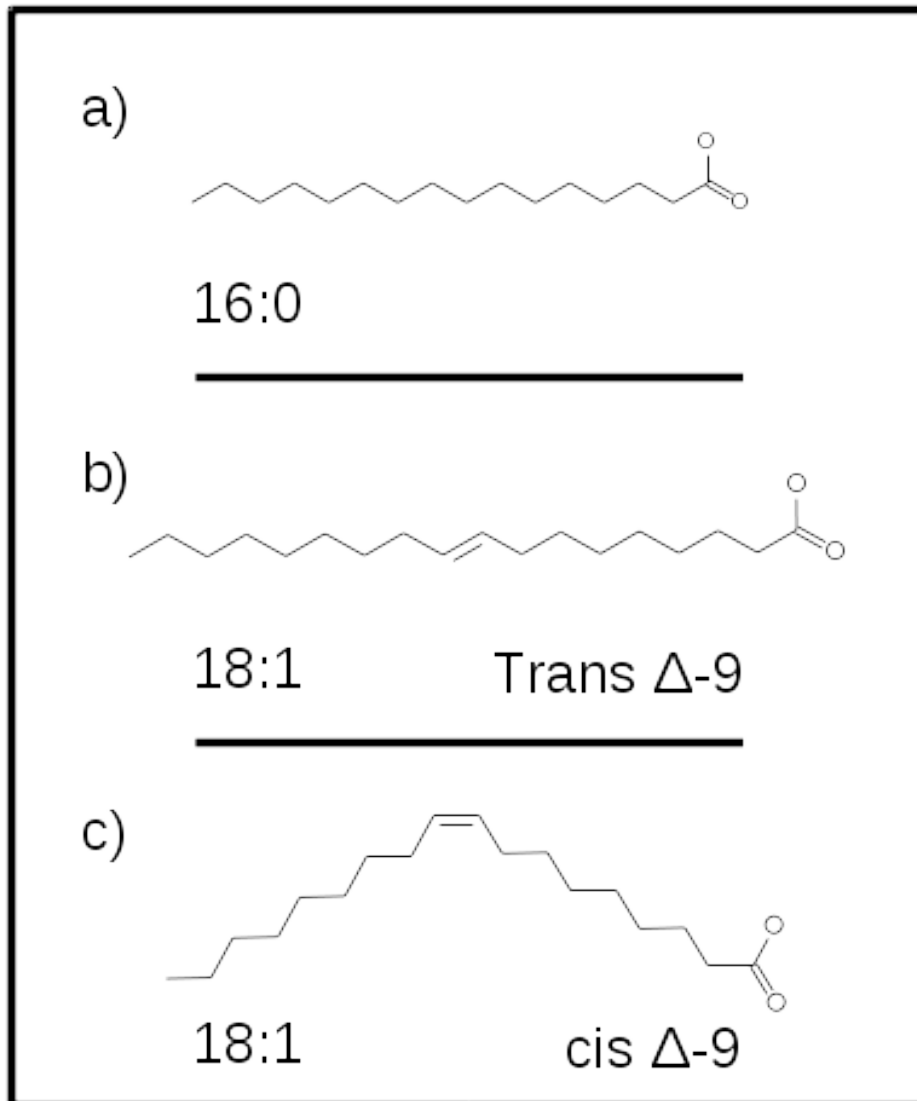


Figure 1.4: Common saturated, trans mono-unsaturated and cis mono-unsaturated free fatty acids, Palmitic acid (C16, fully saturated) (a), Elaidic (C18:1, trans) acid (b) and Oleic (C18:1, cis) acid (c)

Acyls incorporating a *cis* double bond (DOPC used in this study) exhibit an average 'kinked' conformation (c.f. figures 1.1 and 1.4). This results in a structure which tends to inhibit close packing between neighbouring molecules (Israelachvili et al., 1977). This has two effects, the density of molecules is reduced and Van de Waals and London type interactions are less strong (due to increased molecular separation) (Rawicz et al., 2000). Unsaturated lipids therefore tend to have greater mobility and diffuse at faster rates about the bilayer. By contrast, sphingomyelin possesses on one chain a *trans* double bond (the other chain being saturated) resulting in higher packing density due to the straight chain conformation (Filippov et al., 2006). As a result, close packing of chains is not inhibited and diffusion in sphingomyelin membranes proceeds more slowly (relative to a DOPC bilayer) (Lindblom et al., 2006).

If mixtures of saturated and (*cis*) unsaturated lipids are combined in a single bilayer, it is apparent from energy considerations, the minimum energy for the system is attained if the saturated lipids are free to form Van de Waals interactions with themselves (Almeida et al., 2005, Hac et al., 2005, Heimburg, 2008). This is true within a range of concentrations provided that the energy per unit length along the phase boundary required to compensate for chain length mismatch does not dominate (Heimburg, 2008). In order to introduce a DOPC molecule into a region of sphingomyelin, energy would have to be supplied to overcome the Van de Waals and London type forces between the sphingomyelin molecules. This suggests that in a mixed lipid bilayer, the lipids will tend to separate into saturated and unsaturated types. This is indeed what is observed in many experiments and within computational simulations (Niemelä et al., 2007). Separation of the lipids leads to the formation of raft-like domains: membrane regions enriched in sphingolipids and sterols compared to the average ratios present as membrane constituents.

Sterols constitute another important family of lipid molecules. In mammalian cells, cholesterol predominates. Although planar in appearance, due to thermal fluctuations cholesterol can assume different non-planar equilibrium conformations. The relative size of the cholesterol molecule compared to that of the typical cell membrane constituent lipid (the average chain length is C18 for polar lipids) is such that the cholesterol can interdig-

itate within a single leaflet of the bilayer (McIntosh et al., 1992) as shown in a molecular dynamics simulation in figure 1.5. The presence of a small ( $\delta$ ) positive charged chain at the head of the cholesterol molecule coordinates well with the negatively charged phosphate group present in phospholipids, most especially sphingomyelin (Sankaram and Thompson, 1990) leading to intermolecule hydrogen bonding as shown in figure 1.5 (lower). When placed within a membrane containing these lipids, on average the cholesterol molecules will tend to have an orientation. The charged head will align to the leaflet exterior such that energy is minimised through the Coulomb interaction between the cholesterol head and the lipid headgroup (Ohvo-Rekilä et al., 2002). Cholesterol plays an important role in the regulation of membrane phase. Cholesterol has been shown to interact with both cis unsaturated lipids and their saturated counterparts (Ohvo-Rekilä et al., 2002) demonstrating preference for saturated varieties. Within saturated chain systems, cholesterol breaks the molecular order, whilst conversely increasing it in unsaturated bilayer leaflets (Krivanek et al., 2008, Martinez-Seara et al., 2010). There are also specific membrane proteins with motifs for binding cholesterol (Fantini and Barrantes, 2013, Li et al., 2001).

This discussion has so far focused on lateral sorting and diffusion of lipids within a single leaflet of the bilayer. Lipids can also exchange between the leaflets (Flip-Flop), however the timescale for this process, with a typical membrane lipid such as DOPC, is around 24h on the average (Contreras et al., 2010). The long timescales are attributed to the high energy required in order to move the charged lipid headgroup through the hydrophobic membrane interior. It should be noted that in differing membrane systems, shorter, temperature dependant timescales have been demonstrated on the order of a few hours to minutes dependant also upon lipid type (Liu and Conboy, 2005). Note that within actual cell membranes, enzymes known as flippases exist (Daleke, 2007). Flippases assist with lipid exchange between leaflets within the bilayer, drastically reducing the timescale for flip-flop to occur. Investigations within reconstituted GUV have indicated flip-flop timescales of the order of a few minutes in the presence of flippases (Papadopoulos et al., 2007). This enables cells to control the lipid composition in different leaflets in an efficient manner. Each leaflet

can therefore be repurposed for specific tasks or functionality. It should be noted that flippases are still poorly understood and many of the basic principles of action remain to be defined (Poulsen et al., 2008).

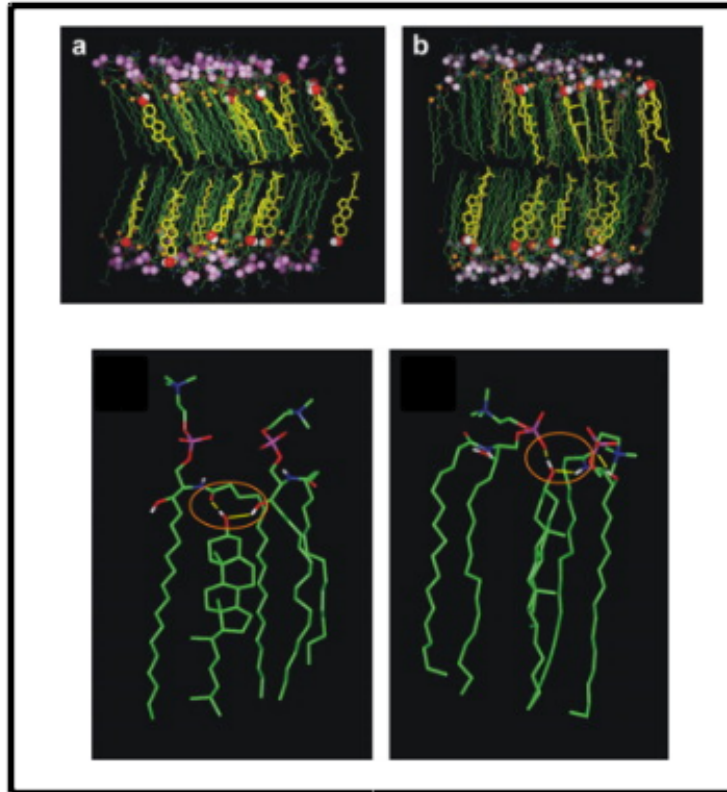


Figure 1.5: Molecular dynamics simulation of cholesterol and sphingomyelin packing demonstrating coordinated molecular packing and cholesterol orientation within each leaflet (top). Hypothesised hydrogen bonding between cholesterol 'head' group and two sphingomyelin molecules shown in circled area (lower). Figures adapted from (Róg and Pasenkiewicz-Gierula, 2006), reproduced with kind permission of Elsevier.

## 1.2 Theoretical introduction to biological membranes

The basic bilayer structure of all lipid membranes is a direct consequence of the amphiphilic nature of the lipid molecules: the simultaneous presence of polar headgroups and apolar acyl chains (Israelachvili et al., 1976). This structure gives rise to interactions with aqueous solvent driven predominantly by hydrophobic forces (Tanford, 1978). In general, acyl chains dissolved within an organic solvent require energy in order to remove them into an aqueous phase (Tanford, 1972a). As a result acyl groups are sequestered within the interior of lipid structures when exposed to water. The free energy associated with the hydrophobic interaction can drive the formation of a range of possible lipid structures (Cullis et al., 1986).

Biologically relevant structures are micelles and bilayers although cubic and other structures are also theoretically possible but are not observed in nature. The molecular conformation and acyl chain length for a particular lipid generally determines its tendency to form micelles or bilayers (Israelachvili et al., 1977, Tanford, 1972b). Shown in figure 1.6, if the lipid head group volume is large compared with the chain density, an invert conical molecular conformation will be assumed. Resultant to this, bilayers will not form as there would exist insufficient chain density to effectively pack the bilayer interior volume (Israelachvili et al., 1976). Lipids of this type have only single acyl chains forming micellar structures. In lipids relevant to biological membranes: bilayers must form, therefore effectively constraining the maximum possible headgroup size in relation to acyl chain density. This precondition holds at least in close vicinity to the bilayer since long chains attached to the headgroup can still permit close packing whilst carrying a larger cargo at the end. Lipid packing is also influenced by headgroup charge (Oda et al., 1999), lipids of like charge will be energetically excluded from close packing due to Coulomb repulsion.

In biological systems lipids tend to have simple, small headgroups and present with a variety of charges (Gennis, 2013) enabling further cellular specialisation such as temperature compensation by membrane charge variation (Hazel and Landrey, 1988). In synthetic systems, both positively and negatively charged bulk membranes can be produced and exhibit a range of behaviours in aqueous buffer (Stamatatos et al., 1988) and when

interacting with biological systems (Carmona-Ribeiro, 1992, Rafalski et al., 1990). Membrane charge has been linked with vesicle fusion as well as selective targeting and delivery of liposomal contained drugs (Cevc, Choi and Maibach, 2005, Kaur et al., 2004).

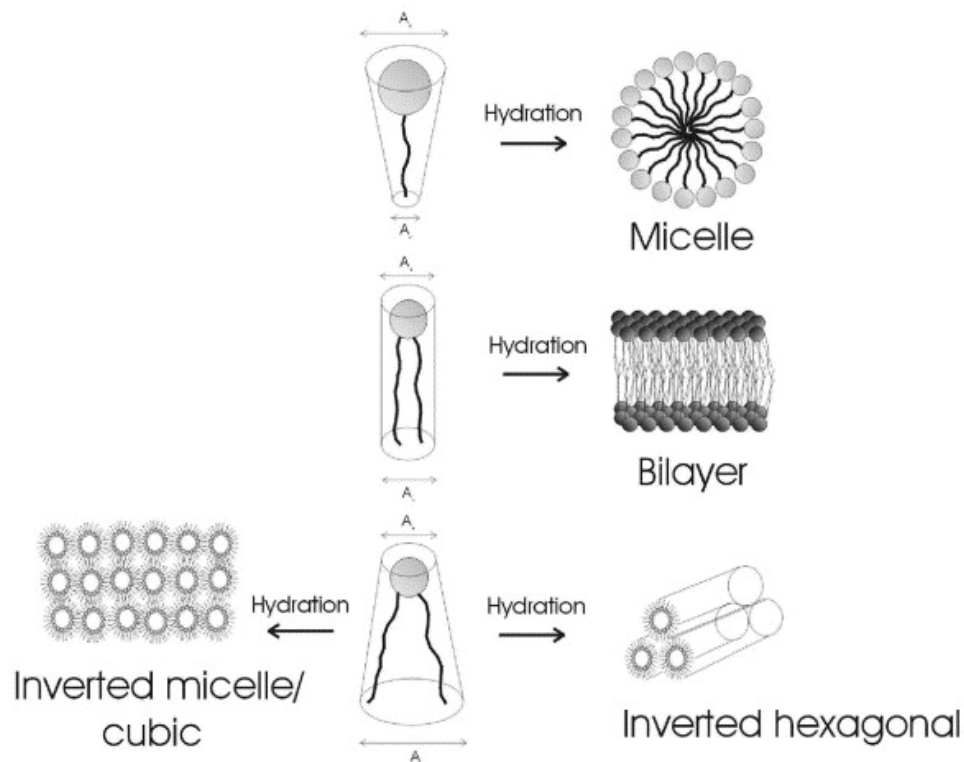


Figure 1.6: Relation of acyl chain density and shape to macroscopic lipid structure formation. High head group volume to chain density ratios give rise to invert conical molecular conformations (top) resulting in micellar structures. Ratios closer to unity result in an even molecular conformation (center) leading to bilayer formation. Inverse micellar and inverted hexagonal structures are also possible as shown below. Reproduced by kind permission of Elsevier from (Hafez and Cullis, 2001)

Historically basic micellar and bilayer structures were first identified and understood more than half a century ago, with lipids having already been identified as oily in nature by the late 18th / early 19th centuries (Chand and Srinivasan, 1904). In the 1920s, Fricke determined, by measuring the capacitance due to red blood cells, and allowing for their shape, that their cell membrane must be 3.3nm thin (Fricke, 1925a,b). This was incorrectly interpreted as implying a mono-layer structure. The first experimental demonstration of the existence of a bilayer was identified by Gorter and Grendel utilising Langmuir techniques (Gorter and Grendel, 1925). The total lipid extract from samples of mammalian erythrocytes was spread into a continuous monolayer at the air-water interface within a Langmuir trough. The interfacial area was measured and compared to an estimate of the total surface area of the erythrocytes themselves. It should be noted that some errors were made, the existence of membrane proteins was not yet known, in addition the degree of lateral membrane pressure of both the erythrocytes and the created monolayer were unknowns. However controlled across many measurements, an approximate ratio of monolayer area to erythrocyte membrane area of 2:1 emerged and was correctly interpreted as a lipid bilayer structure for the cell membrane.

In an actual cell membrane, in addition to the lipid content, there is also a high density of proteins present ( $> 3 \times 10^4 \mu\text{m}^2$ ) (Quinn et al., 1984). As a result in experiments involving actual cell membranes, changes in lipid behaviour due to protein-lipid interactions must be accounted for.

Although the basic lipid structure of the bilayer was resolved by 1925, the structure including protein was not. Various models were proposed prior to 1970 in order to explain protein association with the membrane. These competing models were resolved with the Singer-Nicolson, fluid mosaic model in 1972 (Singer and Nicolson, 1972). Singer and Nicolson proposed that the cell membrane comprised a two-dimensional (2D) fluid of lipid molecules with which proteins could associate in one of two primary ways. As shown in figure 1.7, transmembrane proteins, containing long-chain hydrophobic regions, can transect the bilayer. These proteins can diffuse around the bilayer (Edidin et al., 1976), but are fixed within it as it is energetically unfavourable to remove their transmembrane (hydrophobic) domains into water (Moon et al., 2013). Secondly, proteins can be anchored

to lipids within the bilayer, thereby remaining external to it. This model has been widely supported by experiment and is almost universally accepted.

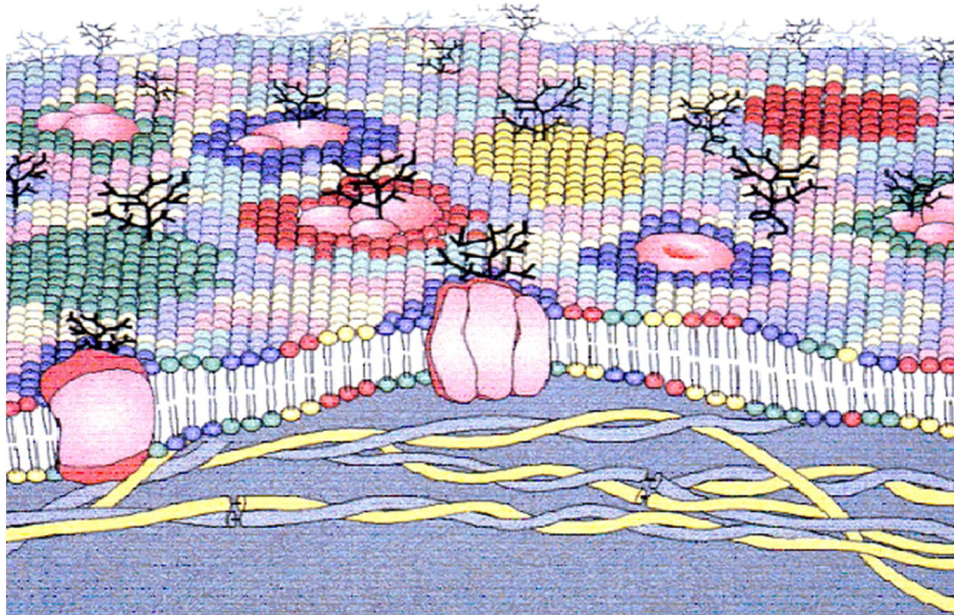
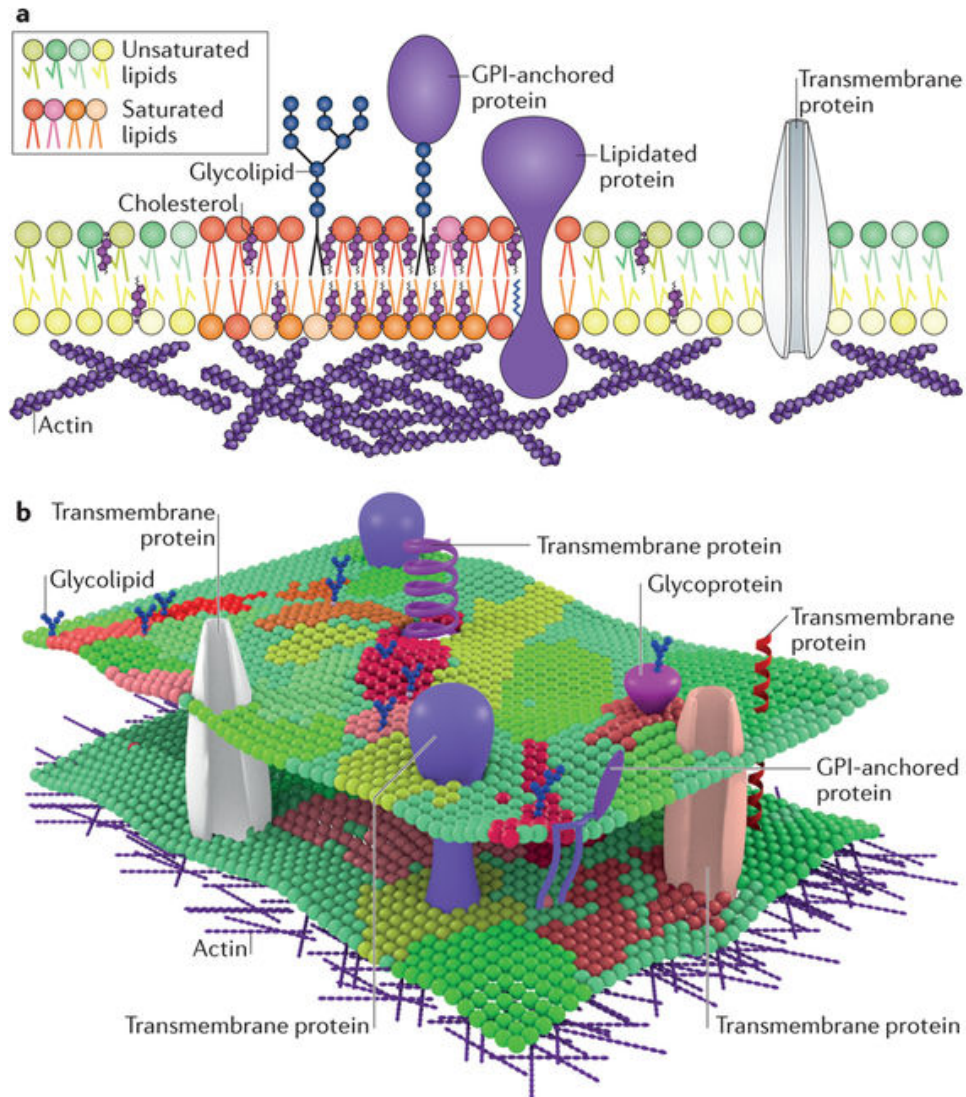


Figure 1.7: Modern interpretation of the Singer-Nicolson fluid mosaic model, taking into account lateral membrane heterogeneity due to preferential lipid - protein sorting leading to the formation of functionally specific membrane regions. Figure reproduced from (Nicolson, 2014) with kind permission of Elsevier.

It should be noted that a naive model for diffusion of lipid and protein membrane constituents leads to an implicit assumption that the bilayer will tend toward homogeneity. More recent models, such as the lipid raft hypothesis, have extended the fluid mosaic view to explain both lipid and protein lateral heterogeneity and observed regions of localised functionality (Simons, 1997). This is phenomenologically shown in figure 1.7, through distinct membrane regions recruiting specific lipid-protein types.

Foremost amongst models extending the Singer Nicholson model are lipid rafts (Simons and Sampaio, 2011). Lipid rafts are seen as phase-separated lipid domains. These domains form naturally as a result of thermodynamic considerations and due to differing headgroup and acyl chain structures of the lipid constituents. Lipid rafts are defined as heterogeneous, transient structures characterised by a more ordered and dense packing of their lipid constituents. As shown in figure 1.8 dense packing requires that the lipids involved possess a molecular conformation allowing for close association with nearest neighbours (Sezgin et al., 2017). Saturated lipids with long, straight acyl chains, and planar sterol molecules are well suited since they can closely align to each other (Róg and Pasenkiewicz-Gierula, 2006). This both increases the density of packing and the electrostatic energy associated with their interaction.



Nature Reviews | [Molecular Cell Biology](#)

Figure 1.8: Lipid rafts are seen as a transient enrichment of saturated lipids, cholesterol, sphingolipids, transmembrane and GPI anchored proteins (a, top). Simplistic binary models of the plasma membrane pertain to raft versus no raft regions, reality is more complex with many possible membrane states mixing properties of both raft and non-raft phases (lower). Figure reproduced from (Sezgin et al., 2017) with kind permission of Nature reviews.

The lipid behaviour considered thus far does not fully account for the environment present within an actual cell. The cellular membrane is a complex, dynamic and highly specialised environment. In order to fully understand the nature of an actual plasma membrane, one must take into account interactions and behaviour due to lipid-lipid, lipid-protein and protein-protein interactions (Lingwood and Simons, 2010). As a result of this complexity, but also due to imposed experimental limitations, many theoretical models have been proposed to explain the physical and chemical properties of these interactions at the micro and nanoscale (Klotzsch and Schütz, 2013).

Lipid-protein interactions can occur through a variety of mechanisms, as suggested in figure 1.8. These can be considered as either passive or active. Passive lipid-protein interactions are driven by hydrophobic considerations rather than an active binding between proteins and lipids (Kobayashi et al., 1998). Transmembrane proteins possess regions comprised of amino acids with apolar side chains such as tryptophan (Engelman et al., 1986). In aqueous solvent, these regions are naturally sequestered within the interior of the lipid bilayer: energy would be required to remove them into solution (Dan and Safran, 1998). Spatial dimensions of (hydrophobic) protein transmembrane regions are not constrained by the dimensions of the lipid bilayer. This can result in mismatch between bilayer thickness and the length of the protein transmembrane region (Mouritsen and Bloom, 1984). As a result, hydrophobic protein moieties could be exposed to water. This energetically unfavourable interaction can drive selective recruitment of longer chain lipids which then shield the transmembrane domain from water. This model is known as the 'mattress' model (due to an envisaged undulating, mattress like structure) and can drive preferential lipid recruitment increasing local membrane heterogeneity, as shown in figure 1.9. This cycle can be seen to obey positive feedback, a protein preferentially recruiting long chain lipids, will form a membrane region suited to other similar proteins (Mouritsen and Bloom, 1993). Thereby the lipid membrane can acquire local functionality through localised passive retention of certain protein types.

In addition, active lipid-protein interactions are present due to binding motifs within certain proteins. Examples of active lipid binding proteins are those with Pleckstrin homology domains (PH Domains) (Ferguson et al.,

1995, Lemmon and Ferguson, 1998) and those with cholesterol binding motifs (Fantini and Barrantes, 2013, Li et al., 2001). PH domains bind specific phosphatidylinositol lipids and have roles in trafficking and recruiting other proteins to sites on the cell membrane (Funamoto et al., 2001, LEMMON and FERGUSON, 2000). Cholesterol recognition amino acid consensus domains (CRAC) by contrast are present within a wide subset of membrane proteins and facilitate cholesterol binding, in some cases regulating protein function and activity (Epanand, 2006, Insall et al., 1994, Li et al., 2001).

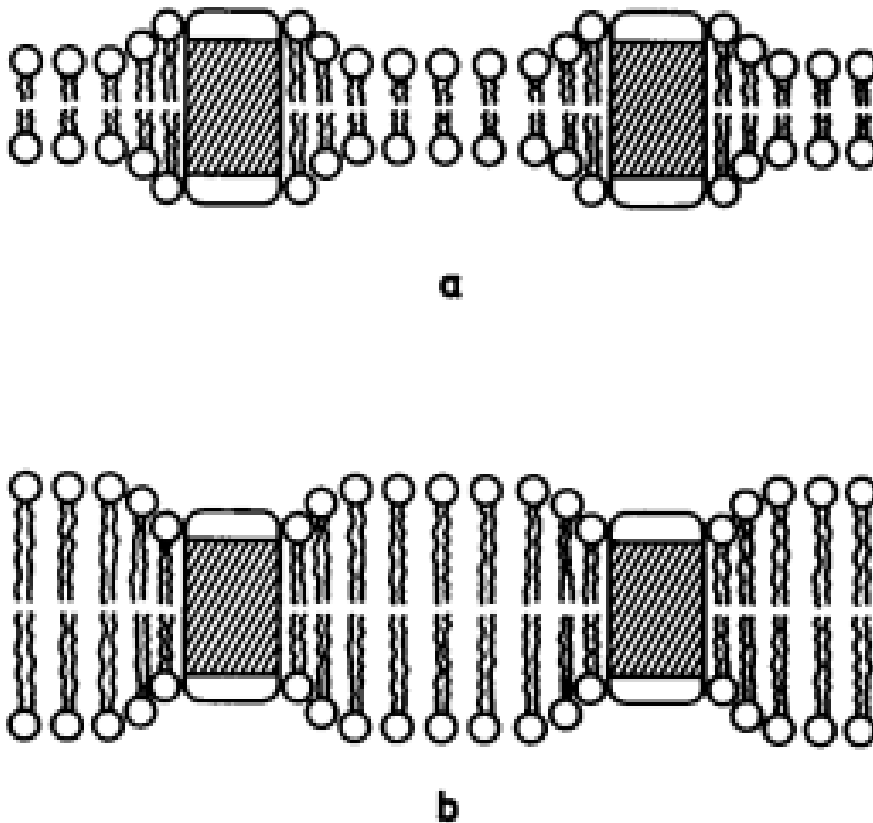


Figure 1.9: Hydrophobic mismatch between transmembrane protein domains and lipid constituents preferentially recruits specific lipids to shield apolar protein regions from aqueous solvent. Figure reproduced from (Mouritsen and Bloom, 1984) with kind permission of Elsevier.

Cholesterol, in addition to its role in regulation of certain proteins also contributes to the regulation of membrane fluidity (Colell et al., 2003). As mentioned previously, the compact planar conformation of cholesterol combined with a charged OH headgroup allows it to pack closely with longer chain, saturated lipids such as Sphingomyelin (Róg and Pasenkiewicz-Gierula, 2006). In combination with Sphingolipids, Cholesterol acts to break molecular order producing the liquid ordered phase in contrast to the solid gel phase seen with pure Sphingomyelin (as discussed in more detail in the next subsection) (Ipsen et al., 1987, Lemmich et al., 1997). In the disordered phase, cholesterol again regulates order, acting to decrease the motility of the lipids (McMullen et al., 2004). These mechanisms are of great biological significance and are implicated in many functional models.

Further to considerations of the variety and complexity of lipid and protein interactions. Studies involving lipids are further complicated by the variety of naturally occurring lipids present. The lipid composition of membranes for a single organism presents significant variation between different cells types, or even between different organelles within the same cell (Heimburg, 2008). In addition, cellular lipid composition is strongly correlated to thermodynamic conditions prevalent at the time of culture and will be seen to change with variation in temperature (de Castro Araújo and Garcia, 2005), pH (Lepage et al., 1987), pressure (DeLong and Yayanos, 1985), and with variations in local electric fields. These effects further support the notion of lipid membranes as being functional structures, in contrast with the traditional view of lipids as a barrier molecule only. The totality of the considerations from this section imply that in order to accurately and reproducibly assess lipid bilayer effects due to the lipids alone, careful control of experimental parameters must be taken. Repeat experiments into lipid bilayer phase, will need to be conducted under identical thermodynamic conditions (pressure, temperature, pH). Due to increased complexity of membrane organisation when considering lipid - protein interactions, this study deliberately limits itself to lipid-lipid interactions only.

### 1.3 Synthetic Model Membranes

This work focuses on the subset of lipid-lipid interactions present in microdomains formed in model membrane systems. Many possible experimental membrane models exist. We have selected and developed giant unilamellar vesicles (GUVs), planar lipid bilayer patches (PLBPs), small unilamellar vesicles (SUVs), surface attached GUV (sGUVs) and planar supported lipid bilayers. Schematic representations of these structures can be seen below in figure 1.10. These models were chosen in order to provide both static and dynamic lipid behaviour across a wide range of membrane sizes, curvatures, constituents and in a variety of buffers.

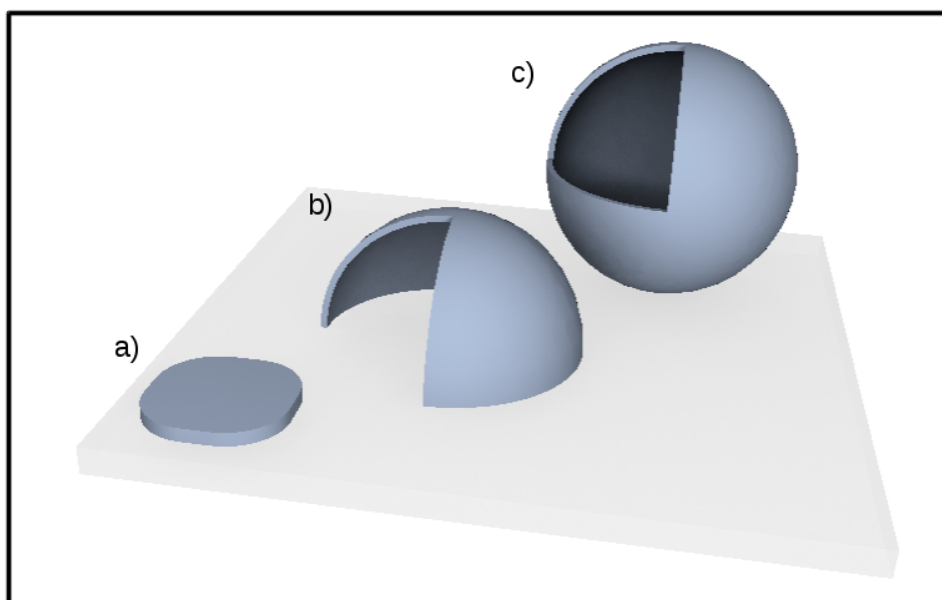


Figure 1.10: Schematic representations of the three primary lipid models used in this study. The Planar lipid bilayer patch (a), surface attached giant unilamellar vesicle (b), and Small or Giant unilamellar Vesicles (c). Spherical structures cutaway to emphasise the bilayer structure. Images not to scale.

PLBPs present a static model of lipid behaviour, charge interactions between the lipid headgroups and hydrophilic substrate render both the patch and its membrane phases immobile (Hamai et al., 2007, Potma and Xie, 2003). This is useful for longer timescales of data acquisition such as those required for chemically specific imaging.

For dynamic investigations, free in solution GUVs and sGUVs present a well formed membrane model. Within these systems, lipids under study are in direct contact with aqueous solvent only and lipid diffusion is thereby unconstrained by the environment. These models therefore represent a closer analogue to the that of an actual cell membrane as compared with the static models.

Over the past 30 years, GUVs have led major progress in our understanding of lipid thermodynamics and behaviour (Chan and Boxer, 2007). The ability to precisely control membrane constituents combined with the ease of self-assembly, controllable nano- to micro-scale object creation and long term stability (Akashi et al., 1996) renders these systems attractive for study in areas as diverse as chemical microreactors (Hase et al., 2007) and drug delivery (Ulrich, 2002). Importantly, they enable the controlled formation and co-existence of lipid ordered and disordered phases in systems comprising mixtures of saturated and unsaturated polar lipids (Baumgart et al., 2003, Veatch et al., 2004, Veatch and Keller, 2003).

The thermodynamic phases present in complex model membranes are grouped according to chain packing order. Lamellar phases are all smectic, possessing both in-plane molecular ordering and a layered 3D structure. The degree of conformational, rotational and translational freedom of the acyl chains leads to their further characterisation into three subgroupings: liquid ordered ( $L_o$ , 'raft-like'), liquid disordered ( $L_d$ ) and gel ( $L_\alpha$ , solid) phases (Van Meer et al., 2008). Predominantly the structure of the lipid acyl chains determines into which phase a given polar lipid will associate, although the head group structure can have an effect as evidenced by changes in labelled lipid phase association upon fluorophore substitution (Baumgart et al., 2007). Mono- and poly- unsaturated chains possess a rigid, cis conformation of CC double bond(s) typically at the chain midpoint ( $\Delta 9$ ) which increases molecular volume and results in an inability to closely pack and interact. These lipids therefore tend to occupy the  $L_d$

phase characterised by loose association and increased intra-bilayer mobility. Saturated lipids can associate more closely, leading to the formation of many charge, Van de Waals and London type interactions between chains. This stabilises lipidic packing, leading to formation of the  $L_o$  raft-like phase with lower lateral and rotational freedom (Lasic, 1993). Gel phases form with predominantly long chain saturated polar lipids. GUVs in the  $L_\alpha$  phase are highly faceted due to increased membrane stiffness. Ternary GUVs comprising DOPC (1,2-Dioleoyl-3-SN-Glycero Phosphatidylcholine), porcine sphingomyelin (PSM) and cholesterol, which are major lipid constituents of all eukaryotic cell lines, represent a relevant model to cell membranes (Devaux, 1991). Coexisting  $L_o$  and  $L_d$  phases can be observed on a macroscopic ( $\mu\text{m}$ ) scale under fluorescence microscopy using certain fluorescent lipid analogues which incorporate into just one phase (Baumgart et al., 2007, Juhasz et al., 2010).

Although GUVs present a closer analogue to an actual cell membrane than supported PLBPs, the components of which remain static due to charge interaction with the hydrophilic substrate, they however can translate in space with obvious limitations for imaging. It is useful to work with a model which combines the microscopic fluidity of GUV membranes, with macroscopically static non-translating structure such as the PLBP. To this end we have developed surface attached GUV (sGUV), as described in detail in section 2.1.3.3

## 1.4 Lipid Rafts

Lipid rafts play an important role across a diverse range of cellular and disease specific processes and models. The first mainstream hypothesis for the existence of lipid rafts was given in the seminal paper by (Simons, 1997), rafts are thought to be transient enrichment of sphingolipids, sterols and specific proteins, within certain membrane micro-domain sites (Ogiso et al., 2015, Simons and Sampaio, 2011). Shown schematically in figure 1.11, lipid rafts are postulated to be between 10 - 200nm in extent within the living cell membrane. Additionally they are posited to exist transiently with lifetimes up to 100 $\mu\text{s}$  (Subczynski and Kusumi, 2003) rendering direct demonstration of their existence challenging with currently available labo-

ratory techniques (Vind-Kezunovic et al., 2008). Due to this difficulty, these living cell estimates for lifetime and size remain contentious. Separation of specific lipids into discrete domains is thought to promote segregation of raft associated membrane proteins, and has provided a theoretical model for local functionalisation of the cell membrane (Lai, 2003). Although direct evidence for the existence of lipid rafts in living cell membranes remains challenging, indirect evidence has been provided by many reports with certain accepted lipid raft systems now known extensively (Sezgin et al., 2017), as detailed below.

Caveolae, localised sack-like invaginations of the plasma membrane, provide evidence for lipid rafts in live cells (Thomas and Smart, 2008). Recruitment of sphingolipids and cholesterol to caveolae sites results in an increase in local membrane curvature leading to an invaginated structure, which is enhanced and stabilised through interaction with the scaffold protein caveolin as shown in figure 1.11. The membrane invagination due to the lipid constituents of caveolae has been evidenced through cholesterol depletion in endothelial cells by the drugs Filipin and Nystatin (Rothberg et al., 1992) resulting in a flattening of the caveolae structure. These results indicate the importance of cholesterol in lipid raft systems, which we will look at further later. Caveolae, and therefore lipid rafts, have roles in signal transduction through shuttling of chemical targets across the plasma membrane (Simionescu et al., 1983). Within this endocytic process, cholesterol is thought to play an important role (Crane and Tamm, 2004) through mediation of membrane phase along the fission / fusion boundary between transport vesicles and the plasma membrane (Simons and Sampaio, 2011). Relative importance of caveolae varies by cell type, reflecting the specialised nature of these structures. In adipocytes, the surface area of the membrane is increased by as much as 50% due to high density of caveolae ( $> 10^6$ ) per cell (Thorn et al., 2003). In contrast primary cultures in bovine brain micro-vessel endothelial cells showed only 3-5% by volume of caveolae at the membrane surface (Guillot et al., 1990). Wide cellular diversification of Caveolae density implies specialisation associated with this raft phase.

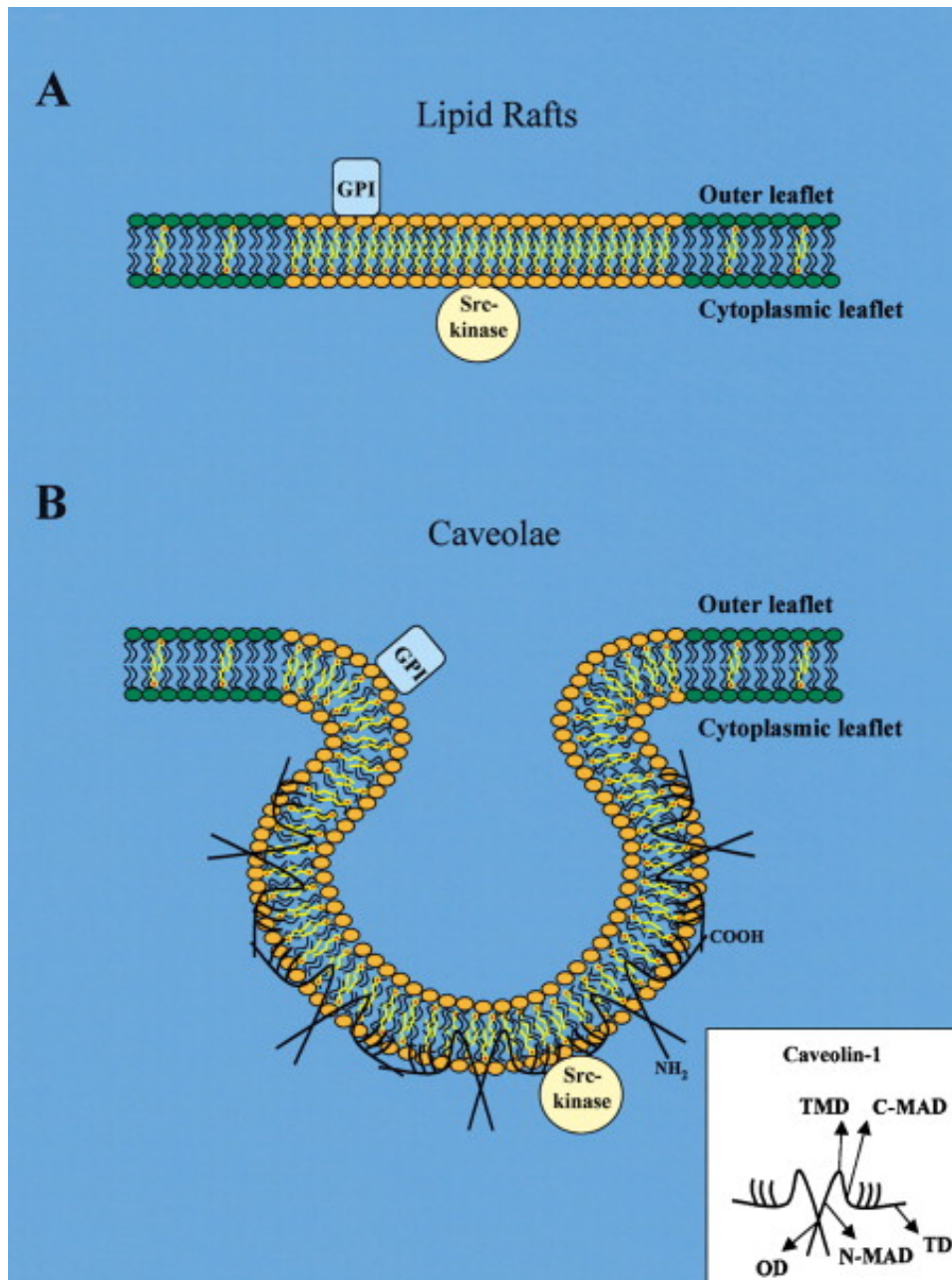


Figure 1.11: Lipid Rafts (shown in A) are distinct areas of lateral heterogeneity enriched in Cholesterol and Sphingolipids (Shown Yellow). By contrast the remaining bilayer is disordered, enriched in Phospholipids. Caveolae (shown in B) comprise a raft domain (Yellow) structurally reinforced by caveolin-1 homooligomers of  $\approx 14$ -16 monomers (shown Black). Figure reproduced by kind permission of Elsevier (Galbiati et al., 2001).

Lipid rafts have furthermore been demonstrated to play a role in heat shock signalling. The highly conserved family of heat shock proteins (HSPs) act in both normal cellular functions and as chaperone molecules in response to thermal stress. HSPs are the most conserved proteins known, existing in all cell types for which studies have been performed (Feder and Hofmann, 1999). In response to cellular stress induced by hyperthermal conditions, HSPs are transiently expressed (Schlesinger et al., 1990). These HSPs assist with maintenance of the correct folding of denatured cytosolic proteins (Jakob et al., 1993). Furthermore, recent studies have demonstrated that HSPs localise within lipid rafts in whole cell membranes (Chen et al., 2005, Wang et al., 2006). Lipid rafts within this context can again be seen to act as membrane organising agents, promoting lateral segregation of HSPs into discrete domains.

Further evidence for the action of lipid rafts occurs as a result of viral transfection events; lipid rafts have been shown to be a requirement for (certain) viral ingress or egress (Brügger et al., 2006). Taking the Ebola and Marburg viruses as an example, studies have shown that the lipid outer leaflet of both contains predominantly raft associated proteins thereby suggesting that viral egress occurs at raft sites (Bavari et al., 2002). Further virus types have also been associated with raft activity, suggesting commonality of the underlying mechanism. The influenza A virus through treatment with the drug family: Interferon. Interferon up-regulates expression of the protein Viperin. In turn Viperin affects membrane fluidity, perturbing formation of lipid rafts. As a result, Influenza A egress from the cell has been shown to be inhibited, suggesting that lipid rafts are a requirement for viral transfection (Wang et al., 2007). The role of cholesterol during raft depletion and HIV transfection has been investigated through cholesterol depletion by methyl  $\beta$ -cyclodextrin (Graham et al., 2003) again showing that perturbation of rafts leads to inhibited viral transfection.

These studies have all associated Lipid rafts with biological processes as the result of indirect measurement. In most conventional studies, lipid rafts and raft associated proteins are identified either through the use of fluorescence based microscopic techniques or through chemical / physical methods that denature or perturb the sample. These existing techniques of analysis, as applied to lipid rafts are reviewed next.

## 1.5 Common techniques for lipid analysis

### 1.5.1 Fluorescence Microscopy

Fluorescence microscopy is ubiquitous in modern biology and has been utilised extensively in order to probe the spatio-temporal distribution and evolution of lipid rafts (Jacobson and Dietrich, 1999). Fluorescently labelled lipid analogues can be used to identify and selectively highlight regions of a sample producing high contrast maps of the distribution of the fluorophore (Munro, 2003). Due to the ease of optical excitation and well defined (wavelength) separation of the Stokes shifted signal; fluorescent probes are widely used (Klymchenko and Kreder, 2014). Fluorophores of relevance to lipid membrane studies appear mainly in the form of labelled lipid analogues (London, 2002). These fluorophores can be easily introduced into a lipid membrane bilayer, normally through direct incorporation into the membrane structure (Baumgart et al., 2007), although post bilayer formation staining has also been performed. A membrane incorporated fluorescent probe may in general display one of three types of behaviour when introduced into bilayers exhibiting complex phase behaviour: preferential partitioning into lipid ordered or disordered domains (a putative model of the lipid raft), fluorophore exclusion from domains or no partitioning behaviour. This preferential partitioning behaviour, within a simple model membrane system can be seen in figure 1.12 below. The exact partitioning behaviour of fluorescent lipid analogues is a complex subject. Historically it was assumed that the structure of the acyl chains of the analogue determined the partitioning behaviour. More recent studies in synthetic lipid membranes have shown that this is not true. Substitution of a head group bound fluorophore can alter phase preference in otherwise identical lipid analogues (Baumgart et al., 2007). Conversely, studies have shown that changes in the lipid constituents can result in (otherwise) identical probes reversing or losing phase preference (Baumgart et al., 2007). In an actual cell membrane, lipids are present in great variety ( $\approx 10^4 - 10^5$  unique species per cell) (van Meer and de Kroon, 2011). Accurate determination of the phase separation behaviour for a given probe under these conditions is challenging. Indeed, during this study I have (anecdotally) observed more evident phase separation into lipid domains when using fluorescently la-

belled model systems compared to nominally identical unlabelled systems. This raises the key question as to whether the partitioning behaviour observed with fluorescent methods is real or the result of a perturbation due to labelling.

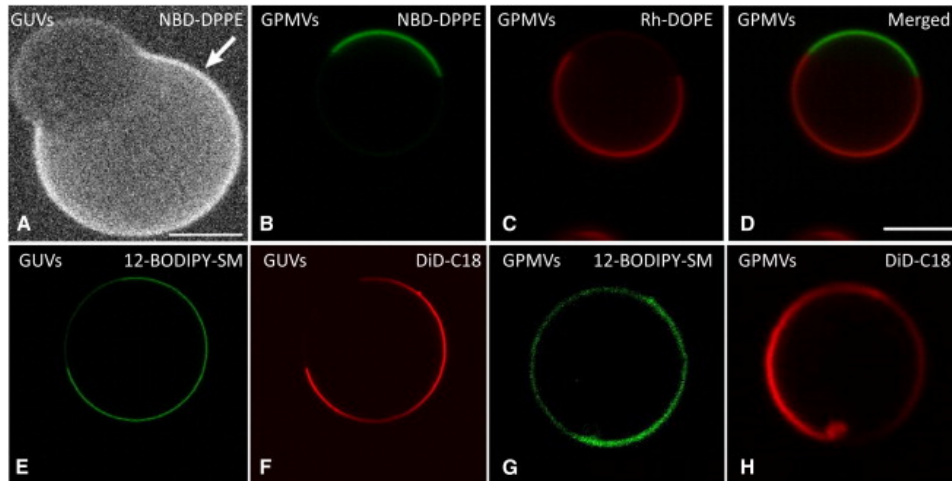


Figure 1.12: Preferential phase partitioning of fluorescent lipid analogues into  $L_o$  and  $L_d$  domains of model and native membranes. (A-D) Confocal microscopy, hemispherical projections of thin walled lipid vesicles labelled with NBD-DPPE or Rh-DOPE. (E-H) Phase partitioning of 12-Bodipy-SM (E and G) and DiD-C18 (F and H) within GUV systems (DOPC/SM/Cholesterol). Figure reproduced by kind permission of Elsevier from (Klymchenko and Kreder, 2014)

### 1.5.2 Cold Detergent extraction

Physical methods for the analysis of lipid rafts often involve disruptive chemical treatment of a sample. Raft associated proteins and lipids are often identified through cold detergent extraction of whole cell membrane fractions (Denny et al., 2001). Sphingomyelins and cholesterol enriched fractions are insoluble in surfactants such as Triton X-100 permitting easy identification and isolation from soluble fractions comprising the remaining lipid and protein content (Melkonian et al., 1999). Proteins collocated within the sphingolipid and cholesterol fractions are assumed to be raft associating (Chamberlain, 2004). Cold detergent extraction, whilst useful, does have issues. Resistance of certain lipid and protein fractions to detergent extraction is a complex process governed by highly dynamic surfactant - substrate

interactions. That these fractions are colocated after processing does not prove the condition existed before (Mukherjee and Maxfield, 2004). In addition, samples are denatured during this form of processing, all spatial information regarding where such fractions might be located within the host cell membrane are lost. Furthermore, it is not possible to observe temporal changes in real time.

### 1.5.3 Metallic nano-particle tracking

Lipid rafts have been extensively investigated under light microscopy through incorporation of lipids or proteins with attached metallic nano-particles or using tagged transmembrane proteins (Murase et al., 2004). In these experiments, it is the diffusion rate of the nano-particle that is measured. As the attached lipid (protein) diffuses, for example through different membrane lipid phases, the diffusion rate of the particle is seen to change (Klotzsch and Schütz, 2013). Compared with chemical methods, diffusion measurements have the advantage of high spatial and temporal resolution. As a result, these methodologies have been applied extensively to studies in living cells. At present, results of nano-particle diffusion studies indicate that lipid diffusion at the cell membrane falls into one of two categories: free diffusion or constrained diffusion (Klotzsch and Schütz, 2013). Under free diffusion, the lipids appear unencumbered and may move about the membrane over distances approaching the micrometer scale. Constrained diffusion occurs when lipids encounter a boundary present at the membrane. This boundary has been attributed to a set of transmembrane proteins which can in general be anchored to the cytoskeleton via cytosolic protein structures (Fujiwara et al., 2002). Lipids diffusing against protein boundaries may encounter permanent entrapment within a localised region or may overcome the resistance of the boundary and move to a new membrane location: the timescales for this process can vary widely.

Unfortunately, as with other methods reviewed, nano-particle diffusion suffers significant drawbacks. The size of nano-particles used is typically in the range of 10-40nm. These particles are massive by comparison to the lipid (protein) to which they are bound. Therefore the diffusion rates are not representative of the natural lipids (proteins) themselves. Secondly,

localised membrane heating due to strong light absorption from metallic nano-particles can result in a perturbation of the membrane state or phase (Urban et al., 2009), thereby rendering results inaccurate. The presence of a nano particle can also cause localised changes in membrane curvature as the bilayer conforms to the nano particle surface. This can induce localised recruitment of lipids to each bilayer leaflet in order to minimise the bending energy of the interaction. This again perturbs the natural state of the membrane within the vicinity of the particle (Wang et al., 2008).

## **1.6 Imaging Modalities**

### **1.6.1 Historical development**

#### **1.6.1.1 Quantitative differential interference contrast microscopy**

Differential interference contrast (DIC) microscopy is a label free imaging technique invented by Georges Nomarski at the Zeiss corporation in the 1950s (Allen et al., 1969). DIC is a widely used technique for the visualisation of transparent (phase) samples both in Biology but also more widely throughout industry such as semiconductor electronics production and testing (Wilhein et al., 2001). The popularity of DIC stems from its inherent ability to visualise non-absorbing, phase objects without the use of exogenous stains. DIC also provides a high level of sensitivity with respect to the axial thickness of the objects as will be shown in section 3.3 where changes in thickness of single lipid bilayers are mapped under DIC to the sub-nm level.

Phenomenologically, as shown in figure 1.13 standard DIC microscopy is an interferometric technique in which initially unpolarised light is split via simple linear polariser into two mutually coherent, orthogonally polarised field components. These components are then spatially offset from one another, along a particular direction, through the action of the Nomarski prism and brought to sharp focus at the plane of the sample. In the absence of any sample, each component will transit with no change to a second Nomarski prism, which will remove the originally induced spatial offset. The components are then interfered at a second linear polariser crossed with the first. With no effect due to the sample, the crossed polarisers will, in the ideal case, block all light resulting in zero signal at the detector. If how-

ever, as in the more general case, the sample is not homogeneous, the two components will during transit acquire a relative phase shift (since they physically transit different locations in the sample). This will result in a rotation of their combined E-field vector and therefore yield a signal at the detector. Since the resulting signal arises from a relative phase change between components, DIC is incredibly sensitive. In the ideal case, one could consider summing the measured changes in DIC signal, along the offset direction, and thereby attempt to measure the total difference in the sample optical path length (sample phase distribution). This would permit nanometric axial measurements of the sample. Unfortunately the DIC signal is sinusoidal in nature which is not conducive to recovery of the sample phase distribution. In addition, the spatial offset of components occurs only along a single direction, therefore no information is present at right angles to this direction. Various methods, as detailed below have been proposed in order to overcome these issues, linearise the resultant DIC signal and restore information in all directions, techniques which we call quantitative DIC.

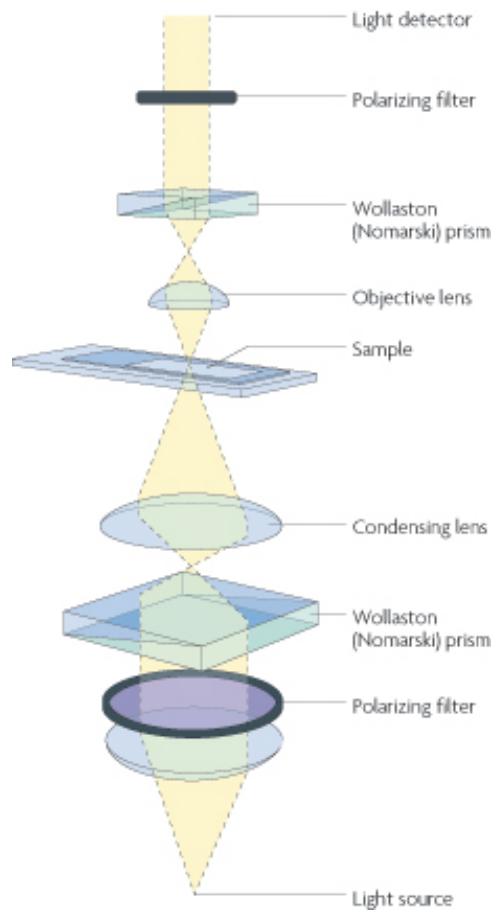


Figure 1.13: Schematic representation of the light train within a standard DIC microscope. Image attributed to Richard Wheeler and released under the GNU free documentation licence, a copy of which is attached to this work.

Quantitative differential interference contrast microscopy (qDIC) is a more recent modification that has been developed by several groups globally since the 1990s. In order to implement qDIC, several limitations inherent to DIC must be overcome. Under DIC the measured response is inherently non-linear (sinusoidal) in nature and varies with changes in object phase between neighbouring points in the sample. These changes arise from both object refractive index variation and thickness distribution. Thus, DIC images encode information regarding local phase changes which obscure the global object phase distribution and in which we cannot deconvolve object thickness from refractive index. In addition, DIC response has a defined directionality imposed by the experimental setup. Phase information is absent orthogonal to this direction. For complicated samples these idiosyncrasies create issues for the simple interpretation of experimental data (Padawer, 1968). As a result of this, most groups developing qDIC have focused on implementing methods that attempt to extract the object phase distribution directly and to ensure that information is obtained in an isotropic manner.

The group of Cogswell et al, has made significant contributions to the field of qDIC since the early 1990s. They have proposed alternate DIC setups such as geometric phase shifting (Cogswell et al., 1997) which separates contributions to image contrast attributable to absorption and phase separately. This permits application of complex phase shifting algorithms in order to extract the object phase, whilst excluding absorptive artefacts. They have also developed both theory and experimental apparatus for confocal qDIC (Cogswell and Sheppard, 1992) which assists in rejecting phase changes that could arise as the result of objects out of focus. In order to remove directionality of the DIC response and extract quantitative information they have proposed a system of repeated imaging in orthogonal directions. Thus each image encodes information about the object phase along a different orthogonal basis. Combined with advanced geometric phase shifting and spiral integration the object phase can be recovered isotropically (Arnison et al., 2004). Other groups have also developed modified DIC setups to permit quantitative imaging. These include the extension of DIC to X-ray imaging (Nakamura and Chang, 2012) and structured aperture illumination (Cui et al., 2008) the exact details of which are unnecessary for the present

study.

Unfortunately, common to all of these qDIC techniques is the use of custom equipment, laborious acquisition procedures and/or the use of advanced software processing techniques. In section 1.6.2.2, I detail the theory underlying a new qDIC technique that I have implemented (Theory: Prof W. Langbein). By contrast to previous techniques, this new method uses a standard DIC capable microscope, acquisition without sample rotation and simple Fourier domain integration to extract the object phase distribution. Under these experimental and analytical conditions, I will also demonstrate that the measured DIC response is linear thereby permitting accurate, quantitative assessment of the thickness of nanometrically thin phase objects.

### 1.6.1.2 CARS Microscopy

Coherent anti-Stokes Raman scattering (CARS spectroscopy) spectroscopy was developed at the Ford motor company in 1965 by Maker and Terhune (Maker, 1965). CARS spectroscopy is a third order non-linear process in which the interference between two light fields is used to coherently drive vibrational resonances of chemical bonds in a sample (see Section 1.6.2.4). These effects are only manifest at high laser intensities for which the E-field strength is comparable to the force felt by atomic electrons. With such force, oscillations of the electron cloud density are no longer linearly proportional to the applied field strength and can be coupled with oscillations of the atomic nucleus along its bond axis. Crucially, coupling to the bond oscillation allows resonant enhancement of inelastically scattered photons present in a third field (often one of the two incoming light fields). This process provides chemically specific information without the use of labels since particular chemical bond oscillations can be directly excited through choice of the relative incident field frequencies.

In its earliest inception, CARS was realised using a pulsed ruby laser as pump field (at frequency:  $\omega$ ), combined with a Raman shifter to generate a second laser beam (Stokes field at frequency:  $\omega - \omega_v$ ) (Maker, 1965). This frequency difference can be tuned to a vibrational resonance ( $\omega_v$ ) of the medium. Maker and Terhune observed that when the excitation pulses

from these beams overlapped both temporally and spatially (i.e. at maximal energy densities), a light field was produced at frequency  $(\omega + \omega_v)$ . This is the CARS signal at the anti-Stokes frequency. Due to constraints imposed by the experimental setup, applications to imaging were not explored at this time.

Laser technology limited the application of CARS to fields outside of fundamental spectroscopy throughout the 1970s, however the underlying theory was developed. The first application of CARS for the generation of imaging contrast was performed in 1982 (Duncan et al., 1982). Implementation was enabled by improvement in laser technology, specifically the advent of modelocked picosecond tunable dye lasers. In their proof of concept experiment Duncan et al (Duncan et al., 1982) utilised a mode-locked Argon-Ion laser pumping two dye lasers to produce beams at the Pump and Stokes frequencies with 80MHz repetition rate and 6ps duration. This source enabled a high peak power at acceptable average powers, and the high repetition rate allowed implementation of fast scanning (note that the Ruby laser has repetition rates in the range of 10Hz). Imaging was performed using galvo-mirrors to raster scan the samples, but a non-colinear geometry was used limiting the spatial resolution. Although this early realisation of a CARS microscope could have led to widespread adoption, this did not occur. In their 1982 paper (Duncan et al., 1982), the researchers were able to demonstrate biological imaging of onion skin saturated with heavy water at the  $2450 \text{ cm}^{-1}$  vibrational band. This enabled high imaging contrast between the cytoplasm and the rest of the cell constituents since there are a lack of competing bond resonances around this heavy water mode.

Development of CARS microscopy resumed in 1999 when Zumbusch et al (Zumbusch et al., 1999) utilised intense pulses of near infra-red light, provided by a solid-state Ti-Sapphire laser, to produce CARS under the tight focusing of a high-numerical aperture microscope objective. They were able to demonstrate CARS imaging in transmission (forward) geometry, and showed inherent 3D optical sectioning with resolution (lateral and axial) comparable to that of two photon fluorescence microscopy. At this time, the ability of CARS microscopy for imaging both lipids, within the CH stretch region ( $2850 - 3050 \text{ cm}^{-1}$ ) and proteins ( $1600 \text{ cm}^{-1}$ ) was demon-

strated. Their use of titanium sapphire, infra-red lasers enabled deeper sample penetration depths (relative to optical frequency excitation) and lowered the non-resonant CARS background due to electronic contributions to the third-order susceptibility (see Section 1.6.2.4).

Over the last 15 years, further specialisation of CARS imaging has occurred. First, CARS was extended into the Epi (backwards) imaging regime (Cheng et al., 2001). Epi CARS benefits from improved image contrast when applied to axially thin samples (compared to the light wavelength) as will be demonstrated in section 1.6.2.5. This configuration helps in eliminating the non-resonant CARS background from the bulk surrounding medium (mostly emitted in forward direction). Further developments directed towards reducing or removing the non-resonant CARS background involved polarisation resolved CARS (Saito et al., 2000), hyperspectral CARS (Masia et al., 2015) and heterodyne CARS (Potma et al., 2006).

Hyperspectral CARS microscopy (also applied in this study) involves the acquisition of a stack of CARS images, each at a particular vibrational frequency across a broad frequency range. In this manner, each spatial point (voxel) in the resultant image (2D or 3D) contains spectrally resolved information (Fussell et al., 2013). This permits more specific chemical analysis and differentiation of chemical species present within the sample. To that end, CARS hyperspectral data analysis has been the subject of a number of very recent works (Di Napoli et al., 2016, Guo et al., 2015, Hong et al., 2016, Karuna et al., 2016, Masia et al., 2015). This is because CARS intensity spectra exhibit a dispersive lineshape (due to the interference with the non-resonant background), and are inherently non-linear in the concentration of chemical components (see Section 1.6.2.4) complicating analysis. Recent advances in data analysis utilise the causal relationship between the real and imaginary parts of the complex susceptibility (Kramers-Krönig relations, PCKK), and enable the recovery the imaginary part of the third-order CARS susceptibility from the measured CARS intensity spectra. This yields a 'Raman like spectrum', linear in the concentration of chemical components, and free from the non-resonant background. An alternative method for phase retrieval, the maximum entropy method (MEM) is also widely used in the literature. Unlike the Kramer-Kronig methods, maximum entropy determines an estimate of the slowly changing CARS non-

resonant background, in order to extract the spectral distribution which best describes the data based upon Bayesian principles (Rinia et al., 2007). The two methods have been shown to be equivalent, in terms of the resultant 'Raman like' spectra (Masia et al., 2015).

### 1.6.1.3 Stimulated Raman Loss Microscopy

In stimulated Raman scattering (SRS), the same third-order nonlinearity as in CARS is observed. However, the components overlapping with the excitation fields are detected. These are the CARS of the Stokes, overlapping with the Pump, giving rise to Stimulated Raman loss (SRL) of the Pump, and the coherent Raman scattering (CRS) of the Pump, overlapping with the Stokes, giving rise to stimulated Raman gain (SRG) of the Stokes. Due to the phase-locked interference of these signals with the excitation fields, the amplitude change (i.e gain or loss) is given by the imaginary part of the CRS susceptibility, resembling a Raman spectrum, while the real part leads to a phase modulation. When detecting the field intensity, a Raman like spectrum is therefore recovered. Another way of understanding this process is using a fully quantized description, in which one photon transferred from the Pump to the Stokes while exciting a vibration (phonon) in the material (Nandakumar et al., 2009). SRL is measured as pump intensity decrease ( $\Delta I_p$ ), while SRG is measured as Stokes intensity increase ( $\Delta I_s$ ). As discussed, the CARS process (section 1.6.1.2) uses principally the same polarisations. However, when detecting the CARS intensity, the signal contains a mixture of a non-resonant contribution due to an electronic, non-resonant contribution to the third order susceptibility, and a vibrationally resonant contribution. CARS spectra therefore present a dispersive lineshape as described in section 1.6.2.4. In SRS, instead, as described, the non-resonant contributions are giving rise to phase modulation.

SRS was first observed in 1962 (Woodbury and Ng, 1962) from nitrobenzene at 0.767 $\mu\text{m}$  using a Ruby Laser. During the 1970s extensive development and use of stimulated Raman spectroscopy (SRS) was employed for studies in gaseous and condensed matter phases (Eesley, 1979, Owyong, 1978). In spite of these advances in spectroscopy, SRS mi-

scopy has been held back due to the low levels of SRS signal produced. The magnitude of the SRS response is proportional to the Raman response (Nandakumar et al., 2009) but is present at frequencies contained in the excitation and so must be separated from their contribution. Typically the ratio of SRL signal to pump would be  $\frac{\Delta I_p}{I_p} < 10^{-4}$  (Freudiger et al., 2008). Recent developments in SRS have therefore focused on better methods to isolate signal from excitation.

Femtosecond SRS microscopy was developed in 2007 (Ploetz et al., 2007). It uses a combination of a picosecond, spectrally narrow Pump beam combined with a femtosecond, broadband Stokes beam. This technique has several advantages. The interference of a spectrally broad Stokes with the narrow Pump can simultaneously excite many vibrational modes of the sample which can then be acquired in parallel. There are several factors against the adoption of femtosecond SRS: high pulse power ( $\sim 270$ nJ) which causes photo-damage in delicate biological samples and the low laser repetition rate, which inhibits fast imaging.

An alternative method to implement SRS was demonstrated in 2008 (Freudiger et al., 2008) and independently in 2009 (Ozeki et al., 2009). Under this approach high repetition rate (76Mhz) picosecond lasers can be used. This enables fast imaging with pulse duration similar to relevant condensed and liquid phase coherence timescales, which are also of the order of a few picoseconds. These conditions are well suited for chemically specific imaging of biological samples. In order to separate the SRS intensity from the excitation and exclude noise, the Stokes (SRL) or Pump (SRG) beam are modulated (In this case at 1.7MHz). Considering the SRL process, pump beam attenuation only occurs simultaneously with stimulated emission of a Stokes Photon. This requires that the Pump-Stokes optical frequency difference is close to a Raman frequency of the medium and that the Stokes beam is present. Therefore fast binary amplitude modulation of the Stokes beam switches on and off the SRL process, transferring the modulation (at resonance) to the pump beam. For detection, lock-in amplification is used, the internal timing of which is phase locked to the modulation frequency. This enables fast sampling of the Pump intensity, in phase with its acquired modulation. The difference ( $\Delta I_p$ ) is measured between maxima and minima of the Pump intensity corresponding to the

SRL signal. For SRG the pump is modulated with the modulation transfer to the Stokes, which is then measured to determine  $\Delta I_s$ . Off resonance no intensity change occurs, thus corresponding to zero SRS signal, however there are systematic backgrounds which can occur due to the nature of this setup. Two photon absorption within the sample can produce bleaching, leading to the formation of a changing background. In addition, Kerr-lensing effects caused by the nature of the modulation and its effect upon the propagation direction of the signal can lead to an additional modulation of the detected amplitude. With lock-in detection at high frequencies, at which microphonic and classical laser noise is suppressed, the shot-noise limit can be reached. SRG has been measured down to  $\frac{\Delta I_p}{I_p} < 10^{-7}$  at an average laser power  $< 40\text{mW}$  (Freudiger et al., 2008). The shot noise limit is around  $10^{-8}\text{Hz}^{-1/2}$  at this power. As a result, SRS is capable of producing high contrast, chemically specific, background free imaging and is ideally suited to biological samples (Signal to noise is comparable between SRS and CARS).

## 1.6.2 Theoretical development

The microscopic techniques used in this study can be broadly classified into linear and non-linear optical methods. In order to elucidate the physical basis of these techniques, let us briefly review the nature of the light-matter interaction occurring in these cases.

Optical radiation incident upon a medium can in general be absorbed (and eventually re-emitted), scattered or transmitted. Contrary to absorption, scattering occurs for all values of the incident optical frequencies (sub-resonant frequencies) relative to the transition frequencies in the medium (although scattering cross-sections are usually enhanced at resonance conditions). The spectrum of the scattered light generally contains an elastic contribution (Rayleigh scattering) where the frequency of the scattered light is equal to that of the incident light, and inelastic contributions where the frequency is different. For the case of vibrationally resonant Raman scattering, the frequency difference between the incident and scattered photons is equal to the transition frequency between two vibrational energy levels of the medium. When scattered photons have lower (higher) frequency,

the process is called Stokes (anti-Stokes) scattering (Raman and Krishnan, 1928). Many spectroscopic and microscopic techniques have evolved to take advantage of this phenomenon. Knowledge is gained of the vibrational energy levels of the medium, whilst using light at optical frequencies. This can be used to understand the chemical structure and map spatial distributions of chemical species with the high spatial resolution provided by focusing fields at the optical wavelengths (400-800nm), as opposed to vibrational infrared absorption.

By contrast, emission-based fluorescence microscopy uses the electronic structure of the sample in question. Chemical contrast can be generated through the use of either exogenous or endogenous labelling. Fluorescence imaging for cell biology applications is wide-spread and relatively simple to implement experimentally due to the inherent properties of the fluorophore: typically large frequency separation (Stokes shift) between the absorption and emission maxima, typically large absorption cross-sections (relative to Raman), high (>50%) quantum efficiency and low rates of photobleaching ( $\Phi_b$ , the probability of a photobleaching event per photon absorbed is  $\approx 10^{-6}$  for most organic dyes (Hinterdorfer and Van Oijen, 2009)). However, the use of exogenous dyes or stains targeted at the particular structure or molecule of interest raises questions as to whether what is observed is real or an artefact, since many studies have indicated a perturbation of native behaviour caused by the incorporation of a fluorescent label (Birch et al., 2017, Bouvrais et al., 2010, Garvik et al., 2009, Leung and Thewalt, 2017).

As a way to overcome the need for fluorescence labelling, vibrational microscopy based on Raman scattering of endogenous chemical bonds has become increasingly applied for imaging in cell biology (Movasaghi et al., 2007).

### 1.6.2.1 Induced Polarisation

In the presence of an optical electric field ( $E$ ), a macroscopic polarisation ( $P$ ) is induced in a medium. When the applied E-field is weak in comparison to the atomic electric field, the force required to displace the electron density distribution can be assumed linear with the magnitude of the dis-

placement. The driven displacement of the electrons with time can then be described as a harmonic oscillator and the induced polarisation of the material is linear in the applied E-field:

$$P = \chi_E \epsilon_0 E \quad (1.1)$$

Where

- $P$  is the macroscopic polarisation density (dipole moment per unit volume) of the medium
- $\chi_E$  is the (linear) susceptibility
- $\epsilon_0$  is the permittivity of free space (Unit  $C^2 N^{-1} m^{-2}$ )
- $E$  is the applied E-field (Unit V/m)

Non-linear optical effects manifest at much higher light intensities for which the E-field component of the radiation is becoming comparable in strength to the atomic field ( $\sim 10^8$  V/cm) (Potma et al., 2012). In this regime the displacement of the electrons exceed the simple harmonic oscillator approximation. When this occurs, the induced dipole moments of the atoms / molecules in the medium (and therefore the macroscopic polarisation) cannot be assumed to vary linearly with the incident field. In other terms, past a certain field strength, the susceptibility will tend to saturate. As a result, higher order components of the susceptibilities begin to exhibit non-vanishing magnitudes. The non-linear susceptibility, like its linear counterpart remains a property of the material, describing the magnitude of the material polarisability in each direction, in response to an applied E-field component in each direction. To describe nonlinear phenomena at various orders in the E-field, the polarisation can be expanded as a Taylor series over powers of the E-field as:

$$P = \epsilon_0 \left[ \chi^{(1)} E^1 + \chi^{(2)} E^2 + \chi^{(3)} E^3 + \dots \right] \quad (1.2)$$

Where

- $\chi^{(n)}$  is the nth order susceptibility (generally these are n+1 order tensors)

- $E^n$  are the  $n$ th power of the field

As a result, an induced polarisation, and in turn radiation, can be generated at optical frequencies which are nonlinear combinations of the optical frequency of the incident E-field, for example second harmonic generation via  $\chi^{(2)}$  (note that second harmonic generation is utilised for frequency doubling many commercial solid state near-infrared lasers to generate visible light outputs). For the CARS and SRS methods discussed in this study, the effects arise as a result of the third order susceptibility  $\chi^{(3)}$ . We note that the  $n$ th order susceptibility is described by a tensor of rank  $(n+1)$  thus allowing for response to occur along different axis, in response to polarised E-field components (Cheng et al., 2002c).

Equation 1.2 assumes that a single field component is used (at a frequency  $\omega$ ), to manifest non-linear effects. More in general a single field, described by a sum of components at different optical frequencies can be combined to generate nonlinear effects. For example, a field with components having an optical frequency difference which coincides with a vibrational resonance in a medium can drive a nonlinearity which is resonantly enhanced by the vibrational response of the medium. Thus, non-linear optics provides a method to drive and probe vibrational properties of a medium, utilising optical frequencies. This is the basis of the CARS and SRL techniques utilised in this study (Potma et al., 2012).

### 1.6.2.2 Quantitative differential interference microscopy

qDIC is conceptually different to the other label free imaging modalities employed in this thesis. I have developed a method to measure the axial thickness of nanometrically thin dielectric materials in transparent samples (lipid bilayers in our case) with high precision, through modification of conventional differential interference contrast (DIC) microscopy.

As shown in figure 1.13 DIC is an interferometric technique in which an initially unpolarised illumination beam is sheared into two linearly orthogonally-polarised, mutually coherent components through the combined action of a polariser, a wave plate and Nomarski prism (Padawer, 1968). Each component transects the sample at a slightly different position along a well-defined shear direction. Due to this spatial offset, changes in the optical

path length between neighbouring points in the sample manifest as a respective change in phase of one beam with respect to the other. Following egress of the object, the beams are sheared back together by an inverted Nomarski prism. The polarisation status of the combined beams is analysed through the use of a second polariser crossed with the first. If during sample transit the relative phase between beams has been altered, rotation of the combined E-field vector occurs, permitting transmission through the final polariser. Thus phase change is encoded as an intensity change in the final image (Allen et al., 1969).

In order to understand the principle of qDIC and how it has been used for quantitative analysis in our measurements, we present here its theoretical description. We start by introducing the incident light field in DIC after transit through a so-called De Senarmont compensator, consisting of an adjustable linear polariser and a quarter wave plate, which enables the introduction of an adjustable phase offset. In general, elliptically polarised light is obtained, described by the light field  $E_i$  (McPhee et al., 2013):

$$E_i = \frac{E_0}{\sqrt{2}} \begin{pmatrix} 1 \\ e^{i\phi_0} \end{pmatrix} \quad (1.3)$$

Where  $\phi_0 = s\theta$  is the phase offset and  $\theta$  is the adjustable angle of the polariser with respect to the fast axis of the quarter waveplate. Transit of elliptically polarised light through a Nomarski prism in the back focal plane of the condenser lens splits the two polarisation components in direction. The two beams transect the sample at a separation given by the shear vector  $s$ . We vectorially define the position of each beam in the sample plane as  $\mathbf{r} \pm \frac{s}{2}$ . Upon object transit these two beams are shifted in phase, we define these two phases as  $\phi_+(\mathbf{r} + \frac{s}{2})$  and  $\phi_-(\mathbf{r} - \frac{s}{2})$ . After recombination of the two beams at a second Nomarski prism, the output beam is transmitted through a second polariser oriented at  $\frac{-\pi}{4}$ . The output field is therefore given by the Jones matrix expansion over all components:

$$E_{\text{out}} = \frac{E_0}{\sqrt{2}} \begin{pmatrix} 1 & -1 \\ -1 & 1 \end{pmatrix} \begin{pmatrix} e^{i\phi_+} & 0 \\ 0 & e^{i\phi_-} \end{pmatrix} \begin{pmatrix} 1 \\ e^{i\phi_0} \end{pmatrix} \quad (1.4)$$

We calculate the image intensity from this equation by noting that  $I_{\text{out}} \propto E_{\text{out}}^2$ :

$$I_{\text{out}}(\mathbf{r}, \phi) = \frac{I_{\text{in}}}{2} [1 - \cos(\phi - \delta(\mathbf{r}))] \quad (1.5)$$

Here  $\delta(\mathbf{r}) = \phi_+ - \phi_-$  is the difference between the phases of the sheared components after object transit and  $I_{\text{in}} \propto E_0^2$  is the incident intensity. To further enhance image contrast, suppress noise and minimise the effects of uneven illumination we acquire two images at equal and opposite initial phase offsets. A difference image between the two enhances DIC image contrast and suppresses local background. The sum image is proportional to the total incident intensity and can be used for normalisation. Formation of the ratio between difference and sum image therefore removes image local offsets and background whilst enhancing object contrast and providing a normalised quantity independent on input intensity. In the limit of  $\delta \ll \phi_0 < \pi$  equation 1.5 can be linearized in  $\delta$  (using a small angle approximation), the final contrast image is then (McPhee et al., 2013):

$$I_c = \frac{I_+ - I_-}{I_+ + I_-} = \frac{\sin \phi_0}{1 - \cos \phi_0} \delta(\mathbf{r}) \quad (1.6)$$

The contrast image scales proportional to the object phase difference  $\delta$ , and the initial phase offset determines the proportionality constant. For  $\phi_0 = \frac{\pi}{2}$  the prefactor is one and the image contrast is simply the difference in phase. By decreasing  $\phi_0$  the contrast can be enhanced. With  $\phi_0 \cong 25.8^\circ$  (corresponding to a polariser angle  $\theta = 12.9^\circ$ ) the prefactor is 4.36. This contrast increase is gained at the expense of the range for which equation 1.6 is valid. However for a GUV  $\delta = 0.02 \ll \phi_0 = 0.45$  (in radians), a value sufficiently small such that linear approximation holds. We note that, given knowledge of the sample structure, specifically the distribution of refractive indices, the phase determined above can be easily converted into a sample thickness distribution.

### 1.6.2.3 Raman Microscopy

For quantitative, chemically specific analysis of molecules in solutions, Raman spectroscopy or microscopy are widely utilised techniques. Herein, we outline the classical theory of Raman scattering. This theory will also serve

as a basis for understanding CARS and SRS. From a microscopic point of view, let us consider the induced dipolar moment of a single molecule  $\mu_{\text{in}}$ . This will relate to the macroscopic polarisation density  $P$  via  $P = N\mu_{\text{in}}$  where  $N$  is the number density of molecules.

At the molecular level  $\mu_{\text{in}}$  is proportional to the local E-field:

$$\mu_{\text{in}} = \epsilon_0 \alpha E_{\text{loc}} \quad (1.7)$$

Where

- $\alpha$  is the polarisability
- $E_{\text{loc}}$  is the local E-field acting at the molecule

The polarisability is generally a tensor of rank 2, describing the polarisation in each direction due to all components of the incident E-field. Notably, for a molecule,  $\alpha$  will change as a function of the nuclear displacement coordinate relative to the equilibrium position of the motion (Potma et al., 2012):

$$\alpha = \alpha_0 + \frac{\partial \alpha}{\partial q} \Delta q \quad (1.8)$$

Where

- $\alpha_0$  is the polarisability at equilibrium
- $\frac{\partial \alpha}{\partial q}$  is the rate of change in polarisability along the nuclear vibrational mode coordinate  $q$
- $\Delta q$  is a small displacement as a sinusoidal function of time, with vibrational mode frequency  $\nu_v$

This model assumes that the nuclear motion is harmonic, valid for small displacements:

$$\Delta q = A_v \cos(2\pi\nu_v t) \quad (1.9)$$

Where

- $A_v$  is the amplitude of motion

- $t$  is time

A monochromatic incident light E-field is also sinusoidal varying with optical frequency  $\nu_o$ :

$$E = E_0 \cos(2\pi\nu_o t) \quad (1.10)$$

where  $E_0$  is the amplitude of the field. Substituting equations 1.8, 1.9 and 1.10 into equation 1.7 and simplifying yields:

$$\begin{aligned} \mu_{in} = & \alpha_0 E_0 \cos(2\pi\nu_o t) \\ & + \frac{A_v E_0}{2} \frac{\partial \alpha}{\partial q} \{ \cos(2\pi t(\nu_o + \nu_v)) + \cos(2\pi t(\nu_o - \nu_v)) \} \quad (1.11) \end{aligned}$$

The first term, to the right hand side of equation 1.11 describes elastic Rayleigh scattering: light is scattered at the same frequency as the incoming field. The second term has two field components shifted to higher or lower frequency than the incoming field by an amount corresponding to the vibrational frequency. These are the anti-Stokes and Stokes Raman scattering terms (Potma et al., 2012). We note that the second term of equation 1.11 is zero if  $\frac{\partial \alpha}{\partial q}$  is zero. The analysis of the symmetry conditions such that this term is non-zero gives rise to the so-called Raman selection rules, whereby only certain modes of vibration are Raman active. The formalism above has been shown for one vibrational mode, for simplicity. In general, a molecule possesses  $3N-6$  ( $3N-5$  for a linear arrangement) such modes, where  $N$  is the number of atoms within the molecule. The optical response for any mode can be understood via a similar analysis as above.

Raman scattering is a very weak effect. Typically it accounts for only 1 photon in  $10^6$  to  $10^8$  scattered corresponding to typical Rayleigh scattering cross section of  $\sim 10^{-29} \text{cm}^2$  per molecule. Notably, Stokes scattered intensities are significantly higher than anti-Stokes at room temperature for vibrational frequencies above  $200 \text{cm}^{-1}$ , due to the reduced occupancy of excited vibrational states (not included in the classical description shown above) (Smith and Dent, 2013). Moreover, in spontaneous Raman scattering, the motion of the nuclei is driven by thermal effects, hence different molecules oscillate at random phases relative to one another. The collective Raman signal from an ensemble of identical vibrating molecules will

therefore be subject to random phase averaging, and will be an incoherent superposition of the Raman scattered light by each molecule. As a result under Raman the signal intensity is linear with the number density of molecules within the excitation volume. These shortcomings often lead to long integration times and slow imaging / spectral acquisition rates.

It can be shown that Raman scattering cross-sections scale as the fourth power of the optical frequency used (Stokes or anti-Stokes shifted) (Colthup, 2012). Hence, in order to maximise signal, high optical frequencies can be utilised (cross sections are also enhanced when the incident optical frequencies are resonant to electronic transitions-so called Resonant Raman scattering). However, since Raman scattering is often measured at the longer Stokes wavelengths, significant fluorescence emission can overlap with it. Due to the orders of magnitude difference between the fluorescence cross section and Raman cross section of typical molecules, fluorescence can dominate over Raman. Compromises therefore have to be made between optimal laser frequencies for scattering and the need to overcome endogenous fluorescence. During this study, lipid auto fluorescence was observed generated by the 532nm excitation laser. The magnitude of the observed fluorescence easily sufficient to obscure the subtle Raman data. Therefore the samples were carefully photo-bleached prior to acquisition of Raman spectra by observing the video rate feed from the linear ccd and acquiring the known detector offset prior to Raman spectral acquisition.

#### **1.6.2.4 CARS Microscopy**

CARS micro-spectroscopy is a powerful modality for imaging of lipids label-free due to the strong vibrational contrast generated across the characteristic lipid  $\text{CH}_2$  and  $\text{CH}_3$  stretch regions (Potma and Xie, 2003). Variations between different lipid types, both due to spectral changes in CH resonances and density considerations, provides a useful mechanism upon which to generate contrast and discriminate lipid species and ordered / disordered phases in lipid membranes consisting of heterogeneous composition. Raman, as discussed in Section 1.6.2.3, also provides label-free chemical contrast, however due to the long imaging timescales required it is practi-

cally unsuitable, unless used for studying static membrane models.

Under CARS micro-spectroscopy two incident light fields, pump and Stokes, are utilised in order to coherently drive vibrational resonances (rather than relying on thermal population). Since the driven oscillation phase is determined by the applied fields, coherent enhancement of the collective Raman scattered light from several identical bonds, via constructive interference, becomes possible, giving rise to a much stronger anti-Stokes field relative to Raman. Vibrational resonances are driven at the difference frequency between the pump and Stokes fields:

$$\Omega = \omega_p - \omega_s \quad (1.12)$$

Where

- $\omega_p$  is the pump laser angular frequency
- $\omega_s$  is the Stokes laser angular frequency

Let us represent the combined incident field as a superposition of plane waves propagating along the z-direction (Cheng et al., 2002c):

$$E = E_{p0}e^{i(\omega_p t - k_p z)} + E_{s0}e^{i(\omega_s t - k_s z)} + C.C. \quad (1.13)$$

Where

- $E_{p0}, E_{s0}$  are the complex amplitudes of the Pump and Stokes fields respectively
- $\omega_p, \omega_s$  are the angular frequencies of the Pump and Stokes fields
- $k_p, k_s$  are the field angular wavenumbers

An induced dipole with polarisability  $\alpha$  placed into an electric field  $E$  will experience a potential energy  $W$  proportional to the field squared:

$$W = \frac{1}{2}\alpha E^2 \quad (1.14)$$

As a result of this potential energy, the dipole experiences a force given by:

$$F = -\nabla W \left( \frac{\partial \alpha}{\partial q} \right)_0 E^2 \quad (1.15)$$

where we have used equation 1.8 for the induced dipolar moment in the presence of a vibrational mode. This force will then act as the driving term of a forced harmonic oscillator for the vibrational displacement coordinate (Demtröder, 1998)  $\Delta q$ :

$$F \propto \frac{\partial^2 q}{\partial t^2} - \gamma \frac{\partial q}{\partial t} + \omega_v^2 q \quad (1.16)$$

Where the damping term phenomenologically describes line broadening due to coupling of the vibrational mode with the environment.

Calculating  $E^2$ , with  $E$  as the sum of pump and Stokes field (equation 1.13) gives rise to terms at the difference frequency  $\Omega$  (equation 1.12) between the two fields which in turn can resonantly drive the nuclear motion and generate sizeable displacements (while the other higher frequency terms in  $E^2$  are too non-resonant and thus unable to effectively drive the nuclear motion). The induced dipole  $\mu_{in}$  proportional to  $\Delta q \frac{\partial \alpha}{\partial q}$  is then found to be (Demtröder, 1998):

$$\mu_{in}(t) \propto \Delta q \frac{\partial \alpha}{\partial q} E \quad (1.17)$$

$$\Delta q \left( \frac{\partial \alpha}{\partial q} \right) = \frac{1}{2m} \left( \frac{\partial \alpha}{\partial q} \right) \frac{E_{p0} E_{s0}}{\omega_v^2 - \Omega^2 - 2i\Omega\Gamma} e^{i\Omega t} \quad (1.18)$$

All symbols take their earlier meanings,  $\Gamma$  is the Lorentzian linewidth of the resonance. In short, this equation shows that under the combined action of two incident fields, nuclear oscillations are driven at the difference frequency between them. This oscillation is resonant with the vibrational frequency and is proportional to product of both field amplitudes. The magnitude of the oscillation is also proportional to the change in polarisability along the nuclear coordinate  $q$  as seen in the case of spontaneous Raman calculated earlier. The field  $E$  in the dipole equation 1.17 (probe field) is actually the pump field which is scattered anti-Stokes in two-beam CARS. The macroscopic non-linear third-order polarisation arising from this driven mode can then be calculated as  $P(t) = N\mu_{in}(t)$  giving for CARS:

$$P^{(3)}(\omega_{as}) \propto \frac{N}{2m} \left( \frac{\partial \alpha}{\partial q} \right)^2 \frac{E_{p0}^2 E_{s0}}{\omega_v^2 - \Omega^2 - 2i\Omega\Gamma} e^{i(2\omega_p - \omega_s)} \propto \chi^{(3)} E_{p0}^2 E_{s0} \quad (1.19)$$

Thus we formally state the third order, non-linear susceptibility as (Potma et al., 2012):

$$\chi^{(3)} \propto \frac{N}{2m} \left( \frac{\partial \alpha}{\partial q} \right)^2 \frac{1}{\omega_v^2 - \Omega^2 - 2i\Omega\Gamma} \quad (1.20)$$

This non-linear, anti-Stokes polarisation can be seen as radiating a field at the anti-Stokes frequency  $\omega_{as} = 2\omega_p - \omega_s$ , with an amplitude proportional to the number density of molecular scatters. Its amplitude also scales quadratically in the pump field and linearly with the Stokes. Notably, this nonlinear dependence on the incident fields makes CARS microscopy a multiphoton modality with an inherent 3D sectioning capability (since only within the focal volume will the incident photon density be high enough to induce significant non-linear polarisation amplitude). The non-linear polarisation has a resonant behaviour in, ie significant anti-Stokes field will occur for  $\Omega \cong \omega_v$ . This forms the basis of the chemically specific imaging contrast seen under CARS between different molecular species.

The measured CARS intensity is proportional to the square of the non-linear polarisation (Potma et al., 2012):

$$I_{as} = |P^{(3)}|^2 \propto |\chi^{(3)}|^2 I_p^2 I_s \quad (1.21)$$

Where

- $I_p^2$  is the squared intensity of the Pump field
- $I_s$  is the intensity of the Stokes Field

Since  $\chi^{(3)}$  is proportional to the number density of bonds  $N$  present within the excitation volume, the measured intensity of CARS is quadratically dependent upon this density. This arises directly as a consequence of the coherent nature of the CARS signal (constructive interference of scattered light from  $N$  oscillators) and accounts for the increased signal strength compared to Raman.

Since  $\chi^{(3)}$  as given in equation 1.20 above is complex. Considering the real and imaginary components separately (Potma et al., 2012):

$$\Re(\chi^{(3)}) \propto \frac{\omega_v^2 - \Omega^2}{(\omega_v^2 - \Omega^2)^2 + 4\Omega^2\Gamma^2} \quad (1.22)$$

$$\Im(\chi^{(3)}) \propto \frac{2\Omega\Gamma}{(\omega_v^2 - \Omega^2)^2 + 4\Omega^2\Gamma^2} \quad (1.23)$$

We find that the classical derivation of the CARS process yields resonant behaviour that is in qualitative agreement with the observed CARS signal intensity (See figure 1.14 below). The real part of  $\chi^{(3)}$  exhibits a dispersive behaviour, it is non-zero also away from the resonant condition (eg  $\Omega \ll \omega_v$ ). The imaginary part of  $\chi^{(3)}$  has a Lorentzian profile, characterised by the linewidth and related to the Raman signal ( $I_{\text{Ram}} \propto \Im(\chi^{(3)})$ ).

The classical description whilst approximately correct (and useful for an intuitive understanding) is unable to explain all observed CARS features since it does not take into account the quantum nature of the light and matter interaction. Under a quantum mechanical treatment, the discrete electronic and vibrational structure of the matter introduces additional terms into the susceptibility due to non-resonant interactions. Off electronic resonance the susceptibility is represented as a sum of two terms, a vibrationally resonant contribution (which simplifies the expression of  $\chi^{(3)}$  versus  $\Omega$  to a complex Lorentzian for  $\Omega \cong \omega_v$ ) and a vibrationally non-resonant term assumed to be constant and real:

$$\chi^{(3)} = \chi_r^{(3)} + \chi_{\text{nr}}^{(3)} \quad (1.24)$$

Where now the resonant part is given by (Potma et al., 2012)  $\chi_r^{(3)}$ :

$$\chi_r^{(3)} = \sum_b \frac{A_b}{\Omega - \omega_v + i\Gamma_b} \quad (1.25)$$

Where  $A_b$  is the amplitude of the resonance at  $\omega_v$ , of linewidth  $\Gamma_b$ , due to all (b) resonances present.

Due to the additional non-resonant contribution, the observed CARS intensity (proportional to  $|\chi^{(3)}|^2$ ) becomes:

$$|\chi^{(3)}|^2 = |\chi_r^{(3)} + \chi_{\text{nr}}^{(3)}|^2 = |\chi_r^{(3)}|^2 + |\chi_{\text{nr}}^{(3)}|^2 + 2\chi_{\text{nr}}^{(3)}\Re(\chi_r^{(3)}) \quad (1.26)$$

The first term in the right hand side contains only the contribution from resonant, vibrational modes of the molecule under investigation with Lorentz-like lineshape. The second term is a spectrally constant non-resonant background. The third term is an interference between the real part of the resonant signal and the non-resonant background, and is responsible for the

observed, dispersive lineshape characteristic of CARS spectra in regions where  $\chi_r^{(3)}$  is smaller than  $\chi_{nr}^{(3)}$ , hence spectra are dominated by this interference term. This can be seen visually in figure 1.14 below in which I have calculated the form of both the resonant and non-resonant contributions to the susceptibility along with their interference and the resultant spectral profile. By comparison to the Lorentzian lineshape observed under Ra-

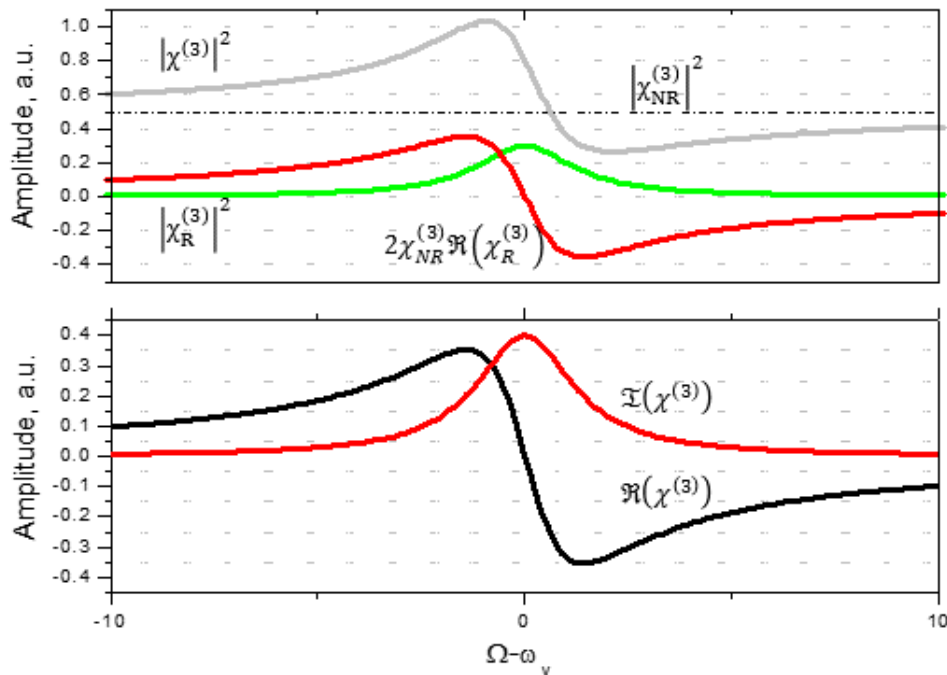


Figure 1.14: Top: Contributions to the observed CARS intensity (gray) due to resonant (green), non-resonant (black) and mixing terms (red). Bottom: Real and Imaginary components of the resonant part of the non-linear susceptibility. Adapted from (Evans and Xie, 2008).

man, CARS spectra comprise both maxima and minima, with the maxima red-shifted with respect to the peak position under Raman. As discussed in the Results, Chapter 4, this CARS non-resonant background and the differential spectral profile have important implications for CARS imaging and data analysis.

### 1.6.2.5 Momentum and propagation considerations

Modern implementations of CARS microscopy are performed under the tight focusing regime with the use of high numerical aperture objective lenses, to achieve high spatial resolution. This provides a range of input spatial propagation vectors. CARS must obey both the law of conservation of energy and that of momentum. Energy conservation dictates that the anti-Stokes field must be at frequency  $\omega_{as} = 2\omega_p - \omega_s$  if the pump and probe fields are at the given frequencies. The momentum of a photon is given by  $p = \hbar k$  where  $k$  is the wavevector for propagation. Hence, conservation of momentum requires:

$$k_{as} = (2k_p - k_s) \quad (1.27)$$

This places a constraint upon the CARS signal directionality and the interaction length with the sample. It can be shown (Cheng et al., 2002c) that the measured CARS intensity is a function of the interaction length  $L$  within the sample and of the wavevector mismatch  $\Delta k = k_{as} - (2k_p - k_s)$ . Within bulk homogeneous media, this dependence can be written as:

$$I_{as} = |P^{(3)}|^2 \propto |\chi^{(3)}|^2 I_1^2 I_2 L^2 \text{sinc}^2\left(\frac{\Delta k L}{2}\right) \quad (1.28)$$

Herein, the significance of a wavevector mismatch becomes apparent. Note that the maximum signal is obtained at a mismatch of zero since  $\text{sinc}(0) = 1$ . This has important implications for forwards and epi propagation of the CARS signal in bulk media. Indeed, it is in the forward direction only that the phase matching condition can be met and  $\Delta k L \approx 0$ .

In the epi direction, the backward propagating CARS wavevectors results in a significant mismatch, which will significantly reduce the measured signal in extended thick media. A wavevector mismatch can still give rise to a significant CARS signal only if:

$$|\Delta k| L \ll \pi \quad (1.29)$$

Note that when high numerical aperture lenses are utilised, the interaction length given by the point spread function along the axial direction is only a few microns in magnitude. The condition in equation 1.28 is therefore generally satisfied in the forward direction. The additional phase mismatch in

the epi direction effectively reduces the interaction length  $L$ . In bulk homogeneous media, this implies to reduce  $L$  to the order of the wavelength of light, therefore significant epi signal can only be realised for thin samples.

This situation is shown schematically in figure 1.15 where the magnitude of the forward to epi signal is drawn aligned to the  $z$  axis, if the sample under investigation is thin by comparison to the laser wavelength, both the epi and forward CARS signals are comparable in magnitude since the relaxed phase matching condition of equation 1.29 is easily met ( $L \approx 0$ ). As the sample thickness increases, incomplete destructive interference of the epi CARS signal occurs, therefore the magnitude of the forward to epi CARS intensity increases (effective increase in interaction length  $L$ ). For samples large compared with the wavelength, little epi CARS signal will be discerned. These considerations have important implications when applied

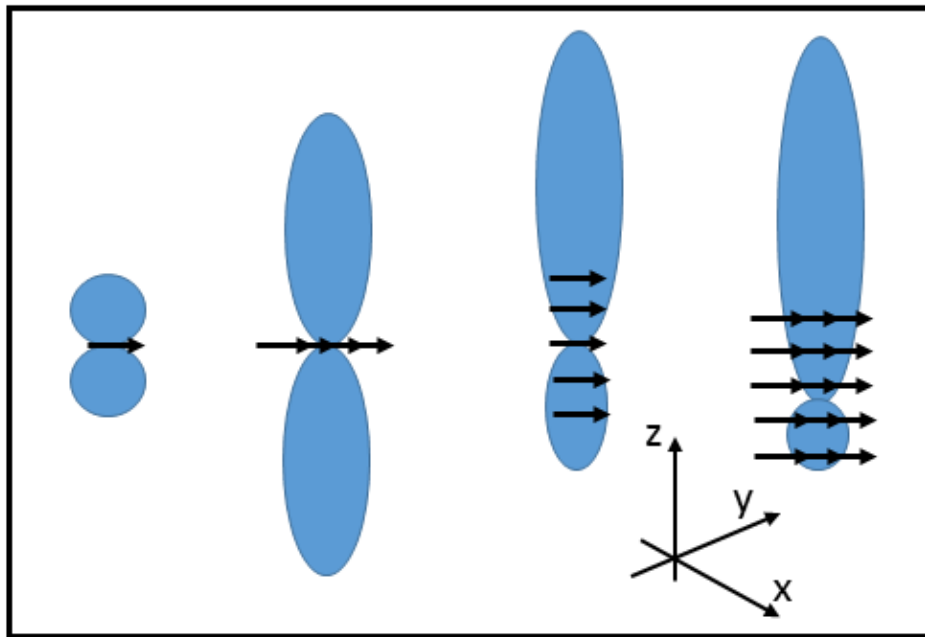


Figure 1.15: CARS Anti-Stokes radiation patterns from single and ensemble Hertzian dipoles due to co-polarized pump and Stokes fields propagating in  $z$ . Adapted from (Cheng et al., 2002a).

to CARS imaging for nanometrically thin samples, such as the  $\sim 4$ nm single lipid bilayers observed during this study. The epi and forward CARS signals are of similar magnitude but are present within a homogeneous

bulk solvent, in this case water or buffer. The epi CARS signal arising from contributions due to the bulk water will be reduced under epi detection relative to the forward direction. Since the CARS signal from water is similar or larger in magnitude to the contribution from a lipid bilayer at frequencies around the CH stretch, epi CARS images possess better contrast than the forward CARS equivalents.

### 1.6.2.6 Stimulated Raman Loss Microscopy

Stimulated Raman loss (SRL) arises from the same physical basis as CARS: The third order, non-linear susceptibility ( $\chi^{(3)}$ ). As stated in section 1.6.1.3, SRL is a Pump-probe process in which simultaneously one photon at a frequency  $\omega_p$  is destroyed and one photon created at a Stokes frequency  $\omega_s$  (Boyd, 2003). Experimentally the process is measured through the attenuation of the Pump beam caused by the stimulated emission of a Stokes photon at vibrational resonance. It can be shown (Freudiger et al., 2008) that the resultant loss in intensity is linearly proportional to both the number of molecules within the excitation volume ( $N$ ) and the Raman cross section  $\sigma_r$ :

$$\Delta I_p \propto -N\sigma_r I_p I_s \quad (1.30)$$

This is advantageous (compared to CARS) when performing data analysis, since comparisons between analyte concentrations are easier (Linear) and spectral information is similar in form (and proportional to) well established Raman data. To understand better this process, we look at the classical description of SRS in the following sections.

Theoretically we may describe SRS by considering the general form of the non-linear polarisability which arises under the plane wave approximation. We model the nuclear oscillation as a classical Hertzian dipole as performed in section 1.6.2.4 for CARS microscopy in equations 1.12 through 1.18.

The induced non-linear polarisation can be shown to be (Potma et al., 2012):

$$P(t) = N \left[ \alpha_0 + \left( \frac{\partial \alpha}{\partial q} \right) \Delta q \right] \left\{ E_{p0} e^{i(\omega_p t - k_p z)} + E_{s0} e^{i(\omega_s t - k_s z)} \right\} + C.C. \quad (1.31)$$

Where all symbols take on their earlier meanings. The form of the driven oscillation  $\Delta q$  is the same derived for CARS and as shown in equation 1.18. Since  $\Delta q$  oscillates at the difference frequency between the Pump and Stokes fields, full expansion of the non-linear polarisation (equation 1.31) contains terms at Stokes, anti-Stokes, Pump and Stokes frequencies. Note also that the expansion contains terms proportional to  $\alpha_0$  corresponding to the linear polarisation and terms proportional to  $\left(\frac{\partial \alpha}{\partial q}\right)$  (non-linear terms). Collecting only the non-linear terms in the expansion, we may write the general non-linear polarisation (Potma et al., 2012) as:

$$P_{NL}(t) = P(\omega_{cs})e^{-i\omega_{cs}t} + P(\omega_{as})e^{-i\omega_{as}t} \\ + P(\omega_p)e^{-i\omega_p t} + P(\omega_s)e^{-i\omega_s t} \quad (1.32)$$

Where  $\omega_{cs} = 2\omega_s - \omega_p$  and  $\omega_{as} = 2\omega_p - \omega_s$  are the coherent Stokes and anti-Stokes (CARS) frequencies. The polarisation arising at the Pump and Stokes frequencies act as the source for Stimulated Raman loss (SRL) and Stimulated Raman Gain (SRG) which are collectively termed stimulated Raman scattering (SRS). Under SRL an attenuation of the intensity of the Pump beam is measured. This arises due to stimulated emission of a Stokes photon with associated energy transfer to the molecule. The polarisation giving rise to this follows from equations 1.31 and 1.32 above and with  $\chi^{(3)}$  as shown in equation 1.20. This SRL polarisation is (Potma et al., 2012):

$$P(\omega_p) \propto \epsilon_0 \chi^{(3)} E_{s0}^2 E_{p0} \quad (1.33)$$

The SRL effect is comparable in magnitude to that of CARS. The detected signal however is not comparable between the two, SRL is weaker and requires more advanced, modulated detection (Potma et al., 2012). As shown in equation 1.33, the polarisation responsible for SRL varies non-linearly with the magnitude of the Stokes E-Field amplitude. This gives rise to the intrinsic 3d sectioning capability seen under SRL since only close to the plane of focus is the photon density sufficiently intense to induce SRL. In addition, since SRL depends upon  $\chi^{(3)}$  its behaviour is resonant in the difference frequency  $\Omega$  as shown in section 1.6.2.4 for CARS which is the basis for the strong contrast seen with all these non-linear techniques.

To calculate the intensity of the SRL signal, a full solution of Maxwell's equations as a function of all four fields ( $\omega_{cs}, \omega_{as}, \omega_p, \omega_s$ ) must be performed. Under a full analysis, the energy exchange between fields and the material, and intra-field exchange must be taken into account. This is beyond the scope of this thesis. Herein I consider the measured intensity qualitatively. Unlike CARS, which probes this disturbance with a third field giving rise to Anti-Stokes emission, under SRL we detect at frequencies close to the Pump frequency ( $\omega_p$ ). As a result, the phase matching condition is simplified and  $\Delta k = 0$ . Under these conditions, it has been shown (Potma et al., 2012) that for an interaction length with the sample  $L$ , the amplitude of the forward propagating stimulated Raman field is:

$$E_p^{\text{stim}}(L) \propto i \frac{\omega_p}{n_p c} \left\{ \chi^{(3)}(\Omega) \right\} E_s E_p E_s L \quad (1.34)$$

Where  $n_p$  is the refractive index of the material at the pump frequency. Since SRL is a coherent process, there exists a well-defined phase relationship between the generating fields and the stimulated field. In the far-field, this phase shift amounts to  $\pi/2$ , which places the imaginary part of the field out of phase with the pump beam. As a result and due to the similar frequencies of Pump and stimulated fields, interference between the two will occur. The total detected intensity is given by (Freudiger et al., 2008):

$$I(\omega_p) \propto |E_p + E_p^{\text{stim}}|^2 \quad (1.35)$$

$$= I_p + \left| \chi^{(3)} \right|^2 I_s^2 I_p L^2 - 2T \left\{ \chi^{(3)} \right\} I_p I_s L \quad (1.36)$$

Where  $E_p$  is the pump beam intensity. Considering the terms to the right hand side of the equality, the first is simply the Pump intensity. The second term is called the intrinsic SRL signal and is similar in dependence and magnitude to the CARS signal. The final term is the interference term which depends upon the imaginary part of  $\chi^{(3)}$ . Within an actual SRL experiment, it is this interference term which is detected:

$$\Delta I_p \propto -2T \left\{ \chi^{(3)} \right\} I_p I_s L \quad (1.37)$$

If we consider figure 1.14, in which the behaviour of the real and imaginary parts of  $\chi^{(3)}$  were shown. The imaginary component has a Lorentzian profile and rapidly vanishes off resonance. This has two effects: the detected

SRL signal is zero off resonance: there is no non-resonant background and the spectral lineshapes are similar to those of spontaneous Raman. At the resonant frequency,  $\text{Im}\{\chi^{(3)}\}$  is positive and therefore our SRL signal manifests as a loss in pump intensity. We note that as given in equation 1.20, is proportional to both the number of molecules in the excitation volume and to the Raman cross section therefore and as stated in equation 1.35, SRL is linear in the concentration of molecules.

## 1.7 Motivation

As discussed above, all existing methods utilised for the study of lipid rafts suffer from severe limitations. Either they denature the samples, or they perturb the system raising questions regarding the relevance of the result. The main motivation of this PhD project was therefore to address these shortcomings, and to develop a suite of novel, label-free optical microscopic techniques directed at studying lipid rafts non-invasively and quantitatively.

We therefore started development with quantitative differential interference contrast microscopy (qDIC), which enables direct assessment of bilayer thickness including inter-phase thickness difference to a sub-nm. With this precision, we have been able to detect phase separated lipid domains in model lipid membranes, with phase assignment consistent with accepted fluorescent techniques. Furthermore, non-linear Coherent Anti-Stokes Raman microscopy (CARS) imaging was developed which enabled us to discriminate lipid phases on the basis of both packing density and chemically sensitive imaging of bilayer components. Stimulated Raman loss (SRL) microscopy, complementary to CARS, was also developed and applied to single lipid bilayers. These label-free techniques were minimally perturbative to the system, hence enabled the observation of the membrane behaviour as close as possible to the natural state. For practical purposes within the duration of this project, and to demonstrate proof of principle application of the techniques, we focused our study on model membrane systems with controlled lipid constituents, rather than cellular membranes, and developed a suite of membrane analogues.

## Materials and Methods

### 2.1 Synthetic membrane Methods

#### 2.1.1 Stock Lipid Handling and preparation

Lipids used in this study are either glycerol- or sphingo-lipids with the addition of the mammalian sterol cholesterol. As detailed earlier, lipids were carefully chosen on the basis of their acyl chain structure such that desired phase separation ( $L_o$  /  $L_d$  phase coexistence) was realised during experiment. These lipids also retain relevance to the basic lipid composition found in mammalian cell types. The primary lipids used were as shown in table 2.1, also listed where available are the miscibility temperatures for the lipids, this is the temperature at which the lipid will 'melt' from the gel phase into the disordered liquid crystalline phase.

Lipid	Chain Length	Saturated / Un-saturated	Double bond position (conformation)	Headgroup	Miscibility Temperature °C
1,2-dioleoyl-sn-glycero-3-phosphocholine	C18:1	Unsaturated	$\Delta 9$ , cis	$C_5H_{14}O^+$ , choline	17 (Silvius, 1982)
Sphingomyelin, Egg	C16:0(86%), C18:0(6%), C22:0(3%)	Saturated	Mixed Sample	$C_5H_{14}NO^+$	39 (Leung et al., 2012)
Sphingomyelin, Porcine	C16:0(2%), C18:0(50%), C20:0(5%), C22:0(7%), C24:0(5%), C24:1(21%)	Predominantly Saturated	Mixed Sample	$C_5H_{14}O^+$ , choline	~39 (Pokorny et al., 2006)
Atto-488 DOPE	C18:1	Unsaturated	$\Delta 9$ , cis	$C_2H_7NO$ , Ethanolamine	Not Established

Table 2.1: Miscibility temperature, structure and headgroup structure for primary lipids, Sterols and synthetic lipid analogues used in this study.

All experimental observations were made with the lipids at ambient temperature, within our laboratory this is generally in the range of 20–22°C. Due to the large difference in miscibility temperature between DOPC and PSM, under experimental conditions phase separation will be present (since the PSM will be sub-miscible). In addition to simple consideration of lipid types, I have considered also effects present due to formation and handling conditions. Lipids, although generally molecularly stable are susceptible to oxidation. Lipid oxides and peroxides have been linked to increased rates of domain formation in synthetic membranes resulting in nascent, non-natural phase behaviour (Muik et al., 2005). It was therefore of the utmost importance to limit the exposure of all stock lipid solutions to the atmosphere, especially at elevated temperatures. In addition, during certain procedures, voltages are present across deposited layers of lipid. High voltages could also induce the formation of lipid peroxides (Zhou et al., 2007), therefore maximum voltages were held low (up to 2V) to prevent such issues during all experiments. All stock lipids as provided are sealed under inert atmosphere (Argon). To enable safe, long term handling of lipids, all procedures were conducted within the confines of a nitrogen cabinet under conditions of constant, forced N<sub>2</sub> flow and positive internal pressure. Lipids were stored in organic solution with high performance liquid chromatography (HPLC+) grade solvents (Sigma-Aldrich) used throughout. When not in use, lipid solutions were sealed under Nitrogen and immediately placed within an airtight container at ≈-25°C until required. In this manner lipids could be retained and used for up to 6 months before new samples were required.

All non-fluorescent lipids used in this study including 1,2-dioleoyl-sn-glycero-3-phosphocholine (DOPC), Porcine sphingomyelin (PSM), Egg sphingomyelin (ESM) and cholesterol along with their deuterated varieties were purchased from Avanti Polar lipids (Alabaster, USA). Prior to use, the purity of each lipid species was confirmed by thin layer chromatography and representative Raman spectra taken for each in the bulk phase. Atto-488 1,2-dioleoyl-sn-glycero-3-phosphoethanolamine (Atto-DOPE) was purchased from ATTO-TEC GMBH (Siegen, Germany) and used without further preparation.

Nitro-2-1,3-BenzoxaDiazol-1,2-dioleoyl-sn-glycero-3-phosphoethanolamine

(NBD-DOPE) and Naphtho[2,3-a]pyrene were from Sigma Aldrich (Dorset, UK) and used as provided. All lipids and fluorescent lipid analogues were suspended in 2:1 Chloroform : Methanol (v/v) and stored at -25°C under inert atmosphere until used.

## 2.1.2 Free in solution bilayer formation

Due to the large number of similar experiments performed, with slightly varying preparatory conditions, this section deals with the lipid concentrations and solvents separately to the methods used for formation of GUV. The sections are cross referenced to the relevant experiments and the exact lipid constituents and methods can be easily construed.

### 2.1.2.1 Lipid Concentrations

For studies into vesicle lamellarity (chapter 3) - DOPC was combined with 0.15 mol% Atto-488-DOPE diluted at 1mg/ml ([DOPC]) in Chloroform : Methanol (2:1 v/v). In raft exhibiting vesicles (Section 3.4.6) a 2:1:1:x molar ratio of DOPC:PSM:Cholesterol at 1mg/ml ([DOPC]) was used where x represents any one of the 3 possible fluorescent species. Naphtho[2,3-a]pyrene and NBD-DOPE were used at 0.5 mol% and ATTO-488 DOPE at 0.15 mol%, formation solution was diluted to 1mg/ml ([DOPC]) in the same solvents as before. Approximately 10µl formation solution was required per protocol. All solvents used were HPLC+ grade.

### 2.1.2.2 Electroformation in H<sub>2</sub>O

Electroformation is a convenient method for formation of large numbers of thin walled vesicular structures. In the vast majority of experiments in this study, electroformed vesicles were used. Since many experiments have been performed with only slightly varying conditions, this method is presented in a general form, with cross references in place where specific concentrations are given.

GUV were electroformed in accordance with methods due to Angelova (Angelova et al., 1992). Typically Platinum electrodes are used for formation, I have used Tantalum electrodes as a suitable high conductivity, low

reactivity and affordable analogue. For each preparation 10 $\mu$ l of lipid solution at 1mg/ml [DOPC] was applied by Hamilton Syringe onto the surface of two parallel tantalum electrodes (1.5cm x 0.5mm  $\varnothing$ , 3mm separation) followed by removal of the solvent under constant stream of nitrogen for  $\approx$ 30s. Complete solvent removal was then affected by confinement of the electrode assembly under high vacuum for a minimum of 1 hour within a nitrogen flushed vacuum desiccator (Eppendorf GmbH, Germany). Following solvent removal electrodes were suspended in 550 $\mu$ l of deionised and degassed water within a 1/2 millilitre Eppendorf tube and sealed into position with dielectric tape as shown in figure 2.1. For phase separated GUV (Sections 3.4.6) the chamber and aqueous solution were preheated to 60°C and held there for the duration of the formation. For single component GUV (Sections 3.4.1) the electroformation was conducted at room temperature (typically 20-22°C). Electroformation was commenced by connecting the electrodes to a function generator (GW Instek, SFG-2010) and subjected to a 1.2V peak to peak square waveform at 10 Hz for 1 hour to induce GUV formation. Waveforms were monitored by connecting an analog oscilloscope (Gould-405) in parallel with the electrodes. Subsequently the voltage was increased to 1.5V peak to peak with sine waveform and the frequency reduced to 5Hz for 1/2 hour then 2Hz for 1/4hr and 1Hz for 1/4 hour to encourage GUV separation from the electrode. For raft exhibiting GUVs the formation chamber was sealed and cooling controlled at 4°C per hour to room temperature inducing raft formation. The use of a square wave for the initial hour was found experimentally to be most significant, this is possibly due to the presence of higher field harmonics inducing abrupt field changes at multiple frequencies. The apparent yield of GUV anecdotally appeared reduced if a triangle or sine waveform was initially used, however this was not systematically investigated.

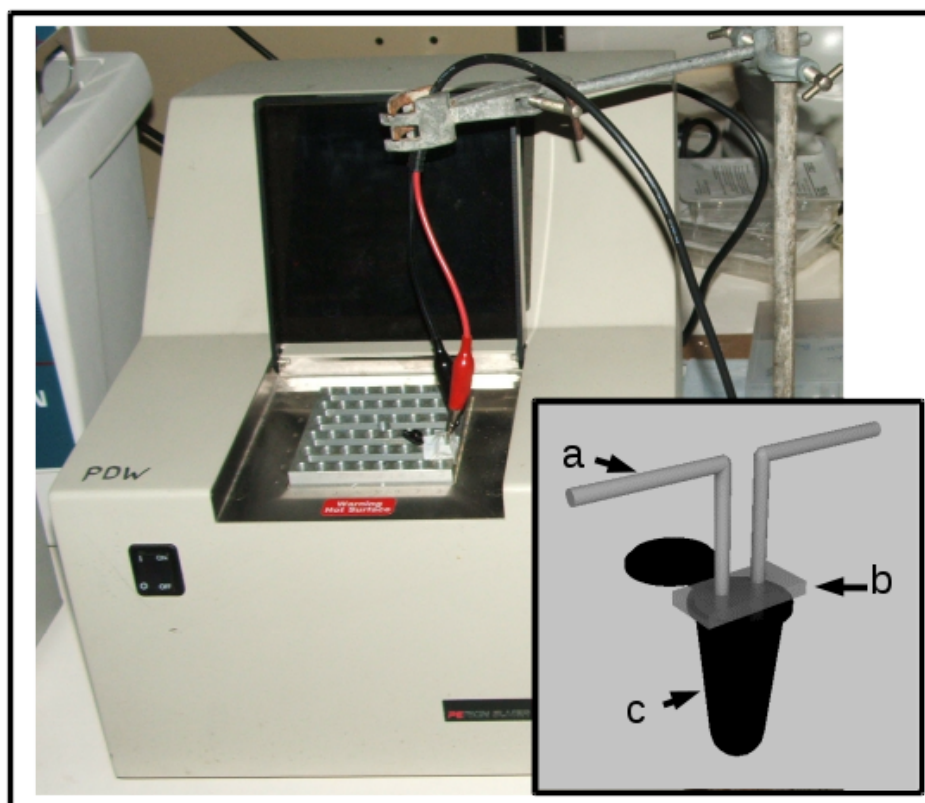


Figure 2.1: GUV electroformation chamber during operation and inset: schematic representation detailing the Tantalum electrodes (a), dielectric spacer (b) and  $\frac{1}{2}$  ml Eppendorf tube utilised as the formation chamber (c).

### 2.1.2.3 Electroformation in Sugar Solutions

Free in solution GUV are preferred for investigations into lipid rafts as the membrane is free from interactions with any surfaces and therefore likely to exhibit the most natural behaviour. As an example of this surface effect, consider planar lipid bilayer patches formed by the rupture of GUV onto a hydrophilic substrate. Although only charge interactions are present between the lipid and surface, these are sufficient to immobilise completely the lipid domains. Unfortunately free in solution GUV are also problematic from an imaging point of view they can translate.

In order to remedy this situation, GUV were created with differing internal and external sugar solutions exploiting the different densities of Sucrose and Glucose to produce Heavy GUV which sink to the base of the imaging chamber. As GUV present an osmotically active barrier both solutions needed to be carefully produced to the same concentration to ensure an isosmotic condition.

Sucrose was prepared in H<sub>2</sub>O at 100mM concentration and the brix value of the solution checked via refractometer measurement. Glucose was made to the same concentration and used without further analysis (correct concentration is inferred since the GUV were stable in both solutions). Vesicles were electroformed at room temperature, with the timings and voltage waveforms described earlier (section 2.1.2.2). Following electroformation the vesicles were diluted 5:1 or 10:1 in 100mM D-glucose solution and transferred to an imaging chamber formed from a 20mm radius, 0.12mm depth imaging spacer (Grace Bio Labs, USA) sandwiched between a #1.5 coverslip (Mensel Glaser, Germany) and 50mm \* 75mm \* 1mm Glass microscopy slide (Fisher Scientific, UK) as shown schematically in figure 2.2.

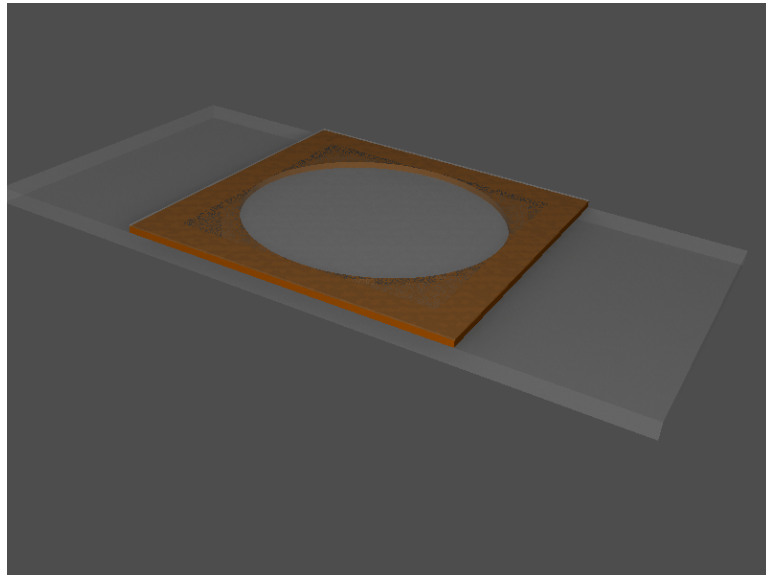


Figure 2.2: Schematic representation of a typical imaging chamber constructed from a 0.5mm imaging spacer, standard microscopy slide and #1.5 coverglass.

Following chamber construction the slide was transferred to an inverted microscope (Eclipse TI-U, Nikon, Japan) and allowed to settle for 30mins prior to imaging. GUV could readily be seen to have migrated to the coverslip surface within this time frame, none were observed at high layers of the solution. This indicates that the formed GUV do not permit transbilayer transport of the sugar solutions over reasonable timescales and that the solution is isosmotic, since over these timescales even small osmotic imbalance would lead to H<sub>2</sub>O diffusion and vesicle rupture. Due to increased viscosity of the solution, thermal oscillation of GUV both in terms of translation and modal bending of the bilayer was anecdotally observed to be reduced.

#### 2.1.2.4 GUV formation by gentle hydration

GUV electroformation presents the simplest and most reliable method for the production of large vesicles however it does suffer from a number of drawbacks. Firstly electroformation cannot proceed at physiological buffer concentrations due to direct ion conduction through the medium (causing significant sample degradation). Secondly, electroformation can produce poor results in the presence of high levels of charged lipids. For these reasons an alternative method was required which would allow for physiologically relevant buffers to be used. For this we selected Gentle Hydration (GH).

It should be noted that GH has a number of disadvantages compared with electroformation: the preparation time is long (overnight incubation), the lipids are potentially exposed to atmospheric oxygen for longer periods (degassed water is used: exposure should be minimal) and the method is expensive in terms of the quantity of lipid consumed per preparation. Therefore GUV electroformation has become the default method used unless experimental requirements dictate otherwise.

In this study we followed the GH method due to Akashi (Akashi et al., 1996). For experiments involving single or double lipid components (Section 3.4.1), solutions were prepared as detailed above (DOPC + 0.5 mol% NBD-DOPE) with the addition of addition of between 2 and 10 mol% of a charged lipid Phosphatidylglycerol (PG). PG was required to obtain suc-

cessful results as noted in the original paper, this is due to charge interaction with the high strength buffers (PBS, 137mM).

For GH 100 $\mu$ l of lipid solution [10mg/ml] ([DOPC]) in 2:1 (v/v) Chloroform : Methanol was deposited onto the walls of a 50ml vacuum flask under rotatory evaporation (Buchi Rotavapor, Switzerland), shown in figure 2.3 below, prior to full solvent removal under high vacuum for 1 hour. The dried lipid film was then partially hydrated under a stream of humidified nitrogen formed by bubbling particle and oxygen free N<sub>2</sub> gas through deionised water heated to 60°C for 15 minutes prior to the addition of PBS (137mMol) preheated to 37°C. The suspension was incubated overnight at a constant temperature of 37°C. The resultant lipid suspensions are highly diffuse (often invisible to the naked eye), comprising of large thin walled lipid structures with little resultant scattering or refraction. Therefore to confirm successful GUV formation the lipid solution was (briefly, < 15s) exposed to UV radiation at 254nm (figure 2.3, b) whereupon a light cloud of lipid material can be seen. The lipid was localised within a discrete sub-volume of the full solution: this was consistently observed.

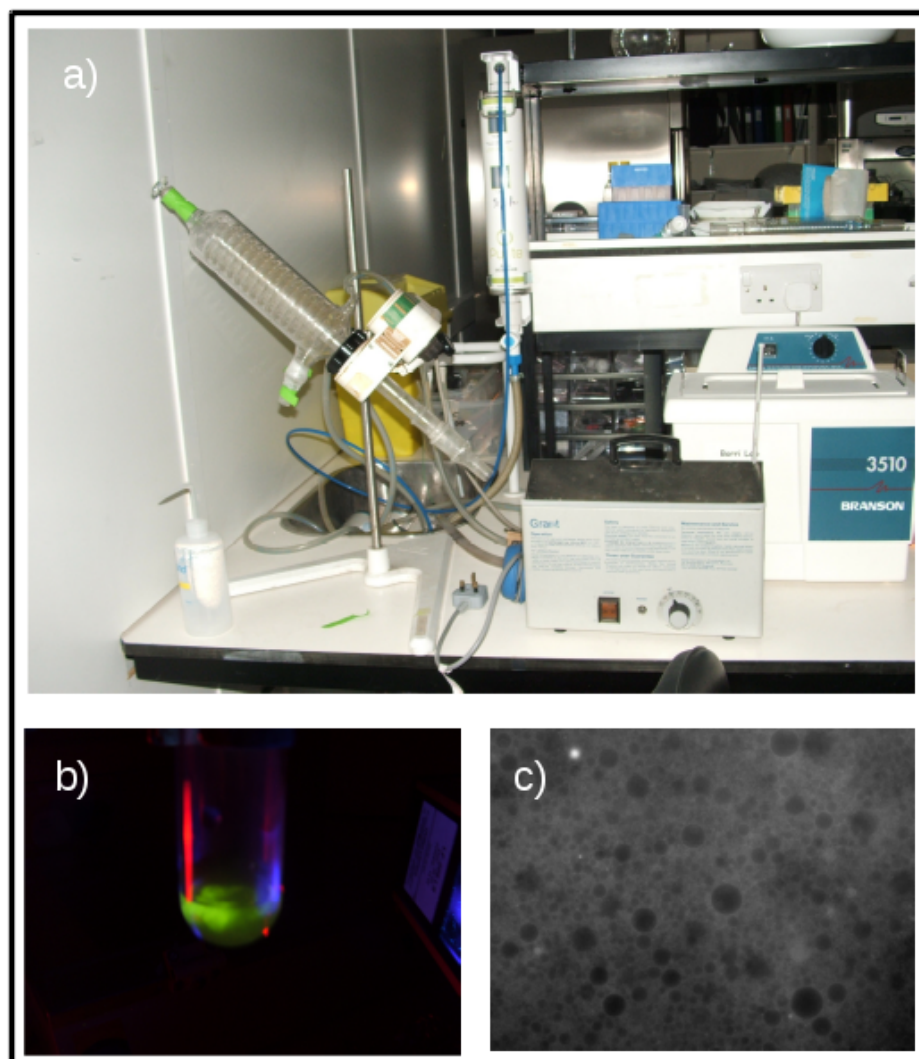


Figure 2.3: Setup utilised for GUV formation by gentle hydration. Rotavapor and water bath (a), UV (254nm) visualisation of the GUV suspension post formation (b). Epi-Fluorescence image of raw GUV suspension demonstration polydisperse structure formation including many thin walled vesicles (c).

In order to image GUV, the lipid cloud was hand extracted from solution by Pasteur pipette. Due to the density of structures seen in the raw suspension (figure 2.3, c) it is necessary, for imaging, to dilute by factors between 10x and 100x (v/v). Mixing of the raw suspension and aqueous phase was conducted by careful hand pipetting so as to avoid GUV rupture. 100x dilution was found empirically to produce a sparse, well separated solution of GUV suitable for extended imaging and was normally used.

Imaging, was conducted on an inverted microscope (Eclipse TI-U, Nikon, Japan) using an imaging chamber constructed from a 20mm diameter, 0.5mm Depth imaging spacer (Grace Bio-Labs, USA) sandwiched between a #1 or #1.5 coverslip (Mensel-Glazer, Germany) and standard 50mm \* 75mm \* 1mm Glass microscopy slide (Fisher-Scientific, UK), shown schematically in figure 2.2.

### **2.1.3 Surface Constrained Bilayer formation**

#### **2.1.3.1 sGUV electroformation - Lipid preparation and deposition**

For CARS and two photon fluorescence (TPE) imaging of single bilayers high laser powers must be used to compensate for the low density of molecular bonds. This leads to issues of sample stability, localised heating and convective / radiative movement induction. For high quality imaging, and forced by the low signal to noise imposed due to the nature of the bilayer, long acquisition timescales were utilised, precluding the use of free in solution GUV. To compensate for this, surface attached GUV (sGUV) were developed on both conductive and dielectric (glass) substrates. Formation from planar conductive surfaces has been performed before (Estes and Mayer, 2005), however sGUV formation from planar dielectrics is novel.

For imaging purposes it is essential that sGUV are presented upon a substrate suitable for microscopic investigations. Custom, indium tin oxide coated (ITO) #1.5 coverslips (22mm\*22mm) and microscope mounting slides (75mm\*50mm\*1.1mm) were obtained from Diamond Coatings (Birmingham, UK). These feature a sputter coated conductive ITO layer of specified thickness 700 nm with typical 10% tolerance (measured thickness was less  $\approx 584\text{nm} \pm 20\text{nm}$ ). These slides retain approximately 90% transmission (at normal incidence) throughout the visible and near IR spectral

regions whilst allowing low ohmic (8-12 ohms/square) resistance to generate the required uniform electric fields across the lipid bilayer. Considerable effort was expended in order to generate the highest possible yield of sGUV upon a given slide, initial efforts utilised drop cast lipid layers, with a move to more precisely controlled spin coating of lipids in later experiments. Spin coating permits reproducible and tightly controlled, uniform deposition of homo-geneous lipid films onto the hydrophilic substrate directly from organic solution.

For drop casting the required singular, double or ternary lipid solution was first prepared at 1mg/ml in 2:1 (v/v) Chloroform : methanol as described elsewhere. Between 10 and 50 $\mu$ l of this solution was spread onto the ITO conductive face following a snake like pattern (Heimburg, 2008). The lipid was immediately dried under constant stream of Nitrogen and placed under high vacuum for a minimum of 1/2 hour to remove all trace of solvent. A formation chamber could then be constructed as described below.

To generate a thin lipid film from organic solution by spin coating, the solvent used for the lipid component is critical. It must not only solubilise the lipid, but also evaporate readily and sufficiently wet the underlying surface so as to inhibit dewetting artefacts. Many solvents and solvent combinations were tried. The underlying surfaces of interest (ITO or Glass) were all hydrophilic, solvents and solvent combinations based around more polar molecular conformations were an obvious target. Highly apolar solvents (E.g. Acetone) could be observed to bead on the ITO / Glass interface and produced inhomogeneous resultant lipid layers. It was determined empirically that for ITO-coated substrates Dichloromethane produced uniform, defect free films with high efficiency. For electroformation from dielectric (glass) substrates a combination of Chloroform : Acetonitrile (95%:5%, v/v) produced the most consistent results. This was attributed to the more polar nature of the Acetonitrile, pure Chloroform produced very poor results in isolation.

In addition to solvent type, two other factors are critical in yielding a film suitable for electroformation, these are the spin speed and angular acceleration utilised. It was determined that the optimal spin speed was 3000rpm with angular acceleration of 3000rpm/s. The high acceleration was found

to be required in order to sufficiently thin the wet film prior to complete solvent removal which occurs extremely fast for the type of organics used. Insufficient acceleration results in an inhomogeneous film attributed to the presence of excess solvent during the evaporation stage. Insufficient rotational speed was found to render a thick film leading to multi-lamellar structure formation instead of GUV. Other studies have indicated that the optimal film thickness is around 10 bilayers or 25 – 50nm (Estes and Mayer, 2005) dependent upon lipids used. In order to quantify the film thickness, qDIC was utilised: A uniform film was partially removed through scratching with a fresh razor oriented perpendicular to the surface. The resultant phase shift in air due to the absence of lipid was then assessed (result not shown). Initial tests indicated a film thickness of between 8 – 16nm for lipid at 5mg/ml total concentration with spin speed variation between 500 – 5000rpm. A linear relation exists between film thickness and initial lipid concentration, therefore the concentration was increased to 10mg / ml to produce the required lipid film depth.

Spin coating was performed with a Laurell (Model, USA) spin coater using an 18mm \* 18mm thin film adapter to hold the coverslip under vacuum, applied to the rear coverslip face. Stock lipid solution in either singular, double or ternary configuration was prepared at 10mg/ml ([Total lipid]) as described elsewhere and the solvent exchanged to Chloroform: Acetonitrile (Glass) or Dichloromethane. Due to the porosity of the glass / ITO surface all coverslips were annealed at 150°C for  $\cong$ 5 minutes in order to remove trace water / solvent contamination resulting from the cleaning procedures as detailed elsewhere. Sufficient quantities of lipid solution, typically 130 – 250 $\mu$ l dependant upon the coverslip dimensions / surface type were applied by Hamilton Syringe to fully cover the glass or ITO surface, with only the corners remaining clear. The spin cycle was then immediately started with the following settings:

- Spin speed: 3000rpm for 4 mins
- Angular acceleration / deceleration: 3000rpm/s

Upon cycle completion the coverglass was immediately removed to high vacuum for a minimum of 1 hour to remove all trace solvent from the bilayer.

Failure to allow sufficient time for solvent removal is terminal for subsequent electroformation.

### **2.1.3.2 sGUV Electroformation from ITO coated surfaces**

In order to electroform from thin coated lipid films on either ITO or glass, separate chambers were required tailored to the properties of both. The ITO coverslips utilised were conductive on only a single face to which the lipid film is applied. As shown in figure 2.4 this face forms an interior surface in the constructed chamber, therefore a low resistance film of conductive silver was applied to both faces across a single edge in order to provide an exterior electrical contact. The silver was painted utilising a thin capillary to wick the solution and deposit. All contacts were painted immediately before first use and prior to annealing of the coverslip such that no trace solvent remains. The silver layer is not covalently attached to the surface, therefore tests were conducted in order to ensure that contamination of the sample by silver could not occur. Tests indicated that the silver layer was largely soluble in acetone, however it proved to be relatively stable to immersion in Chloroform, Methanol, Dichloromethane or Acetonitrile (or relevant combinations) for brief periods. To avoid potential contamination of the lipid layer, care was taken to avoid contact between the organic solution and silver. Subsequent, immediate spin coating will displace the solvent radially across the silver therefore no contamination of the lipid by Silver can occur.

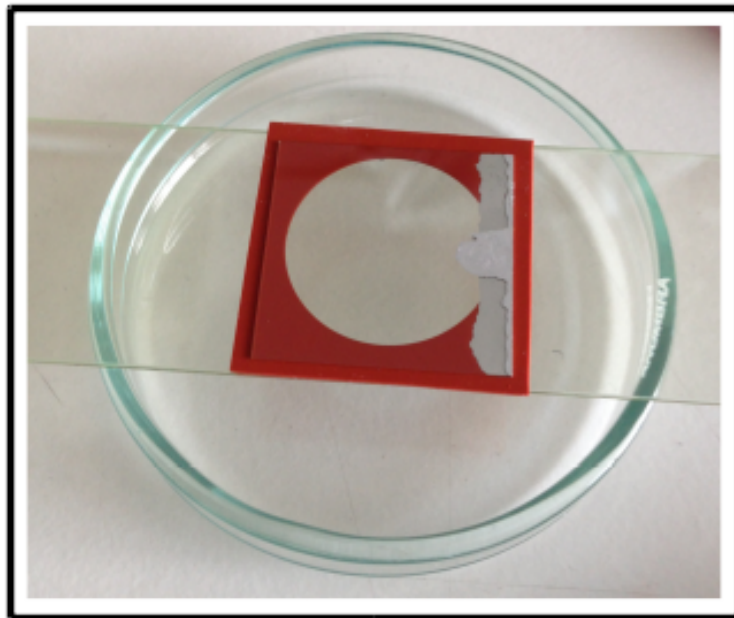


Figure 2.4: Combined sGUV electroformation and imaging chamber utilising ITO coated optical elements.

Following complete solvent removal a chamber was constructed as shown in figure 2.4 by sealing the lipid under  $dH_2O$  with varying diameters (13 – 20mm), fixed thickness 0.12mm imaging spacers (Grace Bio-Labs, USA) and ITO coated microscopy slide (75mm\*50mm\*1.1mm). Electroformation was effected using a  $1.5V_{pp}$  square waveform at 10Hz for 10 minutes. This incomplete formation cycle was found to form a large population of sGUV that remained attached to the surface. Smaller structures, whilst observed, did not appear in high density on smaller timescales. The surface attached GUV were found to be stable across experimental timescales (4-6 hours).

### 2.1.3.3 sGUV electroformation from dielectric substrates

For successful electroformation it is a sufficient requirement that an alternating electric field be present perpendicular to the lipid layer, direct electrical contact between electrode and lipid is not needed. For electroformation upon glass external copper electrodes were utilised as shown in figure 2.5. A thin lipid film was spin coated onto a 24\*24mm #1.5 coverglass (Mensel-Glaser, Germany) as described earlier and the solvent removal completed under high vacuum for 1 hour minimum. A chamber was then formed using a 20mm diameter, 0.5mm depth imaging spacer (Grace Bio-labs, USA) and a standard 75mm\*50mm\*1.1mm microscopy slide (Fisher Scientific, UK). External copper electrodes were custom fabricated from Standard FR4 single sided copper PCB (Maplin Electronics, UK), the conductive face of which was placed into contact with the coverglass and slide respectively and held in place with a g-clamp. The copper plates were then connected to a function generator (GW Instek, Germany) and subjected to a  $1.5V_{pp}$  square waveform at 10Hz for 10 minutes as before. Following formation the chamber was immediately taken for imaging.

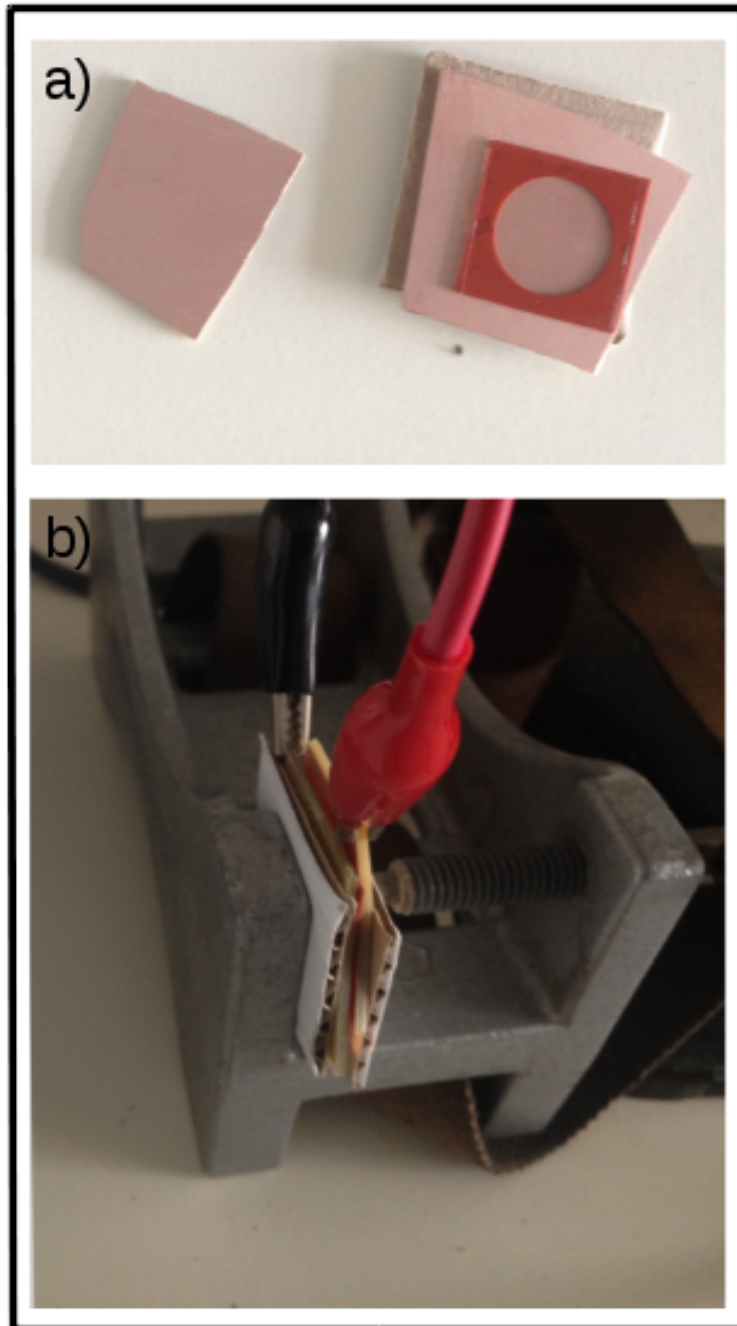


Figure 2.5: Combined sGUV electroformation and imaging chamber with external copper electrodes permitting formation from glass optical elements (a). Chamber during electroformation procedure (b).

#### 2.1.3.4 Biotinylated GUV Formation and surface preparation

Free in solution GUV, due to their inherent ability to translate, present problems for microscopic analysis. In order to overcome this, biotinylated GUV were prepared which could readily bind to a suitably prepared surface. In order to immobilise GUV at the coverslip surface two conditions must be met:

1. The GUV must contain a low mol% of N-Biotin lipid, with the hydrophilic biotin molecule presented at the water interface.
2. The coverslip must contain a layer of neutravidin capable of capturing the lipid head group bound biotin.

Biotinylated DOPE was readily available from Avanti Polar lipids and was incorporated into the GUV formation solution and electroformed into GUV as discussed earlier (section 2.1.2.2). The GUV incorporating Biotin-DOPE are bound to the neutravidin surface by forming a chamber with a suitable imaging spacer (Grace-Biolabs, USA) and incubating for at least 1 hour prior to sealing the chamber with a microscope slide. The protocol for activation of the glass surface with neutravidin is given in appendix B and based loosely upon ones found in the literature c.f. (Pignataro et al., 2000, Yang et al., 1998).

#### 2.1.3.5 PLBP deposition

Free in solution GUV presented many microscopy challenges under non-linear imaging modalities due primarily to the laser powers used and induced GUV motion. As a result, a more stable fixed sample was required that would permit long imaging timescales to be used. Planar Lipid Bilayer patches were ideally suited to this task. Planar lipid bilayer patches were formed through osmotically induced rupture of GUV onto a hydrophilic glass surface. Free in solution GUV of various lipid compositions were prepared as detailed earlier in  $\text{dH}_2\text{O}$ . In order to maximise the yield of PLBPs produced from GUV the glass surface was pretreated to render it hydrophilic as described in appendix C. Due to the barrier presented by the membrane to the saline solution, water can be induced to diffuse out of the GUV by osmosis. This destabilises the membrane, GUV simultaneously in contact

with the glass surface rupture forming a planar patch (Hain et al., 2013, Richter et al., 2006).

In order to maximise the hydrophilicity of the coverslips, surface SiO moieties (Silanol groups) were created by treatment with 3:1 acid Piranha solution (98%  $\text{H}_2\text{SO}_4$  : 30%  $\text{H}_2\text{O}_2$ ) as described separately (see appendix C). Prior to treatment,  $\text{H}_2\text{O}$  can be seen to bead up with high estimated contact angle. Following treatment, water can be seen to spread out into thin films confirming increased hydrophilicity. To the treated glass a thin imaging spacer (120 $\mu\text{m}$  x 20mm  $\varnothing$ , Grace Bio-labs) is attached prior to deposition of and incubation with 60 $\mu\text{l}$  of the aforementioned GUV solution for 30 minutes. The solution is periodically agitated with a 2 $\mu\text{l}$  pipette in order to promote contact and capture of the GUV by the glass surface. Following incubation, GUV sufficiently close to the glass surface can be induced to rupture by introducing 60 $\mu\text{l}$  of 75mM PBS. The process is shown schematically in figure 2.6. After PLBP formation, the coverslip is washed by immersion in excess PBS (75mM) and the chamber thereafter sealed with a clean glass slide. The washing step removes any non-bound lipid content from the chamber, thus permitting imaging without artefacts caused by mobile lipid contaminant. PLBPs are then visualised and pre-characterised at the coverslip surface with DIC or EPI-fluorescence before CARS or SRL study. All coverslips used were of the highest grade, #1.5 24mm\*24mm (Mensel-Glaser, Germany).

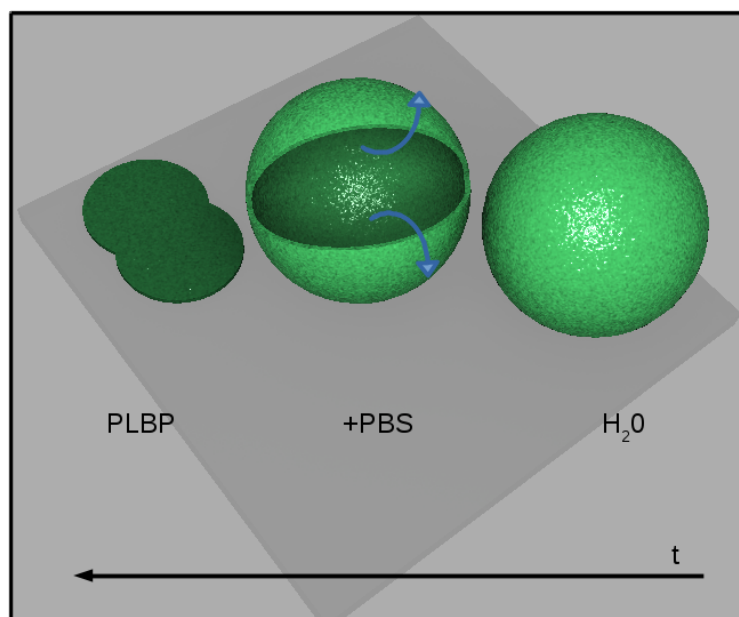


Figure 2.6: Formation of planar lipid bilayer patch from an initial GUV through osmotic rupture driven by addition of phosphate buffered saline, in the presence of a hydrophilic substrate.

### 2.1.4 Thin Layer Chromatography

Qualitative pre-characterisation of the purity of stock lipids was performed using thin layer chromatography. 10 $\mu$ l of single lipid stock at 10mg/ml was spotted onto Aluminium backed 5cmx8cm thin layer chromatography plates (Sigma-Aldrich, Dorset, UK) by Hamilton syringe under inert atmosphere and the solvent allowed to evaporate (~10 minutes). The TLC chamber was preconditioned by lining with filter paper saturated in 64:35:4 (vol%) Chloroform : Methanol : Water, 10ml of which was also added to each side of the chamber. Dried TLC sheets were stood in the solution and the chamber sealed until the solvent line reached close to the top of the paper ( $\approx$ 30 minutes). Plates were developed by charring at 180°C for 45mins, thus the lipid was non-recoverable under this methodology. Lipids were visualised by UV illumination at 254nm, lipid appeared dark against the fluorescent background due to fluorescent zinc-silicate indicator present in the plates. Purity of the lipid samples was confirmed by ensuring that each sample presented only a single band following the TLC run. Samples with multiple bands or streaks were thereby rejected as containing significant contamination. This analysis could not be applied fully to the Sphingomyelin samples since they contain multiple acyl chain lengths. All solvents used were of the highest HPLC+ grade with the exception of water which was of 18.2M $\Omega$  grade (Millipore, USA).

## 2.2 CARS Experimental Setup

The CARS microscope utilised in this study employs a broadband, 5fs Ti:Sa laser source (Venteon, Pulse:one) with spectral width at 10% of maximum of 310nm from 660nm to 970nm (Pope et al., 2013) and laser repetition rate of 80MHz. The time averaged total power output of the laser is approximately 500mW under normal operating conditions. Due to the large spectral bandwidth, this laser enables simultaneous two photon excitation (TPE), CARS microscopy and second harmonic generation (SHG) as shown in figure 2.7. This is performed by separation of the laser spectrum across well-defined ranges using suitable dichroic mirrors which enable efficient splitting of the spectra.

For the CARS experiments detailed in this thesis, the pump beam intensity maxima is normally centred at 689nm with spectral width of 65nm at 10% of maximum. The Stokes beam has centre wavelength around 805nm and a width of 200nm (Pope et al., 2013). The total radiative power of the laser is split evenly between Pump, Stokes and TPE. Utilising these spectral ranges for the Pump and Stokes, the CARS microscope is capable of exciting vibrational resonances in the range of  $1200\text{-}3500\text{cm}^{-1}$  (with specific sub-ranges dictated by the filters present at the detectors). The microscope is therefore capable of imaging within the Raman fingerprint region, and across the full range of CH resonances.

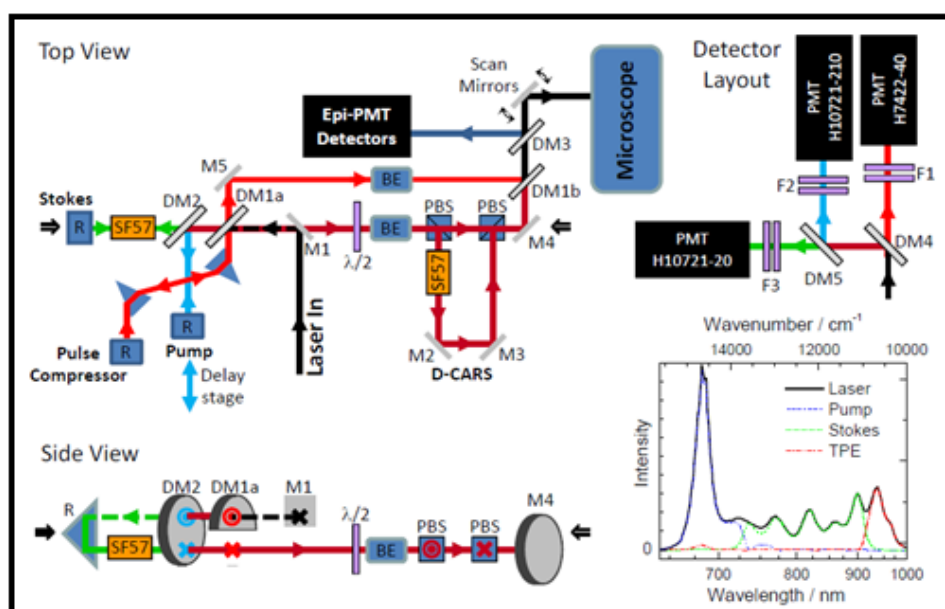


Figure 2.7: Schematic of the CARS / TPE microscope. Top View: Basic components of the optical path detailing the mirrors ( $M_x$ ), dichroic mirrors ( $DM_x$ ), beam expanders (BE), filters ( $F_x$ ) and polarising beam splitters (PBS) used to control the bandwidth of each acquisition modality and shape the spatio-temporal properties of the  $\approx 5\text{fs}$  laser pulses ( $x \in \mathbb{Z}$ ). Inset is the laser spectrum of the Ti:Sa source used. Figure reproduced by kind permission of Dr Ieystn Pope (Pope et al., 2013).

As mentioned, the laser utilised in this study outputs a transform limited pulse width of 5fs (spectral bandwidth equal to the reciprocal of the pulse duration). The short temporal pulse is advantageous for two photon fluorescence applications due to the high peak power present.

For CARS applications this pulse duration is sub-optimal. Typical Raman

vibrational linewidths are of the order of  $10\text{-}20\text{cm}^{-1}$  (which corresponds to picosecond duration pulses) this is in contrast to the  $\sim 1500\text{cm}^{-1}$  bandwidth of a 10fs pulse located in the near infrared (Evans and Xie, 2008). Consequently, wide bandwidth excitation if used, couples only a small part of the pulse energy into resonantly exciting the narrow Raman vibration. The remaining energy excites the constant non-resonant background which is present at all frequencies thus significantly reducing the signal to background ratio of the measurements. In addition, any other Raman resonances within the bandwidth will also be excited, thus spectral resolution is poor if using the broadband pulse as a probe. It can be shown that as the pulse spectral width increases, for constant pulse energy, both the resonant and non-resonant contributions to the signal monotonically increase, however the resonant signal soon reaches saturation whereas the non-resonant signal grows quadratically in the spectral width (see Figure 2.8)(Cheng et al., 2001).

The CARS microscope used in this study overcomes these issues. It provides high signal to background ratio and a spectral resolution down to  $10\text{cm}^{-1}$ , similar to that with ps pulses, by utilising a technique known as spectral focusing.

Spectral focusing is performed by exploiting the frequency dependence (chromatic dispersion) of high refractive index glasses, in a process known as linear chirp described below. In the case of SF57 glass used herein, the refractive index increases with increasing optical frequency, from the near infrared through the blue end of the optical spectrum.

To understand the principle of spectral focusing, let us model the temporal complex electric field vector ( $E$ ) of a light pulse as the product of a time dependent complex amplitude envelope with a monochromatic wave at the carrier frequency:

$$E(t) = E(t)e^{i\psi(t)}e^{i\omega_0 t} \quad (2.1)$$

where  $\psi(t)$  is the time dependent phase of the pulse. Since the rate of change of phase is the instantaneous frequency, we may write the frequency of the pulse as:

$$\omega(t) = \frac{d\psi}{dt} + \omega_0 \quad (2.2)$$

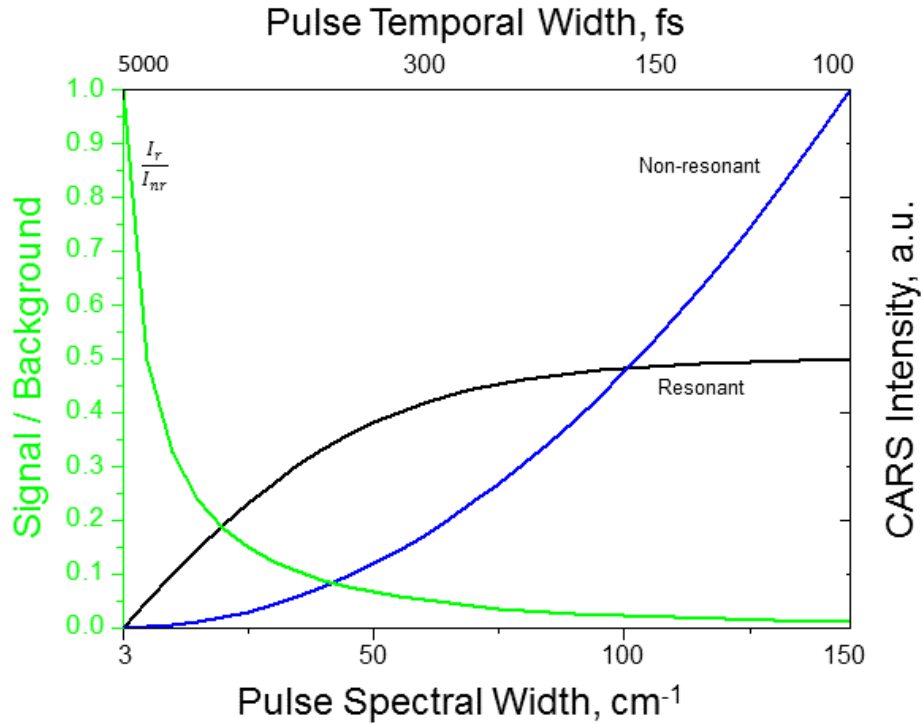


Figure 2.8: CARS resonant and non-resonant signal intensities shown as a function of pulse spectral width, for transform-limited Pump and Stokes pulses of constant pulse energy. Adapted from (Cheng et al., 2001). Intensity ratio demonstrates maximum signal to background ratio for pulse durations in the picosecond timescales. Non-resonant signal has been rescaled by a factor of 0.001 as shown.

where  $\omega(t)$  is the instantaneous frequency. A time varying phase therefore gives rise to a change in the instantaneous frequency (chirp). We next consider how a material may induce chirp by generating phase modulation.

Upon transit through a layer of glass, the optical pulse undergoes group velocity dispersion. This has two effects: The post transit pulse width ( $\tau$ ) is increased  $\{\tau = F\tau_0 | F > 1\}$ , and the instantaneous frequency changes linearly (Hellerer et al., 2004) as a function of the chirp parameter for the material, in accordance with:

$$\omega(t) = \omega_0 + 2bT \quad (2.3)$$

here,  $\omega_0$  is the carrier frequency, and  $b$  is the chirp parameter: proportional to the second derivative of the refractive index versus wavelength and the length of the glass. If such a linear chirp is carefully applied to both the

Pump and Stokes beams, with identical chirp parameter, then the instantaneous frequency difference between carrier frequencies ( $\omega_D = \omega_p - \omega_s$ ) remains constant over time. Furthermore, the spectral bandwidth of the driving vibrational excitation (given by the interference term between Pump and Stokes fields) will be given by the inverse stretched pulse duration  $\Delta\omega/\tau$  (Hellerer et al., 2004) thus providing increased spectral resolution and selectivity. Moreover, if a delay time  $t_0$  is applied to Pump and Stokes beams, the resultant instantaneous frequency difference between the fields varies as  $\omega(t) = \omega_{p0} - \omega_{s0} + 2bt$  (c.f. equation 2.3). In terms of the Pump and Stokes fields, assuming Gaussian temporal profiles, the resultant interference term driving material oscillations can be shown (Rocha-Mendoza et al., 2008) to be:

$$E_p E_s \propto e^{\left[ \frac{-t_0^2}{2\tau^2} - \frac{2\left(t + \frac{t_0}{2}\right)^2}{\tau^2} + i(\omega_{p0} - \omega_{s0} + 2bt_0)t \right]} \quad (2.4)$$

where all the symbols take on the meaning defined above.

In our particular CARS microscope shown in figure 2.7, suitable dichroic mirrors are utilised in order to divide Pump and Stokes beams into separate paths. Due to the differing frequency components present, it is necessary to pre-chirp the Stokes beam using a length of SF57 glass (Pope et al., 2013). This compensates for the lower dispersion present at the longer Stokes wavelengths relative to those seen for the Pump. Separate glass blocks for the Pump are not required since the remaining optics and objectives provide a sufficient and inherent linear chirp. The spectral resolution of the microscope for the measurements shown in this thesis has been determined as  $10\text{cm}^{-1}$  with  $L_1=20\text{mm}$  for Stokes wavelengths addressing the CH-stretch region. The Pump beam is retro-reflected from a movable delay stage (PI, M404.42S) before recombination with the Stokes thus providing the delay  $t_0$  required for control over the instantaneous frequency difference. The temporal accuracy of the delay has been established to be 5fs (Pope et al., 2013).

For microscopy purposes, the Pump and Stokes beams must be tightly focused in the sample. In the setup used in this thesis, the Pump and Stokes beams are coupled into a commercial inverted microscope stand (Nikon, Ti-U). This is equipped with a range of microscope objectives for

focusing, and condensers for signal collection in transmission geometry. For the data in this study, both 20x (0.75NA, Nikon, UK) and 60x (1.27NA, Water immersion, Nikon, UK) objectives were utilised in combination with matched 0.72NA Dry Condenser or 1.4NA Oil immersion condenser. The spatial resolution under CARS excitation has previously been characterised (Pope et al., 2013). For the 0.75NA objective a CARS intensity point-spread function full-width-at-half maximum of  $0.6\mu\text{m}$  (lateral) and  $1.1\mu\text{m}$  (axial) was determined. For the 1.27NA objective, this was measured as  $0.3\mu\text{m}$  (lateral) and  $0.6\mu\text{m}$  (axial).

For imaging, the laser focus is raster scanned in-plane ( $xy$ ) across the sample by a pair of galvo mirrors (Cambridge Technology, UK). The raster scanning is flexible, permitting variable sampling of the diffraction limited focal spot. Normally three samples per resolution were utilised for the data in this thesis, in line with the Nyquist criterion although up to 10 samples per resolution are possible permitting greater averaging and an associated reduction in noise. Axial scanning was achieved by motorised movement of the objective, for the data in this study, where possible, data was acquired in accordance with the Nyquist criterion and three samples were taken per axial resolution ( $\approx 0.2\mu\text{m}$  / step). Due to time constraints, and coupled with the dynamic nature of some samples, this critical sampling was not always achieved and where 3d data are presented, the step size in the axial dimension will be given explicitly. Large scale sample scanning and translation can be achieved by the use of a motorised ( $xy$ ) microscopy stage (Prior, UK).

As shown in figure 2.7 the microscope set-up permits both epi and forward collection of the CARS signal. The CARS signal is spectrally separated from TPE or SHG through the use of dichroic elements. Residual Pump and Stokes beams are rejected through the use of two Semrock FF01-562/40 filters (CH-stretch region  $2700\text{--}3500\text{cm}^{-1}$ ) prior to detection. The CARS signal is detected by a Hamamatsu H7422-40 PMT. In the epi direction a similar arrangement of dichroics and filters is used to separate and measure any CARS signal present.

### 2.2.1 CARS Image acquisition

Acquisition of CARS images suitable for further quantitative analysis required careful planning and experiments when applied to such thin objects as a GUV or PLBP. At the single bilayer level, the focal volume is dominantly occupied by the non-resonant medium. Insufficient resonant material is present to generate a response dominated by the resonant part. It was anticipated therefore that the CARS response would vary linearly with the density of molecular bonds, not scaling as the square as one would expect for full focal occupancy. At this level we therefore operate within a regime of low signal to noise and significant non-resonant background.

Early experimentation yielded insufficient contrast to discriminate PLBPs within a single frame and single-frequency CARS acquisition, using the 60x, 1.27NA WI objective and 1.4NA OI condenser with 10 $\mu$ s pixel dwell times. Multiple (>40) frame averages were required in order to reduce noise and distinguish lipid patches. The more subtle intra-domain contrast could not be evinced at all. Careful systematic consideration of the filters, dichroics and laser spectrum used within our system led to an investigation into their effect upon image contrast of the laser spectrum, especially the location and intensity of the CARS pump beam spectral peak upon imaging contrast. It was determined that of the different possible laser spectral modes of operation, there was essentially one in which the CARS contrast was maximised with respect to imaging PLBPs. The full width at half maximum of the main 689nm peak must also be minimised and the peak intensity simultaneously maximised by tuning the laser cavity as the pump beam is used twice for CARS and therefore critical for contrast generation.

With the laser spectra fully optimised for this setup, we were then able to generate sufficient contrast to see label-free PLBPs in single-frequency and single frame acquisitions using the 60x objective and condenser, 10 $\mu$ s pixel dwell times and 50mW Pump and Stokes powers at the sample. In order to visualise, slight inter-domain contrast, further frame averaging rather than increases in laser dwell time were required. Although increases in dwell time also generate better contrast, the increased effects of local heating on patches is immediately apparent. Photo-damage could be seen after just a few frames at a dwell of 100 $\mu$ s. For all CARS imaging herein, both

for GUV and PLBPs, a fixed dwell time of  $10\mu\text{s}$  was used. This was determined empirically to be the fastest imaging speed possible that still yielded useful contrast.

Similarly, oversampling of the microscope point spread function (where oversampling is defined to mean more samples than that required by Niquist-Shannon Theorem) was found to be highly detrimental to the sample integrity. At 5+ samples per resolution fast photo-damage was readily observed. Therefore a fixed 3 samples per resolution was kept throughout measurements.

Finally, for long hyperspectral image sets, a minimum scan size of around  $12 * 12$  microns was imposed upon acquisition with 10 frames / frequency averaging regardless of patch dimensions. This was due to local heating caused by the frequency of scanning over a single point. Scanning any smaller area than this heated and photo-damaged the sample too rapidly. For data taken at higher number of frame averages, this minimum size requirement was observed to monotonically increase as a function of the number of frames.

## Giant Unilamellar Vesicles

### 3.1 Introduction

Giant unilamellar vesicles (GUV) were the first lipid model membrane developed during this study. GUV were selected from many possible lipid models on the basis of:

- Precisely controlled lipid constituents
- Many possible formation methods
- Free in solution model: Bilayer is contacted only by the formation solution
- GUV model is widely used and supported by the scientific literature

In addition, the symmetric spherical shell shape of the GUV presents a consistent model relative to the imaging setup, i.e. either imaging cuts by optical sectioning or imaging of the GUV poles is possible. Therefore, GUV present a synthetic model of the plasma membrane which is a close analogue to that seen in an actual cell (other models requiring either esoteric lipid species or presenting a bilayer encumbered by interactions with a solid surface). At the outset, it was anticipated that GUV would be used for all intended studies, including Raman and CARS microscopy. This was not achieved however due to deficiencies inherent within the model: Free in solution GUV, due to their tenuous nature ( $\approx 4\text{nm}$  thickness) are subject to Brownian motion which cause oscillations of the membrane on the order

of the resolution of the microscope. This oscillatory blurring of the vesicle periphery was found to inhibit long imaging timescales, such as those required by hyperspectral CARS microscopy (and therefore precluding advanced chemically specific analysis). In addition, the high laser powers needed to develop CARS contrast at the single bilayer level was found to induce convective effects, causing increased bulk translation of the vesicles and an increased oscillation of the bilayer. This effect proved terminal for the model from a high signal to noise CARS microscopy perspective, since averaging of the signal was not possible. These deficiencies drove the development of further downstream models, and further imaging modalities, as detailed in subsequent chapters.

Before utilising a new lipid membrane model, with which we had no knowledge: extensive characterisation of that model was conducted. Fluorescent GUV were created initially from DOPC with a low molecular concentration of a fluorescent lipid analogue. A review of the existing literature identified that GUV could be formed with more than a single bilayer present at the periphery. Crucially, extra bilayers can associate closely, with a spacing much less than the diffraction limit and are therefore unresolved by microscopic investigation. For intended chemically specific investigations within phase separated vesicles, it is important that a single bilayer only be present, otherwise a mixing of the signal due to spatio-temporally overlapped, unresolved phases, could occur. In order to resolve this issue, in a label free manner, a new quantitative DIC microscopy (qDIC) was developed (theory: Prof. W. Langbein) as presented in section 3.3. This new method was compared with the existing method of fluorescence quantisation (section 3.2), across large populations of vesicles, to determine lamellarity. Therein, we have shown qDIC is capable of resolving single bilayer vesicles within a more general population including multi-lamellar structures, and in a manner consistently with accepted fluorescence methods.

In addition we were initially unsure of the partitioning behaviour of the fluorescent lipid analogue (Atto-488 DOPE) used within all systems of interest. The qDIC and fluorescence studies had indicated that this fluorophore did not partition within DOPC vesicles. However within PSM and Cholesterol containing vesicles, the behaviour (of Atto-488 DOPE) was unknown

(no literature could be found pertaining to this system). This partitioning behaviour is important since it serves as the primary indicator of coexisting lipid phases within our experiments. Initial characterisation studies were therefore conducted to characterise partitioning behaviour in increasingly complex lipid models. Single component (DOPC or PSM GUV with low concentration fluorescent lipid analogue), double (DOPC and PSM, DOPC and Cholesterol, PSM and Cholesterol) and finally ternary (DOPC, PSM and Cholesterol) systems were created and analysed under two photon microscopy as shown in section 3.4. These studies demonstrated that the fluorescent lipid analogue Atto-488 DOPE partitioned only (and readily) within the ternary system and therefore served as a good marker for the lipid disordered phase.

Additional fluorescent markers for the liquid disordered phase and ordered phase were used, these were NBD-DOPE and Naphthopyrene. These fluorphores have been used in the literature (Baumgart et al., 2007), within our lipid model systems and presented with known behaviour. Once characterisation methods were in place, initial CARS microscopy studies were conducted, both for single, double and ternary lipid GUV. These studies, conducted at individual frequencies (typically at the  $\text{CH}_2$  asymmetric stretch at  $2850\text{cm}^{-1}$ ), identified deficiencies inherent with the GUV model as discussed earlier. In order to rectify this, two new GUV models were developed:

- Biotinylated GUV: active surface binding.
- Sucrose / Glucose GUV: passive recruitment of GUV to the imaging surface.

Biotinylated GUV, which can be fixed to a suitably treated glass surface are shown in section 3.8. This model removed issues associated with vesicle translation, however the membrane remained subject to Brownian motion and was therefore still poorly suited to hyperspectral CARS microscopy. The Planar Lipid Bilayer Patch (PLBP) was developed as detailed in the subsequent chapter, in order to remove the influence of both Brownian motion and translation.

### 3.2 Fluorescence quantisation

For the qDIC technique described theoretically in section 1.6.2.2, it was necessary to have a separate standard against which to compare, calibrate and validate the new method. Fluorescence quantisation (FQ) was chosen for this purpose due to established use in the literature (Akashi et al., 1996, Chiba et al., 2014), ease of application and spectral separation from qDIC. The phenomenon of FQ is attributable to homogeneous incorporation of a fluorescently labelled lipid throughout a single component lipid system. In the original study due to Akashi et.al (Akashi et al., 1996) fluorescence quantisation was demonstrated through the incorporation of the lipophilic fluorescent probe Octadecyl Rhodamine B Chloride (R18). The probe contains a short acyl chain which is thought to extend into the lipid bilayer, presenting the Rhodamine molecule at the aqueous surface (Isaacs et al., 1986, Lins et al., 2006), results have demonstrated homogeneous incorporation. At high concentrations (in DOPC bilayer from 2-9mol% measured in (Hoekstra et al., 1984)) R18 can undergo fluorescence self-quenching (Hoekstra et al., 1984), this is undesirable as variation from sample to sample could introduce further concentration dependent intensity distributions. In addition, R18 suffers from photo-bleaching, which at low bilayer concentrations would introduce additional variation in measured intensity dependent upon exposure time. In order to overcome these issues, I have utilised a modern, stable and high quantum yield (Lee et al., 2010) ( $>0.8$ ) fluorescent lipid analogue: Atto-488 DOPE (Atto-Tec GmbH, Germany).

DOPC bilayers incorporating low concentrations (0.2 mol% typical) of Atto-488 DOPE exhibit a homogeneous distribution of the fluorophore. Resultant to this, vesicles comprising unresolved multiple peripheral bilayers exhibit quantised levels of a fundamental minimum intensity: corresponding to integer multiples of an individual bilayer. Due to the dimensions of typical giant vesicles (10-100 $\mu\text{m}$ ) compared with the size of the diffraction limit, larger vesicles present more material within the focal volume. Therefore, a radial dependence on the peripheral intensity was observed as shown in figure 3.7.

For the fluorophore (Atto-488 DOPE) used in this study, no prior examples of its use for fluorescence quantisation studies could be found in the

literature. I therefore conducted a preliminary study sampling a significant number ( $n = 466$ ) of vesicles across multiple (3) sample preparations. This was required in order to determine both that quantisation occurs with this fluorophore, but also so that I could monitor the reproducibility of the experimental method. Due to the low concentration of fluorophore used and the difficulty of handling small quantities, I needed to determine the possible extent of variability in the data in order to better gain an idea of the quantity of vesicle measurements required in order to establish an accurate picture of the lamellarity. We also wished to investigate the stability of the fluorescent GUV system and the ratios of unilamellar to multi-lamellar vesicles produced under these conditions. As a result, 3 samples were prepared via electroformation (described in section 2.1.2.2). The vesicles comprised DOPC with (0.2mol%) Atto-488 DOPE, phase partitioning of the fluorophore was not observed. In the case of the first two preparations, large numbers of vesicles were sampled within a single, long data acquisition session (up to 8hrs after production) in order to obtain an accurate picture of the GUV sample and fluorescence prior to any possible sample degradation. In the case of the third set of data, smaller numbers of vesicles were sampled (50 per session) over several days. During the interval GUV samples were held under Nitrogen at 4°C.

Data was acquired using a Nikon inverted microscope (Eclipse Ti-U, Nikon, Japan) with 0.75NA, 20x objective (Nikon CFI Plan Apochromat  $\lambda$  series) and matched 0.72NA dry condenser. A 1.5x tube lens multiplier was utilised to ensure critical sampling at the 12 bit monochrome CCD detector (Hamamatsu Orca-285). Samples were illuminated by metal-halide light source (Prior Lumen 200). All images were acquired in the Epi direction using a GFP filter set (Semrock, USA).

The level of vesicle fluorescence was determined by measuring the average offset between the defocused region of the vesicle and the background taken as a profile across the vesicle diameter, examples of which are shown in figure 3.1. By utilising the total defocused signal, changes in fluorescence proportional to the radius of the vesicle were avoided (c.f. figure 3.7). The analysis was performed by hand using open source software: Imagej (Schindelin et al., 2012, Schneider et al., 2012). Care was taken during analysis to ensure any imperfections, defects or inclusions, which

would distort the intensity measurement, were excluded.

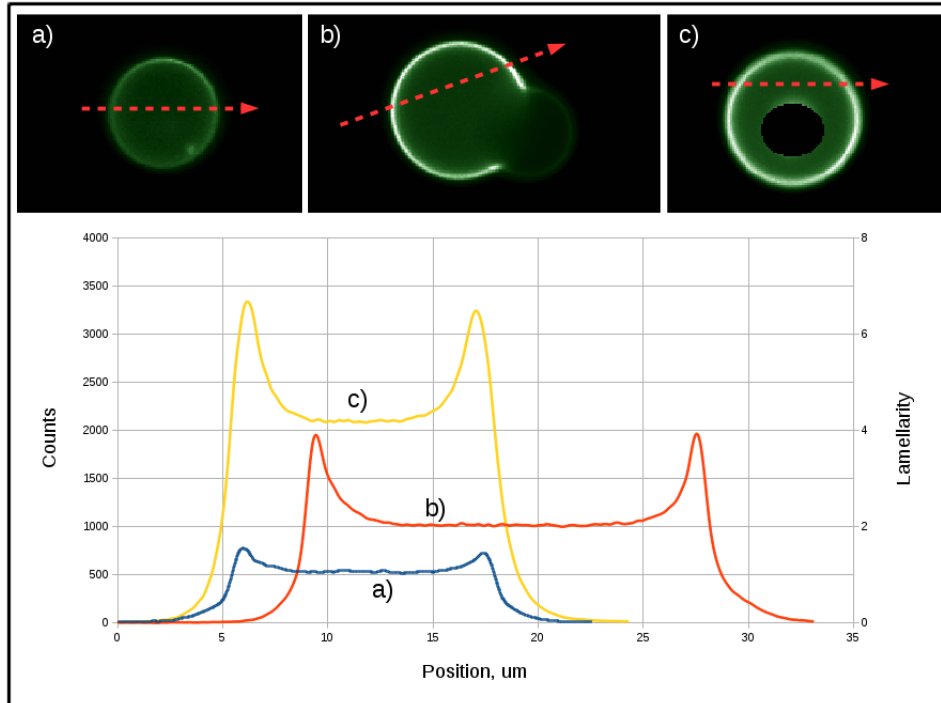


Figure 3.1: Top: background subtracted images of singular (a), double (b) and quad (c) bilayer vesicles and the approximate paths taken for the profile cuts. Bottom: Profile cuts for the vesicles presented as both a background subtracted intensity and lamellarity measure. Note that defects present in (c) were excluded as shown from the analysis. In addition vesicle (b) is unusual, since the outer membrane is larger than the inner and therefore it presents both a single and double profile.

The results for all data sets without normalisation are shown in figure 3.2. The mean and standard deviation for all separate distributions was determined by fitting Gaussian curves to the histogram data using a non-linear least squares method. Set 1 ( $n=161$ ) shows one large population of thin walled vesicles at a mean intensity of  $400 \pm 69$  counts. A small upper population ( $n=3$ ) is apparent centred about a value of 800 (Data not fitted, insufficient samples). Set 2 ( $n=194$ ) comprises a lower population centred on a mean intensity of  $515 \pm 97$  counts and an upper population ( $n=36$ ) at  $1021 \pm 87$  counts (one notable outlier is around 2100 counts: 4 bilayers). Set 3a ( $n=61$ ) demonstrates a lower population at  $196 \pm 22$  counts and an

upper population at  $394 \pm 12$  counts ( $n=11$ , upper). Set 3b ( $n=50$ ) has populations at  $188 \pm 36$  counts and  $405 \pm 32$  counts ( $n=4$ , upper). These results demonstrate that within a single sample preparation, the fluorescence due to Atto-488 DOPE is quantised, with the intensity of all upper distributions an integer multiple of the lowest population (given the standard deviations). A continuous range of intensities due to thin walled vesicles is not seen. The lower population is also significantly offset from zero intensity, if less intense vesicles were present, they have not been observed. Therefore we must conclude that the lower populations represent unilamellar vesicles, since no thinner vesicle is possible. When comparing between different vesicle preparations, we see significant difference can arise between the mean intensities of their populations, such as between sets 2 and 3a,b.

When comparing vesicles from the same preparations (set 3a,b) no significant difference is found between the distributions of vesicle intensities. This implies giant vesicles are relatively stable and that the activity of the fluorophore does not rapidly degrade under these storage conditions.

In order to compare vesicles between sample preparations, which as shown (figure 3.2) can be offset in intensity, I define a lamellarity parameter  $L$  such that  $L = I_s/I_{su}$  where  $I_s$  is the background subtracted intensity across the vesicle midline and  $I_{su}$  the mean of the unilamellar population (for that preparation). As shown in Figure 3.3, converting each vesicle intensity into the dimensionless lamellarity parameter allows demonstrates vesicle quantisation directly. The mean of the lower unilamellar population is  $0.9 \pm 0.16$  and that of the bi-lamellar population  $1.97 \pm 0.17$ .

The fluorescence data as a whole suggests that the probability of a randomly selected, thin walled DOPC giant vesicle of being unilamellar is 88.2%. This probability is highly dependent upon experimental preparation, varying widely between data sets. This data suggests that in order to concretely identify lamellarity on the basis of fluorescence quantisation, large data sets are required. Data sets, the order of Sets 3a and 3b, for which  $n \geq 50$ , would be sufficient to identify lamellarity given that we have now established the method. For correlative fluorescence and qDIC measurements, I decided to ensure  $n > 100$  in order to allow for some failures in the analysis.

This data proves that GUV electroformation is successful at generating

large populations of unilamellar vesicles. Furthermore fluorescence quantisation has been demonstrated successfully with Atto-448 DOPE for the first time. We now proceed to demonstrate correlative qDIC and fluorescence quantisation in giant DOPC vesicles and prove that the two methods yield the same assessment of vesicle lamellarity.

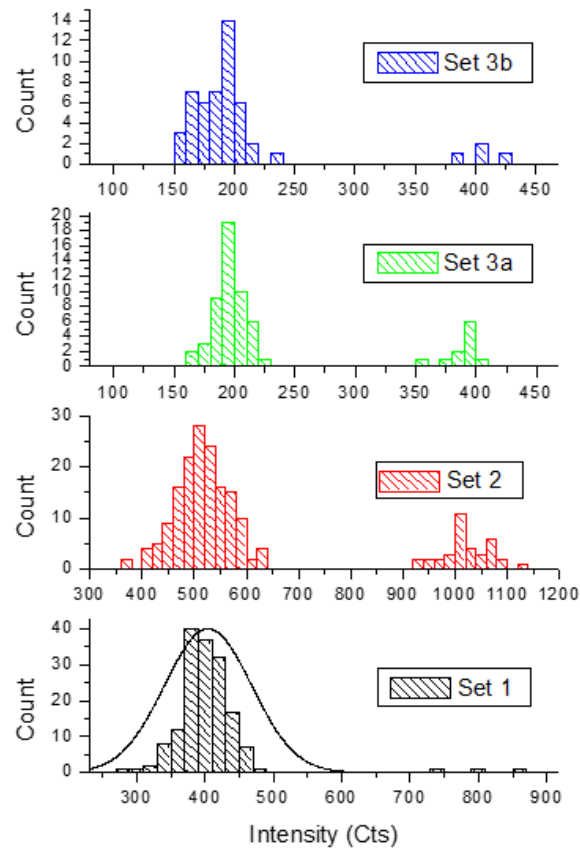


Figure 3.2: Distribution of radial Fluorescence intensities from large populations of thin walled DOPC vesicles sampled from 3 separate preparations ( $n=466$ ), demonstrating quantisation of fluorescence into discrete intensity bands. Note systematic offset of the average (lower intensity band) level between different populations due to slight changes in experimental preparations. A fitted Gaussian distribution is shown in the case of set 1, this was omitted for clarity in the other sets.

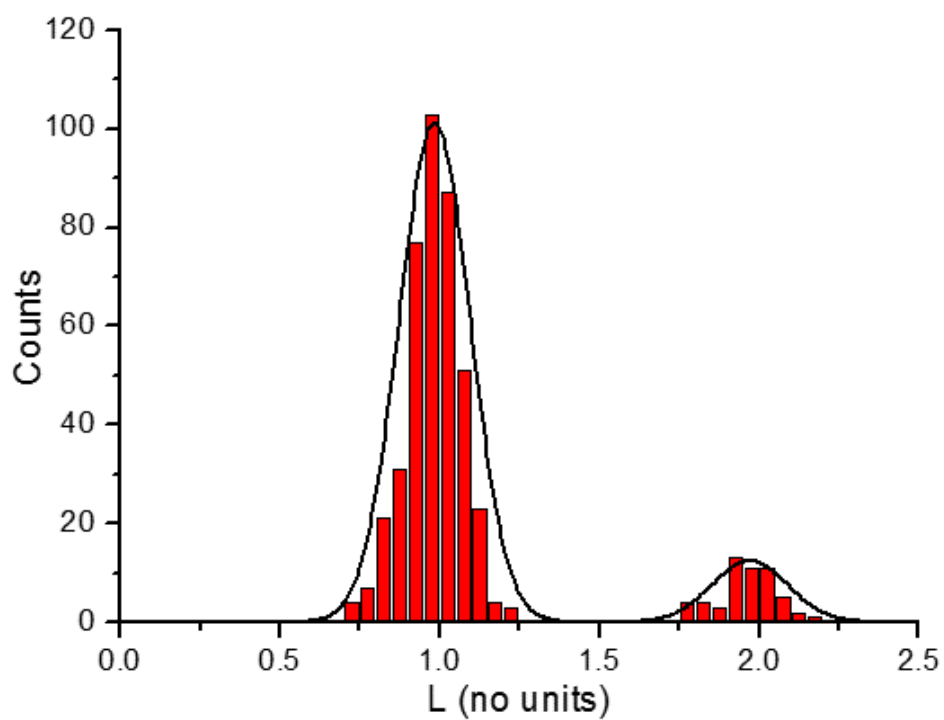


Figure 3.3: Characterisation of DOPC Giant vesicle lamellarity by radial fluorescence from Atto-488 DOPE. Lamellarity parameter  $L$ , as defined in the text, permits direct comparison between different preparations of giant vesicles. Uni- and Bi- lamellar vesicles are apparent across a statistically significant population ( $n=466$ ).

### 3.3 Fluorescence and qDIC assessment of vesicle lamellarity

#### 3.3.1 qDIC Image acquisition and analysis

I have explained in section 1.6.2.2, the theory of qDIC in which two DIC images, acquired at equal and opposite phase offsets can be combined into a single contrast image which linearly encodes the difference in phase between two points separated by a distance comparable to the diffraction limit. Considerable effort was expended in order to identify the best possible method for accurate and reproducible extraction of the DIC response. I carefully consider the methods of image acquisition and analysis which must be applied to qDIC contrast data. These considerations are dominated by the nature of the samples analysed by qDIC: GUVs which are freely suspended in aqueous solvent and spherical in shape, and PLBPs which are immobile and present flat geometry.

The approximate thickness of a DOPC bilayer is 4nm, the DIC signal arising from this small optical path length difference is correspondingly slight. It is therefore important to minimise image noise; contrast images were formed from the mean of 128 images for GUV or 512-4096 images acquired at each phase offset when applied to PLBPs. An analysis of the noise is detailed extensively in the paper (McPhee et al., 2013), it transpires that in the case of GUV, a single image has, in principle, sufficient signal to noise to determine lamellarity (for the experimental setup used in this study). For PLBPs contrast between coexisting lipid liquid phases corresponds to sub-nm thickness variations, therefore requiring a higher degree of noise reduction. Due to the integration and readout times of the CCD (Hamamatsu Orca 285),  $\sim 13$ s was required for each GUV image set and  $\sim 51$ s for PLBPs. These acquisition timescales introduce sample dependent aberrations which must be accounted for. Vesicles free floating in suspension exhibit three types of motion on these timescales, driven by thermal Brownian processes:

1. Modal oscillations of the membrane
2. Deformations of shape

### 3. Rigid Translation

Modal oscillations encode as a slight blurring of the vesicle periphery in the mean images. We account for this motion with an analytical model applied directly to the image data. Vesicles exhibiting bulk shape deformations are minimised through careful control of the experimental conditions: isosmotic, isobaric and isothermal conditions are kept throughout imaging. Deforming vesicles thus constitute only a small number of the large thin walled structures and were ignored for the purposes of this study. Rigid vesicle translation was corrected through the use of Fourier domain image registration to sub-pixel align the images prior to formation of the average.

Precise extraction of phase information and therefore lamellarity was performed through fitting of the GUV profile with a model of the contrast image. Due to the simple spherical geometry of GUV, the optical path length (phase) assessed axially through this sphere is distributed with a profile similar to the fluorescence intensity distribution shown in figure 3.4. DIC contrast arises due to the difference between two such distributions offset with small lateral shear. The fluorescence intensity distribution was therefore used as the basis for our model; convolution of this model with the DIC system response in frequency space therefore yields a DIC contrast model. I define  $A_p$ , the area under the peak around the GV periphery, and  $I_s$ , the intensity difference between the outside and inside of the vesicle as shown in figure 3.4. These parameters allow for quantitative analysis of the GV lamellarity in an analogous method for both fluorescence and qDIC models.  $I_s$  has been utilised and shown in section 3.2 above with regards to fluorescence quantisation.

The fluorescence response due to a GUV imaged at the equatorial plane comprises the summation of a Gaussian function to model edge response, defined as  $A_p$  in figure 3.4 with an error function (erf) to model the out of focus 'step' response  $I_s$ . The formula for our function is given below in equation 3.1. In addition to  $A_p$  and  $I_s$ , we allow for variation of width parameters  $\omega_s$  and  $\omega_p$  (describing the width at edge and interior). This permits precise control over response symmetry and for profile blurring due to modal oscillations of the GUV. We propose that further analysis of width parameters may allow for direct extraction of the biophysical parameters of the system such as the membrane bending rigidity; a systematic study has

not been completed at this time.

$$\phi(\mathbf{r}) = \frac{A_p}{\omega_p \sqrt{\pi}} \exp \left[ - \left( \frac{|\mathbf{r} - \mathbf{R}_c| - R_0}{\omega_p} \right)^2 \right] + \frac{I_s}{2} \left[ \operatorname{erf} \left( \frac{|\mathbf{r} - \mathbf{R}_c| - R_0}{\omega_s} \right) \right] \quad (3.1)$$

where  $R_0$  is the radius of the required model (vesicle) and  $R_c$  the offset of the model (vesicle) centre within the image plane, all other variables were defined earlier.

The final step in image analysis is to fit the model to the observed DIC data. To maximise the use of all available image data, a 2D model is produced by rotation of the model function about a circular or elliptical path modelling the GUV perimeter. The path is based upon an initial guess of the size, position, radius and width of the measured vesicle as shown in figure 3.5.

The model is then optimised so as to reduce the squared residual between the model and the data set as shown in 3.5c and d. The norm for this optimisation was  $\Delta = \frac{\|I_c - I_p\|}{\|I_q\|} < q$  where  $I_s$  and  $I_p$  are the experimental and model intensities respectively and  $q=0.5$  is the required quality factor for the optimisation. Optimisation was implemented in custom Matlab scripts using the 'fminsearch' downhill simplex method. Following optimised fitting, the GUV phase response can be quantified as either the peak or step responses  $A_p$  or  $I_s$ , both of which yield the same assessment of vesicle lamellarity.

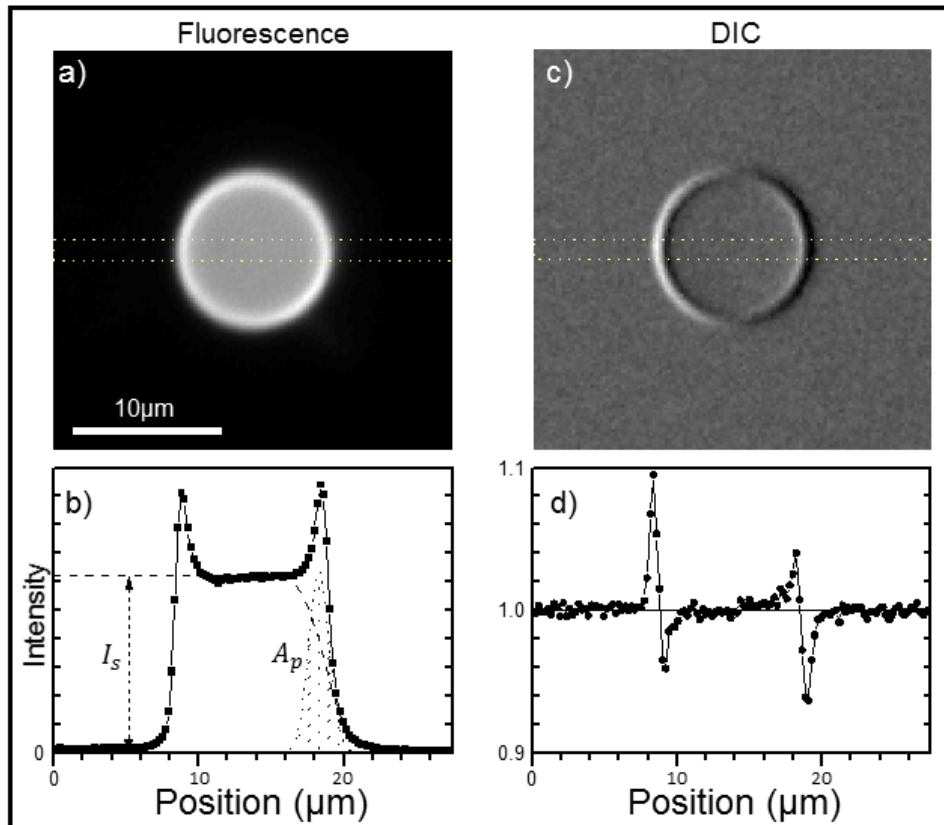


Figure 3.4: Fluorescence and qDIC response for a single GUV composed from DOPC with 0.15 mol% ATTO-488 DOPE. a) Fluorescence response above 535nm from GUV (2500ms exposure, linear scaling). b) Average intensity profile for image rows bounded in yellow in subimage a) note two regions of interest: a defocused average intensity level  $I_s$  within the GUV (symptomatic of the single photon excitation used) and a peak intensity level  $A_p$  at the vesicle periphery due to increased local material within the focal volume. c) Single phase offset, averaged ( $n=128$ ) DIC image of GUV (linear scaling) demonstrating differential DIC response, image rotated such that the shear direction is in x d) Average DIC intensity profile for the rows bounded in yellow within subimage c). Figure reproduced from (McPhee et al., 2013)

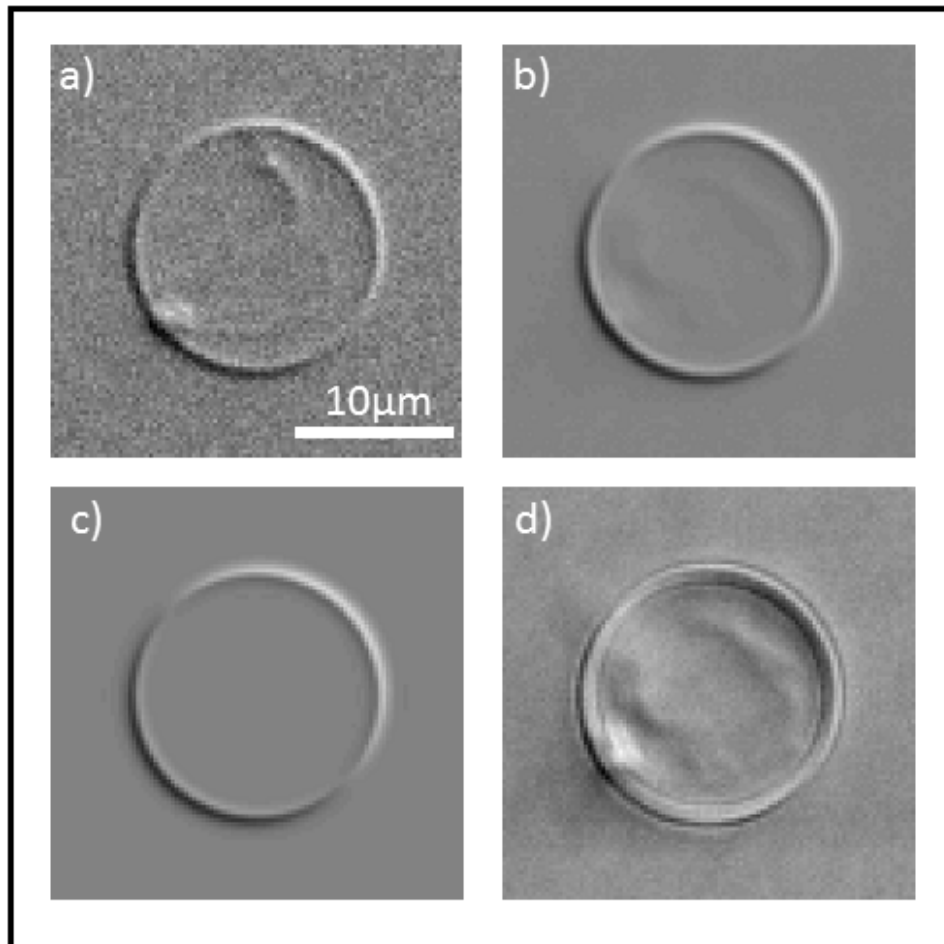


Figure 3.5: Experimental, normalised and background subtracted DIC image of GUV, single frame acquisition. b) Mean contrast image  $I_c$  formed from the average of 128 images at each phase offset. c) Simulated DIC image of GUV formed from an initial estimate of vesicle parameters. d) Residual after optimisation  $(b-c)/c$ . Linear greyscale applied to all images, range -0.1 to 0.1 (a-c) and -0.02 to 0.02 (d). Figure reproduced from (McPhee et al., 2013)

### 3.3.2 qDIC object phase extraction techniques

I have demonstrated how an analytical model of the DIC response due to a GUV has been created, and that this response is fitted directly to contrast images  $I_c$  in order to extract amplitude parameters ( $A_p$ ,  $I_s$ ) to quantify their lamellarity. This approach works only in the case of GUV and is not of general applicability. The contrast images formed under this implementation of qDIC encode linearly the difference in phase between two points separated by the shear offset of the microscope. In theory, integration of GUV contrast images ( $I_c$ ) along the shear direction, between two points A and B yields directly the phase along that path. If this path crosses a boundary between media of different refractive indices or axial thickness then the relative phase is well defined and the absolute thickness could, in principle, be extracted. Therefore, integration of the contrast image should recover the phase distribution across the field of view.

Simple numerical integration of  $I_c$  performed by taking a cumulative summation of pixel values along the shear direction was found to be subject to long period trends, susceptible to noise and produced an inaccurate reconstruction of the phase distribution. To suppress trends and to minimise the effects of image noise, we performed integration in the Fourier domain. The Fourier multiplier ( $\zeta$ ) of the DIC transmission function in terms of the earlier expounded theory is:

$$\zeta = 2i \sin\left(\frac{\mathbf{s} \cdot \mathbf{k}}{2}\right) \quad (3.2)$$

Where the symbols take on the meaning defined earlier. Convolution of the signal with  $\zeta$  in the Fourier Domain, is equivalent to performing differentiation in the spatial domain (thereby accounting for DIC response). Deconvolution of the contrast image with the DIC transmission function should therefore yield the required phase, reversing the differentiation. The inverse transformation was performed by Weiner deconvolution with the Fourier multiplier:

$$G(\mathbf{k}) = \frac{1}{\zeta + \frac{1}{\kappa\zeta^p}} \quad (3.3)$$

Weiner deconvolution minimises RMS noise in the final image at given signal to noise  $\kappa$  whilst also high pass filtering the image, effectively suppressing artefacts seen with simple numerical integration (McPhee et al., 2013).

At low values of  $\kappa$  around 100-150, trends and integration stripe artefacts are strongly suppressed. For phase extraction performed on PLBPs,  $\kappa = 150$  was used throughout. All analysis was performed with custom Matlab scripts.

### 3.3.3 Correlative Fluorescence to qDIC

In section 3.2, I demonstrated the efficacy of fluorescence quantisation (FQ) for vesicle lamellarity assessment. Herein, FQ is combined with qDIC measurements taken upon the same vesicles. In order to avoid unintended excitation of the Atto-488 under DIC, which would introduce absorption artefacts and prevent phase extraction. I have utilised a bandpass filter centred at  $550 \pm 20\text{nm}$  for qDIC excitation. Corresponding fluorescence excitation is over 4 orders of magnitude less than at 488nm (the absorption maximum of the fluorophore) and a pure DIC response is measured. Correlative fluorescence to qDIC analysis performed upon the same vesicles should therefore yield two independent measures of the vesicle lamellarity across a statistically significant population.

Data was acquired using a Nikon inverted microscope (Eclipse Ti-U, Nikon, Japan) with 0.75NA, 20x objective (Nikon CFI Plan Apochromat series) and matched 0.72NA dry condenser. A 1.5x tube lens multiplier was utilised to ensure critical sampling at the 12 bit monochrome CCD detector (Hamamatsu Orca-285). Samples were illuminated by metal-halide light source (Prior Lumen 200). For fluorescence all images were acquired in the Epi direction using a GFP filter set (Semrock, USA). A standard DIC module and slider (Nikon, Japan) were installed into the condenser and objective turret to enable qDIC measurements, the tube lens multiplier was also used. Exposure times were 100ms/frame under DIC and 500ms for fluorescence acquisition. A total of 128 frames per phase were acquired under DIC, a single image was sufficient for fluorescence. For analysis, 145 data sets were acquired, the final number of data sets contributing was  $n=77$ . The deciding factor in the analysis of which vesicles to accept or reject is the q (quality) factor introduced into the analysis in section 3.3.1, in defective vesicles the minimisation algorithm becomes divergent and will end after a maximum number of trials. The primary factors which affect the

ability to minimise the quality factor are:

- Presence of lipid defects
- Non elliptic profile of the vesicle: poor fit with model
- Failure of the registration algorithm

These factors combined lead to the approximately 50% pass rate for the analysis. Examples of typical passing and failing data sets are shown in figure 3.6, for which defects, shape malformations and registration errors can be seen.

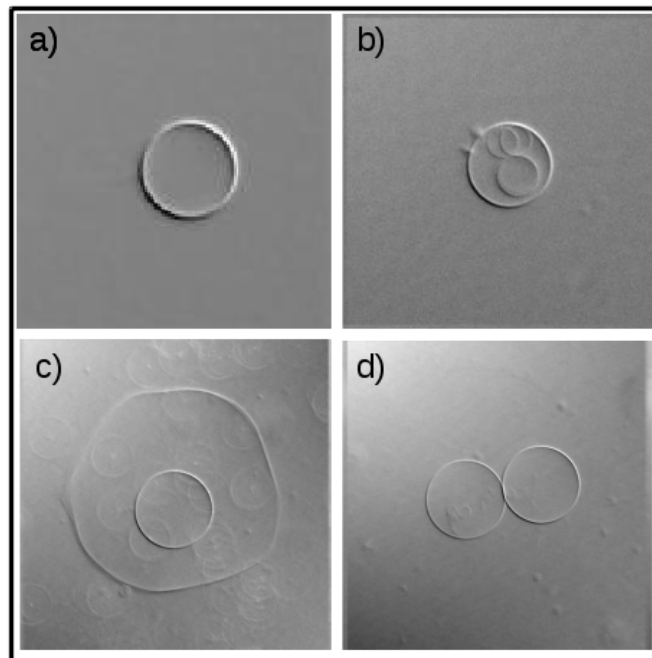


Figure 3.6: Examples of successfully analysed GUV under qDIC imaging (a), and failures due to defects (b), shape (c) and registration errors (d).

Fluorescence analysis was performed with custom Matlab scripts. The scripts permit selection of the vesicle, exclusion of defects and inclusions and automatic determination of the vesicle radius (given an initial guess). Fluorescence data is extracted through fitting of the model shown in figure 3.4 (b), equation 3.1 with optimisation resulting in an estimate of the parameters ( $A_p$ ,  $I_s$ ) quantifying the intensity for both the defocused step region (due to single photon excitation above and below the focal plane) and

the fluorescence intensity at the vesicle periphery. Thus the same analytical model can serve for analysis both fluorescence and qDIC data.

qDIC data analysis was performed with a custom application written in Matlab (version 2012, Mathworks Inc). As discussed vesicle lamellarity can be assessed with qDIC by determining an estimate for either the amplitude at the vesicle perimeter  $A_p$  or the magnitude of the phase across the plateau region interior to the vesicle ( $I_s$ ).

FQ applied to the population of vesicles is shown in figure 3.7. The image background is near constant across the entire population, demonstrating the precise reproducible nature of the experimental conditions. The step and edge metrics result in an obvious quantisation of the vesicle population into one of two levels: uni- and bi-lamellar phases. As shown earlier, vesicles comprising up to 4 bilayers have been observed. The step region comprises defocused light from the sample, as such it is very stably quantised with no radial dependence. The peak metric on the other hand is influenced strongly by the vesicle radius; this effect is attributable to the 3d geometry of the vesicle in relation to the size of the excitation focus of the microscope. Larger vesicles present a greater column of membrane parallel to the focal axis, we therefore generate a monotonic increase in the measured intensity as greater numbers of fluorophores fall within the excitation volume. Allowing for this effect, levels assessed by either metric are quantised and exhibit a Gaussian distribution with the mean of the upper level almost exactly double that of the lower. The standard deviation of the unilamellar population assuming that the mean corresponds to 4nm would be 0.7nm.

For qDIC analysis, in an analogous way the lamellarity assessment can be made on the basis of the intensity assessed at the peak or step region (shown in figure 3.4). The resultant distribution of either metric against the vesicle radius ( $R_0$ ) shows a clear two level system as shown in figure 3.8. The lower of which levels is assumed to correspond to the unilamellar case.  $A_p$  shows a strong dependence upon vesicle diameter (proportional to  $\sqrt{R_0}$ ). This result was expected due to consideration of the vesicle geometry with respect to the illumination beam geometry. We account for this in our final assessment by introducing a lamellarity factor  $L$ , applied to the peak such that  $L = \frac{A_p}{A_{pu}\sqrt{R_0}}$  with  $A_{pu}$  being the calibrated unilamellar mean

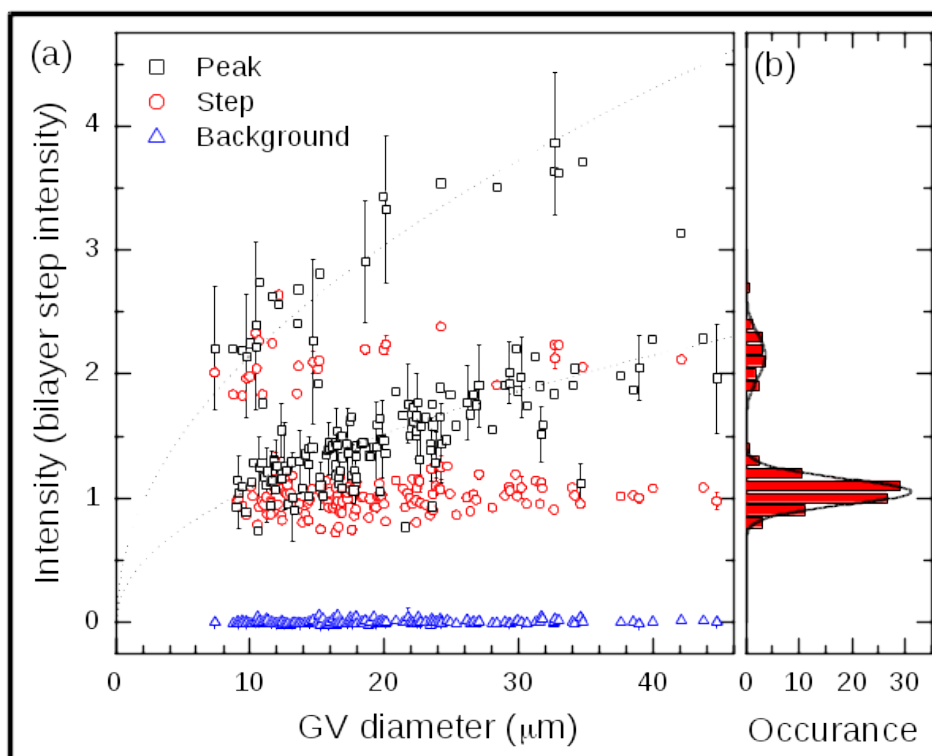


Figure 3.7: Fluorescence measurements of ATTO-488 labelled DOPC vesicles. Intensities of the background, central step region ( $I_s$ ) and mean intensity at the vesicle rim ( $A_p$ ) are shown as labelled and as described in the text. Dashed lines represent  $\sqrt{R_0}$  fit to peak data over the vesicle radius  $R$ . Figure reproduced from (McPhee et al., 2013)

response in  $A_p$ . With the step parameter no such dependence is seen and we define a lamellarity factor  $L$  such that  $L = \frac{I_s}{I_{su}}$  with  $I_{su}$  being calibrated unilamellar GUV mean response in the step.

As shown in figure 3.8, a quantised set of lamellarities, normally distributed about the single and double bilayer levels is observed. Furthermore, as shown in figure 3.9, direct comparison between fluorescence and qDIC assessments performed upon the same vesicles demonstrates both methods lead to the same assessment of vesicle lamellarity over a significant population ( $n=77$ ). By comparison between methods, the standard deviation  $\Delta L = 0.28 \pm 0.02$  for the unilamellar distribution yields a precision estimate of  $\sim 1.1$  nm for the qDIC analysis which is significantly less than the bilayer thickness. We note that this precision is slightly worse than that

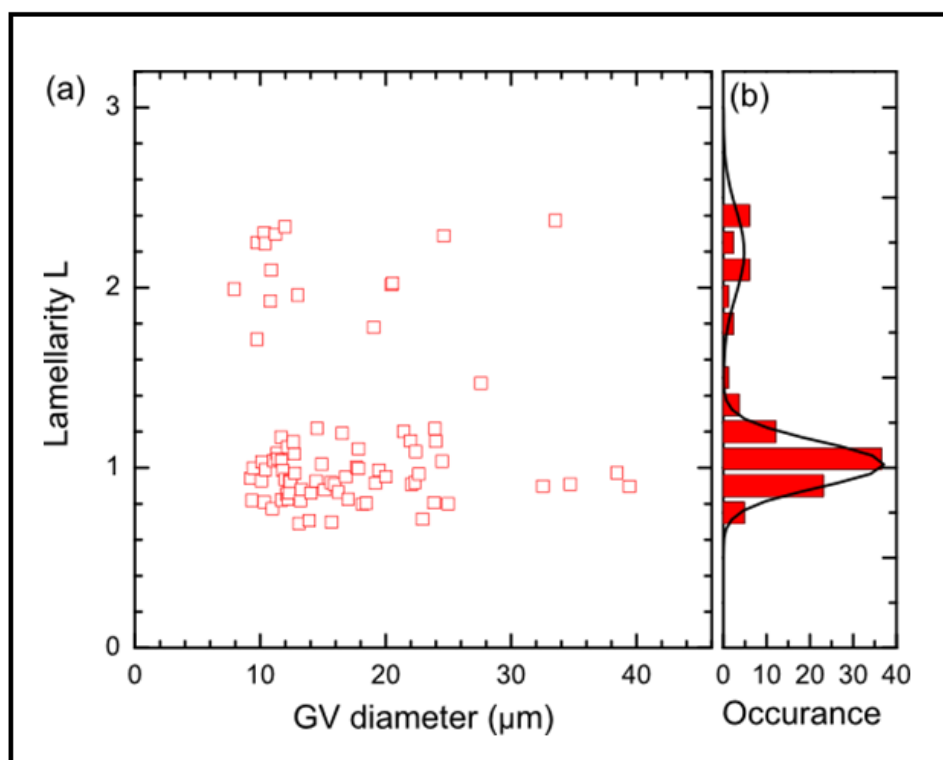


Figure 3.8: Measured qDIC response in terms of vesicle lamellarity ( $L$ ) for a statistically significant ( $n=77$ ) population of thin walled giant vesicles. In this study, two populations of vesicles are seen with lamellarities normally distributed about means of  $\approx 1$  and  $\approx 2$  bilayers i.e. Uni- and Bi- lamellar phases. Figure reproduced from (McPhee et al., 2013)

of the fluorescence only method ( $\approx 0.7\text{nm}$ ). The standard deviation of the lamellarity estimate by qDIC is significantly worse than the absolute measurement error ( $<0.01$ ). For the calibration procedure described, assessment of the mean  $I_{\text{su}}$  and  $A_{\text{pu}}$  is only required to be done once. Changes in lipid constituents will yield only slight changes in DIC response, which although apparent, will not deter from an accurate estimate of the lamellarity of an individual giant vesicle. Compared with FQ this is a significant advantage, avoiding the need to recalibrate with each new sample.

Further analysis of the image noise demonstrates that a single image at each phase offset can be used for successful identification of the lamellarity. This would provide a measurement less subject to fluxions and movement of the vesicle and could in principle be extended to much faster frame rate

acquisition to remove these effects almost entirely or for high throughput analysis of large populations.

We compare lamellarity assessment under both qDIC (using  $L$  assessed by the step parameter) and fluorescence imaging modalities in the correlation plot shown in figure 3.8. A complete correlation between the two methods is observed although we note that the agreement is not 100%. A few non-integer assessments of lamellarity are produced under qDIC. Whilst we do not offer a systematic investigation of this phenomenon here, we suggest that the discrepancy may be due to sub-resolution ( $xy$ ) inclusions of lipid structures that whilst not resolved still register a change in phase. These structures, where present, we manually excluded from the fluorescence analysis thereby producing the discrepancy.

qDIC as demonstrated is therefore a sensitive imaging modality sufficient to distinguish addition or subtraction of individual peripheral bilayers in GUV model systems. qDIC provides a powerful, quantitative and label free alternative to the established method of fluorescence quantisation.

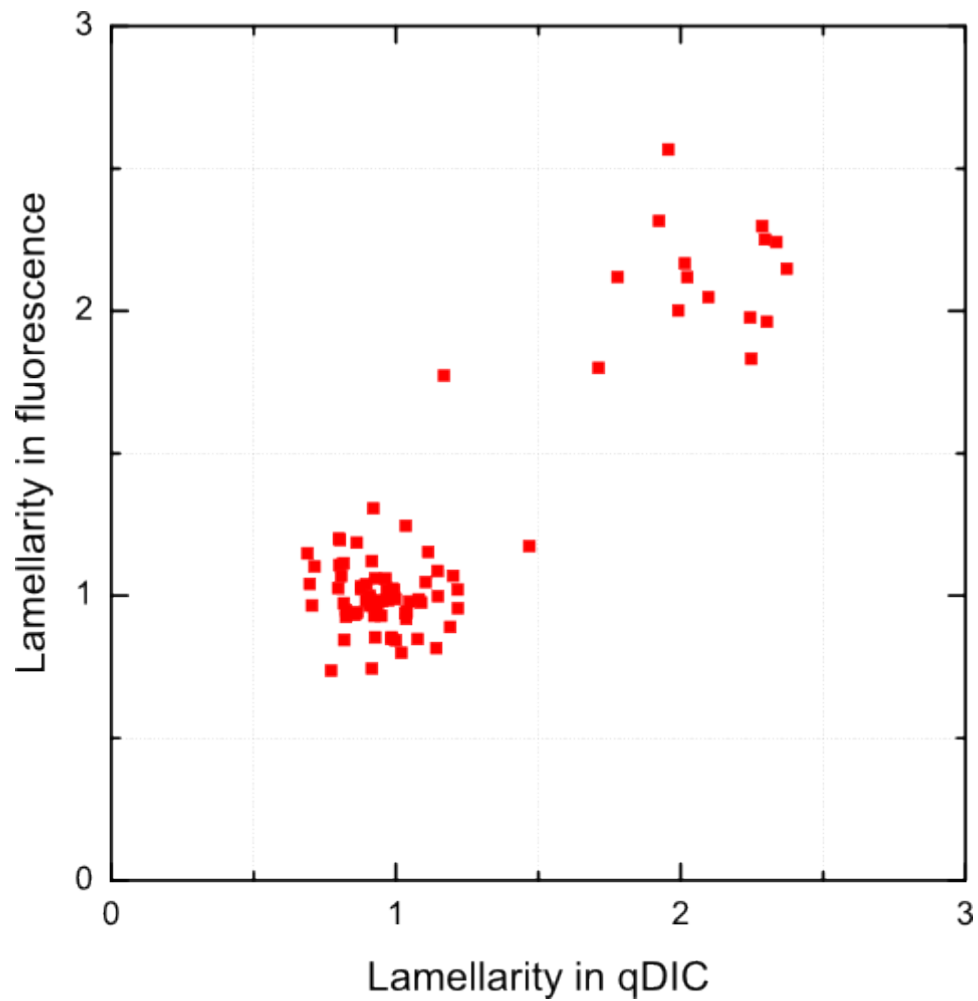


Figure 3.9: Comparison between assessments of vesicle lamellarity as performed by qDIC and fluorescence quantisation (FQ) upon the same thin walled giant vesicles across a significant population ( $n=77$ ). qDIC provides a label free analogue of FQ yielding the same assessment of vesicle thickness. Figure reproduced from (McPhee et al., 2013)

### 3.4 Two photon microscopy of Atto-488 DOPE in giant unilamellar vesicles

As discussed in the chapter introduction (3.1), characterisation of Atto-488 DOPE was conducted in order to understand fully its phase partitioning behaviour since this fluorophore had not been used in this context before and it was unknown whether the probe would partition. Atto-488 was selected due to initial problems caused by photo-bleaching of NBD-DOPE as seen during preliminary fluorescence quantisation assays. Atto-488 with its 90% quantum yield and long lifetimes, combined with good two photon cross-section represented a superior replacement. Atto is available conjugated to a range of lipids (all via amide bond at the headgroup location), we have selected DOPE since many DOPE conjugated fluorophores partition into the liquid disordered phase. The primary purpose of this study was to qualitatively assess the partitioning behaviour of Atto-488 DOPE with our lipids of interest.

Herein vesicles comprising single component (DOPC or PSM), double component (DOPC and PSM, PSM and Cholesterol, DOPC and Cholesterol) or triple component (DOPC, PSM and Cholesterol) with low concentration ( $< 0.5\text{mol}\%$ ) of Atto-488 DOPE were prepared and imaged under two photon microscopy. The fluorescent lipid analogue can partition or aggregate only if it has greater affinity for one or more of the lipid components or greater self-affinity. In single component systems, self-affinity of the analogue, under conditions of free 2d diffusion (within a single bilayer leaflet), could lead to aggregation and separation of the component from the majority lipid constituent. In more complex double and triple component systems, greater affinity for any of the lipid components will drive segregation. It is this partitioning behaviour that makes the analogue useful.

Vesicles were created by the electroformation method (section 2.1.2.2) with the relative concentrations of lipid species shown in table 3.1. Imaging was performed on a modified inverted microscope (Nikon Ti-U, Japan) with 20x (0.75NA) objective magnification and 0.72NA dry condenser. Data was acquired by raster scanning a focused laser beam across the sample, with a dwell time of 10 $\mu\text{s}$  typical with super-sampling of the focal volume by a factor of 3. The acquisition time trace (PMT counts against time) was

then reconstructed into a 2d array of pixels comprising counts per spatial location. In order to sample the whole surface of individual GUV, 3d Image stacks were created by repeated raster scanning of the sample whilst moving the objective up by  $0.5\mu\text{m}$  between each 2d scan.

Data analysis was performed in two stages post stack reconstruction: first image sequences were loaded into the FIJI application and a rigid body registration performed between subsequent frames in order to remove the effects of vesicle translation. Secondly, the registered images were exported and loaded into custom Python scripts for further processing. Within these scripts each registered image stack was compressed, forming two data sets, an average image through the vertical axis of the stack, and a maximum intensity projection along the same axis. The average image suppresses the effects of image noise and presents a profile which is similar in form to that of single photon excitation, since it contains information about all vertical positions within the sample. The maximum intensity projection enhances image contrast within the samples (at the expense of noise) but is good for highlighting extended areas of sample in-homogeneity. Full 3d reconstructions of the data sets were also performed within FIJI and were used as a final visual check of vesicle homogeneity.

### 3.4.1 DOPC giant unilamellar vesicles

Since Atto-488 DOPE had already been extensively used in our fluorescence microscopy assay of DOPC GUV (section 3.2) with no in-homogeneity seen, it was anticipated that this would be confirmed by two photon assay. Since large numbers of vesicles had to be visualised within samples before forming an opinion, we present only typical results demonstrating a standard profile for the different types of lipid vesicles. As shown in figure 3.10, DOPC GUV incorporating Atto-488 DOPE show an azimuthal intensity (fluorescence anisotropy) dependence upon the direction of the laser linear polarisation. This is attributed to the presentation of the Atto-488 molecule at the head group location of the lipids, whilst the molecule can rotate freely around its single bond to the lipid; it is fixed in its vertical presentation (it cannot bend about the bond). In both the average and maximum inten-

<b>Membrane system designation</b>	<b>Lipid Species Present</b>	<b>Relative concentration (mol)</b>
Single	DOPC:Atto-488 DOPE	1 : 0.002
Single	PSM:Atto-488 DOPE	1 : 0.002
Double	DOPC : PSM : Atto-488 DOPE	1:1:0.002
Double	DOPC : Cholesterol : Atto-488 DOPE	1:1:0.002
Double	PSM : Cholesterol : Atto-488 DOPE	1:1:0.002
Triple Ternary /	DOPC : PSM : Cholesterol : Atto Dope	2:1:1:0.002

Table 3.1: Relative concentrations of model lipid species used to characterise the partitioning behaviour of NBD-DOPE within Giant Unilamellar Vesicles.

sity projections, in-homogeneity of the fluorophore is not seen (allowing for the acquisition noise and the possible presence of other lipid structures). The fluorophore appears to be distributed throughout the entire bilayer and demonstrates no aggregation or partitioning behaviour.

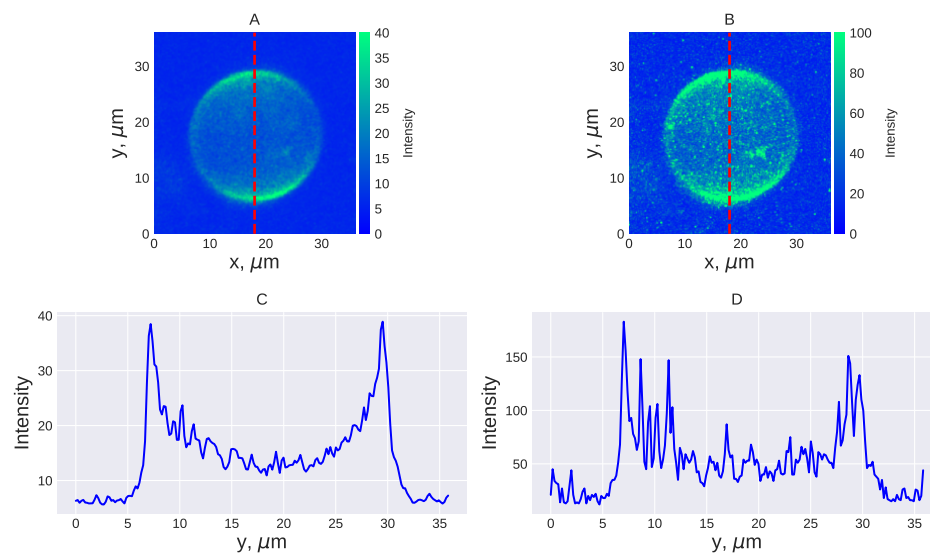


Figure 3.10: Spherical projections of DOPC giant unilamellar vesicles visualised with two photon fluorescence microscopy from incorporated Atto-488 DOPE. Subplot A is an average intensity projection through the imaging stack with the profile for the red dashed line shown in C. Subplot B is a maximum intensity projection through the same vesicle with associated red-line profile in D. An azimuthal intensity distribution of the fluorescence signal can be seen at the vesicle periphery.

### 3.4.2 Porcine Sphingomyelin vesicles

A typical case for porcine Sphingomyelin (PSM) vesicles is shown in figure 3.11. PSM in isolation from other lipid species will present in a gel (solid) phase due to its predominately saturated, long chain length structure (the average chain length is 21 carbon atoms). This enables close packing of neighbouring PSM molecules with high self-affinity. As a result, electroformation of PSM vesicles yields a polydisperse range of multilamellar structures. Due to the solid nature of these PSM vesicles, we do not observe spherical vesicles, instead highly faceted edges are present. These edges can be observed to oscillate as a whole under Brownian motion, confirming their non-fluid nature (result not shown). We do not observe partitioning of the fluorophore, areas of the vesicles absent of Atto-488 are not seen. Therefore, we conclude that even in the solid phase, Atto-488 is homogeneously incorporated.

Note that as shown in the maximum intensity plot of figure 3.11, there appear to be some saturated pixels. However this is an illusion, the data is acquired as a time series trace of the number of photo-electrons registered at the PMT. To convert to an image, a scaling from the photo-electrons to 8bit gray scale must be applied. Therefore, some pixels in the final image may end up with a value of 255, however it does not follow that the original detector was saturated since the applied mapping is controlled under software. For all data shown the PMT is operated at the lower end of its linear range, and therefore has substantial overhead (500 - 8000 counts typical versus max 50000).

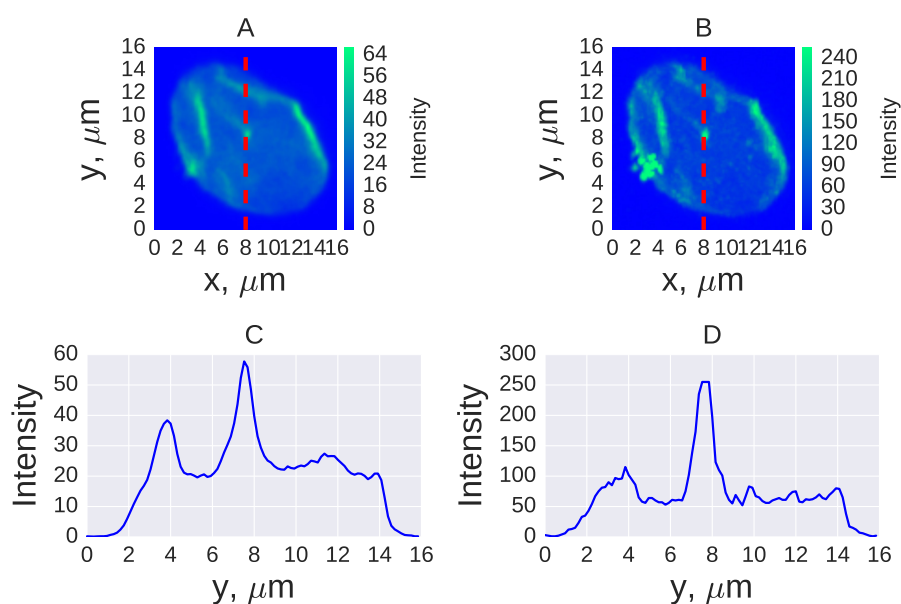


Figure 3.11: Spherical projections of Porcine Spingomyelin (PSM) vesicles visualised with two photon fluorescence microscopy from incorporated Atto-488 DOPE. Subplot A is an average intensity projection through the imaging stack with the profile for the red dashed line shown in C. Subplot B is a maximum intensity projection through the same vesicle with associated red-line profile in D. PSM vesicles are formed from a gel phase lipid by electroformation; this produces a poly-disperse range of multilamellar vesicles with faceted edges: Spherical vesicles are not observed in this phase. (note that image saturation DOES NOT correspond to detector saturation as explained in the text)

### 3.4.3 Sphingomyelin and Cholesterol vesicles

The addition of Cholesterol to Porcine Sphingomyelin (PSM) demonstrates the dual nature of Cholesterol within lipid bilayers. As demonstrated in section 3.4.2 vesicles formed from pure PSM form multilamellar, faceted structures which is attributed to the solid phase of PSM. The addition of Cholesterol acts to break the molecular order of this phase and produces vesicles in a liquid ordered state (Krivanek et al., 2008). As a result, faceted vesicles are no longer seen and GUV typically observed as seen in figure 3.12. Some additional lipid structures are seen during the projections, however these are not part of the bilayer itself and are simply peripheral lipid aggregates (c.f. figure 3.14). PSM and Cholesterol vesicles again present with no apparent partitioning of the Atto-488 DOPE probe.

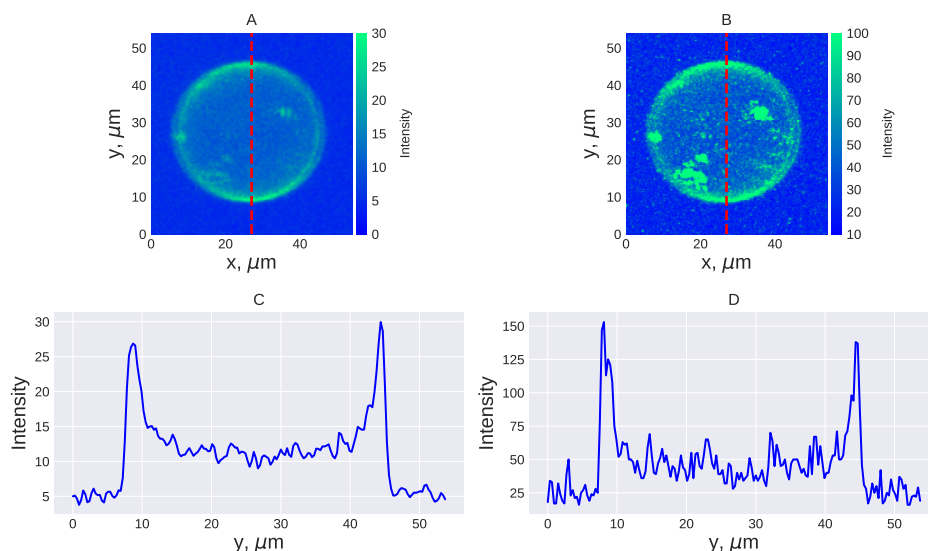


Figure 3.12: Spherical projections of Porcine Sphingomyelin (PSM) and Cholesterol vesicles visualised with two photon fluorescence microscopy from incorporated Atto-488 DOPE. Subplot A is an average intensity projection through the imaging stack with the profile for the red dashed line shown in C. Subplot B is a maximum intensity projection through the same vesicle with associated red-line profile in D.

### 3.4.4 DOPC and Cholesterol vesicles

Cholesterol is expected to promote order when added to pure DOPC vesicles forming a single liquid disordered phase (Brown, 1998). As shown in figure 3.13 we observe homogeneous, thin walled vesicles formed from these constituents. In no cases does the fluorophore appear to be spatially constrained within particular regions of the GUV. Although some highlights are present, by comparison to the 3d reconstruction shown in figure 3.14, we can see that the vesicle has some externally associated lipid structures, which are not examples of partitioning. We must therefore conclude that Atto-488 does not partition within this system either.

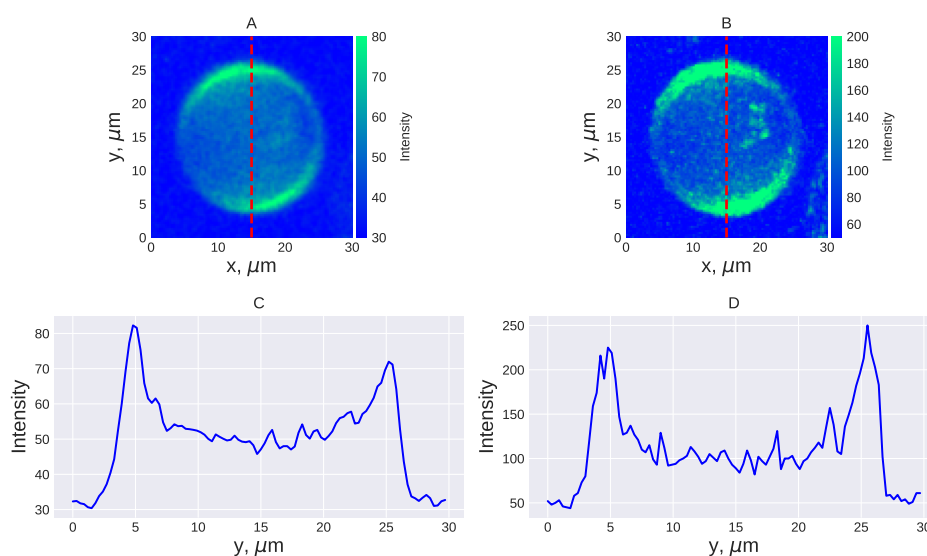


Figure 3.13: Spherical projections of DOPC and Cholesterol vesicles visualised with two photon fluorescence microscopy from incorporated Atto-488 DOPE. Subplot A is an average intensity projection through the imaging stack with the profile for the red dashed line shown in C. Subplot B is a maximum intensity projection through the same vesicle with associated red-line profile in D.

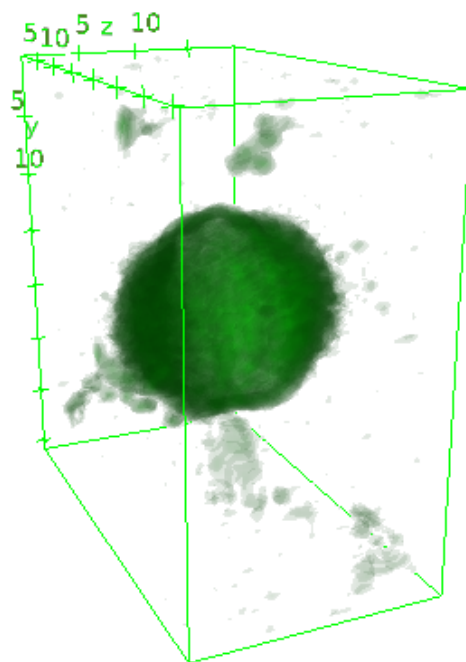


Figure 3.14: 3d Reconstruction of the DOPC and Cholesterol vesicle shown in figure 3.13, demonstrating that highlights seen in the 2d projections are simply peripherally associated aggregate lipid structures and not examples of partitioning behaviour.

### 3.4.5 DOPC and Sphingomyelin vesicles

When combined, DOPC and porcine sphingomyelin (PSM) are seen to form large, thin walled vesicles as shown in figure 3.15. Inhomogeneities of the fluorophore are not seen, however it was anticipated that they could be seen within this system. PSM in isolation forms a solid phase as shown earlier (section 3.4.2) and without the influence of Cholesterol to break this order, it was possible that the PSM and DOPC may separate into a solid phase and disordered phase. No evidence for this segregation has been found and the vesicles present as a single phase formed from a homogeneous mixture of the individual components. Again some peripherally associated lipid structures can be seen as is common with any formation method.

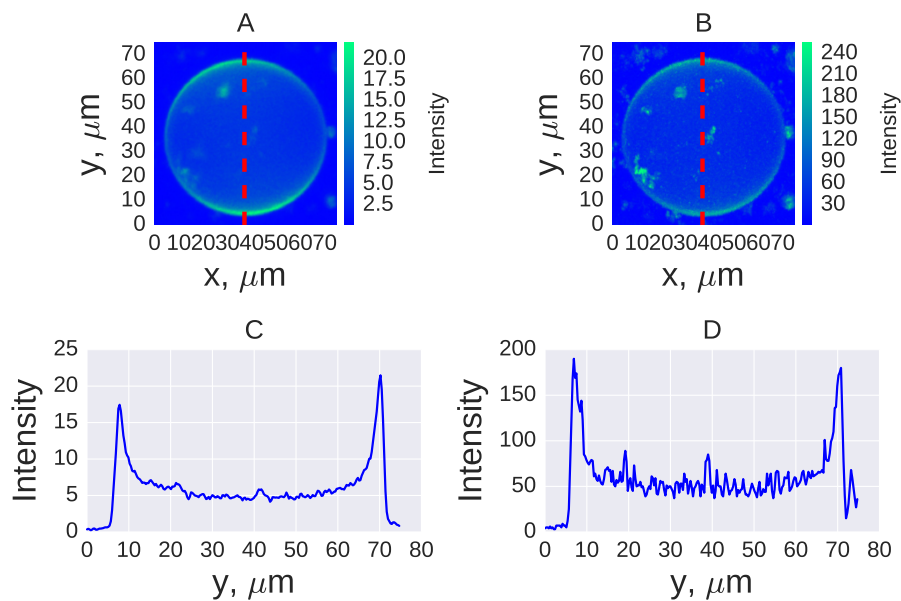


Figure 3.15: Spherical projections of DOPC and Sphingomyelin vesicles visualised with two photon fluorescence microscopy from incorporated Atto-488 DOPE. Subplot A is an average intensity projection through the imaging stack with the profile for the red dashed line shown in C. Subplot B is a maximum intensity projection through the same vesicle with associated red-line profile in D.

### 3.4.6 Ternary giant unilamellar vesicles

In triple component DOPC, PSM and Cholesterol vesicles significant differences are observed compared with all prior systems. As shown in figure 3.16 extended regions at the right hand side and a large region in the lower hemisphere are absent fluorescence. The degree of partitioning is high, with an almost complete absence of signal within this phase. In addition, as shown in the lower images, for which a single cut has been shown, although the GUV contains other vesicles, the high degree of fluorescence partitioning of the containing GUV is clearly observed. In addition, by contrast to the pure PSM vesicles, which are faceted due to the solid lipid phase present, we can conclude from the vesicle curvature that the separate phases are liquid. Regions of reduced fluorescence are not coincident with the azimuthal variation of the fluorescence intensity at the vesicle periphery and very different intensity profiles can be seen. Therefore, we can conclude that uniquely within these ternary systems:

- More than one coexisting lipid liquid phase is present (in all simpler systems only a single phase presents).
- Atto-488 DOPE demonstrates a strong phase preference.

It was anticipated that partitioning would occur into the liquid disordered phase, however on the basis of these preliminary measures, we cannot make this assignment directly as we have no independent measure defining a known phase. In chapter 4 below, in conjunction with planar lipid bilayer patches and using correlative CARS / Two photon measurements, we have been able to demonstrate that this fluorescent lipid analogue partitions to the liquid disordered phase directly.

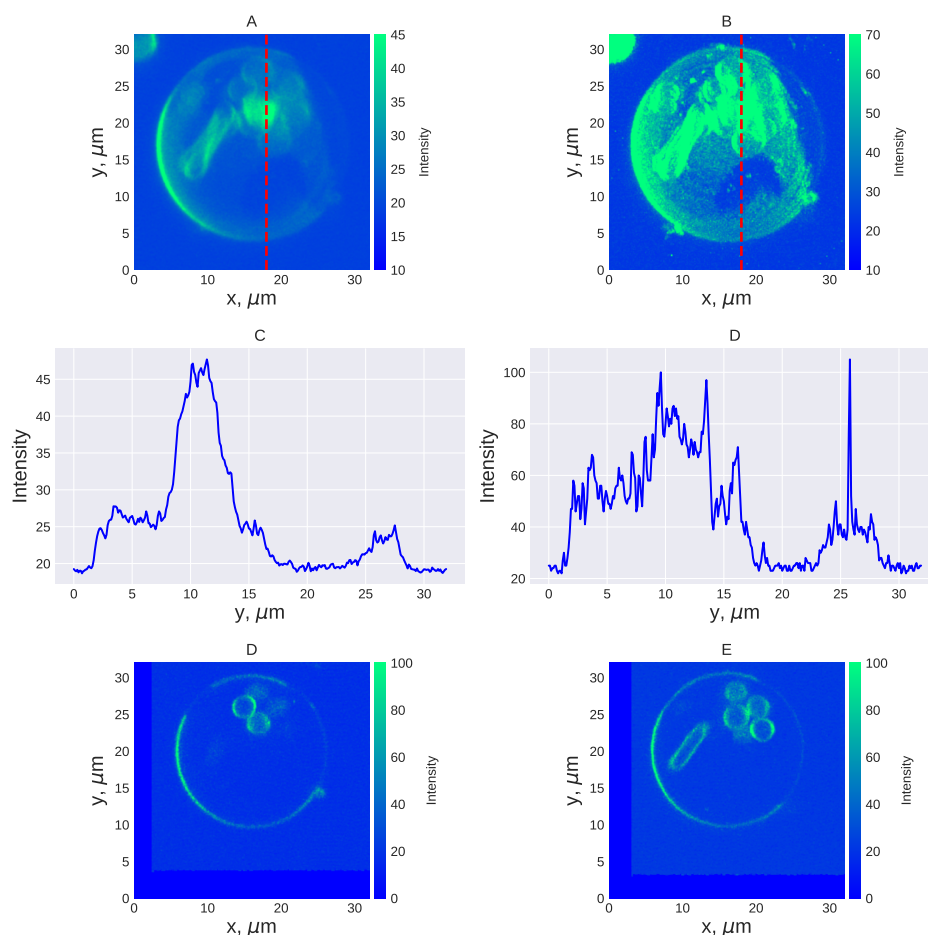


Figure 3.16: Spherical projections of DOPC, Spingomyelin and Cholesterol vesicles visualised with two photon fluorescence microscopy from incorporated Atto-488 DOPE. Subplot A is an average intensity projection through the imaging stack with the profile for the red dashed line shown in C. Subplot B is a maximum intensity projection through the same vesicle with associated red-line profile in D. In evidence is phase separation caused by coexisting lipid liquid phases; note the lack of fluorescence from the right hand region in A or B and the areas without fluorescence in the right hemisphere. In addition, in cuts D and E, the GUV periphery is clearly partitioned in a way not seen in any previous GUV composition.

## 3.5 Fluorescence microscopy of coexisting lipid liquid domains

### 3.5.1 Introduction

Prior to CARS microscopy studies in phase partitioned GUV, it was decided to further characterise the phase partitioning of both the novel Atto-488 DOPE fluorophore, and two widely used fluorophores from the literature. Our two photon microscopy studies had indicated phase preference of Atto-488 DOPE in ternary systems, although definite assignment of the phase was unknown. It was decided to also use NBD-DOPE (Crane and Tamm, 2004, Silva et al., 2007), which is known to have a preference for the liquid disordered phase (in this exact lipid system (Silva et al., 2007)) and Naphthopyrene which is one few available ordered phase markers (Juhász et al., 2010, Zhao et al., 2007). Naphthopyrene is thought to show preference for the ordered phase due to its planar structure as shown in figure 3.17. Due to the predominantly straight chain conformation of the lipid constituents in the ordered phase, Naphthopyrene can pack more easily as compared with the structure predominant in the disordered phase (Baumgart et al., 2007).

In comparison to Atto-488 DOPE, both additional fluorophores are relatively susceptible to photobleaching (c.f. appendix D), however it was anticipated that this may be an advantage in later studies using CARS for which bleaching of the fluorescence signal could be used if cross talk into the CARS channel occurs. Characterisation was conducted with conventional fluorescence microscopy. In order to extract the most information from each vesicle, it was decided to image at lower numerical aperture (NA) such that the microscope depth of field was increased. By imaging only large vesicles ( $> 20\mu\text{m}$ ), at their polar regions, it was anticipated that larger surface areas of the vesicle could be simultaneously imaged (especially at the lower NA) as compared with an equatorial plane image as used in earlier studies. This would enable extended regions of phase partitioning to be visualised and characterised (for example in terms of in plane packing order).

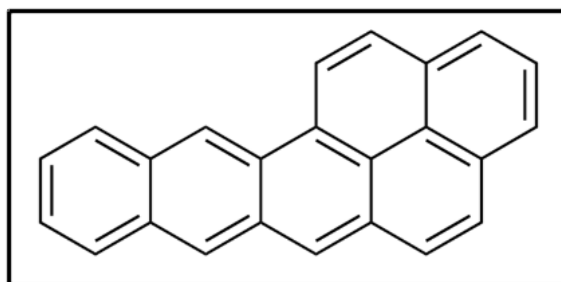


Figure 3.17: Structure of Naphthopyrene, image supplied by the manufacturer, Sigma-Aldrich, UK.

Imaging was conducted on two separate setups: a Leica inverted microscope and an inverted Nikon Ti-U at 40x 0.6NA and 20x (0.75NA) respectively. In both cases illumination was provided by metal halide lamp (Prior Lumen 200, UK). For imaging of Atto-488 or NBD containing vesicles, a standard GFP filter set was used (Semrock, USA), in the case of Naphthopyrene, a DAPI filter set was used (Semrock, USA). In all cases image data was recorded with a cooled CCD (-20°C, Hamamatsu Orca, Japan) detector operating at either 12 bit or 16 bit intensity resolution.

### 3.5.2 Co-existing Lipid liquid phases visualised by NBD-DOPE fluorescence

NBD-DOPE has a well defined preference for the liquid disordered phase in systems comprising DOPC:PSM:Cholesterol (Juhász et al., 2010), vesicles for this study were produced by electroformation (section 2.1.2.2) and incorporated the lipids at 2:1:1 molar concentration respectively. NBD-DOPE was incorporated at 0.5mol% (an increase over that seen in Atto due to the lower quantum efficiency). As shown in figure 3.18 typical false colour fluorescence images of NBD-DOPE vesicles readily reveal coexisting lipid liquid phases. In both cases shown, the liquid ordered phase appears dark due to a lack of fluorophore incorporation. As shown in subplot A, both phases demonstrate a spherical conformation confirming that these are liquid as opposed to a gel phase (c.f. figure 3.11). Spherical conformations present a circular line interface between the phases (Wesolowska et al., 2009) which minimises the line length for a given surface area of the phase (Veatch and Keller, 2003). In order for these geometries to form, it must be energetically favourable for the two phases to separate driving the formation. The two subplots, taken as a whole, exhibit two types of partitioning that is often seen. In subplot A, the lipid liquid phases are completely separate, with no evidence of smaller domains present, this we term equilibrium separation. Equilibrium separation is attributed to gradual merger of smaller, distinct lipid domains over time due to domain diffusion throughout the bilayer driven by Brownian motion. In subplot B, we can see that, although the majority of each phase is now separate, some smaller disordered domains are present within the larger ordered domain towards the

southern vesicle pole. These domains appear to be packed into a face centred hexagonal pattern which implies lateral ordering processes, beyond just simple diffusion are present within the bilayer. Both of these types of packing are common, and further examples are shown later.

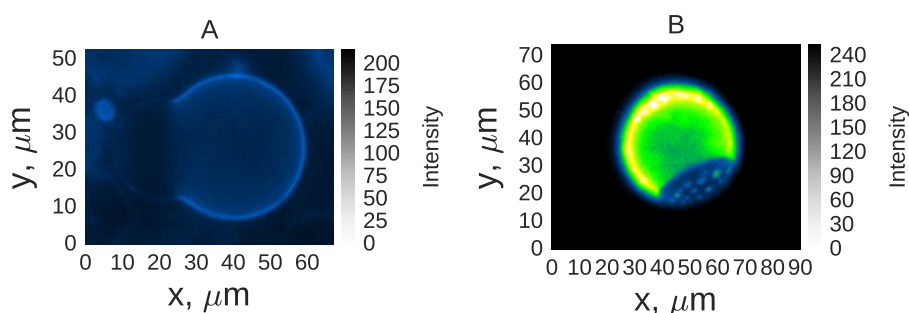


Figure 3.18: False colour images of coexisting lipid liquid phases in DOPC:PSM:Cholesterol vesicles (2:1:1 Molar ratio) visualised under fluorescence imaging from NBD-DOPE (0.5mol%). Note that in both subplot A and B the ordered phase appears dark, whilst the disordered phase shows preferential incorporation of the fluorophore. In both cases the conformation per phase is spherical, minimising the line energy between phases and proving that these are coexisting lipid liquid phases (Veatch and Keller, 2003). The colour used in each image is arbitrary as both images are acquired at 12bit grayscale.

During these experiments, a significant problem with fluorescence only imaging of phase partitioned GUV was encountered. Due to mismatch in vesicle curvature between phases, the vesicle can be susceptible to fission along domain boundaries (driven by Brownian motion of the bilayer). For fluorescence imaging, this presents an issue, since the ordered phase vesicle produced in fission events will not subsequently be visualised. This may contribute to a population of dark vesicles which would be missed in common fluorescence only assays and could lead to an underestimate of the partitioning probability of the system. Issues such as this provide fur-

ther support for use of label free imaging modalities during studies with GUV. An example of such a fissioning event is shown in figure 3.19. It should be noted that few examples of this process have been observed (by us), however due to the short temporal duration of the fission events, there is only limited observation time during which to observe so this result is not unexpected.

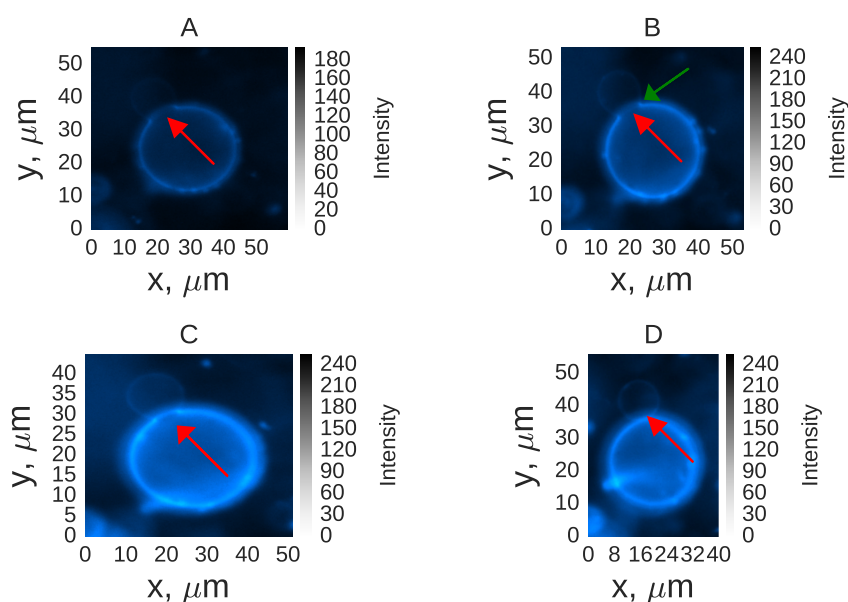


Figure 3.19: False colour images of coexisting lipid liquid phases in DOPC:PSM:Cholesterol vesicles (2:1:1 Molar ratio) visualised under fluorescence imaging from NBD-DOPE (0.5mol%). Images A through D represent a time ordered sequence, approximately 20 seconds apart capturing a vesicle fissioning event along the liquid ordered to disordered phase boundary. As shown in subplot A, the light disordered phase and dark ordered phase are initially conjoined. Evident in B is the abrupt change in curvature between the phases (indicated by the green arrow) and the shrinking interfacial area. In C the interfacial area has further contracted until finally in D the liquid phases have separated into two vesicles. The dark vesicle shed comprises the ordered phase. It is hypothesised that during fluorescence assays on GUV, a significant population of dark vesicles may be hidden from the experimenter.

### 3.5.3 Co-existing lipid liquid phases visualised by Naphtho[2,3-a]pyrene fluorescence

Naphthopyrene is an important ordered phase marker for coexisting lipid liquid phases (of which there are relatively few) (Juhász et al., 2010). The combination of a Naphthalene and Pyrene molecules, Naphthopyrene has a six Carbon ring, planar molecular conformation, as shown in figure 3.17. Due to the planar nature of the molecule, packing into the lipid bilayer is inhibited in the presence of permanent non-straight acyl chain conformations, such as the mid-chain bend due to the *cis* Carbon double bond of DOPC. As a result, it is energetically favourable for Naphthopyrene to pack with the straight chained Sphingomyelin into the ordered phase, whose structure it also perturbs (Leung and Thewalt, 2017). As shown in figure 3.20, the ordered phase within coexisting lipid liquid phases is readily observed. As shown in subplot A, both equilibrium and non-equilibrium partitioning of the lipid constituents is seen. In this case, the lower left vesicle is almost fully partitioned, except a few isolated disordered domains within the more luminous ordered phase. The upper right vesicle of the subplot captures a later stage partitioning than that shown in the case of NBD (figure 3.18 subplot B), with some larger ordered domains present within an extended disordered region. If we contrast the upper right vesicle of subplot A with that depicted in subplot B (or figure 3.18, A) we note that a change in curvature between domains is present in A, but not in B. In addition, the vesicle of subplot B exhibits incomplete partitioning of Naphthopyrene, with a significant signal within the disordered part of the domain. This implies that curvature changes are only present, once a certain level of demixing of the lipid components has occurred. If instead, a significant proportion of DOPC is still present within the ordered domains (or vice versa), it is possible for no curvature change to occur. This further implies that lipid phase separation is a complex process, binary separation into two distinct phases is common, however a continuum of partitioning behaviour is observed.

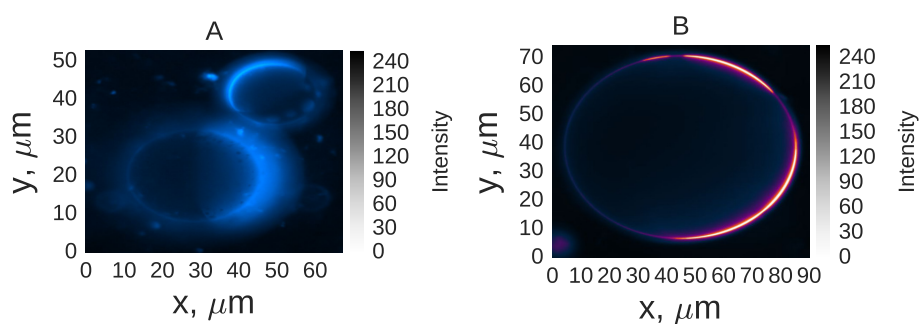


Figure 3.20: False colour images of coexisting lipid liquid phases in DOPC:PSM:Cholesterol vesicles (2:1:1 Molar ratio) visualised under fluorescence imaging from Naphopyrene (0.5mol%). At these concentrations in this lipid system, Naphopyrene shows phase preference for the liquid ordered phase (Juhász et al., 2010). Note in subplot A the change in curvature between the ordered phase (light on RHS of upper right vesicle) and the disordered phase attributed to the change in molecular conformation of the dominant lipid species per phase (DOPC to PSM). In subplot B, a lower degree of demixing occurs, however the light ordered phase is easily distinguished from the dark disordered phase. Images acquired under 12 bit grayscale, the change in colour is used simply to enhance contrast on a per image basis.

### 3.5.4 Co-existing Lipid liquid phases visualised by Atto-488 DOPE fluorescence

As demonstrated previously under two photon microscopy (section 3.4.6), Atto-488 DOPE has demonstrated partitioning within GUV systems. During fluorescence microscopy investigations a number of interesting domain packing geometries have been seen. As shown in figure 3.21 the predominant packing geometry is that of mature large spherical domains, attributed to domain ripening or spinodal decomposition over time (Veatch and Keller, 2005), as seen in subplots A and E. Several other raft packing geometries have also, occasionally been noted such as the hexagonal packing of subplot D and the spiral packing of subplot B which arises as a result of fundamental instability in the system miscibility known as viscous fingering (Veatch and Keller, 2003). Different packing geometries must arise due to localised changes in the thermodynamic conditions of formation (Almeida et al., 2005, Fidorra et al., 2009), otherwise greater profusion of these unusual geometries would be in evidence. It is likely that local changes in the relative concentrations of the lipids, changes in the local electric field during formation or localised pressure or temperature changes may give rise to alternate geometry. In subplot C, the localised curvature due to many closely packed domains is in evidence (subplot C is the equatorial plane of the vesicle pole shown in D). Again the hexagonal packing patterns seen suggest localised in plane lateral ordering occurring due to the lipids themselves, presumably driven by the line energy between the phases arising due to hydrophobic mismatch between average chain length (García-Sáez et al., 2007). It could be argued that some of the packing shapes, such as those seen in subplots D and F could arise from vesicles within vesicles. However this is unlikely, given the depth of field of the objective, it would require the entire cluster of small vesicles to be phase partitioned in exactly the same way (dark uppermost with a light equatorial plane) and with the same orientation relative to the imaging setup. This seems incredibly unlikely to occur and we conclude that in all cases the distribution of intensity arises from domains within a single GUV, consistent with findings in other studies (Baumgart et al., 2003). Further investigations could attempt to measure the surface area per phase and relate that back to the initial lipid

composition, which would strengthen the argument. However since the local formation conditions for each GUV are unique, such a study is likely to prove highly variable, we therefore decided not to pursue it at this time.

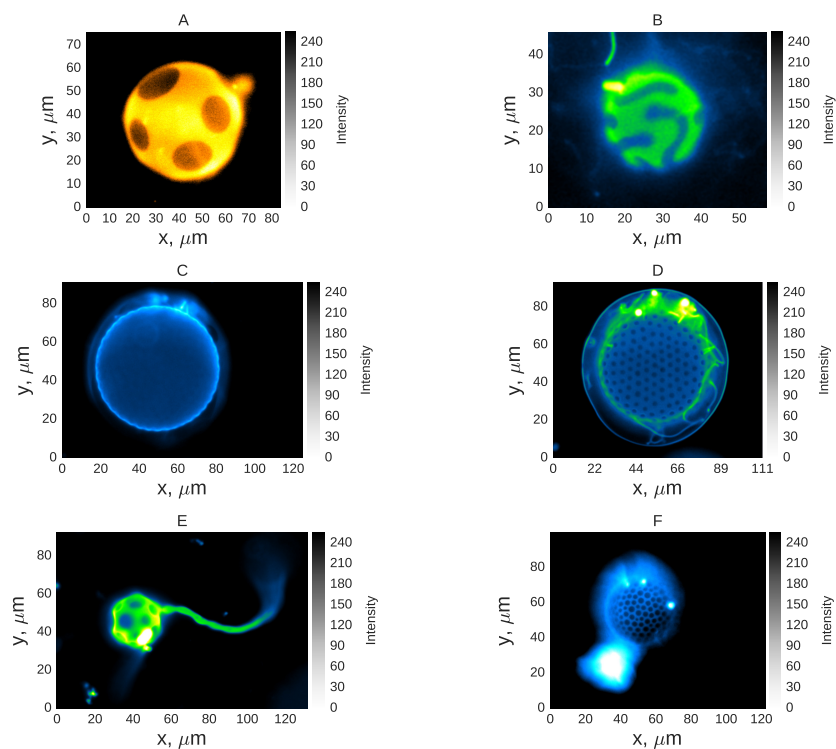


Figure 3.21: Coexisting lipid liquid phases in DOPC:PSM:Cholesterol vesicles (2:1:1 Molar ratio) visualised under fluorescence from Atto-488 DOPE (0.2mol%). Shown in subplots A and E are mature separation of the ordered and disordered phases into large distinct regions with spherical conformation. Subplot B shows a viscous fingering type of domain packing, leading to elongated and unstable packing (Veatch and Keller, 2003). Subplots C, D and F demonstrate formation of many, smaller hexagonally packed domains probably arising from spinodal decomposition of the lipids from a homogeneous state (Veatch and Keller, 2003). In all cases the degree of exclusion of the fluorophore is very high, as such no other conclusion than the coexistence of lipid liquid phases can be supported.

The results of these fluorescence investigations suggest that any one of the fluorescent lipid analogues can be used to visualise coexisting lipid liquid domains. Several different packing states for coexisting domains have been seen, with the most likely state (observed in the overwhelming number of cases) being that of equilibrium separation. Atto-488 DOPE has the added advantage, attributed to its high quantum yield (>80%), of permitting the lowest molar concentration of dye. This is better since it is also therefore the least likely to perturb the endogenous behaviour of the lipids themselves. However further considerations such as the desirability, under certain conditions, of photobleaching can override this consideration. Unfortunately, none of these fluorophores can be used in combination for dual channel imaging of both the ordered and disordered phases simultaneously, however since we had both markers, it was decided not to pursue dual colour imaging at this time.

### **3.6 CARS microscopy of Giant Unilamellar vesicles**

The purpose of this study, taken as a whole, was to develop a suite of label free methods for chemically specific identification of putative lipid raft analogues within model lipid membranes. Therefore, following successful completion of the characterisation of fluorescence standards, CARS microscopy was used to investigate the same set of lipid constituent GUV. It was initially anticipated that simultaneous fluorescence / CARS microscopy would be possible, enabling simple identification of domains within both channels. Unfortunately, for all of the fluorophores characterised, significant fluorescence leakage into the CARS channel was observed (by comparing the CARS signal at resonance to that off-resonance). In order to investigate GUV further with CARS, label free GUV were prepared with a low molar percentage (0.2mol%) of unlabelled DOPE, such that the label free variants were as close in behaviour to the already characterised labelled GUV as possible (and remain relevant to mammalian plasma membrane composition). Working with label free GUV introduces significant problems in terms of imaging and data acquisition (by comparison to fluorescence). Since the GUV are free to translate, and subject to Brownian motion, DIC microscopy must be used in order to initially locate them within the imaging

chamber. Once located, CARS microscopy can be used, at the CH peak around  $2850\text{cm}^{-1}$  in order to render a label free image of the vesicle.

Due to the tenuous nature of a vesicle (4nm thin, pico litre volumes), high laser powers ( $>50\text{mW}$  total pump beam power) are required in order for CARS microscopy to develop sufficient signal to noise to resolve the vesicle against the background due to water. These higher laser powers have two common and pronounced negative effects:

- Localised heating of the buffer, leading to convective motion (of the vesicles).
- Direct bilayer damage (leading to loss of the vesicle)

These combined effects introduce a number of additional constraints into the data acquisition process. Induced motion of the GUV limits both the possible dwell times and prevents us to average over many acquisition frames in order to reduce noise. Increases in laser power could increase signal to noise, however this leads to a high probability for immediate destruction of most vesicles. Therefore, in order to acquire CARS data from GUV, preliminary tests were performed to determine the maximum laser powers ( $\cong 50\text{mW}$  pump power) and dwell times possible ( $10\mu\text{s}$ ). Due to the limited GUV signal, combined with a spectral background due to water, it is important to limit the depth of field under CARS microscopy and maximise collection efficiency. For all data sets in this study a 60x water immersion, 1.27NA objective was used with a 1.4NA oil immersion condenser. It was initially hoped that hyperspectral data could be acquired from vesicles, however due to these aforementioned limitations this proved not to be possible. Therefore, this investigation was limited, by the inherent nature of the GUV samples to imaging primarily at the CH peak (although negative imaging around  $3000\text{cm}^{-1}$  where the water signal dominates the GUV is also possible).

As shown in figure 3.22 CARS microscopy has been used at the CH region peak around  $2850\text{cm}^{-1}$  to visualise label free GUV comprising different lipid constituents. We consider the case of each individual vesicle mixture separately. In subplot A a DOPC unilamellar vesicle is shown, by comparison to the intensity profile shown in subplot C, it is apparent that the level of signal is close to that of the background (primarily the resonant

background due to Water, which possesses a wide resonance). In addition, due to induced movement of the vesicle attributed to localised heating by the CARS laser, only single frame acquisition is possible. This imposes limitations on any reduction in the level of image noise, also the images are subject to random intensity fluctuations due to variable and random output of the laser itself (hence the horizontal striping evident within the figure). Both of these effects can be reduced and / or overcome if additional frame averaging was possible.

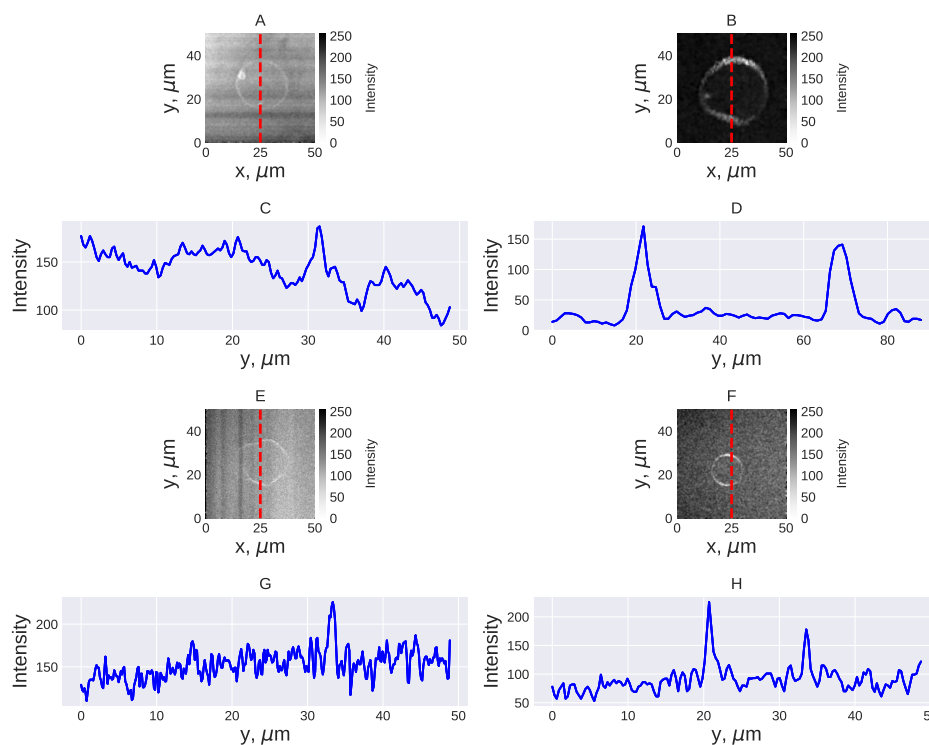


Figure 3.22: Label Free CARS Microscopy of free in solution GU. Shown in Subplot A is a pure DOPC thin walled vesicle with the intensity cross section shown in trace C below. Subplot B depicts a pure PSM multilamellar vesicle showing typical faceted shape due to the solid, gel packing phase of the lipid (profile in subplot D). Subplot E shows a vesicle comprising DOPC and PSM. Unlike in the earlier fluorescence assays, this vesicle demonstrates a phase partitioning between a liquid disordered phase (DOPC) and a faceted gel phase (PSM) which was expected in advance (Nyholm et al., 2011). It is therefore probable that the introduction of the fluorescent probe modifies the lipid packing perturbing the formation of the gel phase which would be consistent with effects seen in the literature (Veatch et al., 2007). The CARS signal from the gel phase is correspondingly large due to the increased average chain length of the lipid, combined with greater packing density. In subplot F a PSM and Cholesterol vesicle is shown demonstrating the breaking of molecular order attributed to the Cholesterol. In order to maintain consistency with the fluorescence assays, a small amount of unlabelled (0.2mol%) of unlabelled DOPE has been used in all cases.

Shown in figure 3.22 subplot B a PSM multilamellar vesicle is imaged at the same  $\text{CH}_2$  stretch ( $2850\text{cm}^{-1}$ ). Due to the solid, gel phase of this vesicle several effects are apparent, oscillatory motion of the vesicle periphery is reduced (due to Brownian motion) and the overall CARS signal is greatly increased due to both the increase in average chain length, packing density and the presence of additional bilayers. Correspondingly, the signal relative to the background is greatly increased as evidenced by the intensity profile in subplot D. The increased mass of the multilamellar vesicle also renders it less susceptible to laser induced motion, which would therefore make vesicles of this type a better target for longer time frame acquisitions such as hyperspectral imaging (as will be shown below). Subplot E demonstrates CARS imaging of a phase partitioned DOPC and PSM vesicle, with coexisting gel and liquid disordered phase as expected from literature (Nyholm et al., 2011). In the earlier fluorescence assays (c.f section 3.4.5) no phase separation was observed in these systems. We hypothesise that the introduction of a fluorophore into the system may yield nascent behaviour not seen in the label free case, however this has not been systematically examined. Finally in subplot F we see the disordering effect of the addition of Cholesterol to PSM (in a manner consistent with that seen in the fluorescence case). The faceted PSM multilamellar vesicles are gone and we recover thin walled spherical vesicles absent of phase partitioning (the vesicle presenting in the liquid ordered state).

In spite of numerous attempts to image label free GUV comprising ternary lipid mixtures (DOPC:PSM:Cholesterol:DOPE), such as the GUV shown in figure 3.23, no conclusive evidence of phase partitioning was seen. This could have arisen by consideration of a number of factors:

- Selection effect: Label free GUV must be located via DIC microscopy, making phase separation in real time harder to locate.
- Fluorescent lipid analogues may promote phase separation resulting in a reduction in label free systems.
- The weak contrast developed from GUV under CARS, combined with high levels of noise may mask the separation.
- Azimuthal variation in the CARS signal due to linear polarisation might

mask natural variations in signal.

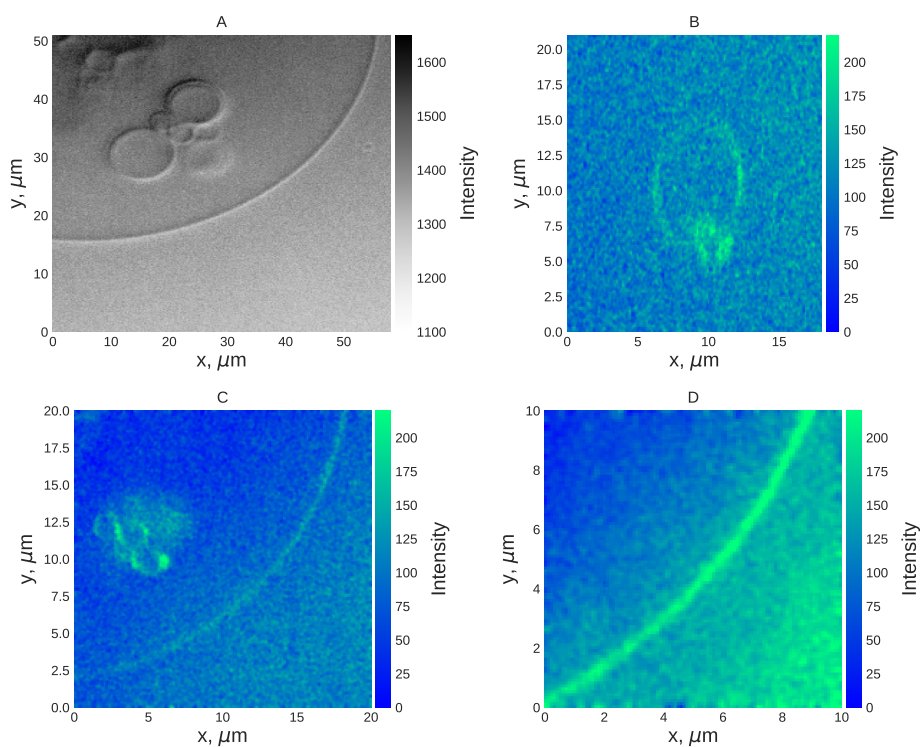


Figure 3.23: Correlative DIC and CARS microscopy of ternary DOPC:PSM:Cholesterol unlabelled vesicles. DIC image of section of large GUV shown (a), no partitioning is apparent. Shown in (c) and (d) are CARS images taken at  $2845\text{cm}^{-1}$  of the same vesicle shown in (a). No phase partitioning is apparent within the given images. Subplot (b) is an alternative unlabelled, free in solution GUV imaged under CARS at  $2845\text{cm}^{-1}$ , again no partitioning is seen, although the azimuthal dependency of the CARS signal (due to linearly polarised excitation) can just be observed.

Before discussing new models, we consider spectral analysis applied to free in solution GUV. The CARS data shown so far has comprised imaging taken at a particular frequency corresponding to the CH<sub>2</sub> symmetric stretch (CARS frequency 2845cm<sup>-1</sup>). Better lipid species discrimination can be made on the basis of hyperspectral data taken across a range of frequencies. This analysis was attempted in two ways, driven by the nature of the vesicles under study. For thin walled vesicles, line scans were taken across the vesicle equatorial plane in order to minimise the time taken and the induced movement in the sample. For larger, multilamellar vesicles, full hyperspectral imaging could be attempted.

### 3.6.1 Hyperspectral CARS of DOPC unilamellar vesicles

In order to extract full spectral information from across the CH region from thin walled DOPC vesicles, line scanning of the target vesicles was attempted. This was a compromised solution forced due to significant movement caused by attempting whole frame scanning of the target. In order to both maximise the resolution, minimise the depth of field and maximise collection efficiency a 60x 1.27NA water immersion objective was used with 1.4NA oil immersion condenser. Line scans were performed from 2200  $\text{cm}^{-1}$  to 4000  $\text{cm}^{-1}$  with a spectral resolution of 10  $\text{cm}^{-1}$ .

As shown in figure 3.24 limited spectral information can be taken from a line scan across a thin walled vesicle. This is primarily due to the wide OH resonance due to water (with peaks around 3200 and 3400  $\text{cm}^{-1}$ ) (Walfen, 1964), which as shown in subplot C still presents a spectrally far more intense signal than the CH stretch due to a single lipid bilayer. In subplot B, the extracted lipid spectra has been processed in order to remove the effects of the water (OH Stretch) resonance. This is performed by measuring the instrument response within a non-resonant medium across the same range of frequencies. In this case, the glass coverslip is an ideal target. Periodically therefore during measurement, the objective focus is lowered such that the full focal volume is within the glass and a full spectrum taken. In addition, the spectrum of the water itself is also taken with the same settings as used for a given experiment. In this manner, a sample spectra can be formed as a quotient to the water spectrum and then multiplied by the water to glass ratio. This effectively removes the effects of the water and produces a spectrum measured relative to a non-resonant medium (Masia et al., 2013). This has been performed in subplot D of the figure demonstrating a level of signal typically around 2% above that of the background medium. Unfortunately given the standard deviation (noisy) of the data, the spectra yielded are not of sufficient quality to claim a definite detection, much less the ability to discriminate different chemical species of lipid.

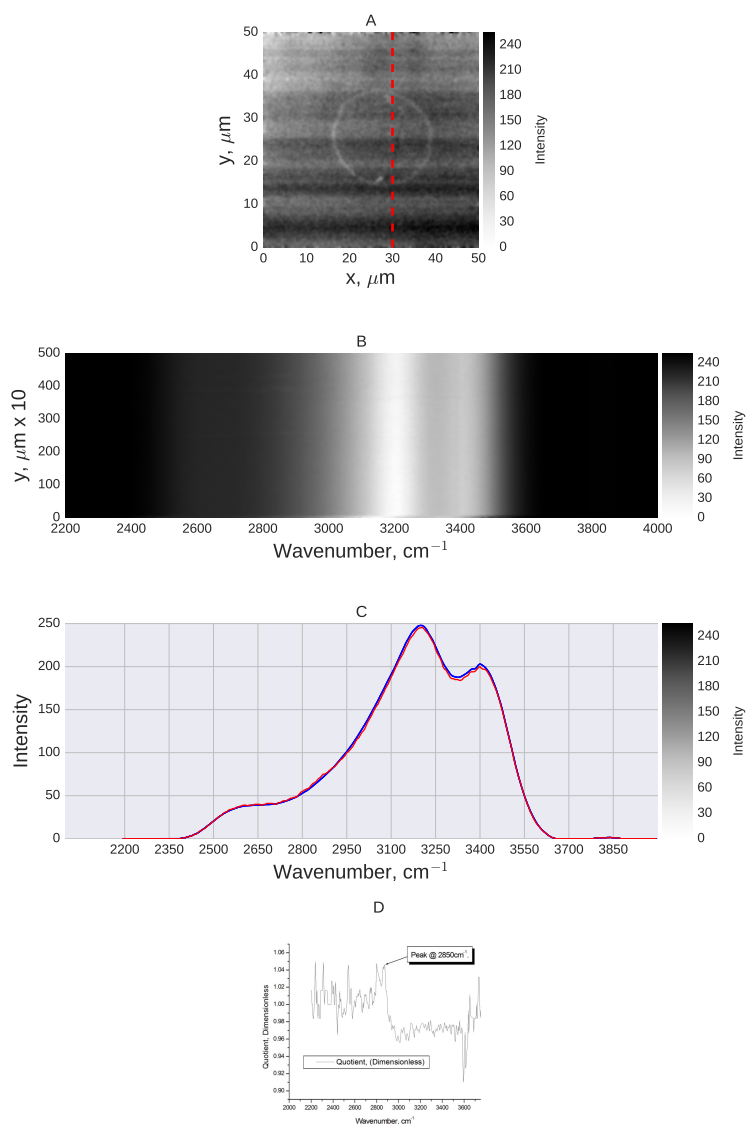


Figure 3.24: Label free CARS microscopy of thin walled DOPC vesicles. In Subplot A , the red line depicts the approximate line of the scan. Subplot B shows an enlarged section of the trace with frequency against position along the line in A. Subplot C shows the extracted average spectra of Water (blue) and the lipid (red), we note the width of the OH stretch in Water with peaks around 3200 and 3400  $\text{cm}^{-1}$ . At the single bilayer level, the signal due to the lipid CH stretch is barely above the OH resonance even at 2850 $\text{cm}^{-1}$ . As shown in subplot D, the lipid signal comprises  $\cong 1\text{-}2\%$  above the OH resonance of the water.

### 3.6.2 Hyperspectral imaging of multilamellar Sphingomyelin vesicles

As shown earlier (c.f. figure 3.22) Sphingomyelin vesicles present a typically multilamellar structure in a densely packed gel phase. As such, they present superior discrimination from the background due to the OH stretch of water. In figure 3.25, hyperspectral imaging stacks have been taken from multilamellar PSM vesicles. This data was acquired with 60x 1.27NA water immersion objective, 1.4NA oil immersion condenser and typical pump power at the sample of 50mW. Imaging was performed at spectral intervals of  $5\text{cm}^{-1}$  (half the spectral resolution) and demonstrate the chemical specificity of CARS microscopy through the differential contrast evinced between the CH signal from the lipid and the OH signal from the background Water. In subplot A, at frequency shifts below  $2800\text{cm}^{-1}$  significant signal is not seen from either the OH stretch modes of the Water or from the CH modes of the lipids. However the combination out of plane scissoring mode of the CH molecule around  $2735\text{cm}^{-1}$  (Socrates, 2001) can be seen. In subplot B, a clear CH region signal, of substantial magnitude is superimposed upon the resonant background due to Water, this is in contrast to the very slight signal seen in the case of a unilamellar vesicle such as that shown in figure 3.24. In Subplot C, the CARS spectra from the PSM vesicle has been ratioed to a non-resonant medium (glass) in order to remove the spectral effects of the surrounding Water, however some residual OH signal is still visible at frequencies past  $3200\text{cm}^{-1}$ .

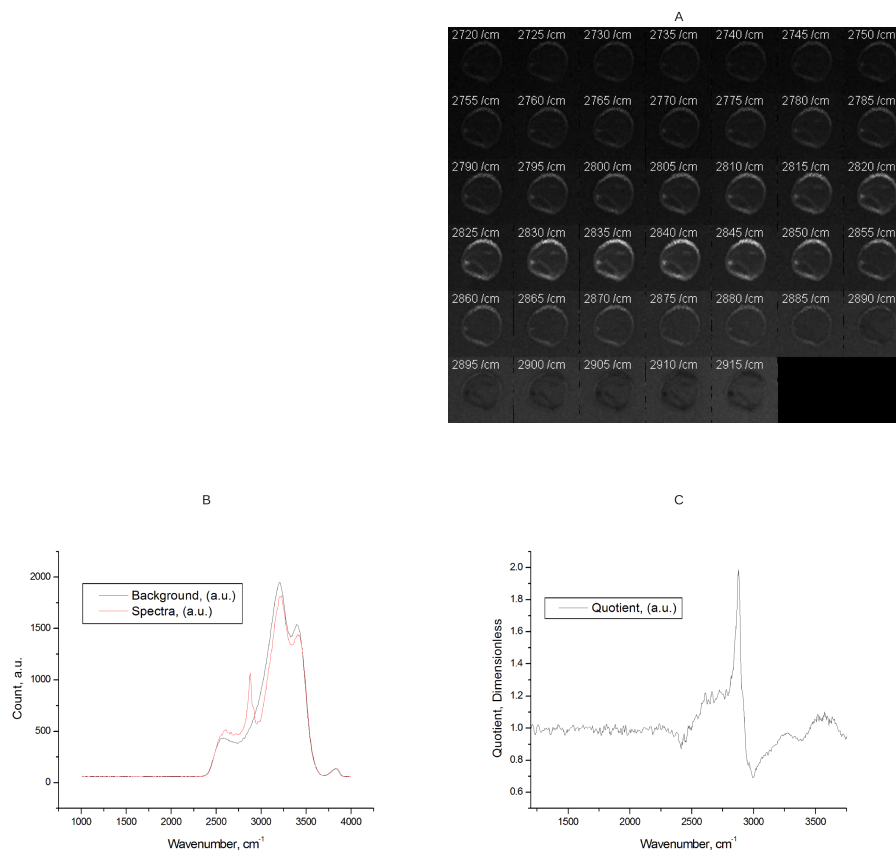


Figure 3.25: Hyperspectral CARS analysis of multilamellar Porcine sphingomyelin vesicles. Shown in subplot A is a hyperspectral imaging stack taken at  $5\text{cm}^{-1}$  intervals (half spectral resolution). The relative response of the CH stretching modes of the lipid is evinced in relation to the OH stretch of the Water. At frequencies below  $2800\text{cm}^{-1}$  both the water and lipid possess little Raman cross section. From around  $2800\text{cm}^{-1}$  the lipid CH stretch dominates over the OH stretching of the Water. At frequencies shifts past  $2900\text{cm}^{-1}$  the OH stretch of the Water becomes the dominant signal with the lipid appearing in negative (with lower cross section than the surrounding medium). These observations are confirmed in subplot B where the lipid signal (red) is contrasted to the background due to Water (black). In Subplot C, the Lipid spectra has been ratioed to a non-resonant medium (glass) showing the strong CH peak at  $2880\text{cm}^{-1}$  characteristic of PSM (c.f. section A.2)

### 3.6.3 Discussion

In both cases of CARS microscopy applied to either unilamellar or multilamellar vesicles, deficiencies present within the GUV model itself are apparent. Principally, unilamellar vesicles are very thin ( $\approx 4\text{nm}$ ) and therefore present insufficient material for coherent CARS enhancement of the signal to evolve (coherent excitement requires full occupancy of the focal volume (Cheng et al., 2002c)). This situation is significantly improved in the case of multilamellar structures, however these are not the target of this study. In addition, significant background due to water causes a loss of contrast during the CARS acquisition (since the background is coherently enhanced, it will always present a significant spectral component to complicate analysis). In addition, hyperspectral imaging of thin walled vesicles has not been possible due to significant induced movement of these structures. Free in solution GUV therefore, whilst presenting an ideal target from a biological point of view, are not well suited to detailed spectral analysis. Finally, due to the lack of lipid material present within a single bilayer, significant laser power must be used in order to produce sufficient signal for data acquisition. This leads to a significant loss of many target vesicles due to direct damage from the laser. At the outset, it was envisaged that the GUV model would be used throughout the study, however initial CARS work with these models has indicated that this is not possible. Before developing new bilayer models it was decided to try and modify the GUV model in order to overcome some of these limitations. These modifications are the subject of the following sections.

## 3.7 Background reduction with $\text{D}_2\text{O}$

As shown previously (c.f. section 3.6.2) the OH stretch resonance due to Water is spectrally broad, with significant signal across the CH region ( $\approx 2800\text{-}3000\text{cm}^{-1}$ ). This has the effect of reducing imaging contrast and enhancing the (undesired) background under CARS. In an attempt to remove this background, heavy Water can be substituted as the formation solution for production and imaging of GUV. From a chemical point of view, heavy Water makes no difference to any possible reactions herein, however

some thermodynamic changes in the lipid behaviour are to be expected since the increase in density from 1g/ml to 1.1g/ml will have some slight effect. Previous studies have shown changes in the miscibility temperature of certain lipid combinations in the presence of heavy water (Knoll et al., 1981) (Miscibility temperature of DPPC shifted by +1.5K under  $D_2O$ ). Within the context of the present study, these slight changes are not significant since they do not effect the ability of the lipids to partition. The deuterium oxide obtained in this study was of the highest grade >99.9% Deuterium (Sigma-Aldrich, UK) and was kept sealed under Argon until use. Electroformation of the vesicles was conducted as described in section 2.1.2.2. The spectra of both water and heavy water were acquired via a line scanning technique from  $2000-4000\text{cm}^{-1}$  with 20x 0.75NA and 0.72NA dry condenser at a spectral resolution of  $10\text{cm}^{-1}$ . An average spectra was taken in each case across the entire length of the line in order to reduce noise.

In figure 3.26, shown in subplot A are a comparison of the spectra for water (blue trace) and heavy water (red trace). Due to the addition of an extra neutron the deuterium atom is heavier which manifests as a redshift in the OD stretch in comparison to the OH stretch of water (Chumaevskii et al., 1999, Wood, 1934). The CARS spectra for water shows peaks at  $\approx 3100$  and  $3300\text{cm}^{-1}$  with the CARS peak for deuterium oxide at  $\approx 2250\text{cm}^{-1}$ . CARS data in the literature, especially concerning heavy water is hard to find, however the Raman peaks of  $D_2O$  are published (Chumaevskii et al., 1999) at  $2390$  and  $2487\text{cm}^{-1}$ , which allowing for the shifted and differential nature of the CARS signal locate the heavy Water spectrum in the correct region. We note that the heavy water spectrum possesses a minima around  $2750\text{cm}^{-1}$  and a local maxima around  $3000\text{cm}^{-1}$  (at less than 10% the comparable level of the OH resonance). In addition to the shifted frequency of the heavy water, we also note that the resonance spectral width is greatly reduced which again is inline with the literature values (c.f. reference (Chumaevskii et al., 1999)). Subplot B shows a unilamellar vesicle comprising Naphthopyrene:DOPC:PSM:CH (0.005:2:1:1 molar ratio respectively) imaged at the CH stretch around  $2850\text{cm}^{-1}$  in a single frame, raster scanned acquisition ( $10\mu\text{s}$  dwell). By comparison to earlier CARS images (c.f. figure 3.24), the apparent contrast is enhanced, with an increased signal present to the lower right hand side of the vesicle (which may indicate

a liquid ordered phase). In subplot C, due to the aforementioned minima of the deuterium Oxide around  $2750\text{cm}^{-1}$ , it has been possible to image the combination band of the lipid at  $2735\text{cm}^{-1}$  even though the Raman cross section is less than 10% for this mode compared with the CH region peak (c.f. section A.2). Imaging of this mode is simply not possible in regular water.

Unfortunately, despite of the success of heavy water in reducing resonant background across the critical CH region, the free in solution GUV are still subject to peripheral oscillations due to Brownian motion and bulk translation of the vesicle due to local convective effects. At standard temperature and pressure, heavy water possesses a dynamic viscosity of 1.24 mPa·s compared to 1.00 mPa·s for Water. It was hoped that this extra viscosity would damp these oscillations and translations, however this did not occur.

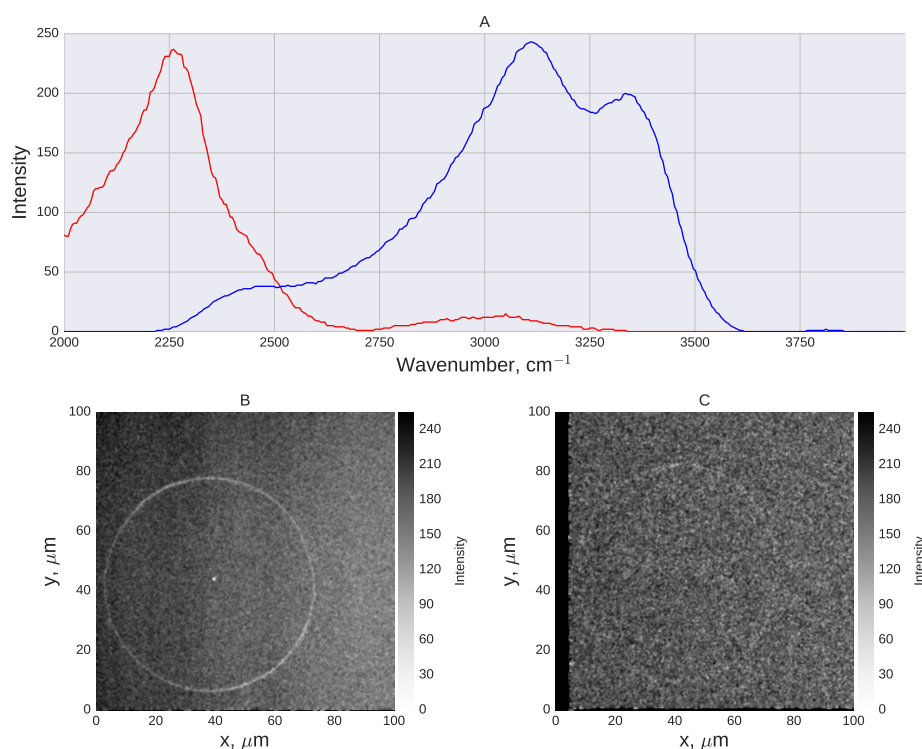


Figure 3.26: CARS spectra of deuterium (red trace) and hydrogen oxide (blue) (subplot A) demonstrating the characteristic redshift of the OD stretch compared with the OH stretch of Water. Subplot B shows a unilamellar vesicle imaged at the  $2850\text{cm}^{-1}$  CH stretch against the lower background due to heavy water. Subplot C shows imaging of the same vesicle at the much weaker  $2735\text{cm}^{-1}$  combination band which would not normally be visible against the resonant background due to water (note that the minimum in the  $\text{D}_2\text{O}$  spectra occurs around this frequency). It should be noted that these images were presented untouched, further contrast enhancements could be made by Fourier filtering both low frequency laser fluctuations and high frequency noise beyond the microscope cutoff.

### 3.8 Biotinylated GUV

During both two photon and CARS acquisition, significant movement of the GUV was observed hampering attempts to both acquire 3d imaging stacks and preventing frame averaging of the data in order to increase the level of signal to noise. Software techniques such as Fourier based image registration, and tracking were attempted, however these were hampered by deformation of the vesicles during motion, preventing the tracking attempts. Therefore in an attempt to fix this, GUV were created with a headgroup attached biotin lipid molecule. By using specially modified, Neutravidin coated coverslips as described in appendix B, GUV coming into contact with the surface are then captured and immobilised as has been demonstrated elsewhere (Jung et al., 2000). The GUV were prepared by electroformation with 0.1mol% Biotin-DOPE with 0.2mol% Naphthopyrene and DOPC : PSM : Cholesterol (2:1:1). The formation solution was then incubated upon a prepared coverslip for 1 hour prior to sealing the chamber and imaging. Imaging was performed with a 60x 1.27NA water immersion objective and 1.4NA oil immersion condenser.

Biotinylated, surface bound GUV proved to be useful in some regards. Whilst the vesicles remained subject to both deformations and oscillations due to Brownian motion. The lack of translation did permit, for the first time an attempt at hyperspectral imaging upon GUV. As shown in figure 3.27 subplot B, a CARS hyperspectral imaging stack was taken from 2820-3020 $\text{cm}^{-1}$  in steps of 5 $\text{cm}^{-1}$  with a single frame at each frequency. This frequency stack was analysed with custom software in order to automatically decompose it into constituent spectra alongside maps of their absolute concentrations. The image in 3.27B is a map corresponding to the spectral component mapping to the lipid. Unfortunately, without further reduction in noise, it was not possible to identify multiple lipid species. Further examination of this image however reveals definite phase partitioning, the change in curvature of the lipid, combined with the increase in lipid signal denotes a more densely packed phase - the Liquid ordered ( $L_O$ ) phase enriched in longer, straight chain sphingomyelins (Bacia et al., 2005, Baumgart et al., 2003, Hanzal-Bayer and Hancock, 2007). This comprises the first time that this distinction has been made in a label free manner using

CARS microscopy. Subplots A and C of the figure denote further examples of Biotinylated GUV imaged under CARS ( $2850\text{cm}^{-1}$ ) and DIC microscopy respectively.

Subplot C shows the largest free in solution GUV found, at close to  $200\mu\text{m}$  in diameter. It was noted during these experiments that many such large GUV were observed. It is hypothesised that the hydrophilic nature of the Biotin molecule (Qi et al., 2004) may assist initial Water ingress between bilayers during formation, allowing larger sections of bilayer to swell and detach forming bigger GUV. However a systematic investigation of the size distribution of Biotinylated GUV was not made at this time. In spite of some promising results, the Biotin GUV did not permit extensive frame averaging and again suggested to us that in order to extract quantitative chemical information from bilayer systems, a move to a new lipid model may be required.

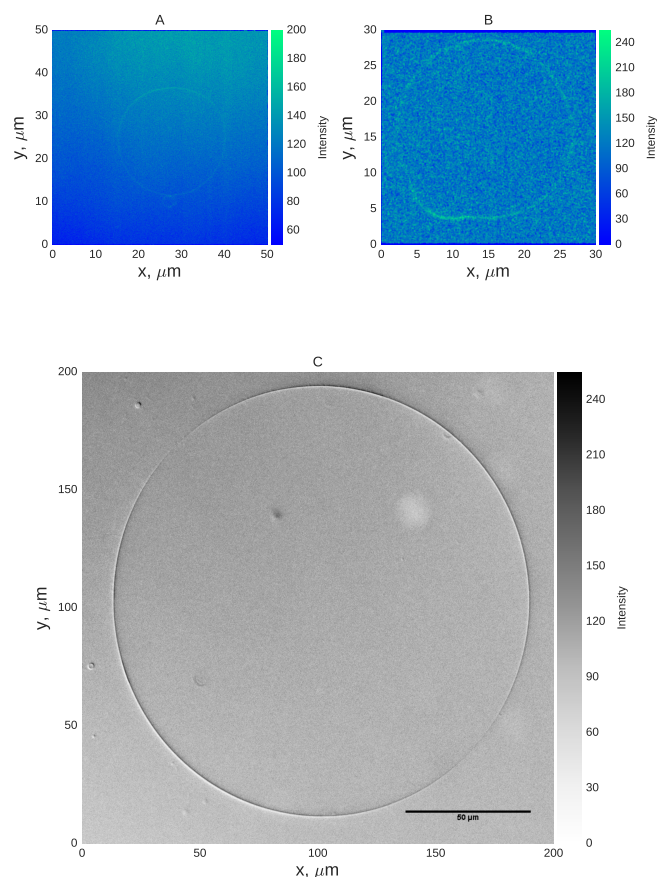


Figure 3.27: Surface bound GUV incorporating 0.1 mol% Biotin-DOPE. Subplot A, a single large vesicle is shown imaged at the CH stretch peak of  $2845\text{cm}^{-1}$  although no phase partitioning of the lipid is present. In Subplot B, due to the surface bound nature of the vesicle, a hyperspectral stack was taken comprising frequencies from  $2820$  to  $3020\text{cm}^{-1}$  in steps of  $5\text{cm}^{-1}$ . Due to vesicle deformation, only a single frame at each frequency was possible. Spectral decomposition was performed with custom analysis software and the image shown is a concentration map corresponding to the single identified lipid spectra. Due to noise levels, multiple lipid spectra were not found. Subplot B also demonstrates phase partitioning, note the change in curvature at the lower left quadrant, combined with the increased signal from this region. This identifies this region as a liquid ordered phase (Baumgart et al., 2003, Potma and Xie, 2003). Subplot C, a DIC image of a Biotinylated super giant unilamellar vesicle has been shown. It was noted that the addition of Biotin-DOPE produced many such large GUV, however a systematic investigation of the size distribution was not made.

### 3.9 Deuterated Sphingomyelin GUV

Earlier in section 3.7 we demonstrated contrast enhancement using deuterium oxide instead of water, therein we were able to image the weakly scattering Raman mode at  $2735\text{cm}^{-1}$  due to the loss of the broad OH Stretch resonance. In these experiments, all of the solvents (except  $\text{D}_2\text{O}$ ), solutes and lipids used possess no Raman resonances within the range of  $2000 - 2400\text{cm}^{-1}$ , this is because few bonds actually present modes at these frequencies. Typical of such bonds are Carbon $\equiv$ Carbon ( $2140\text{cm}^{-1}$ , (Nakamizo et al., 1974)) and Carbon $\equiv$ Nitrogen triple bonds ( $2240\text{cm}^{-1}$ , (Thygesen et al., 2003)), none of which are present within our systems.

In order to map the enrichment of Sphingomyelin which occurs during the formation of a liquid ordered phase, a deuterated sphingolipid would present a red shifted spectrum with a peak around  $2100\text{cm}^{-1}$  about which no other modes would be present yielding potentially high contrast images mapping the distribution of the sphingomyelin. For these experiments a d31 16:0 Sphingomyelin was selected as it was readily available from Avanti Polar lipids. With this variety, only a single acyl chain is deuterated, the other possessing normal hydrogen atoms. Prior to use, I checked with the manufacturer (Avanti Polar lipids Inc, USA) that the deuterium was stable against exchange, which it is with the exception of a single atom at the chain terminus. Therefore hydrogen from the surrounding water will not exchange with the deuterium in the acyl chain and imaging over longer periods at the deuterium frequencies is possible. Vesicles were prepared in water by electroformation and comprised DOPC:Sphingomyelin:Cholesterol at 2:1:1 molar ratio. Imaging was performed with a 1.27NA 60x water immersion objective and 1.4 NA oil immersion condenser by raster scanning with a dwell time of 10us and approximately 50mW pump power (at  $\approx 690\text{nm}$ ) used.

It was hoped to image phase partitioned GUV such that the direct enrichment of the sphingomyelin could be mapped at  $2090\text{cm}^{-1}$  which corresponds to the most intense Raman active  $\text{CD}_2$  stretching mode at  $2100\text{cm}^{-1}$  (Bunow and Levin, 1977), however during these experiments no partitioning was seen. As shown in figure 3.28 in subplot B the total lipid distribution is seen due to the CH region stretch at  $2850\text{cm}^{-1}$ , in subplot A however,

the distribution corresponding to d31 Sphingomyelin is mapped. Unfortunately, most structures formed with this mixture were multilamellar, which was not the target initially. Also the signal developed from the  $\text{CD}_2$  was weak, since only one acyl chain was deuterated. To see a single bilayer at that frequency would have been challenging. Since the model did not seem to be partitioning, and suffered the same problems inherent with the GUV system in general, we discontinued this line of enquiry. We successfully measured the  $\text{CD}_2$  stretch, but the rafts remained elusive. Again these experiments demonstrated the limitation of the GUV model and the difficulty of achieving high quality data from them.

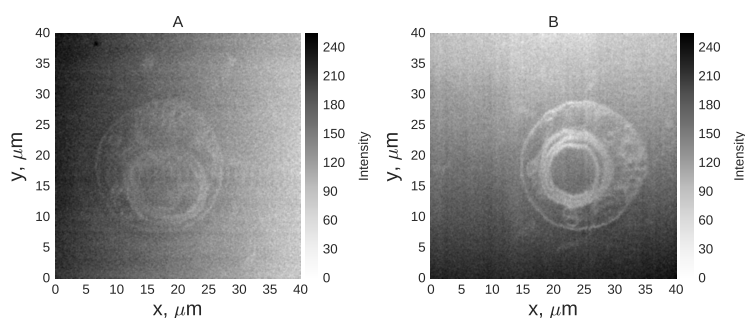


Figure 3.28: Deuterated, d31 (16:0) sphingomyelin vesicles imaged under CARS microscopy at the  $\text{CD}_2$  stretch ( $2090\text{cm}^{-1}$ , Subplot A, (Bunow and Levin, 1977)) and  $2850\text{cm}^{-1}$  (subplot B). Subplot A is a direct mapping of the Sphingolipid distribution within the vesicle. In subplot B, the total lipid distribution is mapped. The vesicles comprise DOPC:Sphingomyelin:Cholesterol at 2:1:1 molar ratio.

### 3.10 Summary

Giant Unilamellar vesicles (GUV) have been developed comprising a range of lipid constituents relevant to mammalian cell lines (Nelson, 1967b, White et al., 1998). Several methods of GUV formation have been shown, with studies being performed on both fluorescently labelled and label free varieties. We have demonstrated that thin walled vesicles can be formed of multiple bilayers, separated by distances less than the diffraction limit and therefore unresolved in optical studies (McPhee et al., 2013). Since it is important to study the properties of only a single bilayer, without perturbation due to additional layers; we have firstly demonstrated a fluorescent method for determining the number of bilayers present in any given vesicle: Fluorescence quantisation. This method was demonstrated across a statistically significant population of vesicles ( $n=466$ ) and showed a predominance for single bilayer vesicles but with significant ( $\cong 10\%$ ) multilamellar structures present. Since it is our goal to work with label free bilayers, free from potential perturbation by fluorescent lipid analogues, we have developed a novel label free technique to assess vesicle lamellarity using quantitative differential interference contrast microscopy (qDIC). Across a statistically significant population of giant thin walled vesicles ( $n=77$ ), we have shown that the accepted fluorescence quantisation technique and our qDIC technique yield the same assessment of bilayer number.

We have then proceeded to develop, through logical stages, a series of GUV of increasing lipid components in order to test for successful formation of each of the possible lipid phases (Lipid Ordered phase, disordered phase and gel phase) and to check for partitioning behaviour of several fluorescent lipid analogues which are typically used as markers for coexisting phases. It was found that in all cases, where vesicles comprise a single lipid phase, homogeneous incorporation of the fluorescent lipid analogue occurs indicating no self affinity of the analogue exists. In the singular case of ternary lipid vesicles, comprising DOPC:PSM:Cholesterol all of the test fluorescent markers (Atto-488-DOPE, NBD-DOPE and Naphopyrene) show a well defined phase preference confirming formation of coexisting lipid liquid phases.

CARS microscopy was then applied to GUV and multilamellar vesicles,

primarily imaging at the CH stretch around  $2850\text{cm}^{-1}$ . However hyperspectral CARS measurements were attempted for certain vesicles (with evidence shown for phase separation). Due to the nature of the bilayer (4nm thin) combined with the high laser powers needed to generate sufficient CARS signal (50mW pump power typical), limitations with the GUV model became apparent.

In an attempt to overcome these limitations modified GUV models were constructed including surface bound Biotinylated GUV, Deuterated GUV (spectral separation from the Water signal) and the use of heavy Water to shift it's spectrum away from the CH region. These methods were only partially successful and suggest the need for a new bilayer model more suited to hyperspectral CARS analysis. A new model: the Planar Lipid Bilayer Patch will be demonstrated in the next chapter.

These GUV techniques are important from a wider perspective, there is substantial research incorporating proteins into GUV (Doeven et al., 2005, Kahya et al., 2001) to measure such parameters as transmembrane diffusion and incorporated ion channel function (Aimon et al., 2011). In addition researchers are incorporating viral proteins into GUV to induce budding (Rossman et al., 2010). The small GUV enclosed volume, typically pico litres are being utilised for single molecule chemistry and advanced immuno assays (Jesorka and Orwar, 2008). Therefore GUV technology is driving fundamental research into important mechanisms, disease models and chemistry within a controlled and vastly simplified model (compared with an actual cell membrane).

We have also developed a suite of label free techniques, such as qDIC and CARS microscopy for the analysis of membranes without the addition of flurophores. This is increasingly important as studies are starting to indicate a link between fluorophore use and perturbation of the system. For example, the degree of partitioning of Naphthopyrene has been found to be linked to the degree to which it perturbs the membrane, altering its phase behaviour (Leung and Thewalt, 2017). Also the behaviour of labelled cell penetrating peptides has been linked to the probe used (Birch et al., 2017). Looking forward therefore, as a group, having a suite of label free GUV techniques will allow future novel research to continue. At present, within our group, there are plans to insert individual transmembrane proteins into

either GUV or droplet interface bilayers and attempt to track their diffusion at the nano scale, including through membrane regions of differing phase.

## Planar Lipid Bilayer Patches

### 4.1 Introduction

In the previous chapter on GUV, we showed examples both of single phase and coexisting phase lipid vesicles imaged under single photon fluorescence, Two photon fluorescence, CARS and DIC microscopy. Across all modalities, several common problems were noted inherent to the nature of the free in solution GUV themselves. Principally these are those of motion of the GUV which limits acquisition timescales and therefore affects the ability to extract the signal of interest from high levels of background and noise. From this data it was clear that a new model would be required such that higher levels of signal to noise could be achieved.

We selected the Planar lipid bilayer patch(es) (PLBPs) as this model for the following reasons:

1. PLBPs are surface attached (due to the affinity between lipid head-group charges and surface charges at the glass interface) and therefore present a static model of the bilayer (Bhatia et al., 2017).
2. PLBPs are formed from GUV (with which we already have significant experience).
3. During GUV formation the lipids comprising the bilayer are free to diffuse and present in a natural state which is then 'frozen' during PLBP formation (Sezgin et al., 2017).

4. PLBPs are easier to locate since they present only at the coverglass surface (important in the case of label free patches).
5. Through careful positioning of the objective focus, the non-resonant medium (glass) can fill some of the focal volume thereby reducing the amount of signal from the OH Stretch of the surrounding water medium.

On the negative side, PLBPs are a static model, so in gaining the ability to image for longer timescales, we give up the ability to temporally resolve dynamic events. There are also some questions as to the degree with which the bilayer lipids are free to flip-flop or diffuse within a single leaflet, FRAP studies do indicate lipid diffusion within PLBPs (Sendecki et al., 2017). On balance however, the gains from this model, from a chemically specific imaging perspective, outweigh the negatives.

As discussed in the materials and methods section 2.1.3.5, PLBPs are formed by osmotically induced rupture of GUV within the presence of a hydrophilic glass substrate (Anderson et al., 2009, Seitz et al., 2000). Within this study, this was performed by forming the GUV in water, incubating them on a piranha etched coverslip and then ‘shocking’ them with a 75mM PBS solution. Since salts contained within the PBS are not membrane permeable, the internal water within the GUV will pass by osmosis to the exterior solution, causing the GUV to ‘deflate’ and destabilise (Jackman et al., 2013). There are therefore several possibilities which can occur with regards to the produced PLBP (Hamai et al., 2007):

1. The GUV can fully rupture forming a single bilayer captured at the surface.
2. The initial GUV may not have been unilamellar and therefore the final PLBP may also not be.

In order to reduce the chances of the last point, the slide is washed prior to formation of the final imaging chamber, which should remove excess bilayers except those bound directly to the surface. It was decided to first conduct a qDIC analysis across a large population of PLBPs in order to assess lamellarity. This also provided an opportunity to test the limit of resolution of the qDIC technique since when assessing GUV, due to the

geometry of the vesicles, slightly more material is presented axially than the 4nm of the bilayer itself. The PLBP by comparison presents a flat geometry with no such enhancement. In addition, phase partitioned PLBPs contain sub-nm changes in membrane thickness between the ordered and disordered lipid phases: qDIC should be able to resolve even these.

Herein, we present first the results of the qDIC study into PLBPs including correlative two photon fluorescence imaging of coexisting lipid liquid phase patches. An analysis of the effects of frame averaging upon noise under CARS imaging then follows before a correlative fluorescence and single frequency CARS study of phase partitioned PLBPs. The results of hyperspectral CARS analysis of both labelled and label free PLBPs are then shown. The chapter closes with preliminary results of the application of stimulated Raman loss microscopy to PLBPs.

## 4.2 Quantitative DIC microscopy of Bilayer Patches

In order to work with label free PLBPs, a method was required in order to locate them and to discriminate any phase partitioning present. Under fluorescence modalities, this task is rather trivial since with all of the 3 fluorescent probes available, clear phase preference has been demonstrated between coexisting liquid ordered and disordered phases. Quantitative DIC microscopy has previously been applied in this study to determine the lamellarity of GUV, however imaging of planar structures presents a more significant challenge as mentioned earlier.

In order to test DIC, labelled GUV were produced from ternary mixtures of lipids (DOPC:PSM:Cholesterol, 2:1:1 molar ratio) incorporating 0.5mol% NBD-DOPE (which has a known preference for the disordered phase (Juhász et al., 2010)). PLBPs were then produced as described in section 2.1.3.5. For all imaging a 60x 1.27NA water immersion objective was used and a 1.4NA oil immersion condenser within a Nikon Ti-U Eclipse inverted microscope. To ensure Nyquist sampling during DIC acquisition a 1.5x tube lens was used. Patches were located using Epi-fluorescence with a GFP filter set (Semrock, USA) with illumination from a prior Lumen 200 metal halide lamp.

Located patches were then imaged by two photon excitation of the NBD

fluorophore via a raster scanning method with a dwell time of  $10\mu\text{s}$  and an image formed from the average of 20 sequentially acquired frames (in order to reduce the noise by a factor of  $\sqrt{20}$ ). For DIC imaging, a  $550\pm 20\text{nm}$  excitation filter was used to prevent fluorescence contamination of the DIC signal. 128 frames were taken with an exposure and readout time of 100ms; these were then subsequently averaged into a floating point image for analysis. For qDIC 128 frame averages were taken at equal and opposite initial phase offsets and processed using in house software in order to extract the absolute phase (see sections 1.6.2.2 and 3.3.1).

As shown in figure 4.1 visualisation of coexisting lipid liquid domains within planar lipid bilayer patches under two photon fluorescence is simply achieved (top subplot). Since the fluorophore used was NBD-DOPE, the lighter coloured regions of the patch correspond to the liquid disordered phase (Baumgart et al., 2007). Considering both the DIC and qDIC images are capable to visualise the patches as a whole. This corresponds to an axial resolution of  $\approx 4\text{nm}$  for the techniques (DOPC bilayer thickness at  $30^\circ\text{C}$ :  $38.4\text{\AA}$ , (Heberle et al., 2013),  $38.7\text{\AA}$ , (Kučerka et al., 2008)). As noted, towards the centre of the patch is a dark area which for the NBD-DOPE marker used indicates a liquid ordered phase. Comparison with both the DIC and qDIC images shows that this region is distinct from the surrounding patch in each case. Considering the interphase thickness difference of  $\approx 8.7\pm 1\text{\AA}$ , (García-Sáez et al., 2007), this corresponds to approximately 6 carbon atom diameters ( $\odot$  Carbon  $\approx 0.14\text{nm}$ , (Slater, 1964)). Therefore, it can be seen that the qDIC technique possesses sub-nm axial resolution. The DOPC of the disordered phase has acyl chains 18 Carbons long whilst the average chain length of the PSM in the enriched ordered phase is 21 (data provided by manufacturer, Avanti Polar Lipids Inc, USA) carbon atoms: a difference of 3 carbon atoms per leaflet.

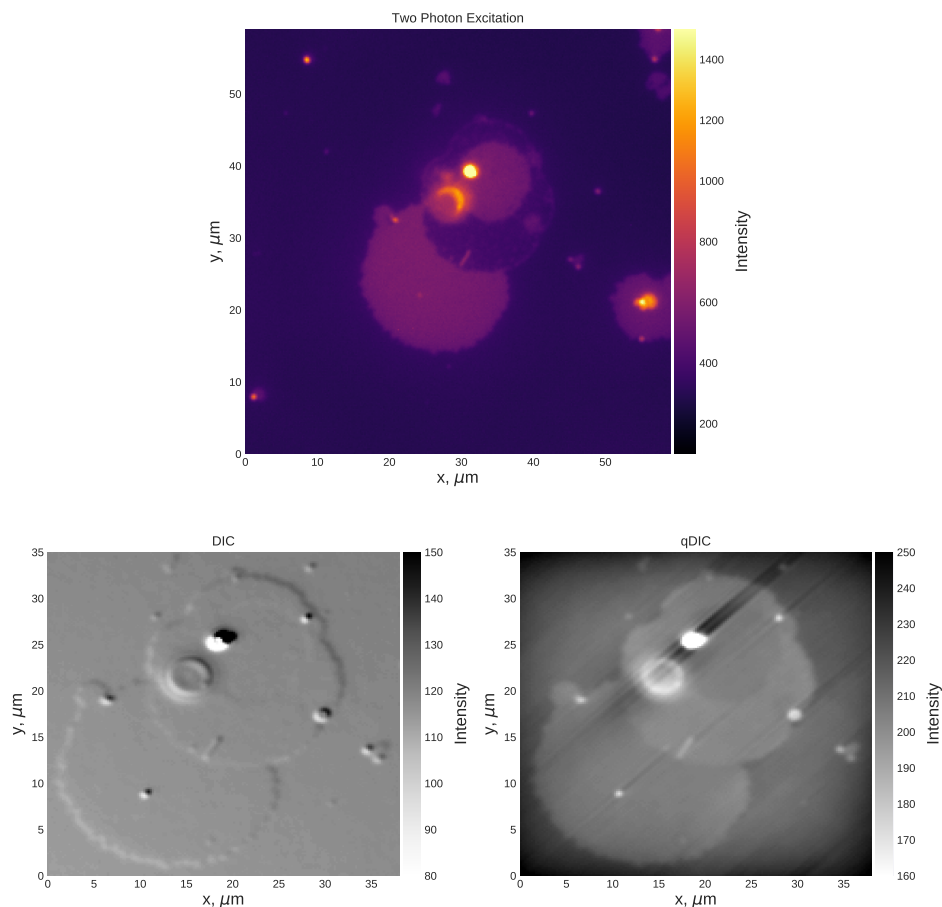


Figure 4.1: Imaging and assessment of a single lipid bilayer under two photon fluorescence (TPF), DIC and qDIC microscopy (note the presence of an attached vesicle, this does not affect the analysis). Top: TPF visualises coexisting lipid liquid phases due to preferential partitioning of the NBD-DOPE fluorescent lipid analogue with the lighter coloured regions corresponding to the disordered phase. DIC plot: Under standard DIC, the separate phases can just be seen and are distributed in accordance with the fluorescence data. qDIC plot: This plot represents the global phase distribution of the patch. A clear change in phase between the ordered and disordered phases can be seen, again the distribution correlates with that seen in the fluorescence image. DIC and qDIC therefore provide a sensitive, label free alternative to fluorescence for the identification of co-existing lipid liquid domains within Planar lipid bilayer patches.

This qDIC analysis of PLBPs can be extended to determine the absolute membrane thickness. To determine membrane thickness 2D Fourier integration was applied to qDIC contrast images producing a new image, figure 4.2, in which object phase not its rate of change is encoded (sections 3.3.1 and 3.3.2). Detailed *a priori* knowledge of object refractive indices, combined with measured object phase permits in plane thickness determination with sub-nm precision. To extract membrane thickness, the difference in object phase between two points (background and membrane) are measured from the integrated image, with background locations denoted by the red and blue rectangles in figure 4.2. Phase difference arises due to the optical path length (OPL) difference between two points in the object. Phase change is related to OPL by  $\Delta\psi = t\Delta nk_0$  where  $\Delta\psi$  is the measured phase difference,  $t$  is the unknown membrane thickness,  $\Delta n$  is the refractive index difference between water and the membrane ( $\cong 0.126$ ) and  $k_0$  is the angular wavenumber of the illumination ray ( $550\pm 20\text{nm}$ ). Solving for  $t$  therefore yields membrane thickness as shown in the lower two subplots of figure 4.2.

It should be noted that there are several sources of error which can change the result. Firstly, the value of the background phase is critical in determining all other measurements since they are taken relative to it. This contributes to a broadening of the measured values of thickness as evident in figure 4.4. Secondly, the wavelength of illumination is not precisely controlled, we use a fairly tight 550nm bandpass filter combined with IR filtering, however the value use for this wavelength will significantly change the result. I have used a fixed value of 550nm throughout. Thirdly, the integration procedure itself is not perfect and introduces artefacts, such as the striping evident along the shear direction and the edge artefacts at the image periphery both evident in figure 4.2, this effect is minimised by averaging across areas, or by plotting a single line profile along the shear direction as in figure 4.3. Lastly, the actual microscopic measurements taken must be very precise. The equal and opposite phase offsets used must be accurately calibrated, along with the entire setup.

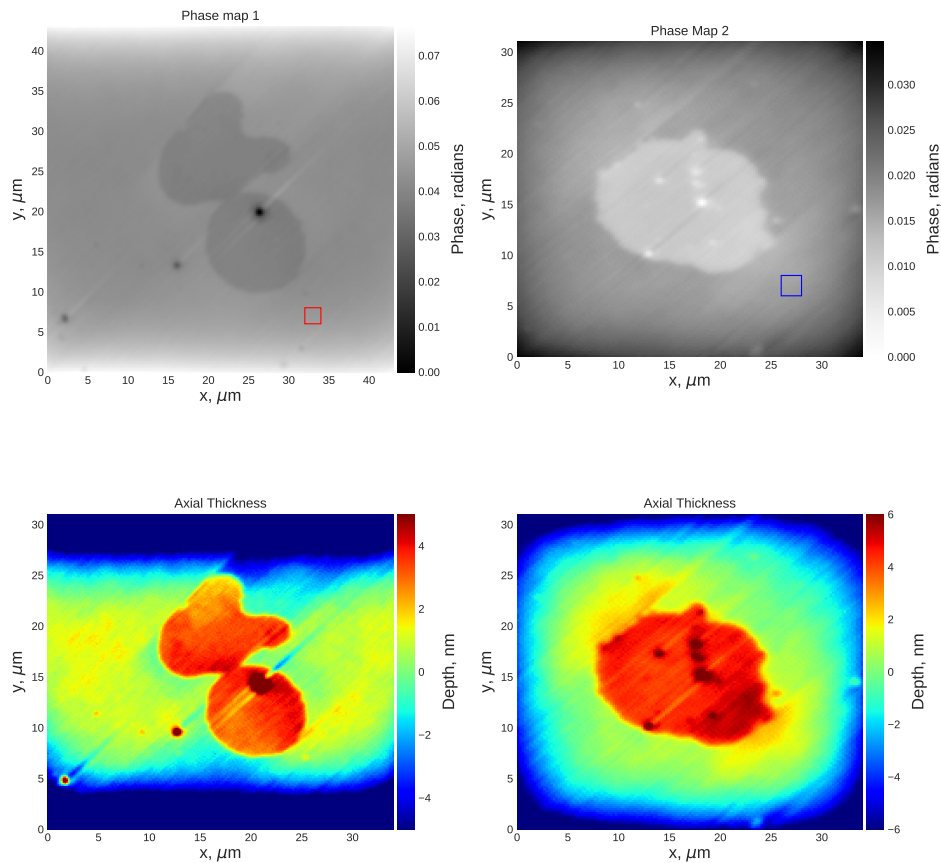


Figure 4.2: Under qDIC a map of the absolute phase, corresponding to the phase shift at each point in the image can be created as shown in the top two subplots. Given absolute phases, and by choosing a suitable reference value for the background (denoted by the rectangles in top subplots), a conversion between radians and thickness can be made if the distribution of refractive indexes is known for the system as described above. Shown in the bottom two subplots are the axial thickness distributions corresponding to the phase maps above. Note that there are significant edge effects due to the Fourier analysis used during the processing. Positioning the object of interest centrally, these effects can be avoided. In both cases, a thickness around 4nm is evident for the bilayers.

We have applied this technique to resolve heterogeneous membrane structure in phase separated PLBPs. Previous studies employing neutron diffraction have demonstrated DOPC bilayer thickness to be  $\approx 4\text{nm}$  (Kučerka et al., 2008) with raft domains  $\approx 8.7 \pm 1\text{Å}$ , thicker (Kučerka et al., 2008). Herein we demonstrate under qDIC compatible results both for a single bilayer, and across a statistically significant population of PLBPs.

In the case of an individual PLBP, accurate assessment of the membrane thickness can be made by analysing a line cut taken along the shear direction of the microscope as mentioned earlier. This is effective since qDIC is an indefinite integration of the DIC data performed along the shear direction. As a result parallel adjacent data will have a varying constant of integration applied to it giving rise to greater variation within the data in a direction perpendicular to the shear. In addition, as discussed in the qDIC theory section, integration of the differential DIC data is performed within the Fourier domain (section 3.3.2). In the spatial domain a simple cumulative sum along the shear direction would yield the phase between two points (this simple approach yields poor results however), in the Fourier domain integration is performed through division by frequency component (or a related multiplier thereof). Considering the case of the DC (zero frequency) component, this means division by zero, which is undefined. Therefore as discussed in section 3.3.2, we have applied Wiener filtering to prevent this situation from occurring. The filtering also helps suppress, although not eliminate, the effects of long period changes or trends in the data (integration is more sensitive to long period data, whereas differentiation enhances short period data). These effects manifest in qDIC as a slowly changing background and also as clear striping along the shear direction following abrupt changes in phase (c.f. Subplot C in figure 4.1, large lipid object in the upper right quadrant). Therefore in order to accurately extract correct phase information from individual PLBPs it is necessary to sample along the shear direction, choosing lines which are free from integration artefacts.

As shown in figure 4.3 qDIC and correlative fluorescence of PLBPs provides the same assessment lipid bilayer phase, with the exception that qDIC can also give the thickness. NBD-DOPE was again used as the fluorescent probe for the disordered phase. We observe a direct spatial correspondence between lipid phase boundaries under both qDIC and flu-

orescence. As shown in Subplot A, the absolute phase is given in the colorbar with darker regions in the qDIC image corresponding to areas of increased phase (i.e. thickness). These map precisely to the liquid ordered phase distinct by its absence of NBD fluorescence in subplot B. qDIC, as opposed to fluorescence can additionally provide direct assessment of the bilayer thickness across different membrane regions. In subplot A a line cut through the sample (along the shear direction) has been used to extract the phase difference between the background (glass / Water), the lipid disordered phase and the ordered phase. In addition the line cut was positioned such that the disordered phase was present upon both sides of the ordered one, hence the two shoulders seen in the recovered thickness (denoted by the blue arrows in subplot C). The line cut is not extended across the entire patch since longer period trends are present thereafter and obscure the data over longer distances. As shown, the disordered phase thickness is estimated as between 3.8nm and 4.2nm consistent with literature values of DOPC bilayer thickness of 38.4Å, (Heberle et al., 2013), 38.7Å, (Kučerka et al., 2008) . The ordered phase was found to be 4.9nm±0.1nm again consistent with the expected increase of  $\approx 8.7 \pm 1 \text{Å}$  (Kučerka et al., 2008).

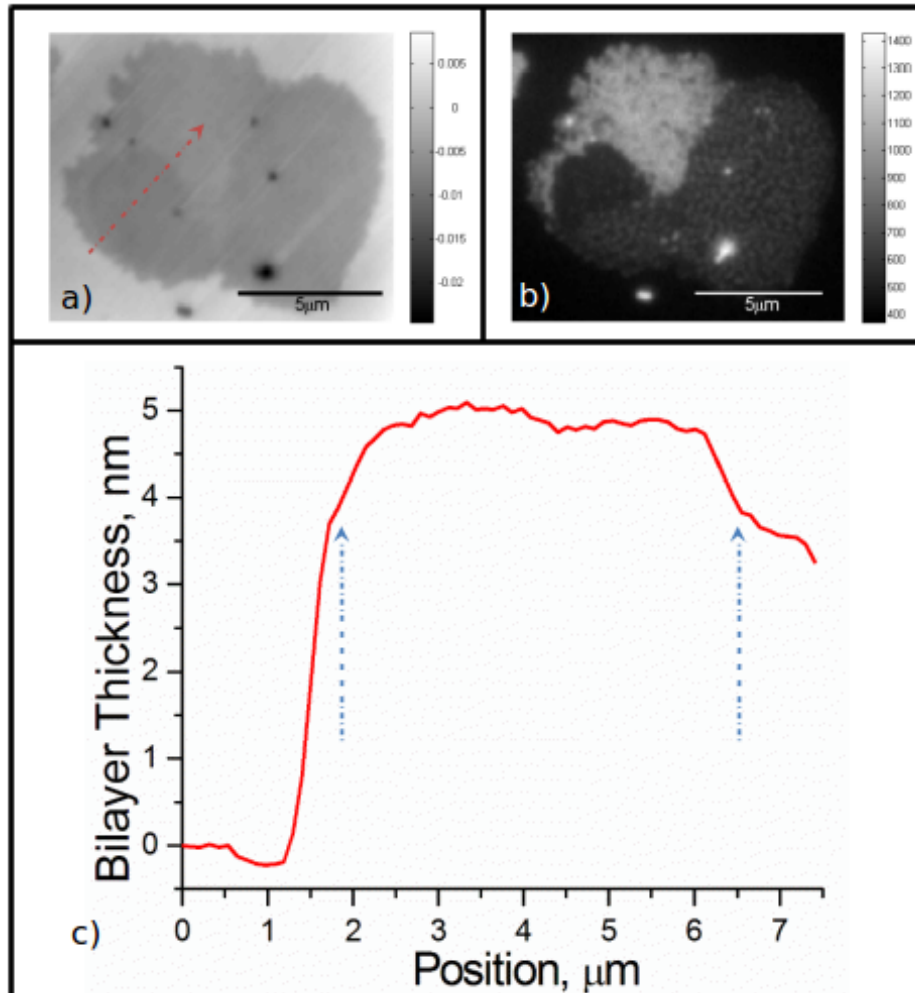


Figure 4.3: Integrated qDIC and correlative fluorescence imaging of lipid phase domains in PLBPs. Lipid ordered (Darker regions) and disordered phases (lighter) are resolved under qDIC (a) and EPI-fluorescence (b) (due to membrane incorporated NBD-DOPE). Red arrow shows approximate path of line profile in c. qDIC profile (c) demonstrates extracted membrane thickness, the ordered phase was found to be  $4.9 \pm 0.1$  nm with the disordered phase between 3.8 nm and 4.2 nm. Blue arrows mark transition regions between disordered and ordered phases along the direction of the cut.

In addition to measurements upon singular PLBPs, a larger experiment was conducted to assess the accuracy of qDIC at estimating the bilayer thickness under more general conditions. For this experiment, a large population of ternary GUV (DOPC:PSM:Cholesterol, 2:1:1 molar ratio) was analysed using the method shown in figure 4.2. These samples presented PLBPs with both lipid liquid phases present. For analysis, two rectangular regions within each qDIC phase image were defined, one outside the PLBP corresponding to the background and another within the patch. Unlike the case of the single line cut, these regions are subject to changes in integration constant and differences in long period trends present in the data. In addition the PLBPs may encompass either or both phases present. The phase difference between the two was converted into nanometers using the earlier formula for the optical path length. The results of this study are shown in figure 4.4 wherein the mean thickness of the population of PLBPs ( $n=83$ ) was determined as  $4.1 \pm 1.46 \text{ nm}$ . Unfortunately given the magnitude of the error involved ( $\pm 1.46 \text{ nm}$ ), which is an average over all causal factors such as integration artefacts, errors in average background determination and errors in data acquisition, all of which tend to broaden the measured distribution of membrane thickness. Given these issues, it is not possible via this method to extract separate liquid ordered versus liquid disordered phase distributions. For individual cases, where the more accurate line methods are used this may be possible, but even then there is still a significant issue with accurate determination of the background phase. With further development of more advanced integration techniques it may be possible to minimise some of these issues.

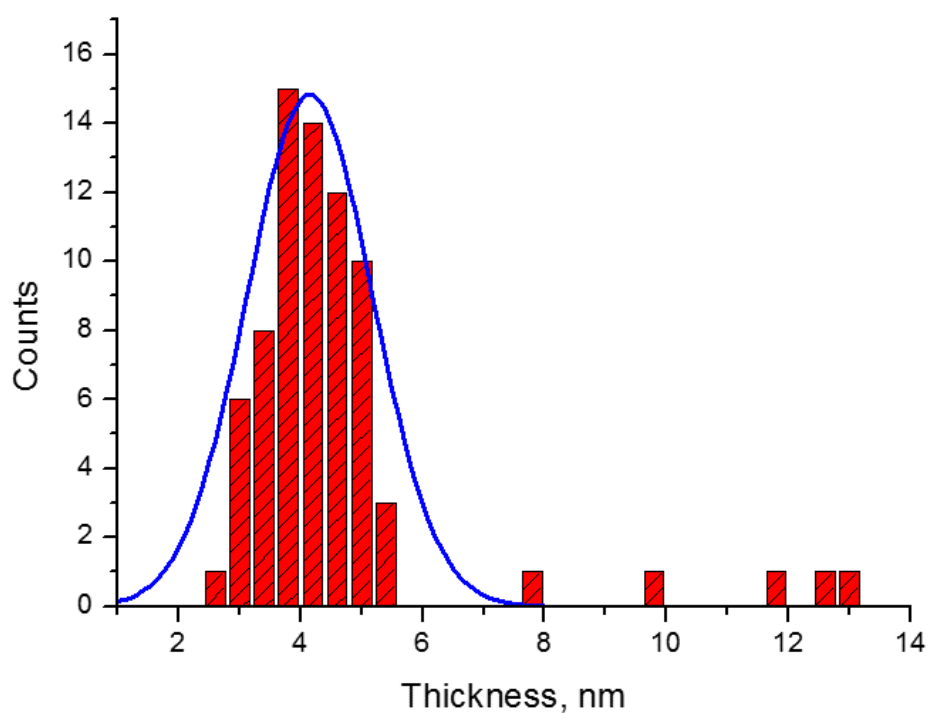


Figure 4.4: Quantitative DIC microscopy assessment of the thickness of a statistically significant population of planar lipid bilayer patches ( $n=83$ ). A Gaussian fit to the unilamellar population was performed and the mean thickness determined as  $4.1 \pm 1.46 \text{ nm}$ . As described in the text, analysis issues such as integration artefacts, accurate background determination and cross phase averaging have broadened the measured distribution. Thereby obscuring the ability to determine the ordered phase separately.

### 4.3 Optimisation of CARS imaging for PLBPs

As mentioned during chapter 3, a key problem with CARS imaging of GUV was attributed to movement (either induced by the laser or due to Brownian motion). This limited our ability to increase the signal to noise within sampled data. The PLBP by contrast is static and many frame averages may be taken, limited only by eventual damage caused to the bilayer by the laser powers used. Therefore, prior to undertaking CARS studies of PLBPs, we decided to quantify the number of frame averages required in order to reduce the noise to acceptable levels.

The noise can be affected by both the number of averages and the dwell time per pixel. It was required to find a compromise between total acquisition time and noise. In addition, longer dwell times induce greater localised heating of the bilayer, with significant damage observed. We therefore tested the image noise for dwell times of 1ms down to 1 $\mu$ s. In all tests a 60x 1.27NA water immersion objective was used with a 1.4NA oil immersion condenser and fixed 75% laser power. All images were raster scanned at 3 samples per resolution and were 50 x 50 $\mu$ m in size. The noise was assessed as the standard deviation over a fixed rectangular region corresponding to the background in each image. The signal to noise ratio was calculated as the average signal from the PLBP ratioed to the noise reading taken. The same patch and regions were used in all data sets.

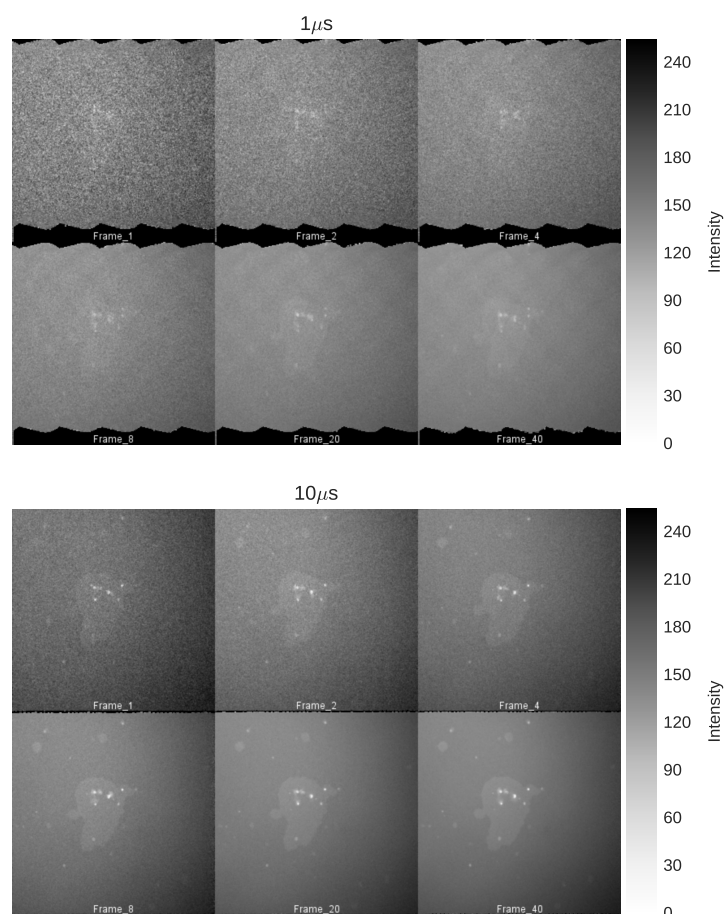


Figure 4.5: Comparison of CARS imaging of a single PLBP at the  $\text{CH}_{2,3}$  stretch peak at  $2850\text{cm}^{-1}$  for dwell times of  $1\mu\text{s}$  (top) and  $10\mu\text{s}$  (lower). The number of frame averages are stated at the bottom of each image. Notice that the patches are barely visible with single frame acquisition (c.f. GUV single frame acquisition).

Figure 4.5 shows for pixel dwell times of  $1\mu\text{s}$  and  $10\mu\text{s}$  the effect of the reduction in noise (and therefore increase in signal to noise) that is possible under CARS by frame averaging. It was the inability to do this that affected data acquisition during GUV studies. The changes in signal to noise versus frame averaging for various dwell times are shown in table 4.1. Evidently the longer dwell times have greater signal to noise, but at the cost of significantly longer total acquisition times. Clearly, from the data given, the most effective method is to simply increase the dwell time, however this comes at the cost of greater local heating of the sample and significantly longer acquisition times. Given the data available, on balance, it was determined that the optimal conditions were to use a dwell time of  $10\mu\text{s}$  with at least 40 frame averages if possible. Additional data was taken with higher numbers of frame averages up to 120 frames, however the additional gain in signal to noise was not worth the extra acquisition time and induced visible bilayer damage.

Dwell Time	1ms	$100\mu\text{s}$	$10\mu\text{s}$	$1\mu\text{s}$
Number of Frames	1	1	40	40
$\sigma$ (Noise)	1.895	2.842	3.722	4.186
Signal	3.70	6.22	6.10	3.97
SNR	1.95	2.19	1.64	0.95
Acquisition Time (s)	251	25.1	100.4	10.04

Table 4.1: Analysis of acquisition times and signal to noise ratio for different dwell times for imaging PLBPs at the  $\text{CH}_2$  peak at  $2850\text{cm}^{-1}$ . It should be noted that at the time our setup could not perform arbitrary dwell times, the ones presented were the only possible.

## 4.4 Correlative CARS and Two Photon microscopy of PLBPs

### 4.4.1 Correlative CARS and two photon imaging of non partitioned PLBPs

The goal from the outset of this study has been to develop a suite of techniques for label free imaging of putative lipid rafts in synthetic lipid membranes. Firstly, prior to examining phase partitioned PLBPs, tests were conducted upon DOPC patches stained with 0.5mol% of NBD-DOPE in order to ensure that:

1. CARS microscopy did not indicate differences in lipid partitioning or density where the established fluorophore did not.
2. To test the level of CARS contrast possible prior to examining phase partitioned systems.

Imaging was conducted using a 60x 1.27NA water immersion objective with 1.4NA oil immersion condenser. For both two photon imaging and CARS a dwell time of 10 $\mu$ s was used as previously established. Two photon images were comprised from the average of 10 frames, whereas for the CARS images 40 frame averages were used. The typical pump power used for the CARS experiments was 50mW at the sample. Two photon imaging was conducted first, and the sample was then fully photo-bleached using the CARS pump beam to multi-photon excite the dye. Given the power present in the pump beam, typically 10 raster scans across the sample are sufficient to remove all residual fluorescence. In this manner, fluorescence was removed from the sample in a short timeframe and the CARS imaging was free from fluorescence artefacts. The sample was monitored visually and under DIC, to check for photo-damage, any visible defects would cause the sample to be rejected. Given that the photo-bleaching takes very few scans compared to the actual CARS measurements, it is unlikely for the bilayer to be damaged during this phase. CARS imaging was conducted by tuning the instantaneous frequency difference between pump and stokes beams to the CH<sub>2</sub> main stretching mode at 2850cm<sup>-1</sup>. If different phases were present, these would be visualised on the basis of the differential

chain lengths and packing density of the phases (Potma and Xie, 2003).

As shown in figure 4.6 , since the imaged bilayers comprise just two components: DOPC and NBD-DOPE, there is not expected to be any partitioning of the fluorophore, analogous to the earlier DOPC vesicle studies. Taking the two photon images, the standard deviation sampled across a range of the bilayer is  $\approx 5$  grayscale units against an average value of  $\approx 155$ . This indicates a very tight spread of the data values and supports the notion that the fluorophore is homogeneously incorporated. In the case of the CARS images, visual inspection and comparison with the two photon fluorescence images indicates that again, there is no apparent partitioning of the lipid present (which would be unexpected given that the bilayer is 99.5mol% DOPC). In the greyscale CARS image, the bilayer signal is superimposed upon a quadratic background due to the OH stretch of water, combined with imaging away from the position of maximum spatial coincidence of the pump and stokes beams. Normally, in order to maximise the CARS signal, imaging is offset by predetermination of the point of maximum signal. When imaging large structures ( $> 50\mu\text{m}$ , a quadratic drop-off in the CARS signal is unavoidable. This control indicates that both under Two photon fluorescence imaging and CARS imaging, it is the distribution of the lipids that gives rise to changes (or not) in the signal observed from the bilayer.

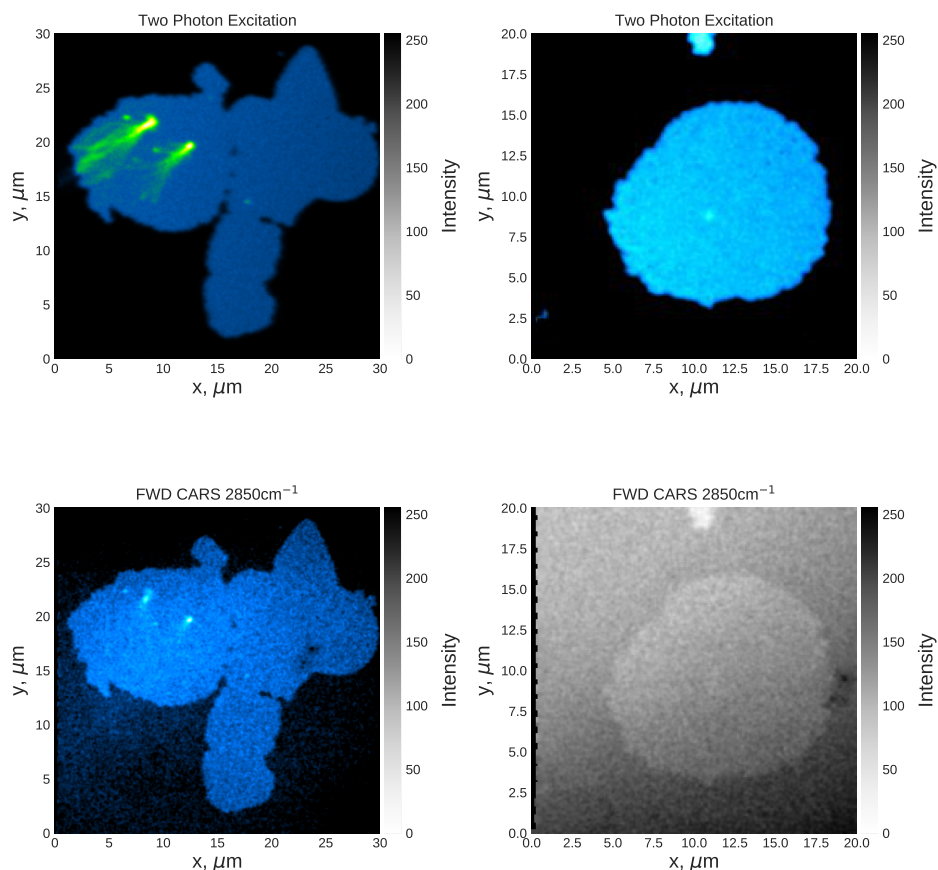


Figure 4.6: Comparison of two photon imaging of single component (DOPC) PLBPs stained with 0.5mol% NBD-DOPE with chemically specific CARS imaging of the same patches taken at the CH<sub>2</sub> resonance peak at 2850cm<sup>-1</sup>. In the first three images, false colour has been applied to aid in visualisation, here differences in colour between the blue and green channel represent differences in intensity in the underlying grayscale image (with green mapped to higher intensities). Note background gradients present in the greyscale CARS image, this is caused by imaging away from the position of maximum spatial coincidence of the pump and stokes beams and does not represent structure present in the sample.

#### 4.4.2 Correlative CARS and two photon microscopy of partitioned PLBPs

In the previous section (4.4) we have shown examples of the application of two photon and CARS microscopy to non-partitioned PLBPs. In all cases seen, the labelled and label free methods are in agreement regarding the lack of separation of the lipids. In this section we examine more advanced PLBPs comprising phase separated lipid combinations.

The PLBPs were created with DOPC:PSM:Cholesterol (2:1:1 molar ratio) with 0.5mol% NBD-DOPE. NBD was chosen since it has a well established partitioning behaviour with these lipid components (Baumgart et al., 2007), and is simple to photobleach prior to CARS measurements (acquired sequentially), removing the possibility of fluorescence cross talk into the CARS channel. Imaging was performed as before with 60x, 1.27NA water immersion objective and 1.4NA oil immersion condenser. All images were formed by raster scanning the samples with a dwell time of 10 $\mu$ s. Pump power at the sample was  $\approx$ 50mW, the CARS images were raster scanned at the CH<sub>2</sub> main stretching mode at 2850cm<sup>-1</sup>. Two photon images were formed from the average of 20 sequential frame acquisitions whereas the CARS images are formed from 40 frame averages. Images have been presented in false colour, with grayscale intensity mapped onto changes in colour as shown in the colour bar, to enhance visual contrast with limits applied (as shown) to the range of image intensity, but are otherwise untouched.

For the PLBPs shown in figure 4.7 clear partitioning of the constituent lipids has occurred. Of note is the clear contrast reversal between the two photon images and the CARS data sets, this is consistent with the literature (Potma and Xie, 2003). The NBD-DOPE marker localises to the liquid disordered phase which is characterised by a relative enrichment of DOPC over the other components. DOPC has a cis Carbon double bond at the acyl chain mid-position which gives it's chains a 'kinked' conformation which inhibits close packing. By contrast, within the sphingomyelin enriched liquid ordered phase, the acyl chains present a straight conformation and have, on the average, a longer chain length (21 Carbons vs 18 for DOPC) with greater packing density (Simons, 1997, Veatch and Keller,

2003). Therefore, under CARS imaging at the  $\text{CH}_2$  stretch ( $2850\text{cm}^{-1}$ ) the ordered phase presents a significant increase in CH bonds, yielding an increased intensity of the CARS signal. It is for this reason that the contrast reversal between the images occurs. We note that from these arguments, sphingomyelin enrichment within the liquid ordered phase can be inferred from the single frequency CARS data. These results essentially confirm those that have been shown previously (Potma and Xie, 2003). Single frequency CARS imaging is therefore compatible with, and a viable alternative to, conventional fluorescence labelling for coexisting lipid liquid phase determination. Although in these experiments a fluorescent lipid analogue was used, we will later demonstrate phase partitioning within label free PLBPs for which only CARS and our qDIC methods are capable of phase identification. Furthermore, we will extend the state of the art by determining the dominant lipid species per phase from hyperspectral CARS data.

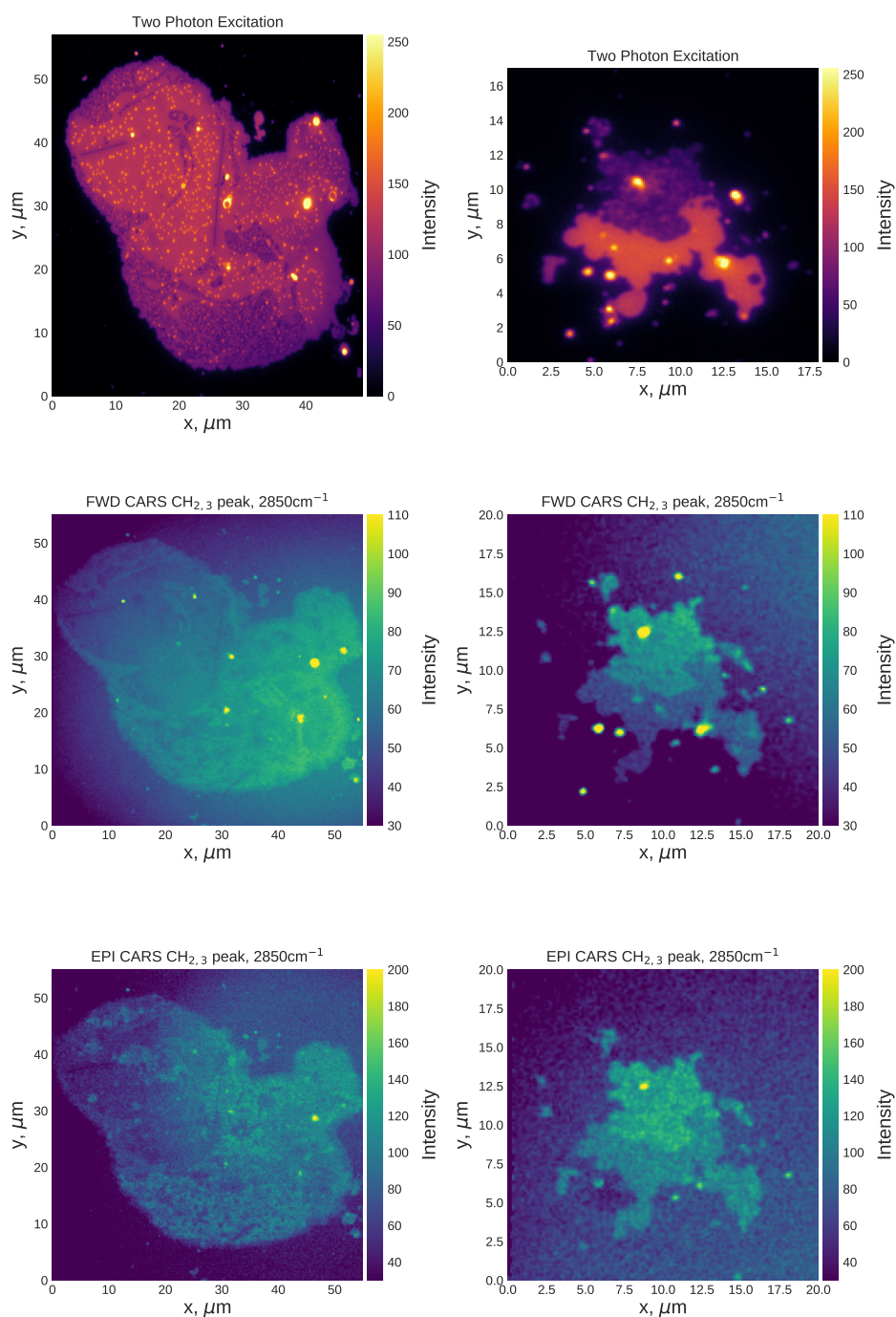


Figure 4.7: Comparative analysis of phase separated PLBPs under CARS and Two Photon fluorescence imaging. Patches comprise DOPC:PSM:Cholesterol (2:1:1 molar ratio) with 0.1mol% NBD-DOPE. In all cases we observe a characteristic contrast inversion between the fluorescence and CARS images (as explained in the text). These figures demonstrate that, at the single bilayer level CARS microscopy provides a label-free alternative to traditional fluorescence imaging for the determination of plasma membrane phase.

## 4.5 Hyperspectral CARS imaging of PLBPs

### 4.5.1 Hyperspectral CARS of homogeneous PLBPs

Prior to studies in phase separated lipid membranes and due to shortcomings in the GUV model, single species DOPC PLBPs were developed to calibrate both fluorescence and CARS responses within this new model. Single frequency ( $2850\text{cm}^{-1}$ ) CARS and correlative TPE fluorescence were combined to establish a baseline signal in each lipid phase (ordered phase signals are higher due to increased lipid packing density) and to eliminate the possibility of fluorophore / lipid heterogeneity prior to application in more complex systems. These results were shown in section 4.4.2.

Hyperspectral CARS (HCARS) applied across the  $\text{CH}_2$  and  $\text{CH}_3$  region from  $2700\text{cm}^{-1}$  to  $3100\text{cm}^{-1}$  (resolution  $10\text{cm}^{-1}$ ) was used in order to extract the Raman like spectra of DOPC at the single bilayer level for use as a spectral control for the disordered phase in phase partitioned PLBPs. It should be noted that Raman cannot be applied at the level of a single bilayer without utilising complex experimental setups, such as total internal reflection Raman (Lee and Bain, 2005) or tip enhanced Raman (Opilik et al., 2011) and long integration times. We verified that this was the case by attempting our own Raman measurements upon PLBPs: without success. Unfortunately, there is simply insufficient material presented by a single bilayer to generate a sufficient Raman signal for detection.

Systematic consideration of the experimental setup and parameters identified key metrics for quantification of the analysis. Unsaturated DOPC possessing (*cis*  $\Delta 9$ ) double bonds shows considerable Raman signal increase around  $2930\text{cm}^{-1}$  relative to PSM due to increased  $\text{CH}_3$  stretching modes present (Cheng et al., 2002b). Spectral manifestation of this effect can be seen as both an increase in the full width at half maximum (FWHM) of DOPC (across the Raman region  $2800 - 3000\text{cm}^{-1}$ ) and as an increase in signal around  $2930\text{-}2940\text{cm}^{-1}$ . We therefore correlate the degree of unsaturation with the FWHM and as a quotient between DOPC and PSM signals at  $2930\text{cm}^{-1}$  (experimental DOPC maxima). PSM by contrast has longer average chain length, is more saturated and packs at greater density (Brown, 1998, Mombelli et al., 2003). We would therefore expect signal increase relative to DOPC at frequencies around  $2850\text{-}2880\text{cm}^{-1}$

as demonstrated in figure 4.7. Previous Raman measurements of bulk phase lipid stocks (c.f appendix A.2) have confirmed these frequencies ( $2880\text{cm}^{-1}$ ,  $2930\text{cm}^{-1}$ ) as important for differentiating between the primary lipid species. It was required to establish whether the spectral differences seen in bulk are replicated in lipids within a single bilayer as it is known that the spectra are a function of lipid state (Orendorff et al., 2002).

For the CARS microscopy, PLBPs were imaged using a 60x, 1.27NA water immersion objective through a #1.5 coverslip with 40 (Single frequency) or 10 (HCARS) frame averages: increasing signal to noise. As shown in section 4.3, 40 frame averages were determined to be the minimum for optimal imaging, however under hyperspectral CARS, due to the number of data sets required to capture a wide range of frequencies at high resolution, any more than 10 frame averages caused significant bilayer damage (universally to all samples measured). 10 frame averages were therefore empirically determined as the maximum possible. TPE was performed sequentially on the same setup with 20 frame averages utilised. Fluorescent PLBPs were selectively photobleached prior to CARS imaging by raster scanning the CARS pump beam, set to deliver approximately 50mW of pulsed power for  $\approx 20\text{s}$ , by which time the fluorescence signal drops to  $<10\%$  of its initial level. These short photo-bleaching timescales were not observed to damage the samples.

Furthermore, systematic study has revealed that image to image contrast is strongly correlated with the objective focus of the microscope. Standard thermal drift of the focus was found to be 100-200nm per 5 minute interval. The focal position is extremely important, given the lack of lipid material within the focal volume, contrast is maximised by placing as much of the focal volume into the non-resonant medium (coverglass) as possible. Given image acquisition times of 12s per frame for a  $15\times 15\mu\text{m}$  sample, substantial time is taken for 60 frame averages; focal shifts will exert an effect upon the relative image to image contrast under both forward and Epi CARS. To minimise these effects, HCARS images taken at multiple frequencies were imaged before and after acquisition at  $2850\text{cm}^{-1}$  to confirm focal stability, thus enabling comparisons between images to be taken. Images demonstrating significant changes in contrast were thus excluded from analysis. Lateral variation in the intensity profile due to varying spa-

tial overlap of the pump and Stokes beams manifests as a gradient in x and y direction of the images, this was corrected prior to analysis with a polynomial fit (2nd order) to the background and subtraction of the effect.

Analysis of the CARS hyperspectral data was performed with custom software (Masia et al., 2015). Within software singular value decomposition (SVD) was used to denoise the data prior to non-negative matrix factorisation (nNMF) which performs an automatic decomposition of the hyperspectral stack into spectral components along with absolute concentration maps showing the spatial distribution of these components.

The results of this analysis applied to pure DOPC PLBPs are shown in figure 4.8 . Both under TPE and CARS the patches appear homogeneous, with no fluorophore or lipid partitioning even at high image contrast (for comparative phase separated contrast see Figure 4.7).

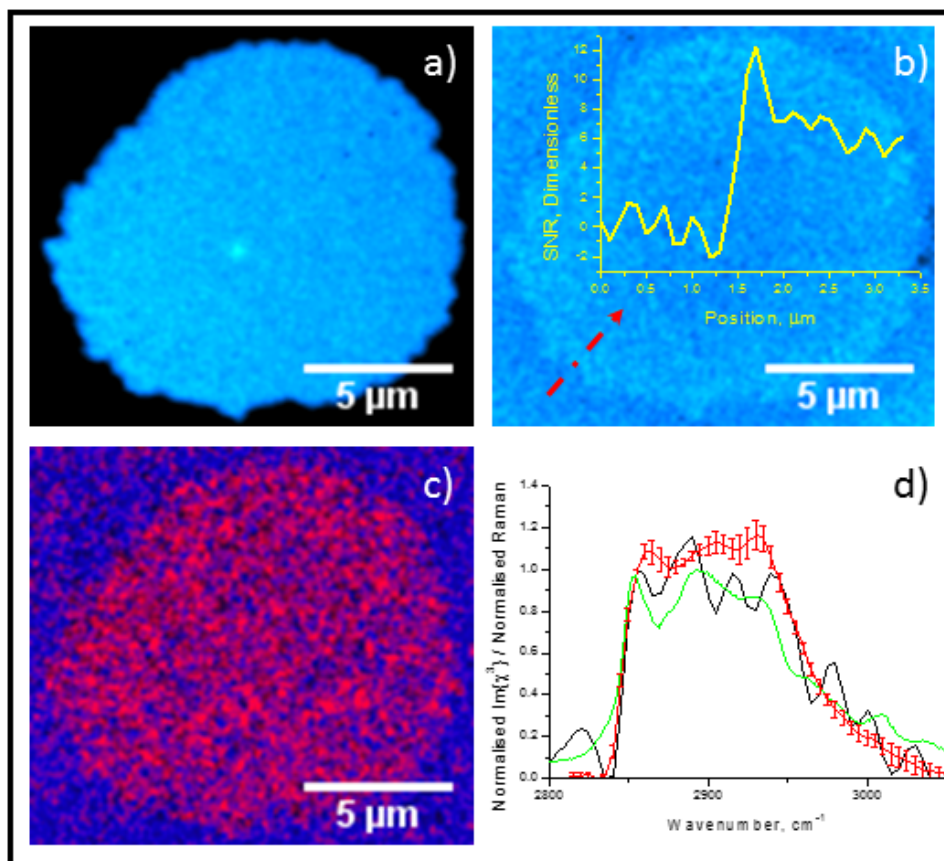


Figure 4.8: CARS and TPE microscopy applied to DOPC PLBPs. Under TPE and CARS single component DOPC PLBPs appear homogeneous as shown in sub-figures a) and b). CARS at the level of a single bilayer produces good signal to noise (5-7x typical) as shown in the profile cut inset in b). Hyperspectral CARS combined with phase retrieval and non-negative matrix factorisation maps distributions of chemical species c): DOPC appears in red with background due to water in blue. In d) nNMF Extracted Raman like CARS spectra for a single bilayer (black) and mean (red,  $n=5$ , error bars plot standard error of the mean) are compared against bulk Raman spectra taken from the same DOPC stock solution.

Signal to noise was assessed by comparing the background subtracted membrane signal as a quotient to the standard deviation of the background. As shown inset in Figure 4.8b a cut through the patch shows signal of at least 5x the noise allowing for unambiguous identification of membrane to background regions. Hyperspectral CARS combined with phase retrieval and nNMF (see (Masia et al., 2013)) have been used to recover the Raman like spectra of DOPC at the single bilayer level. nNMF permits unsupervised spectral decomposition and concentration mapping with respect to spectral components present in the data. Extracted Raman like spectra are shown in Figure 4.8c and d. In Figure 4.8c we demonstrate clear discrimination of DOPC PLBP from background due to Water through images formed by spatial mapping of absolute spectral concentration of each component in different colour channels. Associated spectra are shown in Figure 4.8d which for clarity have a small scaling factor (1.05-1.2) applied to induce an offset. At the level of a single data set, noise complicates the analysis. It is still possible to identify DOPC by comparison of the individual bilayer spectra with either the Raman or HCARS average (Results not shown). The average standard error (SE) over all points within the average spectra was 0.03 (no units, Normalised scale) which compares favourably with the maximum value of 1.16 (taken at  $2930\text{cm}^{-1}$ ). This equates to a 2.6% error in peak level determination. Key spectral frequencies at  $2880\text{cm}^{-1}$  ( $\text{CH}_2$  asymmetric stretch, (Cheng et al., 2002b)) and  $2930\text{cm}^{-1}$  ( $\text{CH}_3$ , (Wei et al., 2013)) show little deviation from the level seen in bulk (appendix A.2) and therefore serve as key discriminators with respect to the levels in Sphingomyelin, permitting their use as spectral  $L_D$  phase markers. Spectral reproducibility between different PLBPs can be seen in Figure 4.8d (red trace) demonstrating excellent experimental and analytical reproducibility for the applied methods. The FWHM calculated from the average DOPC spectra, taken relative to the maxima at  $2930\text{cm}^{-1}$  was  $115 \pm 10\text{cm}^{-1}$ .

Similar analysis was applied to homogeneous PSM enriched PLBPs as reference for the  $L_o$  phase in ternary lipid systems. PLBPs were prepared at 2:1:1 molar ratios of PSM:DOPC:CH and were seen to lack phase separation. Observation of the parent GUV population indicated that phase separation was occurring at these lipid ratios. It is therefore probable, given that the PLBPs are formed from this population that phase sepa-

rated PLBPs could have been found. It was important for us to characterise homogeneous PSM enriched PLBPs as unknown degrees of DOPC:PSM separation could induce significant unknown spectral changes complicating comparison to the Raman spectra of each individual compounds, potentially providing an ambiguous set of reference spectra. Therefore, the patches were preselected on the basis of the homogeneity of their fluorescent signal. Imaging conditions were the same as for the DOPC patches, with pre-bleaching of the NBD fluorophore prior to CARS imaging.

As shown in figure 4.9a and b, TPE and CARS ( $2850\text{cm}^{-1}$ ) have been used to confirm lipid and fluorophore homogeneity in PSM enriched PLBPs. Inset in Figure 4.9b is the point to point signal to noise ratio for the cut shown in red calculated as a background subtracted quotient to the background standard deviation as before. The SNR is 3 times higher for the  $L_0$  patches than that seen in DOPC with a typical level around 15x the noise.

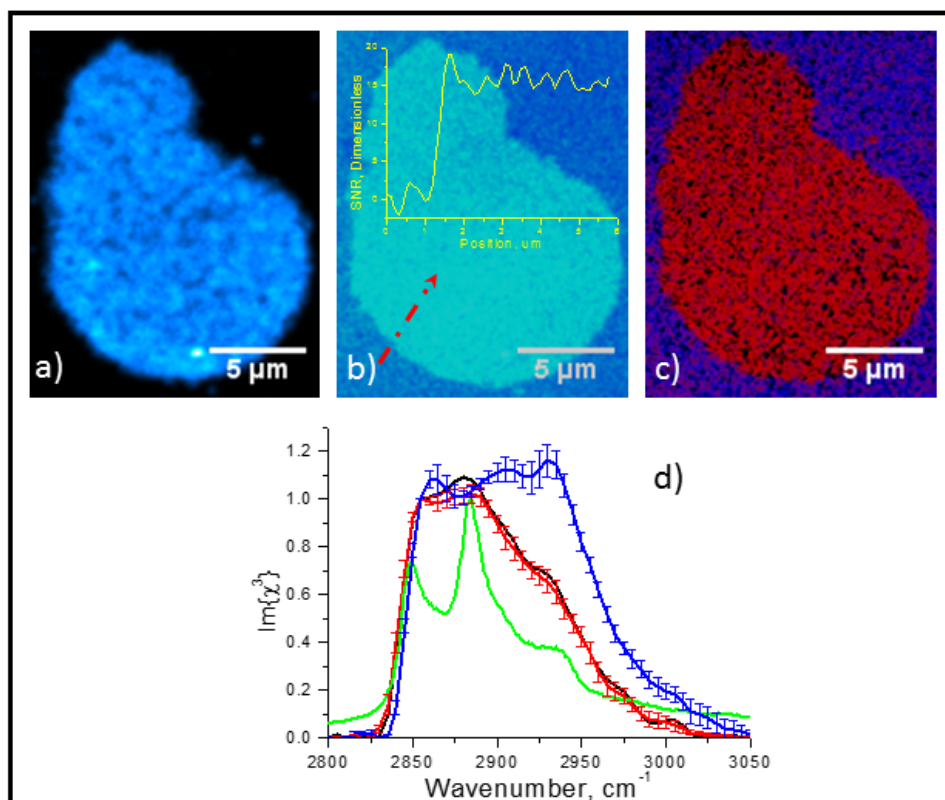


Figure 4.9: Hyperspectral CARS and nNMF applied to uniform PSM enriched PLBPs. Shown in (a) TPE image, at high contrast of single PSM enriched patch. (b) CARS image of the same patch taken at the CH<sub>2</sub> lipid peak (2850cm<sup>-1</sup>) with inset signal to noise ratio taken across the cut denoted by the red arrow. (c) HCARS absolute spectral concentration map of background (blue) and lipid (red). (d) comparison of average PSM rich PLBP spectra (red) and individual patch spectrum (Black) to the control spectra under RAMAN: DOPC (blue) and PSM (green). Spectra shown with standard errors.

To recover the Raman like spectra, hyperspectral CARS was utilised with phase retrieval and nNMF as before. Patches are clearly differentiated from the background due to water (Figure 4.9c) and appear homogeneous. In Figure 4.9d the Raman like spectra of this individual PLBP is shown in black, with the mean taken over 5 patches in red. Average standard error over all points in the mean spectra was 0.02 a 2% error relative to the PSM maxima at  $2880\text{cm}^{-1}$  ( $\text{CH}_2$  asymmetric stretch, (Cheng et al., 2002b)), comparing favourably with that seen for DOPC PLBPs. For comparison, the Raman spectra of bulk PSM is shown in green. PSM enrichment has produced a characteristic spectral distribution interposed between that of PSM and DOPC. The FWHM of the PSM average spectra was found to be  $100\pm 10\text{cm}^{-1}$  showing significant ( $15\text{cm}^{-1}$ ) reduction in spectral bandwidth by comparison to DOPC. It should be noted that the FWHM error was estimated from the spectral resolution of the setup and as such represents the maximum determination error. Monte Carlo simulation over the fitting and extraction parameters would likely lower this estimate but has not been attempted at the present time. The frequency difference around  $2930\text{cm}^{-1}$  between PSM and DOPC under bulk Raman is reproduced. A quotient formed from the normalised DOPC and PSM signals at the  $2930\text{cm}^{-1}$  ( $\text{CH}_3$  stretch, (Wei et al., 2013)) gave a value of  $1.87\pm 0.01$ , close to the factor of 2 difference seen in the bulk lipid Raman spectra shown appendix A figure A.4. This demonstrates a decreased population of  $\text{CH}_3$  present in  $L_0$  phase. The observed decrease in spectral bandwidth and nearly two fold change in  $\text{CH}_3$  activity provide strong evidence for efficient spectral discrimination of  $L_0$  to  $L_D$  phases. HCARS with unsupervised nNMF has thus provided a convenient, rapid and effective set of methodologies for application in lipid determination at the single bilayer level.

## 4.6 Hyperspectral CARS, qDIC and Fluorescence of labelled PLBPs

Partitioned ternary PLBPs comprising DOPC:PSM:Cholesterol (2:1:1 molar ratio) as shown in Figure 4.10 demonstrate good contrast under both forward TPE and forward CARS (FCARS) modalities.  $L_0$  domains under

TPE appear dark due to preferential incorporation of the fluorophore into the disordered phase. Under FCARS a clear reversal of domain contrast can be seen at  $2850\text{cm}^{-1}$  with respect to the fluorescence image. Greater intensity from the  $L_o$  phase at  $2850\text{cm}^{-1}$  is understandable in terms of the increased packing density of the lipids therein (Potma and Xie, 2003). To further confirm correlation between domain assignment under CARS and fluorescence, TPE images were processed in Imagej with an edge extraction algorithm (Sobel kernel) to determine patch and domain boundaries. Edge maps are shown in figure 4.10b and c overlaid onto the FCARS and HCARS images. From this we infer that CARS assignments due to changes in packing density and chemical constituents respectively are spatially coherent with changes in fluorophore partitioning providing analogous label-free methodologies. Normalised FCARS profiles taken as a background subtracted quotient to the background demonstrate excellent contrast up to 25% with a further 5-10% contrast developed between the  $L_o$  and  $L_d$  phases (see Figure 4.10b inset). qDIC analysis (shown in Figure 4.10d) shows a disordered phase thickness of  $4.9\pm 0.1\text{nm}$  with the disordered phase less defined between 3.8 and 4.2nm (c.f. figure 4.3).

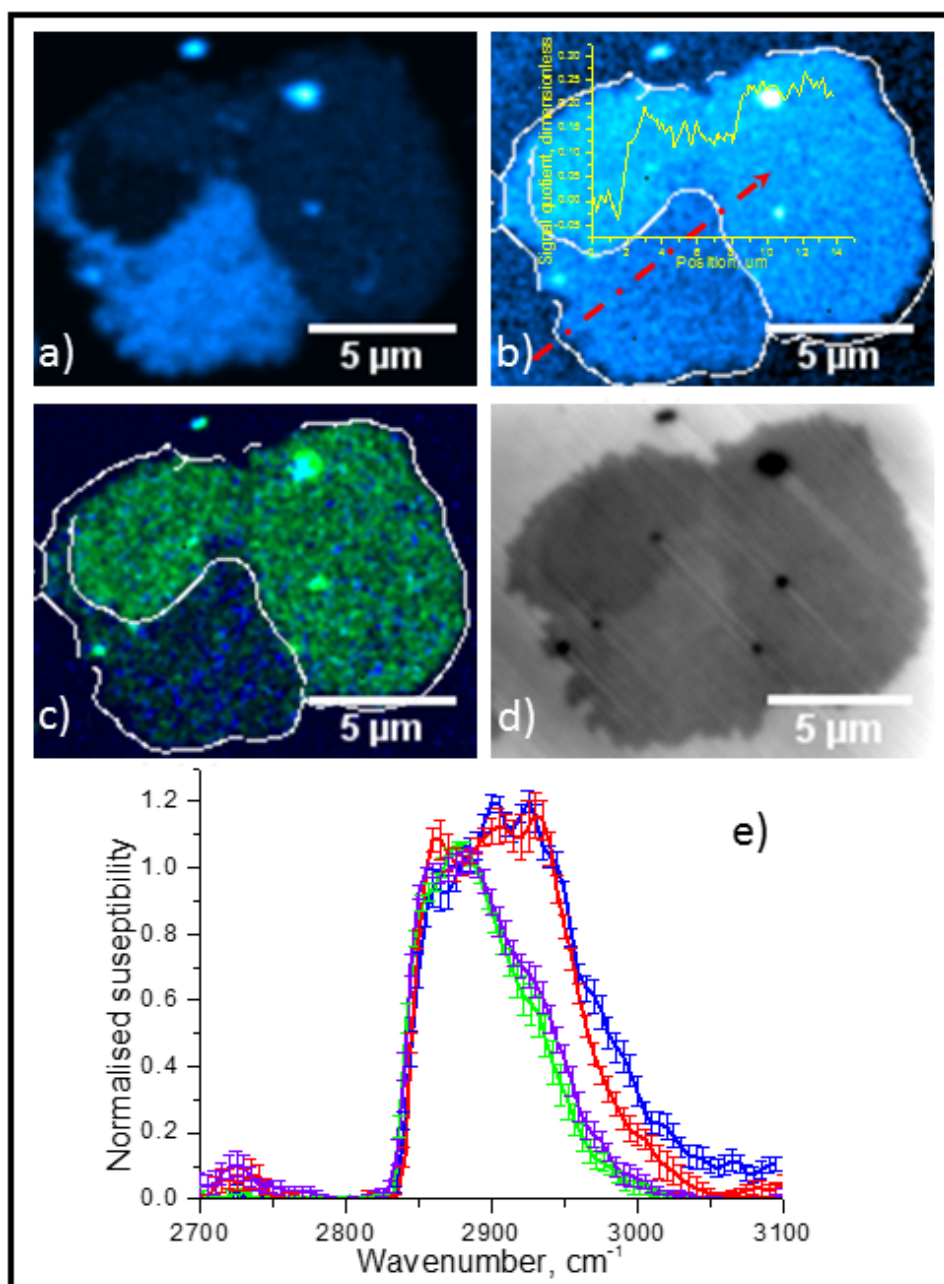


Figure 4.10: CARS, TPE and qDIC applied to labelled phase separated PLBPs. Shown in (a) TPE image of NBD-DOPE distribution within PLBP,  $L_o$  phase appears dark. (b) Single frequency CARS ( $2850\text{cm}^{-1}$ ) image showing clear contrast between ordered (lighter) and disordered (darker) phases. Overlaid TPE edge map confirms domain correlation between (a), (b) and (c). (c) HCARS image of absolute spectral concentration for the species shown in (e). (d) qDIC phase image confirming changes in underlying membrane thickness. (e) average spectra taken over  $n=10$  patches for  $L_o$  phase (green),  $L_d$  phase (blue) with control DOPC (red) and PSM enriched patches (violet). Spectra shown with standard errors.

HCARS mapping of the patch is shown in Figure 4.10c with corresponding spectral analysis shown below. Hyperspectral data was acquired between  $2700\text{cm}^{-1}$  and  $3100\text{cm}^{-1}$  in frequency steps of  $5\text{cm}^{-1}$  (Resolution  $10\text{cm}^{-1}$ ). For analysis, data sets were first cropped and masked to exclude artefacts and then decomposed into SVD spectral basis prior to Phase corrected Kramers-Kronig phase retrieval. Lateral offset of the CARS pump and Stokes beams leads to uneven excitation especially apparent at the high laser powers used. Regions of the image corresponding to background were fitted by second order polynomials and the images corrected prior to non-negative matrix factorisation of the data (Further details on nNMF appear in (Masia et al., 2013)).

Average nNMF spectra for the different domains are shown green and blue inset in Figure 4.10e with corresponding domains in Figure 4.10c. Average curves were formed from the NMF spectra of 10 data sets taken across two sessions from separate PLBP samples. Spectral deviation was minimised prior to formation of the average by normalising individual spectra to their own maxima. Also shown are the control spectra of DOPC and unpartitioned PSM enriched PLBPs seen earlier. To enable direct comparison, correction for session to session variation in the microscope setup was required. Spectra were rigidly translated such that the peak at  $2850\text{cm}^{-1}$  was coincident (typical correction:  $7.5\text{cm}^{-1}$ , resolution:  $10\text{cm}^{-1}$ ). Additionally a small scaling factor (1.05-1.2) was applied to correct for normalisation differences between data sets, since slight variation in the maximum height of the spectral envelope occurs (whilst the overall spectral envelope is highly conserved). Close correspondence is observed between control spectra and extracted phase domain spectra from labelled partitioned PLBPs. The FWHM for  $L_o$  and  $L_d$  phases was  $100\pm 10\text{cm}^{-1}$  and  $126\pm 10\text{cm}^{-1}$  respectively with maxima found at  $2880\text{cm}^{-1}$  and  $2930\text{cm}^{-1}$ . These compare favourably with the distribution and maxima found for the DOPC and PSM enriched patches found earlier. Slight increase in the spectral width of the  $L_d$  phase is attributed to background variation between different samples at frequencies beyond  $2970\text{cm}^{-1}$  and is not significant. Difference spectra found by subtraction of control PSM and DOPC average spectra from  $L_o$  and  $L_d$  spectra respectively showed no significant deviation (result not shown) thereby permitting easy and unequivocal identifica-

tion of  $L_o$  and  $L_d$  on the basis of dominant lipid constituents (Blue areas in Figure 4.10c  $L_d$  DOPC, green  $L_o$  PSM). Average standard errors were again found to be 2% for both distributions at maxima. A spectral quotient formed between  $L_o$  and  $L_d$  phases at  $2930\text{cm}^{-1}$  was found to be  $2.08\pm 0.01$  consistent with the control measurement of  $1.87\pm 0.01$  and the bulk phase factor of  $\approx 2$  (appendix A). The slight increase may be indicative of greater  $L_o$  phase PSM enrichment in these patches than that achievable in the control measurements thereby further depleting the  $\text{CH}_3$  population in this phase. We have shown that for fluorescently labelled PLBPs exhibiting  $L_o / L_d$  phase partitioning CARS and qDIC can be used for domain identification analogously to fluorescence. In addition, qDIC permits direct extraction of domain thickness and hyperspectral CARS can identify the dominant lipid constituents per phase. These methods extend the previous state of the art in this field permitting full characterisation of lipid phase behaviour in model membrane systems.

#### 4.7 Hyperspectral CARS, qDIC and Fluorescence of label-free PLBPs

Fluorescence microscopy created a revolution in biophysical sciences advancing and furthering our knowledge of complex biological systems and processes, a role that it continues today. In recent decades however, greater understanding of the role played by exogenous fluorophore incorporation within sensitive biological systems has started to be understood. Perturbation of system dynamics through fluorophore usage is widely known and in part has driven the development of label free, chemically specific imaging modalities such as CARS (for example changes in model membrane bending elasticity is probe dependant (Bouvrais et al., 2010)). We have applied CARS and qDIC to label-free ternary PLBPs in order to observe lipid phase behaviour in the absence of this perturbative influence. PLBPs were formed from GUV comprising DOPC:PSM:CH in 2:1:1 molar ratios. In place of the labelled NBD-DOPE we included 0.5mol% of unlabelled DOPE such that the system represented the closest possible analogue to the labelled systems discussed previously.

Shown in Figure 4.11a and b are the HCARS concentration map and qDIC mapping of lipid phase domain structure for a typical label-free PLBP. Under forward HCARS clear discrimination of the ordered phase (shown green) and disordered phase (shown blue) are observed. Phase domains identified by the two independent techniques correlate between data sets. Figure 4.11c shows mean label-free ordered phase and disordered phase spectra against the control PLBP spectra taken for DOPC and PSM enriched patches.  $L_d$  and DOPC spectra are, to within the limits of experimental precision, identical demonstrating that DOPC is the majority lipid constituent found in the  $L_d$  phase within these model membranes.  $L_o$  to PSM control spectral comparison shows a slight reduction in the FWHM to  $78 \pm 10 \text{cm}^{-1}$  that is attributed to a higher degree of PSM enrichment for the  $L_o$  phase than that which can be attained within the control membrane setup. Further evidence for greater PSM enrichment is provided by the quotient between phases at  $2930 \text{cm}^{-1}$  which increases slightly to  $2.22 \pm 0.01$  in label-free patches. Figure 4.11d compares both  $L_o$  and  $L_d$  phases between the labelled and label-free membrane data sets. Within the limits set by experimental and analytical precision only slight differences can be observed. A slight change in the FWHM of  $22 \text{cm}^{-1}$  is observed along with associated increase in the  $\text{CH}_3$  quotient at  $2930 \text{cm}^{-1}$ . Spectrally the label-free patches show on the average a slightly quicker decay to zero i.e. a slightly more pronounced resonance. This may be attributable to a better defined separation of the lipid constituents, free from the influence of the fluorophore. Further careful study would be required to firm up this assertion however.

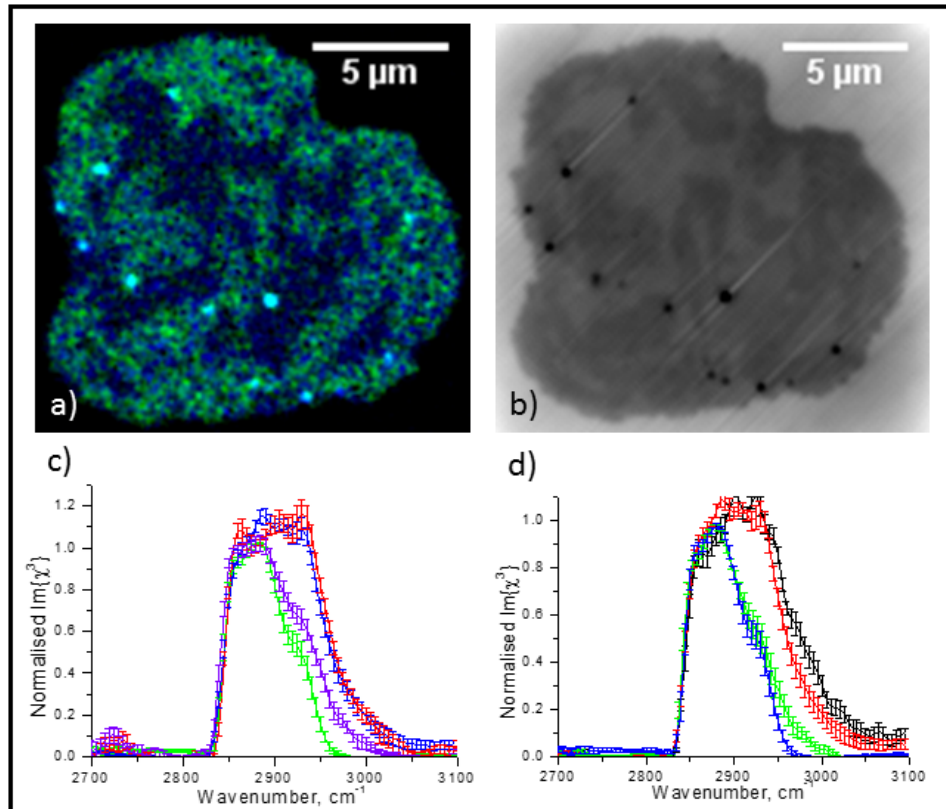


Figure 4.11: Hyperspectral CARS and qDIC applied to label free PLBPs. (a) HCARS mapping of lipid components showing  $L_o$  phase in green,  $L_d$  in blue. (b) qDIC image demonstrating sub-nm thickness differences between  $L_o$  and  $L_d$  phases. (c) comparison of average  $L_o$  (green) and  $L_d$  (blue) phase spectra to control DOPC (red) and PSM enriched (violet) spectra for  $n=10$  patches. (d) Comparison of domain spectra between labelled and unlabelled patches. Spectra shown with standard errors

We have demonstrated, for the first time, full HCARS analysis applied at the level of an individual bilayer in order to map lipid constituent distribution in label-free PLBPs. Combined with qDIC analysis, this provides a clear and unambiguous picture of fundamental lipid behaviour based upon generally applicable arguments regarding behaviour of saturated vs unsaturated lipids. As a result, these techniques should prove useful to more complex lipid systems such as those comprising cell membrane extracts and may prove generally useful within the lipid field enabling minimally perturbative studies on membrane systems.

## 4.8 Stimulated Raman loss of PLBPs

As discussed in section 1.6.2.6, stimulated Raman loss (SRL) microscopy provides another label free, chemically specific imaging modality to complement CARS microscopy (Freudiger et al., 2008). Unlike CARS, the signal under SRL is proportional to the Raman cross section and is not differential in nature (unlike CARS) (Saar et al., 2010). This presents some advantages:

1. The spectra is linear in the concentration of the analytes (Nandakumar et al., 2009).
2. SRL spectra do not require phase retrieval.
3. Raman resonances are often less broad than their CARS counterparts (discussed below) (Ozeki et al., 2009).

Towards the end of this PhD, the opportunity arose to take simultaneous CARS and SRL measurements on a new setup that had been completed. The SRL setup is driven by an optical parametric oscillator (OPO) such that the bond frequencies are driven by tuning the laser output to a certain frequency relative to another fixed frequency. As such, the setup is not well suited for hyperspectral imaging, as to scan across a range of frequencies would require continual retuning of the OPO output.

For these experiments therefore, we compared simultaneously acquired CARS and SRL upon label-free ternary PLBPs. The patches comprised DOPC:PSM:Cholesterol in 2:1:1 molar ratio. Imaging was performed with

a 60x 1.27 NA water immersion objective and 1.4NA oil immersion condenser. The OPO output was tuned to 656nm relative to the idler at 400nm, driving the CH region peak at  $2850\text{cm}^{-1}$ . Dwell times were 0.1ms and a minimum of 10 frame averages used. In contrast to the earlier CARS measurements, total power at the sample was much lower with 4mW in the primary beam. This allows for significantly less damage to the bilayer. The laser repetition rate is 80MHz and the modulation frequency for the detection is set at 2MHz.

As mentioned in section 1.6.2.6, SRL uses a modulated signal with lock-in detection to eliminate background, in principle close to that of the shot noise of the detector. In addition, unlike CARS it does not suffer from a non-resonant background. Furthermore, in consideration of imaging the CH modes of lipids, the CARS OH Stretch resonance from water is very broad, extending with significant amplitude into the CH region. By contrast the Raman resonance of Water is less broad (Louvel et al., 2015) which significantly lowers the background and increases the contrast seen under SRL.

In figure 4.12 we demonstrate direct comparison between images of PLBPs and vesicles simultaneously acquired under both CARS and SRL imaging modes. It is immediately apparent that the contrast of the SRL images is enhanced compared with the CARS images due to the clear reduction in background. Although both imaging modes are probing the same resonances, the CARS imaging actually carries more information since both the real and imaginary parts of  $\chi^{(3)}$  are present. By comparison the SRL is proportional only to the imaginary part (Nandakumar et al., 2009) and therefore directly proportional to the Raman spectra. It was hoped to be able to image phase partitioning with the SRL technique, however during the course of these experiments, partitioned PLBPs could not be conclusively found. Hyperspectral data was taken from patches, however due to the nature of the setup, the bandwidth is limited to just  $100\text{cm}^{-1}$ , in order therefore to produce spectra from  $2700\text{-}3100\text{cm}^{-1}$  would have required continual retuning of the output laser frequency of the OPO. A process that would have required very careful calibration to ensure that each spectral region could be properly 'stitched' to the next without overlap or loss of data. Even in spite of the preliminary nature of these SRL experiments, I

feel that the technique could be of great applicability to studies at the single bilayer level. Primarily this is due to the enhanced contrast and the far lower power levels required, which will induce far less damage to these sensitive bilayers. Alternatively, with lower power comes the ability to take further averages, increasing signal to noise. Due to the non-differential nature of the SRL signal, there tends to be less spectral overlap between different bonds, and therefore the possibility for better discrimination of chemical species. Finally, the analysis for SRL is easier than for CARS, requiring no phase recovery (Yu et al., 2014).

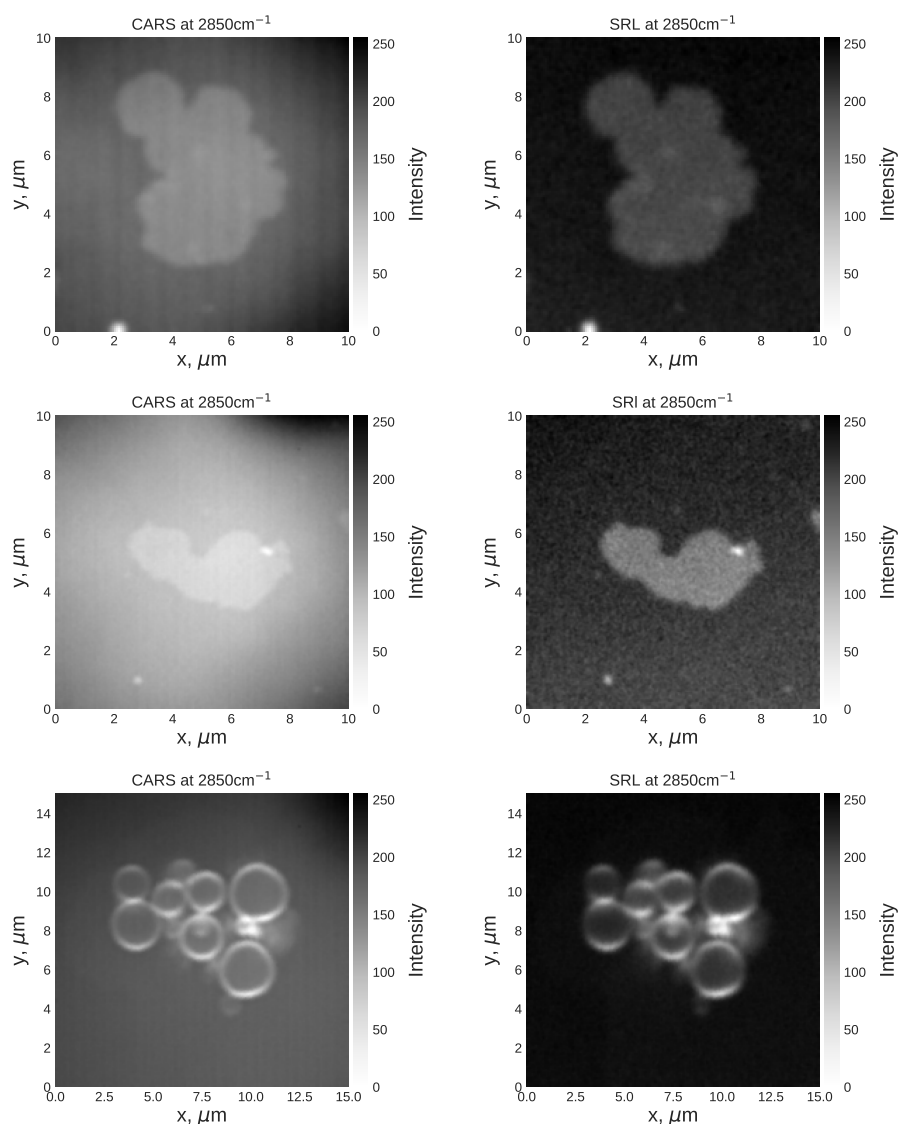


Figure 4.12: Simultaneously acquired label free images of ternary (DOPC:PSM:Cholesterol, 2:1:1 molar ratio) PLBPs and vesicles under SRL. All images were acquired at the CH<sub>2</sub> stretch peak at 2850cm<sup>-1</sup> the spectral resolution for both was 50cm<sup>-1</sup>. Notice the enhanced contrast and lower background apparent in the SRL images. The top PLBP may have areas of phase partitioning at the left hand edge. Given the low power (4mW) requirements versus that of CARS (>50mW), narrower spectral resonance and lower background, SRL is a very promising label free imaging modality for investigations at the single bilayer level.

## 4.9 Summary

In this chapter we have demonstrated a static bilayer model: the Planar lipid bilayer patch. Firstly we applied the technique of quantitative DIC microscopy within the context of a flat bilayer geometry and demonstrated that qDIC could visualise these objects even though they are just 4nm thin. We then extended the limits of the qDIC by examining phase partitioned patches and showed that thickness differences of just  $\approx 0.9\text{nm}$  between phases could not only be visualised but also quantitatively measured. Within the larger field of model membrane research where the visualisation of raft domains is done by fluorescence methods (Veatch and Keller, 2003) which are known to modify the properties of the system under investigation (Leung and Thewalt, 2017, Veatch et al., 2007), label free optical techniques such as qDIC allow for a minimally disruptive method to view the true nature of the system.

We then proceeded to demonstrate correlative CARS and two photon microscopy applied to both partitioned and non-partitioned PLBPs. We showed that both methods led to the same assessment of coexisting lipid liquid phase but that CARS did so on the basis of the chemical constituents and their inherent organisation and packing densities allowing us to infer the relative distributions of different lipid types. The CARS analysis was then extended by taking a series of hyperspectral stacks of both partitioned and homogeneous PLBPs across the spectral region from  $2700\text{cm}^{-1}$  to  $3100\text{cm}^{-1}$ . We were able to show that the liquid disordered phase was predominately composed of DOPC from the close spectral match with the known Raman spectrum for this lipid. We were also able to prove that the liquid ordered phase had a spectra closer in nature to that of pure Sphingomyelin, directly indicating it's enrichment within that phase. Again, in terms of fundamental membrane research, the ability to distinguish domains without the use of fluorophores is a major advantage. Within the wider field, more complex planar lipid bilayers exist which incorporate high densities of proteins (Milhiet et al., 2006), single ion channels (Suzuki et al., 2007) or nanodisks, with scaffold proteins (Skar-Gislinge et al., 2010). The possible additional incites that could be gained through the ability to distinguish and quantitatively map not only the distribution but absolute con-

centration of lipid and protein content at the single bilayer level, without the use of perturbative elements cannot be understated. It is therefore a future goal of this work to extend the analysis towards protein incorporating membranes, initially those formed from polymer supported erythrocyte ghosts (Tanaka and Sackmann, 2005). Finally we demonstrated correlative, simultaneous CARS and SRL imaging of both vesicles and PLBPs. This showed the reduction in background and the associated increase in contrast possible with SRL. Unfortunately, as discussed in the text, hyperspectral SRL was not possible at this time, but I predict that once available it will permit a degree of spectral discrimination in excess of that possible with the present CARS based techniques given that Raman resonances tend to be better defined than the differential CARS signals. The lower power requirement of SRL is also a major advantage over the CARS setup, potentially permitting longer imaging timescales, higher averaging and less bilayer damage.

## 5.1 Thesis Summary

In **Chapter 1** we gave a contextual overview of the project, starting with the basics of the types and structure of lipids through the the different types of structures they can form: micelles, bilayers, cubic phases etc. The modern view of the lipid membrane as explained by the Singer-Nicholson fluid mosaic model of 1972 (Singer and Nicolson, 1972). It also explained additions to this model such as the mattress model (Mouritsen and Bloom, 1984) and lipid rafts (Simons, 1997) to explain more recently observed membrane behaviour. Due to the the complex nature of an actual cell membrane (as explained), including the presence of a high density of membrane associated proteins, the decision was taken to simplify the task and study synthetic lipid membranes, whose exact constituents were under our control and crucially which would not spectrally overlap with proteins (Movasaghi et al., 2007). Several synthetic lipid models were then proposed to investigate putative lipid rafts: the Giant Unilamellar vesicle and Planar lipid Bilayer patches. An explanation was given for the thermodynamic reasons underlying lipid phase separation.

We gave an overview as to the nature of lipid rafts and their hypothesised structure and roles. As stated lipid rafts have been implicated in both normal cellular processes and in disease models, some of which such as caveolae, heat shock response and viral transfection were discussed at length.

We then proceeded to examine the state of the art with regards to analysis of lipid rafts and the shortcomings of most of the existing techniques. Methods for examining lipid rafts either involve the use of perturbative elements such as fluorescence probes or destructive methods such as analysis of cellular extracts. This then provided the motivation and outlook for this study: to develop a novel suite of label free, chemically specific optical techniques for identification, classification and non-perturbative raft analysis.

A background introduction and basic explanation of DIC microscopy was given along with more recent work by other groups into developing a quantitative version. The chapter continued with an historical introduction to the development of the chemically specific CARS microscopy and Stimulated Raman loss. Chapter 1 concluded with the theoretical concepts needed to understand the experimental work undertaken during this study. Basic theories of Raman, CARS and Stimulated Raman loss microscopy were expounded. In addition, our modification to DIC microscopy: quantitative DIC microscopy was also explained.

**Chapter 2** Materials and methods covered all of the procedures for lipid handling, sample preparation, quality control and details of the CARS microscopy setup. Common pitfalls, and errors encountered were also mentioned along with the steps taken to mitigate these issues. Details of the CARS experimental setup were given along with the methods of image acquisition and analysis.

**Chapter 3** deals solely with our work to develop and characterise Giant unilamellar vesicles. Several methods of vesicle formation have been shown: Gentle Hydration and Electroformation. Due to the nature of vesicle formation, thin walled vesicles can present with more than one bilayer at the periphery, separated by a distance less than the diffraction limit. For our studies, it is important that vesicles be unilamellar, so as not to confuse the signal with that from additional material in a different lipid liquid phase. In the literature, we identified a commonly used technique to quantify the number of bilayers based upon the intensity of the fluorescence signal from the membrane (Akashi et al., 1996). This method of course assumes a homogeneous incorporation of the fluorescent label into each membrane. We conducted a large scale study, utilising this method by measuring a pop-

ulation of  $n=466$  separate DOPC vesicles stained with Atto-488 DOPE. A quantised rather than continuous distribution of membrane intensities was found thereby indicating that vesicles can form only with integer numbers of complete bilayers, with the lowest intensity distribution assumed to correspond to that of the unilamellar population.

This fluorescence based assay was then extended by using our new qDIC microscopy to analyse a significant population of fluorescent vesicles ( $n=145$ ) which were simultaneously analysed by fluorescence quantisation. Our results show that qDIC produces the same assessment of vesicle lamellarity, but without the need for exogenous fluorescent labelling. This is important as many studies have started to indicate the effect of fluorophore incorporation upon the state of the membrane (Bouvrais et al., 2010), its molecular order (Leung and Thewalt, 2017), inducement of curvature changes by GFP incorporation (Stachowiak et al., 2012) and changes in membrane stiffness caused by a fluorescent cholesterol analogue (Garvik et al., 2009).

Following this study, we begin to characterise Atto-488 DOPE labelled unilamellar vesicles of increasing complexity. This primary motivation was that this fluorescent lipid analogue has not (to our knowledge) been used in the literature before and so we check for partitioning in all of our possible GUV systems. We found that in all cases that GUV presented in a single lipid phase (Liquid Disordered, liquid ordered or gel phase) the fluorophore was homogeneously incorporated. These studies also highlighted the important role of Cholesterol in membranes: within a gel phase, Cholesterol breaks the lipid order forming a liquid ordered phase. Within the disordered phase Cholesterol promotes order. In vesicles comprising coexisting lipid liquid phases, Atto-488 DOPE has shown phase preference for the disordered phase as expected, which was determined alongside CARS measurements. In addition, two other fluorescent phase markers were utilised Naphtho[2,3-a]pyrene and NBD-DOPE, which are known to partition into the ordered and disordered phases respectively with these lipid constituents (DOPC:PSM:Cholesterol) (Baumgart et al., 2007). We then showed, with all three fluorescent markers phase separation within ternary GUV, including examples of different types of domain packing arising from differing thermodynamic processes.

CARS microscopy and Hyperspectral CARS microscopy were then applied to label free GUV with mixed results. Due to the tenuous nature of the vesicles themselves, combined with the high laser powers needed to extract signal from a layer two molecules thin; CARS imaging of GUV proved problematic. Examples were shown imaged at the CH stretch ( $2850\text{cm}^{-1}$ ) as well as a complete spectra taken from a multilamellar PSM vesicle in a gel phase. These results are important, since in these freely floating systems, we have avoided the use of exogenous fluorescence labelling (with the associated problems given earlier). Given our desire to use this model if at all possible, due to the unconstrained nature of the contained lipids, we were motivated to develop some further modifications of GUV.

Several modified GUV models were created including biotinylated GUV, bound to a Neutravidin surface (in an attempt to prevent laser induced vesicle translation), examples of single frequency imaging, including possibly phase separated GUV were shown. Attempts to extract hyperspectral data from these models was unsuccessful however. Imaging of GUV electroformed within Deuterium Oxide was also shown which permitted a reduction in the resonant background due to Water (since the heavy Water spectrum is red shifted). Using this technique we were also able to image the weak combination scissoring mode at  $2735\text{cm}^{-1}$  which is not normally possible. It was hoped that the slight increase in viscosity might assist with oscillatory motion of the vesicle periphery, however this was not observed to occur.

Deuterated Sphingomyelin vesicles were imaged at both  $2850\text{cm}^{-1}$  and at  $2100\text{cm}^{-1}$ , these deuterated systems show some potential at background reduction due to the absence of Raman active modes at frequencies around  $2100\text{cm}^{-1}$ . In addition, by incorporation of just a single deuterated lipid, it's distribution can be directly mapped since no other lipid will have an active mode at those frequencies. It is hypothesised that a ratiometric analysis of the signal at  $\approx 2100\text{cm}^{-1}$  to that at  $2850\text{cm}^{-1}$  may allow the elucidation of the relative in-bilayer concentration.

Label free GUV were also imaged under CARS microscopy, however due to their free in solution nature, and thermally driven motion, they have proved to be a very hard system to work with, principally since they must be located under DIC and then imaged under CARS. These shortcomings

contributed to our desire to create a model better suited to chemically specific analysis.

**Chapter 4** Due to the limitations seen with CARS imaging of GUV, we developed a new surface bound, static model bilayer called planar lipid bilayer patch(es) (PLBPs). Since this model is created by an osmotically induced rupture onto a hydrophilic substrate (Castellana and Cremer, 2006, Richter et al., 2006) from a parent population of GUV, it shares many of the positive aspects of that system. The lipid phases are formed in a free to diffuse environment that is then frozen upon PLBP formation (Hamai et al., 2007, Li et al., 2005), therefore the distribution of the lipid is relevant thermodynamically. Secondly, should protein be incorporated into the GUV, this will be transferred to the PLBP also.

Firstly, a new qDIC study was performed upon PLBPs in order to elucidate that they comprised a single lipid bilayer and secondly to determine that the technique had sufficient axial resolution to visualise single bilayers (4nm thin) without geometric enhancement as seen in the case of GUV. This study was then extended using phase partitioned PLBPs, for which the difference in membrane thickness between the disordered and ordered phases was less than a nm (Kučerka et al., 2008). qDIC was able not only to visualise this sub-nm contrast, but we were also able to quantify it. Larger scale studies (n=83) of PLBPs indicated the limitations imposed on the qDIC method by both the techniques used for analysis and the nature of the setup. The ability to visualise sub-nm structures is important however, and we would propose extending the qDIC to PLBPs incorporating a high density of membrane bound protein, such as GPI-anchored or transmembrane varieties to ascertain the wider applicability of the technique.

A brief study was then conducted to optimise the CARS imaging conditions for PLBPs before correlative fluorescence / CARS studies were conducted in phase partitioned PLBPs. We have been able to demonstrate that CARS microscopy at the CH<sub>2</sub> stretch frequency (2850cm<sup>-1</sup>) is as capable at determining coexisting lipid liquid phases as fluorescent microscopy techniques. Although this is clearly done on a different molecular basis, in this case the density of CH bonds present within the sample (Potma and Xie, 2003) rather than an exogenous marker. This phase discrimination is due to the change in average chain length and packing density between the

ordered and disordered lipid phases. This allowed us to infer sphingomyelin enrichment was occurring within the ordered phase. These techniques are important since we wish to study all of our systems without perturbation due to the introduction of a foreign molecule such as a fluorescent lipid analogue and the associated problems given above.

Hyperspectral CARS was next applied to PLBPs in order to extract full spectral information across the CH region from  $2700\text{cm}^{-1}$  to  $3100\text{cm}^{-1}$ . By use of hyperspectral stack decomposition into constituent spectra, combined with a mapping of their absolute concentrations across the images. We were able to demonstrate directly that in both labelled and unlabelled PLBPs with coexisting lipid liquid domains that the ordered phase was spectrally closer to that of Sphingomyelin and the disordered phase closer to DOPC. Thereby, and for the first time under CARS, demonstrating directly the molecular mechanism underlying putative lipid raft formation in model membranes. These techniques should be of wide applicability, firstly we propose to extend to studies in PLBPs incorporating proteins. In spite of significant overlap across the CH region between lipid and protein, other studies by our group have shown the capacity to discriminate them on a hyperspectral basis (Di Napoli et al., 2016, Masia et al., 2013), albeit in molecularly dense systems.

If model membranes could be fabricated with rafts and incorporating sufficient density of raft associated protein, it would be interesting to try and collocate them on the basis of full hyperspectral information. In the wider field, lipid rafts within actual cell membranes are often located or inferred through the use of either protein / polymer / lipid bound nanoparticle diffusion (Lasne et al., 2006, Rong et al., 2009) or analogous super-resolution fluorescence techniques (Eggeling et al., 2009). The work herein is laying the ground work for surface enhanced, nanoscopy which offers the prospect to monitor membrane lipid / protein content and diffusion with high spatiotemporal resolution and without the induced perturbation of the system associated with nano-particles or fluorophores. This could have very widespread applicability, not just for fundamental membrane research, but also for cellular processes such as endo- or exo-cytosis, or cellular trafficking.

Finally, we covered a direct comparison between simultaneously ac-

quired CARS and SRL at the CH stretch ( $2850\text{cm}^{-1}$ ) for a series of PLBPs and vesicles. I have demonstrated certain advantages of SRL with regards to reduction in background, superior imaging contrast, narrower spectral features and lower optical power requirements as compared to CARS microscopy. Unfortunately, the SRL was only available late in the PhD, however I believe that given the lower heating associated with the greatly reduced laser powers (4mW instead of  $\approx 50\text{mW}$ ) GUV studies with SRL might be more successful since the induced thermal motion of the targets should be greatly reduced. Again, the extension of SRL into hyperspectral imaging and the associated chemical specificity and concentration mapping are potentially of widespread use in the field for much the same reasons given above for CARS.



## Raman analysis of bulk lipids

### A.1 Introduction

Lipids constitute a spectrally well characterised class of biomolecules (Czaramara et al., 2015). Polar lipids are the predominant constituent of all cell walls and plasma membranes, where they form a bilayer, and as such are common to all cellular life. Lipids also occur within cells, in an aggregated form, known as lipid droplets. As shown in section 1.4, lipids have also been implicated in many disease and normal cellular function models, taking on an active rather than just passive role (such as just a simple barrier molecule).

Numerous recent studies have utilised lipid droplets extensively for analysis by CARS microscopy (Billecke et al., 2014, Bradley et al., 2016, Paar et al., 2012, van Zutphen et al., 2014). Demonstrating, for example, the remodelling of lipid droplets through directed transfer (of lipids) (Paar et al., 2012) or to quantify the size and distribution of droplets in mouse oocyte development (Bradley et al., 2016). This interest in lipid droplets is motivated by both the fundamental importance of the underlying phenomena, but also due to the (relative) ease of CARS imaging applied to lipid droplets. Strong vibrational resonances are presented by lipid molecules across the CH region ( $2600\text{-}3100\text{cm}^{-1}$ ) which combined with the high lipid packing density present within lipid droplets yields strong CARS contrast. Relatively few studies have been performed at the single bilayer level, presumably due to the lack of inherent molecular scatterers, relative to lipid droplets. Contrast

can still be developed (within the CH region) down to the single bilayer level using a highly optimised CARS setup as was first performed in (Potma and Xie, 2003). Our interest is in developing and characterising synthetic lipid bilayers, more specifically to discriminate differing lipid components on this basis. In order to achieve this we exploit contrast in the CH region developed due to overlapping contributions from methyl ( $\text{CH}_3$ ), methylene ( $\text{CH}_2$ ) and methine (CH) groups. This can create issues for data analysis, since the contribution from one is not, in general, separable from another.

Herein, we have applied both Raman and Hyperspectral CARS analysis to bulk phase samples of our main lipid moieties. We will demonstrate that, with sufficiently simple lipid constituents, the different lipid components are in principle differentiable through comparison of whole CH region spectra due to changes in incorporated groups located within the lipid acyl chains.

## A.2 Raman microscopy

Simultaneous chemically specific analysis of multiple lipid species is complicated through inter-species spectral overlap across the CH stretch region (Slipchenko et al., 2009). To better understand the inherent spectral differences between three target species: Cholesterol, Sphingomyelin and DOPC, we measured the Raman spectrum of each species in the bulk phase, from  $500\text{cm}^{-1}$  to  $\approx 3500\text{cm}^{-1}$ . This allowed identification of frequency targets for inter-species contrast under CARS. DOPC, relative to PSM contains a greater number of cis C=C double bonds present at the  $\Delta 9$  mid chain position (Yeagle, 2011). The presence of these double bonds forms a bend, about which the acyl chain cannot rotate. Thus inhibiting tight lipid packing, leading to the formation of a  $L_d$  phase (Hammond et al., 2005). The presence of additional double bonds relative to Sphingomyelin, presents a valid spectroscopic target since the magnitude of the =C-H stretch mode signal around  $3010\text{cm}^{-1}$  is proportional to the bond density (Freudiger et al., 2008).

Samples were produced by drop casting a lipid-solvent solution (2:1 Chloroform : Methanol, v/v), under continuous stream of Nitrogen directly onto a microscope coverslip. The coverslip was then removed to high vacuum for a minimum of 30 minutes to remove all trace solvents. An imaging

chamber was constructed using a 20mm diameter, 500 $\mu$ m imaging spacer (Grace Bio-Labs, USA), attaching the coverslip to the microscopy slide (25x75x1.1mm, Fisher Scientific).

Data was acquired on an inverted microscope (TI-U, Nikon, Japan). Thick regions of the cast lipid sample were located by DIC microscopy at 20x (0.75NA) objective magnification. A 0.72NA dry condenser was used and the DIC illumination was provided from a Metal Halide lamp (Nikon, Japan), filtered to remove IR frequencies, and bandpass filtered to provide a well defined illumination wavelength (550 $\pm$ 20nm). Raman spectra were acquired in the reverse direction utilising a 532nm laser for illumination. Spectral acquisition was performed with a Spectrometer (Yobin John) equipped with cooled (-60°C) CCD detector. Internally, the spectrometer employed a 600 lines per mm diffraction grating, providing a spectral resolution of  $\approx 2.3\text{cm}^{-1}$ . Spectra were acquired within two distinct spectral regions ( $\approx 500\text{cm}^{-1}$  to  $2100\text{cm}^{-1}$ ,  $2100$  to  $3500\text{cm}^{-1}$ ) and stitched together during post acquisition analysis. The region around  $2100\text{cm}^{-1}$  is suitable for combining the spectral regions across all samples presented as they are devoid of Raman resonances near this frequency.

During acquisition, considerable initial auto-fluorescence was observed due to the frequency of laser used. Video mode spectral acquisition was used to monitor fluorescence levels until the detector offset was reached, confirming complete photo-bleaching of the sample. Raman data was then immediately acquired with 60s integration time across each spectral region.

### A.2.1 Spectral Analysis of DOPC

As shown in figure A.1, Raman active modes are found in both the fingerprint and CH regions of the spectra and arise principally due to the modes of the acyl chains. Considering first the fingerprint region shown in figure A.1a. A mode is present at  $1070\text{cm}^{-1}$  which is due to the C-C out of phase aliphatic stretch (Beattie et al., 2004). The next mode present around  $1280\text{cm}^{-1}$  is a combination of the CH<sub>2</sub> twisting and scissor deformations appearing double peaked. The mode at  $1440\text{cm}^{-1}$  is due to further CH<sub>2</sub> twisting deformations (Beattie et al., 2004). The  $1650\text{cm}^{-1}$  mode is characteristic of the C=C olefinic double bond and is a stretching defor-

mation (Beattie et al., 2006). The mode at  $1730\text{cm}^{-1}$  is characteristic of the backbone molecule glycerol, and is due to the C=O carbonyl stretch (Sadeghi-Jorabchi et al., 1990).

Although some of these modes show potential for the discrimination of different lipid species, such as the C=C oscillation (due to higher numbers of C=C double bonds present in DOPC), all of the resonances are weak by comparison to the CH region, for which an approximate 5 fold increase in the scattering cross section is observed. Figure A.1b shows an expanded section through the CH region of the spectra from  $2700\text{cm}^{-1}$  to  $3200\text{cm}^{-1}$ . Key resonances and their spectroscopic assignments are at  $2850\text{cm}^{-1}$  ( $\text{CH}_{2,3}$ ),  $2880\text{cm}^{-1}$  ( $\text{CH}_2$  stretch, (Camp Jr et al., 2014)),  $2940\text{cm}^{-1}$  ( $\text{CH}_3$  stretch, (Wei et al., 2013)) and  $3010\text{cm}^{-1}$  (C=C-H, (Heinrich et al., 2008)) As we will show later, these frequencies present targets for lipid to lipid contrast under the chemically specific CARS microscopy.

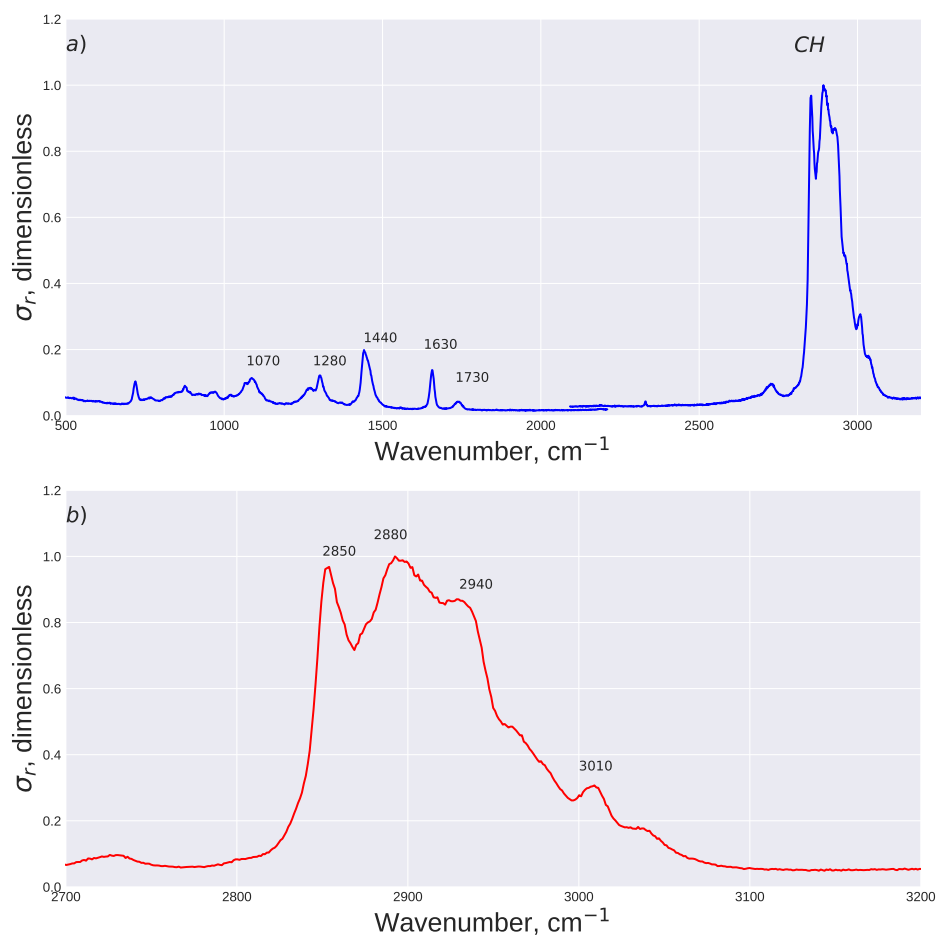


Figure A.1: Raman spectra of drop cast, bulk phase DOPC lipid. Shown in (a) is the normalised Raman cross section  $\sigma_r$  from 500 to 3200  $\text{cm}^{-1}$ , encompassing both the fingerprint and CH regions. In (b)  $\sigma_r$  is shown highlighting the CH region only. As shown in (a) Raman resonances are present at ( $\approx 1080\text{cm}^{-1}$ ) due to the aliphatic C-C stretch (Vandenabeele et al., 2000), whereas the resonance at  $\approx 1300\text{cm}^{-1}$  is due to a twisting deformation of the  $\text{CH}_2$  molecule. The resonance present at  $\approx 1440\text{cm}^{-1}$  is associated with a scissoring deformation of the  $\text{CH}_2$  molecule. Due to the increase population of CC double bonds present in DOPC, the resonance ( $\approx 1650\text{cm}^{-1}$ ) associated with it provides some potential for the mapping of this molecule, however the overall Raman cross section for this mode is low compared with that seen in the CH region. The final resonance identified is that associated with the CO double bond at  $\approx 1730\text{cm}^{-1}$ .

### A.2.2 Spectral Analysis of Sphingomyelin

In contrast to DOPC, the Raman spectra for Porcine Sphingomyelin (PSM) is shown in figure A.2. As identified in subplot a) there are several Raman active modes with appreciable contrast in the fingerprint region. A resonance is present around  $\approx 1080\text{cm}^{-1}$ , associated with the CC aliphatic stretch is seen (also present with DOPC). A second Raman resonance is present at  $1300\text{cm}^{-1}$  associated with the  $\text{CH}_2$  twisting distortion. As with DOPC a final resonance is present at  $1440\text{cm}^{-1}$  associated with  $\text{CH}_2$  scissoring. Within the CH region, highlighted in figure A.2, certain differences are present relative to DOPC. The CH region resonances are approximately 7 times greater than the maximum magnitude observed within the fingerprint region (PSM). This implies that imaging, at the single bilayer level would not be possible with present technology (within the fingerprint region). A similar set of CH region resonances are observed between DOPC and PSM and arise on the same chemical basis. The Raman resonance at  $2880\text{cm}^{-1}$  was found to be greater in magnitude than that present at  $2850\text{cm}^{-1}$  in the case of PSM. The resonance at  $2940\text{cm}^{-1}$  is present however at a reduced magnitude relative to DOPC.

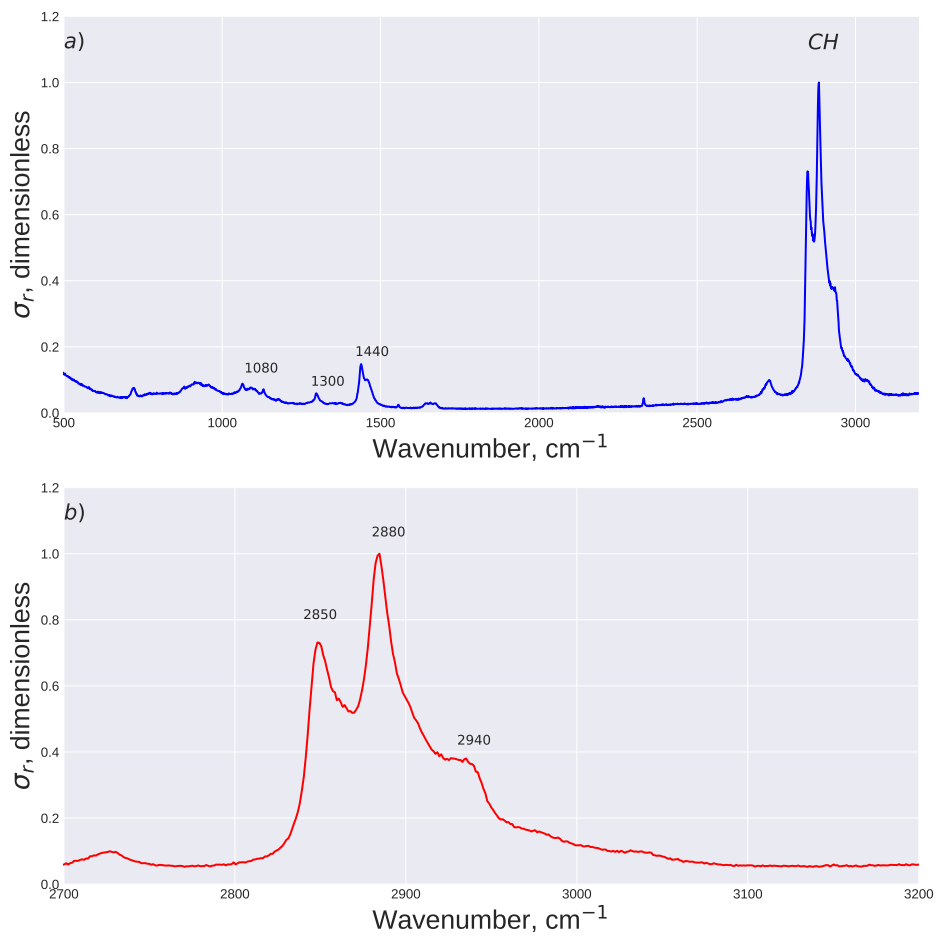


Figure A.2: Raman spectra of drop cast Porcine Sphingomyelin.

### A.2.3 Spectral Analysis of Cholesterol

Shown in figure A.3, is the spectra of Cholesterol. Within the fingerprint region, due to the different ring-like Carbon structure, we expect there to be resonances not present within the two other model lipids. The resonance seen at  $930\text{cm}^{-1}$  is present in the case of Cholesterol but absent in the other models, this Raman mode is a combination of acyl stretch and rocking modes associated with the  $\text{CH}_3$  moiety. The Raman cross section presents at a sub-threshold level respective to CARS imaging, therefore this mode will not be usable at the single bilayer level. Cholesterol presents a Raman resonance at  $1750\text{cm}^{-1}$  with increased cross section relative to the other model lipid species. This mode is due to the  $\text{C}=\text{O}$  stretch. At the single bilayer level, imaging for Cholesterol would be best achieved within the CH region (for which the largest cross section is seen). As shown in figure A.3, Cholesterol presents a broad set of  $\text{CH}_{2,3}$  resonances. In particular, Cholesterol exhibits relatively high cross section around the  $2900 - 2940\text{ cm}^{-1}$  range. In ternary lipid systems, employed for phase separated studies, this could potentially interfere with imaging specificity. Compared with DOPC or PSM, Cholesterol has only 9  $\text{CH}_{2,3}$  molecules (c.f. PSM has an average of 21 Carbons per chain). Therefore under imaging conditions, within the bilayer, it is expected that the signal contribution attributable to Cholesterol will be negligible compared with the other species under test.

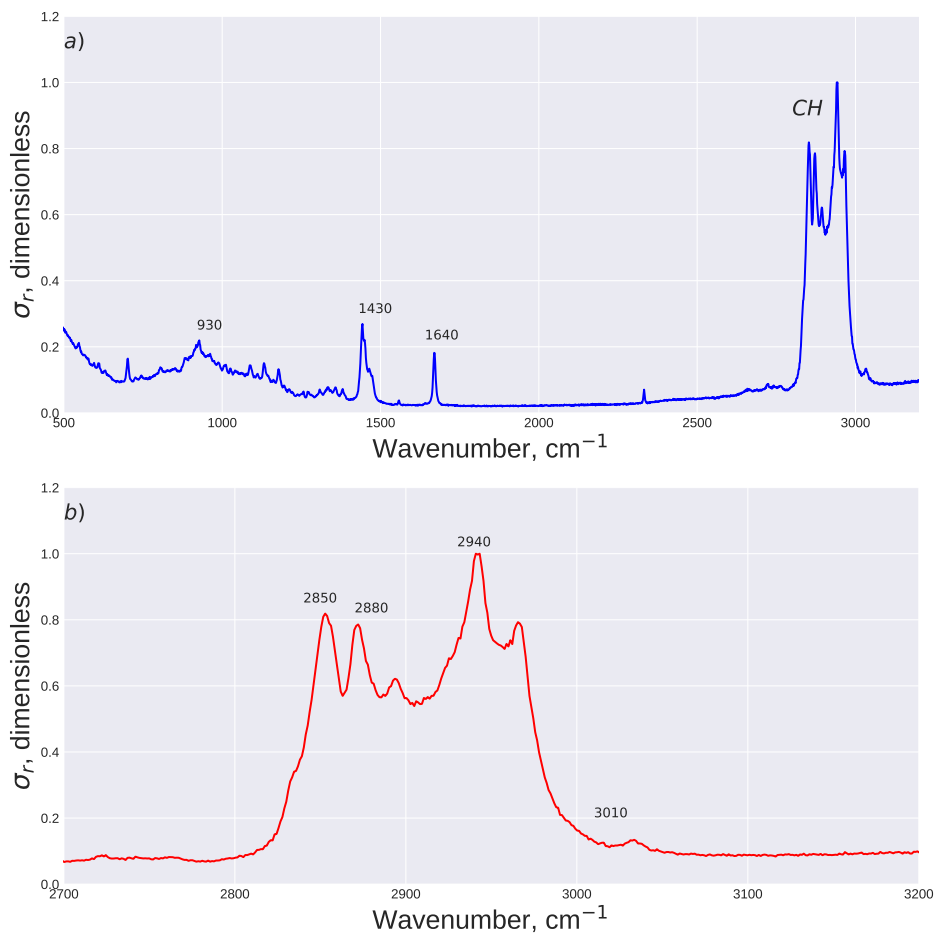


Figure A.3: Raman Spectra of Cholesterol.

#### A.2.4 Spectral basis for chemically sensitive imaging

Shown in figure A.4 are the spectra for all model lipids. Considering the full spectra (figure A.4, top) it is clear that many fingerprint region modes are shared between all of the lipids. In addition, as mentioned previously, the fingerprint region signal is at best 20% that of the CH region. Therefore, for single bilayer level imaging, we will need to consider the CH region more carefully. Shown in figure A.4 (middle) are the CH region spectra for all species, note the spectral width of Cholesterol in this region, this would potentially be a complicating factor for specific imaging. However, since the Cholesterol signal is very slight compared to the other species, it can effectively be ignored. Shown in figure A.4 (bottom) is the difference between the normalised Raman spectra for DOPC and PSM, for imaging purposes the 30% difference in magnitude between DOPC and PSM around  $2850\text{cm}^{-1}$  is a potential target. It is estimated that the best frequency for DOPC to PSM discrimination will be those around  $2940\text{cm}^{-1}$  where a 50% difference in normalised scattering cross section is seen. This is characteristic of the narrow spectral width in the CH region of the more saturated species such as PSM (Heinrich et al., 2008). Finally, potential imaging contrast may be developed based on the olefinic band seen around  $3010\text{cm}^{-1}$ , as mentioned this mode is a result of the C=C-H bond stretch which is characteristic of the unsaturated lipids such as DOPC (Heinrich et al., 2008).

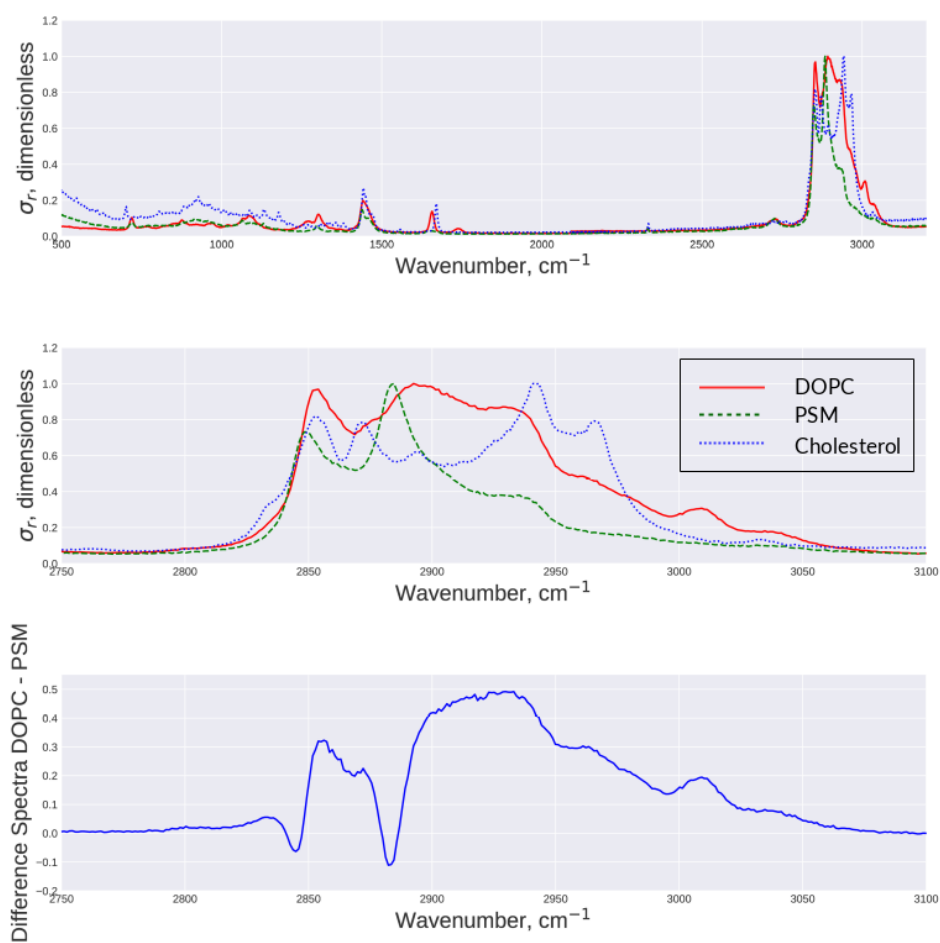


Figure A.4: Comparison of spectra for model lipids



## Neutravidin binding protocol

The protocol for the preparation of glass coverslips with an attached layer of Neutravidin is as follows, as utilised in section 2.1.3.4.

1. Fresh #1.5 coverslips (Menzel Glazer, Germany) were precleaned by sonication in Acetone and dried under continuous stream of Nitrogen.
2. Pre-cleaned coverslips were activated with acid Piranha solution as detailed in appendix C.
3. Within a Nitrogen chamber, under conditions of forced positive pressure, activated coverslips were incubated for 1 hour with a 2% (v\ v) APTES ((3-Aminopropyl)triethoxysilane) solution in Acetone (Sigma-Aldrich, UK).
4. The Coverslips were then washed with excess Toluene (within a Nitrogen cabinet), keeping track of the APTES treated face.
5. The active face of each coverslip was then incubated (under Nitrogen) for 1 hour with 200 $\mu$ l of 1mM Biotin NHS ester dissolved in DMSO (Dimethyl Sulfoxide) forming a covalent bond with the amine groups present at the surface.
6. The coverslips were washed in triple distilled Water (Millipore, 18.2M $\Omega$ ), keeping track of the treated face and dried under Nitrogen.
7. The Biotinylated face of each coverslip was then incubated for 1 hour with a 1 $\mu$ M solution of Neutravidin in PBS (Phosphate Buffered Saline, 135mM).

8. The coverslips were washed again with triple distilled Water (Millipore 18.2M $\Omega$ ), then dried and sealed under Nitrogen.
9. Coverslips can be stored in the fridge at 4°C and for several days remain active.



## Piranha Protocol

### Introduction

Piranha solution is often utilised both within industry and in a Laboratory context for both the cleaning and activation of Silicon and glass surfaces. Due to its high acidity and reactivity it possesses the capacity to both dehydrate organic contaminants, dissolve elemental carbon deposits, strip contaminating metal ions & Hydroxylate glass surfaces rendering them hydrophilic. There are many different formulations of this solution, all of which are referred to as Piranha solution or etch. The basic components are concentrated Sulphuric acid (always the majority constituent v/v) and Hydrogen peroxide (less than 30% v/v). Within the context of our present research there are two projects for which the cleaning and activation of glass coverslips, slides and silica beads prior to Silane coupling is required. These are the quantitative differential interference contrast and Nanoscope projects for which the preparation of thin, homogeneous surface bound monolayers of nano-particles and DNA / protein nanotethers are required.

### Background Chemistry

Upon mixing of the two components, two separate and powerful reactions begin. The first and faster reaction is the dehydration reaction under the action of the Sulphuric Acid.



The second, slower reaction liberates free Oxygen through direct interaction between the Peroxide & the Sulphuric acid:



It is this liberation of the reactive atomic Oxygen that gives Piranha the ability to both dissolve Carbon and Hydroxylate the glass surface forming an increased surface density of SiOH (silanol) groups to provide a better target for Silane coupling compounds. It should already be clear from the reactions and discussions above that Piranha Solution poses a significant risk to any lab users coming into contact with it. All of the reactions are highly exothermic and the liberation of Oxygen provides a significant further risk. The solution also reacts explosively with any organic solvents and so must be conducted in isolation within the confines of a fume hood. To minimise risks, only small volumes of solution should be used, for most purposes 20ml maximum will suffice.

**Personal Protective equipment (PPE) requirements:**

All of the following must be used and / or available; as applicable below: Goggles, Rubber Apron, Rubber Gloves, Lab Coat, Fume Hood (with integral sink and tap), acid storage cupboard, glass beakers (100mL, 2L), flat bottomed glass containment vessel (30cm Diameter x 10cm deep), forceps (PTFE), cleanroom wipes, ice, millipore 18.5MΩ grade water, Oxygen free N<sub>2</sub>, seal-able acid waste disposal bags & Acid Spill kit.

**Compatible materials:**

Pyrex / Borosilicate glassware (Heat stable to minimum 240 degrees Celsius), PTFE (Teflon).

**Incompatible Materials**

Unless on the compatibles list all other materials should be assumed to be incompatible and restricted from coming into contact with undiluted / unreacted solution.

**Protocol**

1. Remove all Organic solvents and chemicals from fume hood (Both hoods if they share a common exhaust), clean surfaces with Chloroform / water and allow fume hood to dry and evacuate ( 15 mins).
2. Place flat glass containment vessel in centre of fume hood, on hot plate @ 60 degrees and pour in small layer of water (2cm deep). Allow sufficient time for water to warm.
3. Prepare a large 2L glass beaker with crushed ice water and place into back of fume hood.
4. Prepare a second 100mL beaker with  $DH_2O$ , place within fume hood.
5. Put on all PPE for acid handling (Apron, gloves, goggles, lab coat).
6. Put sign on fume hood sash warning other users of Piranha use.
7. Turn on tap within fume hood, it must run for entire duration of the protocol (For immediate decontamination of minor spills).
8. Remove 98% Sulphuric Acid from storage cupboard and measure 15ml into a clean beaker. Place at side of fume hood.
9. Place Sulphuric acid bottle back into acid storage cupboard, ensure that no acid drips down the outside of the bottle (remove carefully with wetted cleanroom wipes).
10. Remove 30% Hydrogen Peroxide stock solution from fridge and measure out 5ml (3:1 acid:peroxide) into separate clean Pyrex beaker. Keep away from acid beaker.
11. Place Hydrogen peroxide bottle back into fridge.
12. Using PTFE forceps slowly immerse required glass slides or cover slips into the beaker of sulphuric acid, allow to lay horizontally on the bottom.
13. Place Sulphuric acid beaker into containment vessel, allow to equilibrate for a few minutes.(Lessens risk of heat shocks to glass)

14. Using glass pipette SLOWLY add Hydrogen Peroxide to the sulphuric acid.
15. Solution will boil, close fume hood sash immediately.
16. Allow to react for 30 - 60 minutes, do not leave unattended.
17. Using PTFE forceps carefully remove cover slips / slides from the solution and immediately immerse within a 100mL beaker of  $DH_2O$ .
18. Turn off hot plate and leave reaction mix to cool for 4 hours minimum.
19. Rinse slides / coverslips in 5 x  $DH_2O$  washes.
20. Dry coverslips / slides under stream of  $N_2$  working the water away from the centre of the glass. Handle only by edges.
21. Once reaction mix is spent, dilute by pouring small amounts (1-2mL) into the large beaker of ice water until gone.
22. Rinse reaction beaker in excess water under the tap until decontaminated.
23. Pour diluted reaction mix and Ice-water slowly into sink with tap running, rinse container several times after.
24. Rinse containment vessel in excess water.
25. Dry all containers with cleanroom wipes.
26. Dispose of all used wipes in suitable sealed acid disposal bag.
27. Empty and clean Fume hood surfaces with excess water and allow to dry.



## **Atto-488 and NBD-DOPE Photobleaching**

In order to test the effectiveness of Atto-488 DOPE against NBD-DOPE for measurements of vesicle lamellarity, two samples of DOPC GUV were electroformed as described elsewhere each containing either 0.5mol% of NBD-DOPE or 0.5mol%

For imaging, a 20x 0.75NA Objective was used with a GFP filter-set (Semrock, USA) within an inverted Nikon Ti-U Eclipse setup. Illumination was provided by a prior lumen metal halide lamp set to minimum power. Images of GUV were brought into focus and imaged at 5 second intervals under continuous illumination in the Epi direction. For analysis, the temporal image stacks were loaded into imagej and an annulus created around individual GUV post image registration. The mean intensity with the annulus was taken as a measure of the fluorescence intensity. The results are plotted in figure D.1, clearly at the same concentration, the Atto-488 DOPE is significantly more resistant to photobleaching losing approximately 10% of its initial intensity in the same time that NBD loses 90%.

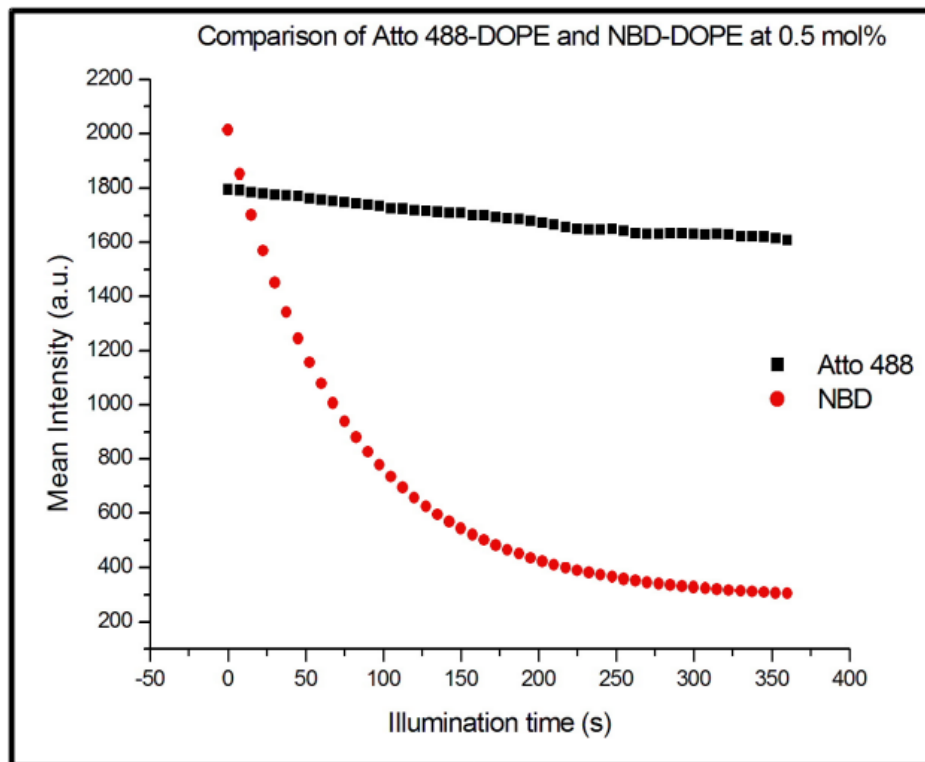


Figure D.1: Comparison of photobleaching between Atto-488-DOPE and NBD-DOPE at 0.5mol% in DOPC GUV.

## Bibliography

- S. Aimon, J. Manzi, D. Schmidt, J. A. P. Larrosa, P. Bassereau, and G. E. Toombes. Functional reconstitution of a voltage-gated potassium channel in giant unilamellar vesicles. *PloS one*, 6(10):e25529, 2011.
- K.-i. Akashi, H. Miyata, H. Itoh, and K. Kinoshita Jr. Preparation of giant liposomes in physiological conditions and their characterization under an optical microscope. *Biophysical journal*, 71(6):3242, 1996.
- R. Allen, G. David, and G. Nomarski. The zeiss-nomarski differential interference equipment for transmitted-light microscopy. *Zeitschrift fur wissenschaftliche Mikroskopie und mikroskopische Technik*, 69(4):193–221, 1969.
- P. F. Almeida, A. Pokorny, and A. Hinderliter. Thermodynamics of membrane domains. *Biochimica et Biophysica Acta (BBA)-Biomembranes*, 1720(1):1–13, 2005.
- T. H. Anderson, Y. Min, K. L. Weirich, H. Zeng, D. Fygenson, and J. N. Israelachvili. Formation of supported bilayers on silica substrates. *Langmuir*, 25(12):6997–7005, 2009.
- M. Angelova, S. Soleau, P. Méléard, F. Faucon, and P. Bothorel. Preparation of giant vesicles by external ac electric fields. kinetics and applications. In *Trends in colloid and interface science VI*, pages 127–131. Springer, 1992.

- M. R. Arnison, K. G. Larkin, C. J. Sheppard, N. I. Smith, and C. J. Cogswell. Linear phase imaging using differential interference contrast microscopy. *Journal of microscopy*, 214(1):7–12, 2004.
- K. Bacia, P. Schwille, and T. Kurzchalia. Sterol structure determines the separation of phases and the curvature of the liquid-ordered phase in model membranes. *Proceedings of the National Academy of Sciences of the United States of America*, 102(9):3272–3277, 2005.
- P. G. Barton and F. Gunstone. Hydrocarbon chain packing and molecular motion in phospholipid bilayers formed from unsaturated lecithins. synthesis and properties of sixteen positional isomers of 1, 2-dioctadecenoyl-sn-glycero-3-phosphorylcholine. *Journal of Biological Chemistry*, 250(12):4470–4476, 1975.
- T. Baumgart, S. T. Hess, and W. W. Webb. Imaging coexisting fluid domains in biomembrane models coupling curvature and line tension. *Nature*, 425(6960):821–824, 2003.
- T. Baumgart, G. Hunt, E. R. Farkas, W. W. Webb, and G. W. Feigenson. Fluorescence probe partitioning between l o/ l d phases in lipid membranes. *Biochimica et Biophysica Acta (BBA)-Biomembranes*, 1768(9): 2182–2194, 2007.
- S. Bavari, C. M. Bosio, E. Wiegand, G. Ruthel, A. B. Will, T. W. Geisbert, M. Hevey, C. Schmaljohn, A. Schmaljohn, and M. J. Aman. Lipid raft microdomains a gateway for compartmentalized trafficking of ebola and marburg viruses. *The Journal of experimental medicine*, 195(5):593–602, 2002.
- J. R. Beattie, S. E. Bell, and B. W. Moss. A critical evaluation of raman spectroscopy for the analysis of lipids: fatty acid methyl esters. *Lipids*, 39(5):407–419, 2004.
- J. R. Beattie, S. E. Bell, C. Borggaard, A. Fearon, and B. W. Moss. Prediction of adipose tissue composition using raman spectroscopy: average properties and individual fatty acids. *Lipids*, 41(3):287–294, 2006.

- T. Bhatia, F. Cornelius, and J. H. Ipsen. Capturing suboptical dynamic structures in lipid bilayer patches formed from free-standing giant unilamellar vesicles. *nature protocols*, 12(8):1563, 2017.
- N. Billecke, G. Rago, M. Bosma, G. Eijkel, A. Gemmink, P. Leproux, G. Huss, P. Schrauwen, M. K. Hesselink, M. Bonn, et al. Chemical imaging of lipid droplets in muscle tissues using hyperspectral coherent raman microscopy. *Histochemistry and cell biology*, 141(3):263–273, 2014.
- D. Birch, M. V. Christensen, D. Staerk, H. Franzyk, and H. M. Nielsen. Fluorophore labeling of a cell-penetrating peptide induces differential effects on its cellular distribution and affects cell viability. *Biochimica et Biophysica Acta (BBA)-Biomembranes*, 1859(12):2483–2494, 2017.
- H. Bouvrais, T. Pott, L. A. Bagatolli, J. H. Ipsen, and P. Méléard. Impact of membrane-anchored fluorescent probes on the mechanical properties of lipid bilayers. *Biochimica et Biophysica Acta (BBA)-Biomembranes*, 1798(7):1333–1337, 2010.
- R. W. Boyd. *Nonlinear optics*. Academic press, 2003.
- J. Bradley, I. Pope, F. Masia, R. Sanusi, W. Langbein, K. Swann, and P. Borri. Quantitative imaging of lipids in live mouse oocytes and early embryos using cars microscopy. *Development*, pages dev–129908, 2016.
- R. E. Brown. Sphingolipid organization in biomembranes: what physical studies of model membranes reveal. *Journal of cell science*, 111(1):1–9, 1998.
- B. Brügger, B. Glass, P. Haberkant, I. Leibrecht, F. T. Wieland, and H.-G. Kräusslich. The hiv lipidome: a raft with an unusual composition. *Proceedings of the National Academy of Sciences of the United States of America*, 103(8):2641–2646, 2006.
- M. R. Bunow and I. W. Levin. Raman spectra and vibrational assignments for deuterated membrane lipids: 1, 2-dipalmitoyl phosphatidylcholine-d9 and-d62. *Biochimica et Biophysica Acta (BBA)-Lipids and Lipid Metabolism*, 489(2):191–206, 1977.

- C. H. Camp Jr, Y. J. Lee, J. M. Heddleston, C. M. Hartshorn, A. R. H. Walker, J. N. Rich, J. D. Lathia, and M. T. Cicerone. High-speed coherent raman fingerprint imaging of biological tissues. *Nature photonics*, 8(8): 627, 2014.
- A. Carmona-Ribeiro. Synthetic amphiphile vesicles. *Chemical Society Reviews*, 21(3):209–214, 1992.
- E. T. Castellana and P. S. Cremer. Solid supported lipid bilayers: From biophysical studies to sensor design. *Surface Science Reports*, 61(10): 429–444, 2006.
- G. Cevc. Transfersomes, liposomes and other lipid suspensions on the skin: permeation enhancement, vesicle penetration, and transdermal drug delivery. *Critical Reviews in Therapeutic Drug Carrier Systems*, 13.
- L. H. Chamberlain. Detergents as tools for the purification and classification of lipid rafts. *FEBS letters*, 559(1-3):1–5, 2004.
- Y.-H. M. Chan and S. G. Boxer. Model membrane systems and their applications. *Current opinion in chemical biology*, 11(6):581–587, 2007.
- R. Chand and R. Srinivasan. Lipid and phospholipids synthesis by fusarium sp. n-9 part iii influence of temperature and ph on the production of fat in the cells of fusarium sp. n-9. 1904.
- S. Chen, D. Bawa, S. Besshoh, J. W. Gurd, and I. R. Brown. Association of heat shock proteins and neuronal membrane components with lipid rafts from the rat brain. *Journal of neuroscience research*, 81(4):522–529, 2005.
- J.-x. Cheng, A. Volkmer, L. D. Book, and X. S. Xie. An epi-detected coherent anti-stokes raman scattering (e-cars) microscope with high spectral resolution and high sensitivity. *The Journal of Physical Chemistry B*, 105(7):1277–1280, 2001.
- J.-X. Cheng, Y. K. Jia, G. Zheng, and X. S. Xie. Laser-scanning coherent anti-stokes raman scattering microscopy and applications to cell biology. *Biophysical journal*, 83(1):502–509, 2002a.

- J.-x. Cheng, A. Volkmer, L. D. Book, and X. S. Xie. Multiplex coherent anti-stokes raman scattering microspectroscopy and study of lipid vesicles. *The Journal of Physical Chemistry B*, 106(34):8493–8498, 2002b.
- J.-X. Cheng, A. Volkmer, and X. S. Xie. Theoretical and experimental characterization of coherent anti-stokes raman scattering microscopy. *JOSA B*, 19(6):1363–1375, 2002c.
- M. Chiba, M. Miyazaki, and S. Ishiwata. Quantitative analysis of the lamellarity of giant liposomes prepared by the inverted emulsion method. *Biophysical journal*, 107(2):346–354, 2014.
- M. Choi and H. Maibach. Liposomes and niosomes as topical drug delivery systems. *Skin pharmacology and physiology*, 18(5):209–219, 2005.
- N. Chumaevskii, M. Rodnikova, and D. Sirotkin. Raman spectra of light and heavy water in the o h and o d stretching vibrations region. *Journal of molecular liquids*, 82(1):39–46, 1999.
- C. J. Cogswell and C. Sheppard. Confocal differential interference contrast (dic) microscopy: including a theoretical analysis of conventional and confocal dic imaging. *Journal of Microscopy*, 165(1):81–101, 1992.
- C. J. Cogswell, N. I. Smith, K. G. Larkin, and P. Hariharan. Quantitative dic microscopy using a geometric phase shifter. In *BiOS'97, Part of Photonics West*, pages 72–81. International Society for Optics and Photonics, 1997.
- A. Colell, C. García-Ruiz, J. M. Lluís, O. Coll, M. Mari, and J. C. Fernández-Checa. Cholesterol impairs the adenine nucleotide translocator-mediated mitochondrial permeability transition through altered membrane fluidity. *Journal of Biological Chemistry*, 278(36):33928–33935, 2003.
- N. Colthup. *Introduction to infrared and Raman spectroscopy*. Elsevier, 2012.
- F. Contreras, L. Sánchez-Magraner, A. Alonso, F. M. Goñi, et al. Transbilayer (flip-flop) lipid motion and lipid scrambling in membranes. *FEBS letters*, 584(9):1779–1786, 2010.

- I. R. Cooke and M. Deserno. Coupling between lipid shape and membrane curvature. *Biophysical journal*, 91(2):487–495, 2006.
- J. M. Crane and L. K. Tamm. Role of cholesterol in the formation and nature of lipid rafts in planar and spherical model membranes. *Biophysical journal*, 86(5):2965–2979, 2004.
- X. Cui, M. Lew, and C. Yang. Quantitative differential interference contrast microscopy based on structured-aperture interference. *Applied Physics Letters*, 93(9):091113, 2008.
- P. R. Cullis, M. J. Hope, and C. P. Tilcock. Lipid polymorphism and the roles of lipids in membranes. *Chemistry and physics of lipids*, 40(2-4):127–144, 1986.
- K. Czamara, K. Majzner, M. Pacia, K. Kochan, A. Kaczor, and M. Baranska. Raman spectroscopy of lipids: a review. *Journal of Raman Spectroscopy*, 46(1):4–20, 2015.
- D. L. Daleke. Phospholipid flippases. *Journal of biological chemistry*, 282(2):821–825, 2007.
- N. Dan and S. Safran. Effect of lipid characteristics on the structure of transmembrane proteins. *Biophysical journal*, 75(3):1410–1414, 1998.
- S. de Castro Araújo and V. M. T. Garcia. Growth and biochemical composition of the diatom *Chaetoceros cf. wighamii* brightwell under different temperature, salinity and carbon dioxide levels. i. protein, carbohydrates and lipids. *Aquaculture*, 246(1-4):405–412, 2005.
- E. F. DeLong and A. A. Yayanos. Adaptation of the membrane lipids of a deep-sea bacterium to changes in hydrostatic pressure. *Science*, 228(4703):1101–1103, 1985.
- W. Demtröder. *Laser Spectroscopy: basic concepts and instrumentation*. Springer-Verlag, 1998.
- P. W. Denny, M. C. Field, and D. F. Smith. Gpi-anchored proteins and glycoconjugates segregate into lipid rafts in kinetoplastida. *FEBS letters*, 491(1-2):148–153, 2001.

- P. F. Devaux. Static and dynamic lipid asymmetry in cell membranes. *Biochemistry*, 30(5):1163–1173, 1991.
- C. Di Napoli, I. Pope, F. Masia, W. Langbein, P. Watson, and P. Borri. Quantitative spatiotemporal chemical profiling of individual lipid droplets by hyperspectral cARS microscopy in living human adipose-derived stem cells. *Analytical chemistry*, 88(7):3677–3685, 2016.
- M. K. Doeven, J. H. Folgering, V. Krasnikov, E. R. Geertsma, G. van den Bogaart, and B. Poolman. Distribution, lateral mobility and function of membrane proteins incorporated into giant unilamellar vesicles. *Biophysical journal*, 88(2):1134–1142, 2005.
- M. D. Duncan, J. Reintjes, and T. Manuccia. Scanning coherent anti-stokes raman microscope. *Optics letters*, 7(8):350–352, 1982.
- M. Edidin, Y. Zagayansky, and T. Lardner. Measurement of membrane protein lateral diffusion in single cells. *Science*, 191(4226):466–468, 1976.
- G. Eesley. Coherent raman spectroscopy. *Journal of Quantitative Spectroscopy and Radiative Transfer*, 22(6):507–576, 1979.
- C. Eggeling, C. Ringemann, R. Medda, G. Schwarzmann, K. Sandhoff, S. Polyakova, V. N. Belov, B. Hein, C. von Middendorff, A. Schönle, et al. Direct observation of the nanoscale dynamics of membrane lipids in a living cell. *Nature*, 457(7233):1159, 2009.
- D. Engelman, T. Steitz, and A. Goldman. Identifying nonpolar transbilayer helices in amino acid sequences of membrane proteins. *Annual review of biophysics and biophysical chemistry*, 15(1):321–353, 1986.
- R. M. Epand. Cholesterol and the interaction of proteins with membrane domains. *Progress in lipid research*, 45(4):279–294, 2006.
- D. J. Estes and M. Mayer. Electroformation of giant liposomes from spin-coated films of lipids. *Colloids and Surfaces B: Biointerfaces*, 42(2):115–123, 2005.
- C. L. Evans and X. S. Xie. Coherent anti-stokes raman scattering microscopy: chemical imaging for biology and medicine. *Annu. Rev. Anal. Chem.*, 1:883–909, 2008.

- J. Fantini and F. J. Barrantes. How cholesterol interacts with membrane proteins: an exploration of cholesterol-binding sites including crac, carc, and tilted domains. *Frontiers in physiology*, 4:31, 2013.
- M. E. Feder and G. E. Hofmann. Heat-shock proteins, molecular chaperones, and the stress response: evolutionary and ecological physiology. *Annual review of physiology*, 61(1):243–282, 1999.
- K. M. Ferguson, M. A. Lemmon, J. Schlessinger, and P. B. Sigler. Structure of the high affinity complex of inositol trisphosphate with a phospholipase c pleckstrin homology domain. *Cell*, 83(6):1037–1046, 1995.
- M. Fidorra, A. Garcia, J. H. Ipsen, S. Härtel, and L. Bagatolli. Lipid domains in giant unilamellar vesicles and their correspondence with equilibrium thermodynamic phases: a quantitative fluorescence microscopy imaging approach. *Biochimica et Biophysica Acta (BBA)-Biomembranes*, 1788(10):2142–2149, 2009.
- A. Filippov, G. Orädd, and G. Lindblom. Sphingomyelin structure influences the lateral diffusion and raft formation in lipid bilayers. *Biophysical journal*, 90(6):2086–2092, 2006.
- C. W. Freudiger, W. Min, B. G. Saar, S. Lu, G. R. Holtom, C. He, J. C. Tsai, J. X. Kang, and X. S. Xie. Label-free biomedical imaging with high sensitivity by stimulated raman scattering microscopy. *Science*, 322(5909):1857–1861, 2008.
- H. Fricke. The electric capacity of suspensions with special reference to blood. *The Journal of general physiology*, 9(2):137–152, 1925a.
- H. Fricke. The electric capacity of suspensions of red corpuscles of a dog. *Physical Review*, 26(5):682, 1925b.
- T. Fujiwara, K. Ritchie, H. Murakoshi, K. Jacobson, and A. Kusumi. Phospholipids undergo hop diffusion in compartmentalized cell membrane. *The Journal of cell biology*, 157(6):1071–1082, 2002.
- S. Funamoto, K. Milan, R. Meili, and R. A. Firtel. Role of phosphatidylinositol 3 kinase and a downstream pleckstrin homology domain-containing

- protein in controlling chemotaxis in *Dictyostelium*. *The Journal of cell biology*, 153(4):795–810, 2001.
- A. Fussell, E. Garbacik, H. Offerhaus, P. Kleinebudde, and C. Strachan. In situ dissolution analysis using coherent anti-stokes raman scattering (cars) and hyperspectral cars microscopy. *European journal of pharmaceuticals and biopharmaceutics*, 85(3):1141–1147, 2013.
- F. Galbiati, B. Razani, and M. P. Lisanti. Emerging themes in lipid rafts and caveolae. *Cell*, 106(4):403–411, 2001.
- A. J. García-Sáez, S. Chiantia, and P. Schwille. Effect of line tension on the lateral organization of lipid membranes. *Journal of Biological Chemistry*, 282(46):33537–33544, 2007.
- O. Garvik, P. Benediktson, A. C. Simonsen, J. H. Ipsen, and D. Wüstner. The fluorescent cholesterol analog dehydroergosterol induces liquid-ordered domains in model membranes. *Chemistry and physics of lipids*, 159(2):114–118, 2009.
- R. B. Gennis. *Biomembranes: molecular structure and function*. Springer Science & Business Media, 2013.
- E. Gorter and F. Grendel. On bimolecular layers of lipoids on the chromocytes of the blood. *The Journal of experimental medicine*, 41(4):439–443, 1925.
- D. R. Graham, E. Chertova, J. M. Hilburn, L. O. Arthur, and J. E. Hildreth. Cholesterol depletion of human immunodeficiency virus type 1 and simian immunodeficiency virus with  $\beta$ -cyclodextrin inactivates and permeabilizes the virions: evidence for virion-associated lipid rafts. *Journal of virology*, 77(15):8237–8248, 2003.
- F. L. Guillot, K. L. Audus, and T. J. Raub. Fluid-phase endocytosis by primary cultures of bovine brain microvessel endothelial cell monolayers. *Microvascular research*, 39(1):1–14, 1990.
- F. D. Gunstone, J. L. Harwood, and A. J. Dijkstra. *The lipid handbook with CD-ROM*. CRC press, 2007.

- B. Guo, K. Tsia, J. Xu, W. Shi, and J. Yao. Broadband enhanced hyperspectral coherent anti-stokes raman scattering by gold shell particles and gold surface. In *Conference on Lasers and Electro-Optics/Pacific Rim*, page 28H1\_2. Optical Society of America, 2015.
- A. E. Hac, H. M. Seeger, M. Fidorra, and T. Heimburg. Diffusion in two-component lipid membranes: a fluorescence correlation spectroscopy and monte carlo simulation study. *Biophysical journal*, 88(1):317–333, 2005.
- I. M. Hafez and P. R. Cullis. Roles of lipid polymorphism in intracellular delivery. *Advanced drug delivery reviews*, 47(2-3):139–148, 2001.
- N. Hain, M. Gallego, and I. Reviakine. Unraveling supported lipid bilayer formation kinetics: osmotic effects. *Langmuir*, 29(7):2282–2288, 2013.
- C. Hamai, P. S. Cremer, and S. M. Musser. Single giant vesicle rupture events reveal multiple mechanisms of glass-supported bilayer formation. *Biophysical journal*, 92(6):1988–1999, 2007.
- A. Hammond, F. Heberle, T. Baumgart, D. Holowka, B. Baird, and G. Feigenson. Crosslinking a lipid raft component triggers liquid ordered-liquid disordered phase separation in model plasma membranes. *Proceedings of the National Academy of Sciences of the United States of America*, 102(18):6320–6325, 2005.
- M. F. Hanzal-Bayer and J. F. Hancock. Lipid rafts and membrane traffic. *FEBS letters*, 581(11):2098–2104, 2007.
- M. Hase, A. Yamada, T. Hamada, D. Baigl, and K. Yoshikawa. Manipulation of cell-sized phospholipid-coated microdroplets and their use as biochemical microreactors. *Langmuir*, 23(2):348–352, 2007.
- J. R. Hazel and S. R. Landrey. Time course of thermal adaptation in plasma membranes of trout kidney. i. headgroup composition. *American Journal of Physiology-Regulatory, Integrative and Comparative Physiology*, 255(4):R622–R627, 1988.
- F. A. Heberle, R. S. Petruzielo, J. Pan, P. Drazba, N. Kucerka, R. F. Standaert, G. W. Feigenson, and J. Katsaras. Bilayer thickness mismatch

- controls domain size in model membranes. *Journal of the American Chemical Society*, 135(18):6853–6859, 2013.
- T. Heimburg. *Thermal biophysics of membranes*. John Wiley & Sons, 2008.
- C. Heinrich, A. Hofer, A. Ritsch, C. Ciardi, S. Bernet, and M. Ritsch-Marte. Selective imaging of saturated and unsaturated lipids by wide-field confocal microscopy. *Optics Express*, 16(4):2699–2708, 2008.
- T. Hellerer, A. M. Enejder, and A. Zumbusch. Spectral focusing: High spectral resolution spectroscopy with broad-bandwidth laser pulses. *Applied Physics Letters*, 85(1):25–27, 2004.
- P. Hinterdorfer and A. Van Oijen. *Handbook of single-molecule biophysics*. Springer Science & Business Media, 2009.
- D. Hoekstra, T. De Boer, K. Klappe, and J. Wilschut. Fluorescence method for measuring the kinetics of fusion between biological membranes. *Biochemistry*, 23(24):5675–5681, 1984.
- W. Hong, C.-S. Liao, H. Zhao, W. Younis, Y. Zhang, M. N. Seleem, and J.-X. Cheng. In situ detection of a single bacterium in complex environment by hyperspectral confocal imaging. *ChemistrySelect*, 1(3):513–517, 2016.
- W. Hubner and A. Blume. Interactions at the lipidwater interface. *Chemistry and Physics of Lipids*, 96(1):99 – 123, 1998. ISSN 0009-3084. doi: [https://doi.org/10.1016/S0009-3084\(98\)00083-8](https://doi.org/10.1016/S0009-3084(98)00083-8). URL <http://www.sciencedirect.com/science/article/pii/S0009308498000838>.
- R. Insall, A. Kuspa, P. J. Lilly, G. Shaulsky, L. R. Levin, W. F. Loomis, and P. Devreotes. Crac, a cytosolic protein containing a pleckstrin homology domain, is required for receptor and G protein-mediated activation of adenylyl cyclase in dictyostelium. *The Journal of Cell Biology*, 126(6):1537–1545, 1994.
- J. H. Ipsen, G. Karlström, O. Mourtsen, H. Wennerström, and M. Zuckermann. Phase equilibria in the phosphatidylcholine-cholesterol system. *Biochimica et Biophysica Acta (BBA)-Biomembranes*, 905(1):162–172, 1987.

- B. S. Isaacs, E. J. Husten, C. T. Esmon, and A. E. Johnson. A domain of membrane-bound blood coagulation factor va is located far from the phospholipid surface. a fluorescence energy transfer measurement. *Biochemistry*, 25(17):4958–4969, 1986.
- J. N. Israelachvili, D. J. Mitchell, and B. W. Ninham. Theory of self-assembly of hydrocarbon amphiphiles into micelles and bilayers. *Journal of the Chemical Society, Faraday Transactions 2: Molecular and Chemical Physics*, 72:1525–1568, 1976.
- J. N. Israelachvili, D. J. Mitchell, and B. W. Ninham. Theory of self-assembly of lipid bilayers and vesicles. *Biochimica et Biophysica Acta (BBA)-Biomembranes*, 470(2):185–201, 1977.
- J. A. Jackman, J.-H. Choi, V. P. Zhdanov, and N.-J. Cho. Influence of osmotic pressure on adhesion of lipid vesicles to solid supports. *Langmuir*, 29(36):11375–11384, 2013.
- K. Jacobson and C. Dietrich. Looking at lipid rafts? *Trends in cell biology*, 9(3):87–91, 1999.
- U. Jakob, M. Gaestel, K. Engel, and J. Buchner. Small heat shock proteins are molecular chaperones. *Journal of Biological Chemistry*, 268(3):1517–1520, 1993.
- A. Jesorka and O. Orwar. Liposomes: technologies and analytical applications. *Annu. Rev. Anal. Chem.*, 1:801–832, 2008.
- J. Juhasz, J. H. Davis, and F. J. Sharom. Fluorescent probe partitioning in giant unilamellar vesicles of lipid raftmixtures. *Biochemical Journal*, 430(3):415–423, 2010.
- L. S. Jung, J. S. Shumaker-Parry, C. T. Campbell, S. S. Yee, and M. H. Gelb. Quantification of tight binding to surface-immobilized phospholipid vesicles using surface plasmon resonance: binding constant of phospholipase a2. *Journal of the American Chemical Society*, 122(17):4177–4184, 2000.

- N. Kahya, E.-I. Pécheur, W. P. de Boeij, D. A. Wiersma, and D. Hoekstra. Reconstitution of membrane proteins into giant unilamellar vesicles via peptide-induced fusion. *Biophysical Journal*, 81(3):1464–1474, 2001.
- A. Karuna, F. Masia, P. Borri, and W. Langbein. Hyperspectral volumetric coherent anti-stokes raman scattering microscopy: quantitative volume determination and nacl as non-resonant standard. *Journal of Raman Spectroscopy*, 2016.
- I. P. Kaur, A. Garg, A. K. Singla, and D. Aggarwal. Vesicular systems in ocular drug delivery: an overview. *International journal of pharmaceutics*, 269(1):1–14, 2004.
- E. Klotzsch and G. J. Schütz. A critical survey of methods to detect plasma membrane rafts. *Philosophical Transactions of the Royal Society of London B: Biological Sciences*, 368(1611):20120033, 2013.
- A. S. Klymchenko and R. Kreder. Fluorescent probes for lipid rafts: from model membranes to living cells. *Chemistry & biology*, 21(1):97–113, 2014.
- W. Knoll, J. Haas, H. B. Stuhrmann, H.-H. Földner, H. Vogel, and E. Sackmann. Small-angle neutron scattering of aqueous dispersions of lipids and lipid mixtures. a contrast variation study. *Journal of Applied Crystallography*, 14(3):191–202, 1981.
- T. Kobayashi, F. Gu, and J. Gruenberg. Lipids, lipid domains and lipid–protein interactions in endocytic membrane traffic. In *Seminars in cell & developmental biology*, volume 9, pages 517–526. Elsevier, 1998.
- R. Krivanek, L. Okoro, and R. Winter. Effect of cholesterol and ergosterol on the compressibility and volume fluctuations of phospholipid-sterol bilayers in the critical point region: a molecular acoustic and calorimetric study. *Biophysical journal*, 94(9):3538–3548, 2008.
- N. Kučerka, J. F. Nagle, J. N. Sachs, S. E. Feller, J. Pencer, A. Jackson, and J. Katsaras. Lipid bilayer structure determined by the simultaneous analysis of neutron and x-ray scattering data. *Biophysical journal*, 95(5):2356–2367, 2008.

- E. C. Lai. Lipid rafts make for slippery platforms. *J Cell Biol*, 162(3):365–370, 2003.
- D. D. Lasic. *Liposomes: from physics to applications*. Elsevier Science Ltd, 1993.
- D. Lasne, G. A. Blab, S. Berciaud, M. Heine, L. Groc, D. Choquet, L. Cognet, and B. Lounis. Single nanoparticle photothermal tracking (snapt) of 5-nm gold beads in live cells. *Biophysical journal*, 91(12):4598–4604, 2006.
- C. Lee and C. D. Bain. Raman spectra of planar supported lipid bilayers. *Biochimica et Biophysica Acta (BBA)-Biomembranes*, 1711(1):59–71, 2005.
- J. Lee, S. Lee, K. Rangunathan, C. Joo, T. Ha, and S. Hohng. Single-molecule four-color fret. *Angewandte Chemie International Edition*, 49(51):9922–9925, 2010.
- J. Lemmich, K. Mortensen, J. H. Ipsen, T. Hønger, R. Bauer, and O. G. Mouritsen. The effect of cholesterol in small amounts on lipid-bilayer softness in the region of the main phase transition. *European biophysics journal*, 25(4):293–304, 1997.
- M. Lemmon and K. Ferguson. Pleckstrin homology domains. In *Protein modules in signal transduction*, pages 39–74. Springer, 1998.
- M. A. LEMMON and K. M. FERGUSON. Signal-dependent membrane targeting by pleckstrin homology (ph) domains. *Biochemical Journal*, 350(1):1–18, 2000.
- C. Lepage, F. Fayolle, M. Hermann, and J. Vandecasteele. Changes in membrane lipid composition of clostridium acetobutylicum during acetone-butanol fermentation: effects of solvents, growth temperature and ph. *Microbiology*, 133(1):103–110, 1987.
- S. S. Leung and J. Thewalt. Link between fluorescent probe partitioning and molecular order of liquid ordered-liquid disordered membranes. *The Journal of Physical Chemistry B*, 121(6):1176–1185, 2017.

- S. S. Leung, J. V. Busto, A. Keyvanloo, F. M. Goñi, and J. Thewalt. Insights into sphingolipid miscibility: separate observation of sphingomyelin and ceramide n-acyl chain melting. *Biophysical journal*, 103(12):2465–2474, 2012.
- H. Li, Z.-x. Yao, B. Degenhardt, G. Teper, and V. Papadopoulos. Cholesterol binding at the cholesterol recognition/interaction amino acid consensus (crac) of the peripheral-type benzodiazepine receptor and inhibition of steroidogenesis by an hiv tat-crac peptide. *Proceedings of the National Academy of Sciences*, 98(3):1267–1272, 2001.
- L. Li, H. Wang, and J.-X. Cheng. Quantitative coherent anti-stokes raman scattering imaging of lipid distribution in coexisting domains. *Biophysical journal*, 89(5):3480–3490, 2005.
- Y. Li-Beisson, B. Shorrosh, F. Beisson, M. X. Andersson, V. Arondel, P. D. Bates, S. Baud, D. Bird, A. DeBono, T. P. Durrett, et al. Acyl-lipid metabolism. *The arabidopsis book*, page e0161, 2013.
- G. Lindblom, G. Orädd, and A. Filippov. Lipid lateral diffusion in bilayers with phosphatidylcholine, sphingomyelin and cholesterol: An nmr study of dynamics and lateral phase separation. *Chemistry and physics of lipids*, 141(1):179–184, 2006.
- D. Lingwood and K. Simons. Lipid rafts as a membrane-organizing principle. *science*, 327(5961):46–50, 2010.
- L. Lins, B. Charlotiaux, C. Heinen, A. Thomas, and R. Brasseur. de novo design of peptides with specific lipid-binding properties. *Biophysical journal*, 90(2):470–479, 2006.
- L. Lis, d. McAlister, N. Fuller, R. Rand, and V. Parsegian. Interactions between neutral phospholipid bilayer membranes. *Biophysical journal*, 37(3):657, 1982.
- J. Liu and J. C. Conboy. 1, 2-diacyl-phosphatidylcholine flip-flop measured directly by sum-frequency vibrational spectroscopy. *Biophysical journal*, 89(4):2522–2532, 2005.

- E. London. Insights into lipid raft structure and formation from experiments in model membranes. *Current opinion in structural biology*, 12(4):480–486, 2002.
- M. Louvel, A. Bordage, C. Da Silva-Cadoux, D. Testemale, E. Lahera, W. Del Net, O. Geaymond, J. Dubessy, R. Argoud, and J.-L. Hazemann. A high-pressure high-temperature setup for in situ raman spectroscopy of supercritical fluids. *Journal of Molecular Liquids*, 205:54–60, 2015.
- P. Maker. Pd maker and rw terhune, phys. rev. 137, a801 (1965). *Phys. Rev.*, 137:A801, 1965.
- H. Martinez-Seara, T. Róg, M. Karttunen, I. Vattulainen, and R. Reigada. Cholesterol induces specific spatial and orientational order in cholesterol/phospholipid membranes. *PloS one*, 5(6):e11162, 2010.
- F. Masia, A. Glen, P. Stephens, P. Borri, and W. Langbein. Quantitative chemical imaging and unsupervised analysis using hyperspectral coherent anti-stokes raman scattering microscopy. *Analytical chemistry*, 85(22):10820–10828, 2013.
- F. Masia, A. Karuna, P. Borri, and W. Langbein. Hyperspectral image analysis for cars, srs, and raman data. *Journal of Raman Spectroscopy*, 46(8):727–734, 2015.
- T. J. McIntosh, S. A. Simon, D. Needham, and C. H. Huang. Structure and cohesive properties of sphingomyelin/cholesterol bilayers. *Biochemistry*, 31(7):2012–2020, 1992.
- S. McLaughlin, G. Szabo, G. Eisenman, and S. Ciani. Surface charge and the conductance of phospholipid membranes. *Proceedings of the National Academy of Sciences*, 67(3):1268–1275, 1970.
- T. P. McMullen, R. N. Lewis, and R. N. McElhaney. Cholesterol–phospholipid interactions, the liquid-ordered phase and lipid rafts in model and biological membranes. *Current opinion in colloid & interface science*, 8(6):459–468, 2004.

- C. McPhee, G. Zorinants, W. Langbein, and P. Borri. Measuring the lamellarity of giant lipid vesicles with differential interference contrast microscopy. *Biophysical journal*, 105(6):1414–1420, 2013.
- K. A. Melkonian, A. G. Ostermeyer, J. Z. Chen, M. G. Roth, and D. A. Brown. Role of lipid modifications in targeting proteins to detergent-resistant membrane rafts many raft proteins are acylated, while few are prenylated. *Journal of Biological Chemistry*, 274(6):3910–3917, 1999.
- P.-E. Milhiet, F. Gubellini, A. Berquand, P. Dosset, J.-L. Rigaud, C. Le Grimmellec, and D. Lévy. High-resolution afm of membrane proteins directly incorporated at high density in planar lipid bilayer. *Biophysical journal*, 91(9):3268–3275, 2006.
- C. R. Miller, B. Bondurant, S. D. McLean, K. A. McGovern, and D. F. O'Brien. Liposome-cell interactions in vitro: effect of liposome surface charge on the binding and endocytosis of conventional and sterically stabilized liposomes. *Biochemistry*, 37(37):12875–12883, 1998.
- E. Mombelli, R. Morris, W. Taylor, and F. Fraternali. Hydrogen-bonding propensities of sphingomyelin in solution and in a bilayer assembly: a molecular dynamics study. *Biophysical journal*, 84(3):1507–1517, 2003.
- C. P. Moon, N. R. Zaccai, P. J. Fleming, D. Gessmann, and K. G. Fleming. Membrane protein thermodynamic stability may serve as the energy sink for sorting in the periplasm. *Proceedings of the National Academy of Sciences*, 110(11):4285–4290, 2013.
- O. Mouritsen and M. Bloom. Mattress model of lipid-protein interactions in membranes. *Biophysical journal*, 46(2):141–153, 1984.
- O. Mouritsen and M. Bloom. Models of lipid-protein interactions in membranes. *Annual review of biophysics and biomolecular structure*, 22(1):145–171, 1993.
- Z. Movasaghi, S. Rehman, and I. U. Rehman. Raman spectroscopy of biological tissues. *Applied Spectroscopy Reviews*, 42(5):493–541, 2007.

- B. Muik, B. Lendl, A. Molina-Díaz, and M. J. Ayora-Cañada. Direct monitoring of lipid oxidation in edible oils by fourier transform raman spectroscopy. *Chemistry and physics of lipids*, 134(2):173–182, 2005.
- S. Mukherjee and F. R. Maxfield. Membrane domains. *Annu. Rev. Cell Dev. Biol.*, 20:839–866, 2004.
- S. Munro. Lipid rafts: elusive or illusive? *Cell*, 115(4):377–388, 2003.
- K. Murase, T. Fujiwara, Y. Umemura, K. Suzuki, R. Iino, H. Yamashita, M. Saito, H. Murakoshi, K. Ritchie, and A. Kusumi. Ultrafine membrane compartments for molecular diffusion as revealed by single molecule techniques. *Biophysical journal*, 86(6):4075–4093, 2004.
- M. Nakamizo, R. Kammereck, and P. Walker Jr. Laser raman studies on carbons. *Carbon*, 12(3):259–267, 1974.
- T. Nakamura and C. Chang. Nanoscale quantitative phase imaging using xor-based x-ray differential interference contrast microscopy. *Ultramicroscopy*, 113:139–144, 2012.
- P. Nandakumar, A. Kovalev, and A. Volkmer. Vibrational imaging based on stimulated raman scattering microscopy. *New Journal of Physics*, 11(3):033026, 2009.
- D. L. Nelson, A. L. Lehninger, and M. M. Cox. *Lehninger principles of biochemistry*. Macmillan, 2008.
- G. J. Nelson. Composition of neutral lipids from erythrocytes of common mammals. *Journal of lipid research*, 8(4):374–379, 1967a.
- G. J. Nelson. Lipid composition of erythrocytes in various mammalian species. *Biochimica et Biophysica Acta (BBA)-Lipids and Lipid Metabolism*, 144(2):221–232, 1967b.
- G. L. Nicolson. The fluidmosaic model of membrane structure: Still relevant to understanding the structure, function and dynamics of biological membranes after more than 40years. *Biochimica et Biophysica Acta (BBA)-Biomembranes*, 1838(6):1451–1466, 2014.

- P. S. Niemelä, S. Ollila, M. T. Hyvönen, M. Karttunen, and I. Vattulainen. Assessing the nature of lipid raft membranes. *PLoS computational biology*, 3(2):e34, 2007.
- T. K. Nyholm, D. Lindroos, B. Westerlund, and J. P. Slotte. Construction of a dopc/psm/cholesterol phase diagram based on the fluorescence properties of trans-parinaric acid. *Langmuir*, 27(13):8339–8350, 2011.
- R. Oda, I. Huc, M. Schmutz, S. Candau, and F. MacKintosh. Tuning bilayer twist using chiral counterions. *Nature*, 399(6736):566, 1999.
- H. Ogiso, M. Taniguchi, and T. Okazaki. Analysis of lipid-composition changes in plasma membrane microdomains. *Journal of lipid research*, 56(8):1594–1605, 2015.
- H. Ohvo-Rekilä, B. Ramstedt, P. Leppimäki, and J. P. Slotte. Cholesterol interactions with phospholipids in membranes. *Progress in lipid research*, 41(1):66–97, 2002.
- L. Opilik, T. Bauer, T. Schmid, J. Stadler, and R. Zenobi. Nanoscale chemical imaging of segregated lipid domains using tip-enhanced raman spectroscopy. *Physical Chemistry Chemical Physics*, 13(21):9978–9981, 2011.
- C. J. Orendorff, M. W. Ducey, and J. E. Pemberton. Quantitative correlation of raman spectral indicators in determining conformational order in alkyl chains. *The Journal of Physical Chemistry A*, 106(30):6991–6998, 2002.
- A. Owyong. High-resolution cw stimulated raman spectroscopy in molecular hydrogen. *Optics letters*, 2(4):91–93, 1978.
- Y. Ozeki, F. Dake, S. Kajiyama, K. Fukui, and K. Itoh. Analysis and experimental assessment of the sensitivity of stimulated raman scattering microscopy. *Optics express*, 17(5):3651–3658, 2009.
- M. Paar, C. Jüngst, N. A. Steiner, C. Magnes, F. Sinner, D. Kolb, A. Lass, R. Zimmermann, A. Zumbusch, S. D. Kohlwein, et al. Remodeling of lipid droplets during lipolysis and growth in adipocytes. *Journal of Biological Chemistry*, 287(14):11164–11173, 2012.

- J. Padawer. The nomarski interference-contrast microscope. an experimental basis for image interpretation. *Journal of the Royal Microscopical Society*, 88(3):305–349, 1968.
- A. Papadopoulos, S. Vehring, I. López-Montero, L. Kutschenko, M. Stöckl, P. F. Devaux, M. Kozlov, T. Pomorski, and A. Herrmann. Flippase activity detected with unlabeled lipids by shape changes of giant unilamellar vesicles. *Journal of Biological Chemistry*, 282(21):15559–15568, 2007.
- B. Pignataro, C. Steinem, H.-J. Galla, H. Fuchs, and A. Janshoff. Specific adhesion of vesicles monitored by scanning force microscopy and quartz crystal microbalance. *Biophysical journal*, 78(1):487–498, 2000.
- E. Ploetz, S. Laimgruber, S. Berner, W. Zinth, and P. Gilch. Femtosecond stimulated raman microscopy. *Applied Physics B*, 87(3):389–393, 2007.
- A. Pokorny, L. E. Yandek, A. I. Elegbede, A. Hinderliter, and P. F. Almeida. Temperature and composition dependence of the interaction of  $\delta$ -lysin with ternary mixtures of sphingomyelin/cholesterol/popc. *Biophysical journal*, 91(6):2184–2197, 2006.
- I. Pope, W. Langbein, P. Watson, and P. Borri. Simultaneous hyperspectral differential-cars, tpf and shg microscopy with a single 5 fs ti: Sa laser. *Optics express*, 21(6):7096–7106, 2013.
- E. Potma, S. Mukamel, J. Cheng, and X. Xie. Coherent raman scattering microscopy. 2012.
- E. O. Potma and X. S. Xie. Detection of single lipid bilayers with coherent anti-stokes raman scattering (cars) microscopy. *Journal of Raman spectroscopy*, 34(9):642–650, 2003.
- E. O. Potma, C. L. Evans, and X. S. Xie. Heterodyne coherent anti-stokes raman scattering (cars) imaging. *Optics letters*, 31(2):241–243, 2006.
- L. R. Poulsen, R. López-Marqués, and M. Palmgren. Flippases: still more questions than answers. *Cellular and molecular life sciences*, 65(20): 3119–3125, 2008.

- K. Qi, Q. Ma, E. E. Remsen, C. G. Clark, and K. L. Wooley. Determination of the bioavailability of biotin conjugated onto shell cross-linked (sck) nanoparticles. *Journal of the American Chemical Society*, 126(21): 6599–6607, 2004.
- P. Quinn, G. Griffiths, and G. Warren. Density of newly synthesized plasma membrane proteins in intracellular membranes ii. biochemical studies. *The Journal of cell biology*, 98(6):2142–2147, 1984.
- M. Rafalski, J. Lear, and W. DeGrado. Phospholipid interactions of synthetic peptides representing the n-terminus of hiv gp41. *Biochemistry*, 29(34): 7917–7922, 1990.
- C. Raman and K. Krishnan.  $h\nu$  o  $h\nu$ . *Nature*, 121:501, 1928.
- B. Ramstedt and J. P. Slotte. Interaction of cholesterol with sphingomyelins and acyl-chain-matched phosphatidylcholines: a comparative study of the effect of the chain length. *Biophysical journal*, 76(2):908–915, 1999.
- W. Rawicz, K. Olbrich, T. McIntosh, D. Needham, and E. Evans. Effect of chain length and unsaturation on elasticity of lipid bilayers. *Biophysical journal*, 79(1):328–339, 2000.
- R. P. Richter, R. Bérat, and A. R. Brisson. Formation of solid-supported lipid bilayers: an integrated view. *Langmuir*, 22(8):3497–3505, 2006.
- H. A. Rinia, M. Bonn, M. Müller, and E. M. Vartiainen. Quantitative cars spectroscopy using the maximum entropy method: the main lipid phase transition. *ChemPhysChem*, 8(2):279–287, 2007.
- I. Rocha-Mendoza, W. Langbein, and P. Borri. Coherent anti-stokes raman microspectroscopy using spectral focusing with glass dispersion. *Applied Physics Letters*, 93(20):201103, 2008.
- T. Róg and M. Pasenkiewicz-Gierula. Cholesterol-sphingomyelin interactions: a molecular dynamics simulation study. *Biophysical journal*, 91(10):3756–3767, 2006.
- G. Rong, H. Wang, and B. M. Reinhard. Insights from a nanoparticle minute: Two-dimensional membrane profiling through silver plasmon ruler tracking. *Nano letters*, 10(1):230–238, 2009.

- J. S. Rossman, X. Jing, G. P. Leser, and R. A. Lamb. Influenza virus m2 protein mediates escrt-independent membrane scission. *Cell*, 142(6): 902–913, 2010.
- K. G. Rothberg, J. E. Heuser, W. C. Donzell, Y.-S. Ying, J. R. Glenney, and R. G. Anderson. Caveolin, a protein component of caveolae membrane coats. *Cell*, 68(4):673–682, 1992.
- B. G. Saar, C. W. Freudiger, J. Reichman, C. M. Stanley, G. R. Holtom, and X. S. Xie. Video-rate molecular imaging in vivo with stimulated raman scattering. *science*, 330(6009):1368–1370, 2010.
- H. Sadeghi-Jorabchi, P. Hendra, R. Wilson, and P. Belton. Determination of the total unsaturation in oils and margarines by fourier transform raman spectroscopy. *Journal of the American Oil Chemists Society*, 67(8):483–486, 1990.
- Y. Saito, T.-a. Ishibashi, and H.-o. Hamaguchi. Polarization-resolved coherent anti-stokes raman scattering (cars) spectroscopy: a new probe of molecular symmetry through accurate determination of the raman depolarization ratio. *Journal of Raman Spectroscopy*, 31(8-9):725–730, 2000.
- M. B. Sankaram and T. E. Thompson. Interaction of cholesterol with various glycerophospholipids and sphingomyelin. *Biochemistry*, 29(47):10670–10675, 1990.
- J. Schindelin, I. Arganda-Carreras, E. Frise, V. Kaynig, M. Longair, T. Pietzsch, S. Preibisch, C. Rueden, S. Saalfeld, B. Schmid, et al. Fiji: an open-source platform for biological-image analysis. *Nature methods*, 9(7):676–682, 2012.
- M. J. Schlesinger et al. Heat shock proteins. *J Biol Chem*, 265(21):12111–12114, 1990.
- C. A. Schneider, W. S. Rasband, K. W. Eliceiri, et al. Nih image to imagej: 25 years of image analysis. *Nat methods*, 9(7):671–675, 2012.
- M. Seitz, E. Ter-Ovanesyan, M. Hausch, C. K. Park, J. A. Zasadzinski, R. Zentel, and J. N. Israelachvili. Formation of tethered supported bilay-

- ers by vesicle fusion onto lipopolymer monolayers promoted by osmotic stress. *Langmuir*, 16(14):6067–6070, 2000.
- A. M. Sendeck, M. F. Poyton, A. J. Baxter, T. Yang, and P. S. Cremer. Supported lipid bilayers with phosphatidylethanolamine as the major component. *Langmuir*, 33(46):13423–13429, 2017.
- E. Sezgin, I. Levental, S. Mayor, and C. Eggeling. The mystery of membrane organization: composition, regulation and roles of lipid rafts. *Nature Reviews Molecular Cell Biology*, 2017.
- L. C. Silva, R. F. de Almeida, B. M. Castro, A. Fedorov, and M. Prieto. Ceramide-domain formation and collapse in lipid rafts: membrane reorganization by an apoptotic lipid. *Biophysical journal*, 92(2):502–516, 2007.
- J. R. Silvius. Thermotropic phase transitions of pure lipids in model membranes and their modifications by membrane proteins. *Lipid-protein interactions*, 2:239–281, 1982.
- N. Simionescu, F. Lupu, and M. Simionescu. Rings of membrane sterols surround the openings of vesicles and fenestrae, in capillary endothelium. *The Journal of cell biology*, 97(5):1592–1600, 1983.
- K. Simons. Functional rafts in cell membranes. nature 38, k., and ikonon, e.(2000). how cells handle cholesterol. *Science*, 290:1721, 1997.
- K. Simons and J. L. Sampaio. Membrane organization and lipid rafts. *Cold Spring Harbor perspectives in biology*, 3(10):a004697, 2011.
- S. J. Singer and G. L. Nicolson. The fluid mosaic model of the structure of cell membranes. *Science*, 175(4023):720–731, 1972.
- N. Skar-Gislinge, J. B. Simonsen, K. Mortensen, R. Feidenhansl, S. G. Sligar, B. Lindberg Møller, T. Bjørnholm, and L. Arleth. Elliptical structure of phospholipid bilayer nanodiscs encapsulated by scaffold proteins: casting the roles of the lipids and the protein. *Journal of the American Chemical Society*, 132(39):13713–13722, 2010.
- J. C. Slater. Atomic radii in crystals. *The Journal of Chemical Physics*, 41(10):3199–3204, 1964.

- M. N. Slipchenko, T. T. Le, H. Chen, and J.-X. Cheng. High-speed vibrational imaging and spectral analysis of lipid bodies by compound raman microscopy. *The Journal of Physical Chemistry B*, 113(21):7681–7686, 2009.
- D. M. Small. Lateral chain packing in lipids and membranes. *Journal of Lipid Research*, 25(13):1490–1500, 1984.
- E. Smith and G. Dent. *Modern Raman spectroscopy: a practical approach*. John Wiley & Sons, 2013.
- G. Socrates. *Infrared and Raman characteristic group frequencies: tables and charts*. John Wiley & Sons, 2001.
- J. C. Stachowiak, E. M. Schmid, C. J. Ryan, H. S. Ann, D. Y. Sasaki, M. B. Sherman, P. L. Geissler, D. A. Fletcher, and C. C. Hayden. Membrane bending by protein–protein crowding. *Nature cell biology*, 14(9):944, 2012.
- L. Stamatatos, R. Leventis, M. J. Zuckermann, and J. R. Silvius. Interactions of cationic lipid vesicles with negatively charged phospholipid vesicles and biological membranes. *Biochemistry*, 27(11):3917–3925, 1988.
- W. K. Subczynski and A. Kusumi. Dynamics of raft molecules in the cell and artificial membranes: approaches by pulse epr spin labeling and single molecule optical microscopy. *Biochimica et Biophysica Acta (BBA)-Biomembranes*, 1610(2):231–243, 2003.
- H. Suzuki, K. V. Tabata, H. Noji, and S. Takeuchi. Electrophysiological recordings of single ion channels in planar lipid bilayers using a poly-methyl methacrylate microfluidic chip. *Biosensors and Bioelectronics*, 22(6):1111–1115, 2007.
- M. Tanaka and E. Sackmann. Polymer-supported membranes as models of the cell surface. *Nature*, 437(7059):656, 2005.
- C. Tanford. Hydrophobic free energy, micelle formation and the association of proteins with amphiphiles. *Journal of molecular biology*, 67(1):59–74, 1972a.

- C. Tanford. Micelle shape and size. *The Journal of Physical Chemistry*, 76 (21):3020–3024, 1972b.
- C. Tanford. The hydrophobic effect and the organization of living matter. *Science*, 200(4345):1012–1018, 1978.
- C. M. Thomas and E. J. Smart. Caveolae structure and function. *Journal of cellular and molecular medicine*, 12(3):796–809, 2008.
- H. Thorn, K. G. Stenkula, M. Karlsson, U. Örtengren, F. H. Nystrom, J. Gustavsson, and P. Strålfors. Cell surface orifices of caveolae and localization of caveolin to the necks of caveolae in adipocytes. *Molecular biology of the cell*, 14(10):3967–3976, 2003.
- L. G. Thygesen, M. M. Løkke, E. Micklander, and S. B. Engelsen. Vibrational microspectroscopy of food. raman vs. ft-ir. *Trends in Food Science & Technology*, 14(1-2):50–57, 2003.
- J. Towey and L. Dougan. Structural examination of the impact of glycerol on water structure. *The Journal of Physical Chemistry B*, 116(5):1633–1641, 2011.
- A. S. Ulrich. Biophysical aspects of using liposomes as delivery vehicles. *Bioscience reports*, 22(2):129–150, 2002.
- A. Urban, M. Fedoruk, M. Horton, J. Radler, F. Stefani, and J. Feldmann. Controlled nanometric phase transitions of phospholipid membranes by plasmonic heating of single gold nanoparticles. *Nano letters*, 9(8):2903–2908, 2009.
- G. van Meer and A. I. P. M. de Kroon. Lipid map of the mammalian cell. *Journal of Cell Science*, 124(1):5–8, 2011. ISSN 0021-9533. doi: 10.1242/jcs.071233. URL <http://jcs.biologists.org/content/124/1/5>.
- G. Van Meer, D. R. Voelker, and G. W. Feigenson. Membrane lipids: where they are and how they behave. *Nature reviews Molecular cell biology*, 9 (2):112–124, 2008.
- T. van Zutphen, V. Todde, R. de Boer, M. Kreim, H. F. Hofbauer, H. Wolinski, M. Veenhuis, I. J. van der Klei, and S. D. Kohlwein. Lipid droplet

- autophagy in the yeast *saccharomyces cerevisiae*. *Molecular biology of the cell*, 25(2):290–301, 2014.
- P. Vandenabeele, B. Wehling, L. Moens, H. Edwards, M. De Reu, and G. Van Hooydonk. Analysis with micro-raman spectroscopy of natural organic binding media and varnishes used in art. *Analytica Chimica Acta*, 407(1):261–274, 2000.
- S. Veatch, I. Polozov, K. Gawrisch, and S. Keller. Liquid domains in vesicles investigated by nmr and fluorescence microscopy. *Biophysical journal*, 86(5):2910–2922, 2004.
- S. L. Veatch and S. L. Keller. Separation of liquid phases in giant vesicles of ternary mixtures of phospholipids and cholesterol. *Biophysical journal*, 85(5):3074–3083, 2003.
- S. L. Veatch and S. L. Keller. Seeing spots: complex phase behavior in simple membranes. *Biochimica et Biophysica Acta (BBA)-Molecular Cell Research*, 1746(3):172–185, 2005.
- S. L. Veatch, S. S. Leung, R. E. Hancock, and J. L. Thewalt. Fluorescent probes alter miscibility phase boundaries in ternary vesicles. *The Journal of Physical Chemistry B*, 111(3):502–504, 2007.
- D. Vind-Kezunovic, C. H. Nielsen, U. Wojewodzka, and R. Gniadecki. Line tension at lipid phase boundaries regulates formation of membrane vesicles in living cells. *Biochimica et Biophysica Acta (BBA)-Biomembranes*, 1778(11):2480–2486, 2008.
- G. Walrafen. Raman spectral studies of water structure. *The Journal of Chemical Physics*, 40(11):3249–3256, 1964.
- B. Wang, L. Zhang, S. C. Bae, and S. Granick. Nanoparticle-induced surface reconstruction of phospholipid membranes. *Proceedings of the National Academy of Sciences*, 105(47):18171–18175, 2008.
- R. Wang, J. T. Kovalchin, P. Muhlenkamp, and R. Y. Chandawarkar. Exogenous heat shock protein 70 binds macrophage lipid raft microdomain and stimulates phagocytosis, processing, and mhc-ii presentation of antigens. *Blood*, 107(4):1636–1642, 2006.

- X. Wang, E. R. Hinson, and P. Cresswell. The interferon-inducible protein viperin inhibits influenza virus release by perturbing lipid rafts. *Cell host & microbe*, 2(2):96–105, 2007.
- L. Wei, Y. Yu, Y. Shen, M. C. Wang, and W. Min. Vibrational imaging of newly synthesized proteins in live cells by stimulated raman scattering microscopy. *Proceedings of the National Academy of Sciences*, 110(28):11226–11231, 2013.
- O. Wesolowska, K. Michalak, J. Maniewska, and A. B. Hendrich. Giant unilamellar vesicles—a perfect tool to visualize phase separation and lipid rafts in model systems. *Acta Biochimica Polonica*, 56(1):33, 2009.
- T. White, S. Bursten, D. Federighi, R. A. Lewis, and E. Nudelman. High-resolution separation and quantification of neutral lipid and phospholipid species in mammalian cells and sera by multi-one-dimensional thin-layer chromatography. *Analytical biochemistry*, 258(1):109–117, 1998.
- T. Wilhein, B. Kaulich, E. Di Fabrizio, F. Romanato, S. Cabrini, and J. Susini. Differential interference contrast x-ray microscopy with submicron resolution. *Applied Physics Letters*, 78(14):2082–2084, 2001.
- R. Wood. Raman spectrum of heavy water. *Physical Review*, 45(6):392, 1934.
- E. Woodbury and W. Ng. Ruby laser operation in near ir, 1962.
- Q. Yang, X.-Y. Liu, S.-i. Ajiki, M. Hara, P. Lundahl, and J. Miyake. Avidin–biotin immobilization of unilamellar liposomes in gel beads for chromatographic analysis of drug–membrane partitioning. *Journal of Chromatography B: Biomedical Sciences and Applications*, 707(1-2):131–141, 1998.
- P. L. Yeagle. *The structure of biological membranes*. CRC press, 2011.
- Y. Yu, P. V. Ramachandran, and M. C. Wang. Shedding new light on lipid functions with cars and srs microscopy. *Biochimica et Biophysica Acta (BBA)-Molecular and Cell Biology of Lipids*, 1841(8):1120–1129, 2014.

- J. Zhao, J. Wu, H. Shao, F. Kong, N. Jain, G. Hunt, and G. Feigenson. Phase studies of model biomembranes: macroscopic coexistence of  $l_{\alpha}+$   $l_{\beta}$ , with light-induced coexistence of  $l_{\alpha}+$   $l_o$  phases. *Biochimica et Biophysica Acta (BBA)-Biomembranes*, 1768(11):2777–2786, 2007.
- Y. Zhou, C. K. Berry, P. A. Storer, and R. M. Raphael. Peroxidation of polyunsaturated phosphatidyl-choline lipids during electroformation. *Bio-materials*, 28(6):1298–1306, 2007.
- A. Zumbusch, G. R. Holtom, and X. S. Xie. Three-dimensional vibrational imaging by coherent anti-stokes raman scattering. *Physical review letters*, 82(20):4142, 1999.

## List of Abbreviations

$L_{\alpha}$	Solid, gel lipid phase
$L_d$	Lipid-liquid disordered phase
$L_o$	Lipid-liquid ordered phase
APTES	(3-Aminopropyl)triethoxysilane
Atto-DOPE [N]	Atto-488 1,2-dioleoyl-sn-glycero-3-phosphoethanolamine
Biotin-DOPE	N-Biotin-1,2-dioleoyl-sn-glycero-3-phosphoethanolamine
CARS	Coherent Anti-Stokes Raman scattering microscopy
dH <sub>2</sub> O	Deionised Water
DIC	Differential interference contrast microscopy
DMSO	Dimethyl Sulfoxide
DOPC	1,2-dioleoyl-sn-glycero-3-phosphocholine
ESM	Egg sphingomyelin
GH	Gentle Hydration method of GUV formation
GUVs	Giant Unilamellar Vesicles
HCARS	Hyperspectral CARS microscopy

- ITO Indium Tin Oxide
- MEM Maximum entropy method of Phase retrieval
- NBD-DOPE Nitro-2-1,3-BenzoxaDiazol-1,2-dioleoyl-sn-glycero-3-phosphoethanolamine
- nNMF non-negative matrix factorisation
- OPO Optical Parametric Oscillator
- PBS Phosphate Buffered Saline
- PCKK phase-corrected Kramers Krönig
- PLBP(s) Planar Lipid Bilayer patch (patches)
- PSM Porcine sphingomyelin
- qDIC Quantitative differential interference contrast microscopy
- sGUV Surface Attached Giant unilamellar vesicles
- SHG Second harmonic generation microscopy
- SRG Stimulated Raman Gain
- SRL Stimulated Raman Loss
- SRS Stimulated Raman Scattering microscopy
- SVD Singular Value Decomposition
- Ti:Sa Titanium-Sapphire
- TPE Two Photon Fluorescence
- TPE Two Photon excitation microscopy

## GNU Free Documentation License

Version 1.3, 3 November 2008

Copyright © 2000, 2001, 2002, 2007, 2008 Free Software Foundation, Inc.

`<https://fsf.org/>`

Everyone is permitted to copy and distribute verbatim copies of this license document, but changing it is not allowed.

### Preamble

The purpose of this License is to make a manual, textbook, or other functional and useful document “free” in the sense of freedom: to assure everyone the effective freedom to copy and redistribute it, with or without modifying it, either commercially or noncommercially. Secondly, this License preserves for the author and publisher a way to get credit for their work, while not being considered responsible for modifications made by others.

This License is a kind of “copyleft”, which means that derivative works of the document must themselves be free in the same sense. It complements the GNU General Public License, which is a copyleft license designed for free software.

We have designed this License in order to use it for manuals for free software, because free software needs free documentation: a free program should come with manuals providing the same freedoms that the software does. But this License is not limited to software manuals; it can be used for any textual work, regardless of subject matter or whether it is published

as a printed book. We recommend this License principally for works whose purpose is instruction or reference.

## 1. APPLICABILITY AND DEFINITIONS

This License applies to any manual or other work, in any medium, that contains a notice placed by the copyright holder saying it can be distributed under the terms of this License. Such a notice grants a world-wide, royalty-free license, unlimited in duration, to use that work under the conditions stated herein. The “**Document**”, below, refers to any such manual or work. Any member of the public is a licensee, and is addressed as “**you**”. You accept the license if you copy, modify or distribute the work in a way requiring permission under copyright law.

A “**Modified Version**” of the Document means any work containing the Document or a portion of it, either copied verbatim, or with modifications and/or translated into another language.

A “**Secondary Section**” is a named appendix or a front-matter section of the Document that deals exclusively with the relationship of the publishers or authors of the Document to the Document’s overall subject (or to related matters) and contains nothing that could fall directly within that overall subject. (Thus, if the Document is in part a textbook of mathematics, a Secondary Section may not explain any mathematics.) The relationship could be a matter of historical connection with the subject or with related matters, or of legal, commercial, philosophical, ethical or political position regarding them.

The “**Invariant Sections**” are certain Secondary Sections whose titles are designated, as being those of Invariant Sections, in the notice that says that the Document is released under this License. If a section does not fit the above definition of Secondary then it is not allowed to be designated as Invariant. The Document may contain zero Invariant Sections. If the Document does not identify any Invariant Sections then there are none.

The “**Cover Texts**” are certain short passages of text that are listed, as Front-Cover Texts or Back-Cover Texts, in the notice that says that the Document is released under this License. A Front-Cover Text may be at most 5 words, and a Back-Cover Text may be at most 25 words.

A “**Transparent**” copy of the Document means a machine-readable copy, represented in a format whose specification is available to the general public, that is suitable for revising the document straightforwardly with generic text editors or (for images composed of pixels) generic paint programs or (for drawings) some widely available drawing editor, and that is suitable for input to text formatters or for automatic translation to a variety of formats suitable for input to text formatters. A copy made in an otherwise Transparent file format whose markup, or absence of markup, has been arranged to thwart or discourage subsequent modification by readers is not Transparent. An image format is not Transparent if used for any substantial amount of text. A copy that is not “Transparent” is called “**Opaque**”.

Examples of suitable formats for Transparent copies include plain ASCII without markup, Texinfo input format, LaTeX input format, SGML or XML using a publicly available DTD, and standard-conforming simple HTML, PostScript or PDF designed for human modification. Examples of transparent image formats include PNG, XCF and JPG. Opaque formats include proprietary formats that can be read and edited only by proprietary word processors, SGML or XML for which the DTD and/or processing tools are not generally available, and the machine-generated HTML, PostScript or PDF produced by some word processors for output purposes only.

The “**Title Page**” means, for a printed book, the title page itself, plus such following pages as are needed to hold, legibly, the material this License requires to appear in the title page. For works in formats which do not have any title page as such, “Title Page” means the text near the most prominent appearance of the work’s title, preceding the beginning of the body of the text.

The “**publisher**” means any person or entity that distributes copies of the Document to the public.

A section “**Entitled XYZ**” means a named subunit of the Document whose title either is precisely XYZ or contains XYZ in parentheses following text that translates XYZ in another language. (Here XYZ stands for a specific section name mentioned below, such as “**Acknowledgements**”, “**Dedications**”, “**Endorsements**”, or “**History**”.) To “**Preserve the Title**” of such a section when you modify the Document means that it remains a section “Entitled XYZ” according to this definition.

The Document may include Warranty Disclaimers next to the notice which states that this License applies to the Document. These Warranty Disclaimers are considered to be included by reference in this License, but only as regards disclaiming warranties: any other implication that these Warranty Disclaimers may have is void and has no effect on the meaning of this License.

## **2. VERBATIM COPYING**

You may copy and distribute the Document in any medium, either commercially or noncommercially, provided that this License, the copyright notices, and the license notice saying this License applies to the Document are reproduced in all copies, and that you add no other conditions whatsoever to those of this License. You may not use technical measures to obstruct or control the reading or further copying of the copies you make or distribute. However, you may accept compensation in exchange for copies. If you distribute a large enough number of copies you must also follow the conditions in section 3.

You may also lend copies, under the same conditions stated above, and you may publicly display copies.

## **3. COPYING IN QUANTITY**

If you publish printed copies (or copies in media that commonly have printed covers) of the Document, numbering more than 100, and the Document's license notice requires Cover Texts, you must enclose the copies in covers that carry, clearly and legibly, all these Cover Texts: Front-Cover Texts on the front cover, and Back-Cover Texts on the back cover. Both covers must also clearly and legibly identify you as the publisher of these copies. The front cover must present the full title with all words of the title equally prominent and visible. You may add other material on the covers in addition. Copying with changes limited to the covers, as long as they preserve the title of the Document and satisfy these conditions, can be treated as verbatim copying in other respects.

If the required texts for either cover are too voluminous to fit legibly, you should put the first ones listed (as many as fit reasonably) on the actual cover, and continue the rest onto adjacent pages.

If you publish or distribute Opaque copies of the Document numbering more than 100, you must either include a machine-readable Transparent copy along with each Opaque copy, or state in or with each Opaque copy a computer-network location from which the general network-using public has access to download using public-standard network protocols a complete Transparent copy of the Document, free of added material. If you use the latter option, you must take reasonably prudent steps, when you begin distribution of Opaque copies in quantity, to ensure that this Transparent copy will remain thus accessible at the stated location until at least one year after the last time you distribute an Opaque copy (directly or through your agents or retailers) of that edition to the public.

It is requested, but not required, that you contact the authors of the Document well before redistributing any large number of copies, to give them a chance to provide you with an updated version of the Document.

## 4. MODIFICATIONS

You may copy and distribute a Modified Version of the Document under the conditions of sections 2 and 3 above, provided that you release the Modified Version under precisely this License, with the Modified Version filling the role of the Document, thus licensing distribution and modification of the Modified Version to whoever possesses a copy of it. In addition, you must do these things in the Modified Version:

- A. Use in the Title Page (and on the covers, if any) a title distinct from that of the Document, and from those of previous versions (which should, if there were any, be listed in the History section of the Document). You may use the same title as a previous version if the original publisher of that version gives permission.
- B. List on the Title Page, as authors, one or more persons or entities responsible for authorship of the modifications in the Modified Version, together with at least five of the principal authors of the Document (all of its principal authors, if it has fewer than five), unless they release you from this requirement.
- C. State on the Title page the name of the publisher of the Modified Version, as the publisher.

- D. Preserve all the copyright notices of the Document.
- E. Add an appropriate copyright notice for your modifications adjacent to the other copyright notices.
- F. Include, immediately after the copyright notices, a license notice giving the public permission to use the Modified Version under the terms of this License, in the form shown in the Addendum below.
- G. Preserve in that license notice the full lists of Invariant Sections and required Cover Texts given in the Document's license notice.
- H. Include an unaltered copy of this License.
- I. Preserve the section Entitled "History", Preserve its Title, and add to it an item stating at least the title, year, new authors, and publisher of the Modified Version as given on the Title Page. If there is no section Entitled "History" in the Document, create one stating the title, year, authors, and publisher of the Document as given on its Title Page, then add an item describing the Modified Version as stated in the previous sentence.
- J. Preserve the network location, if any, given in the Document for public access to a Transparent copy of the Document, and likewise the network locations given in the Document for previous versions it was based on. These may be placed in the "History" section. You may omit a network location for a work that was published at least four years before the Document itself, or if the original publisher of the version it refers to gives permission.
- K. For any section Entitled "Acknowledgements" or "Dedications", Preserve the Title of the section, and preserve in the section all the substance and tone of each of the contributor acknowledgements and/or dedications given therein.
- L. Preserve all the Invariant Sections of the Document, unaltered in their text and in their titles. Section numbers or the equivalent are not considered part of the section titles.

- M. Delete any section Entitled “Endorsements”. Such a section may not be included in the Modified Version.
- N. Do not retitle any existing section to be Entitled “Endorsements” or to conflict in title with any Invariant Section.
- O. Preserve any Warranty Disclaimers.

If the Modified Version includes new front-matter sections or appendices that qualify as Secondary Sections and contain no material copied from the Document, you may at your option designate some or all of these sections as invariant. To do this, add their titles to the list of Invariant Sections in the Modified Version’s license notice. These titles must be distinct from any other section titles.

You may add a section Entitled “Endorsements”, provided it contains nothing but endorsements of your Modified Version by various parties—for example, statements of peer review or that the text has been approved by an organization as the authoritative definition of a standard.

You may add a passage of up to five words as a Front-Cover Text, and a passage of up to 25 words as a Back-Cover Text, to the end of the list of Cover Texts in the Modified Version. Only one passage of Front-Cover Text and one of Back-Cover Text may be added by (or through arrangements made by) any one entity. If the Document already includes a cover text for the same cover, previously added by you or by arrangement made by the same entity you are acting on behalf of, you may not add another; but you may replace the old one, on explicit permission from the previous publisher that added the old one.

The author(s) and publisher(s) of the Document do not by this License give permission to use their names for publicity for or to assert or imply endorsement of any Modified Version.

## 5. COMBINING DOCUMENTS

You may combine the Document with other documents released under this License, under the terms defined in section 4 above for modified versions, provided that you include in the combination all of the Invariant Sections of all of the original documents, unmodified, and list them all as

Invariant Sections of your combined work in its license notice, and that you preserve all their Warranty Disclaimers.

The combined work need only contain one copy of this License, and multiple identical Invariant Sections may be replaced with a single copy. If there are multiple Invariant Sections with the same name but different contents, make the title of each such section unique by adding at the end of it, in parentheses, the name of the original author or publisher of that section if known, or else a unique number. Make the same adjustment to the section titles in the list of Invariant Sections in the license notice of the combined work.

In the combination, you must combine any sections Entitled “History” in the various original documents, forming one section Entitled “History”; likewise combine any sections Entitled “Acknowledgements”, and any sections Entitled “Dedications”. You must delete all sections Entitled “Endorsements”.

## 6. COLLECTIONS OF DOCUMENTS

You may make a collection consisting of the Document and other documents released under this License, and replace the individual copies of this License in the various documents with a single copy that is included in the collection, provided that you follow the rules of this License for verbatim copying of each of the documents in all other respects.

You may extract a single document from such a collection, and distribute it individually under this License, provided you insert a copy of this License into the extracted document, and follow this License in all other respects regarding verbatim copying of that document.

## 7. AGGREGATION WITH INDEPENDENT WORKS

A compilation of the Document or its derivatives with other separate and independent documents or works, in or on a volume of a storage or distribution medium, is called an “aggregate” if the copyright resulting from the compilation is not used to limit the legal rights of the compilation’s users beyond what the individual works permit. When the Document is included

in an aggregate, this License does not apply to the other works in the aggregate which are not themselves derivative works of the Document.

If the Cover Text requirement of section 3 is applicable to these copies of the Document, then if the Document is less than one half of the entire aggregate, the Document's Cover Texts may be placed on covers that bracket the Document within the aggregate, or the electronic equivalent of covers if the Document is in electronic form. Otherwise they must appear on printed covers that bracket the whole aggregate.

## 8. TRANSLATION

Translation is considered a kind of modification, so you may distribute translations of the Document under the terms of section 4. Replacing Invariant Sections with translations requires special permission from their copyright holders, but you may include translations of some or all Invariant Sections in addition to the original versions of these Invariant Sections. You may include a translation of this License, and all the license notices in the Document, and any Warranty Disclaimers, provided that you also include the original English version of this License and the original versions of those notices and disclaimers. In case of a disagreement between the translation and the original version of this License or a notice or disclaimer, the original version will prevail.

If a section in the Document is Entitled "Acknowledgements", "Dedications", or "History", the requirement (section 4) to Preserve its Title (section 1) will typically require changing the actual title.

## 9. TERMINATION

You may not copy, modify, sublicense, or distribute the Document except as expressly provided under this License. Any attempt otherwise to copy, modify, sublicense, or distribute it is void, and will automatically terminate your rights under this License.

However, if you cease all violation of this License, then your license from a particular copyright holder is reinstated (a) provisionally, unless and until the copyright holder explicitly and finally terminates your license, and

(b) permanently, if the copyright holder fails to notify you of the violation by some reasonable means prior to 60 days after the cessation.

Moreover, your license from a particular copyright holder is reinstated permanently if the copyright holder notifies you of the violation by some reasonable means, this is the first time you have received notice of violation of this License (for any work) from that copyright holder, and you cure the violation prior to 30 days after your receipt of the notice.

Termination of your rights under this section does not terminate the licenses of parties who have received copies or rights from you under this License. If your rights have been terminated and not permanently reinstated, receipt of a copy of some or all of the same material does not give you any rights to use it.

## 10. FUTURE REVISIONS OF THIS LICENSE

The Free Software Foundation may publish new, revised versions of the GNU Free Documentation License from time to time. Such new versions will be similar in spirit to the present version, but may differ in detail to address new problems or concerns. See <https://www.gnu.org/licenses/>.

Each version of the License is given a distinguishing version number. If the Document specifies that a particular numbered version of this License “or any later version” applies to it, you have the option of following the terms and conditions either of that specified version or of any later version that has been published (not as a draft) by the Free Software Foundation. If the Document does not specify a version number of this License, you may choose any version ever published (not as a draft) by the Free Software Foundation. If the Document specifies that a proxy can decide which future versions of this License can be used, that proxy’s public statement of acceptance of a version permanently authorizes you to choose that version for the Document.

## 11. RELICENSING

“Massive Multiauthor Collaboration Site” (or “MMC Site”) means any World Wide Web server that publishes copyrightable works and also provides prominent facilities for anybody to edit those works. A public wiki

that anybody can edit is an example of such a server. A “Massive Multi-author Collaboration” (or “MMC”) contained in the site means any set of copyrightable works thus published on the MMC site.

“CC-BY-SA” means the Creative Commons Attribution-Share Alike 3.0 license published by Creative Commons Corporation, a not-for-profit corporation with a principal place of business in San Francisco, California, as well as future copyleft versions of that license published by that same organization.

“Incorporate” means to publish or republish a Document, in whole or in part, as part of another Document.

An MMC is “eligible for relicensing” if it is licensed under this License, and if all works that were first published under this License somewhere other than this MMC, and subsequently incorporated in whole or in part into the MMC, (1) had no cover texts or invariant sections, and (2) were thus incorporated prior to November 1, 2008.

The operator of an MMC Site may republish an MMC contained in the site under CC-BY-SA on the same site at any time before August 1, 2009, provided the MMC is eligible for relicensing.

## **ADDENDUM: How to use this License for your documents**

To use this License in a document you have written, include a copy of the License in the document and put the following copyright and license notices just after the title page:

Copyright © YEAR YOUR NAME. Permission is granted to copy, distribute and/or modify this document under the terms of the GNU Free Documentation License, Version 1.3 or any later version published by the Free Software Foundation; with no Invariant Sections, no Front-Cover Texts, and no Back-Cover Texts. A copy of the license is included in the section entitled “GNU Free Documentation License”.

If you have Invariant Sections, Front-Cover Texts and Back-Cover Texts, replace the “with . . . Texts.” line with this:

with the Invariant Sections being LIST THEIR TITLES, with the Front-Cover Texts being LIST, and with the Back-Cover Texts being LIST.

If you have Invariant Sections without Cover Texts, or some other combination of the three, merge those two alternatives to suit the situation.

If your document contains nontrivial examples of program code, we recommend releasing these examples in parallel under your choice of free software license, such as the GNU General Public License, to permit their use in free software.

## Publications, achievements and conference proceedings

### Conferences and Proceedings

Elements of this work have been presented either in oral or poster presentations at the following conferences:

1. **C.McPhee**, W. Langbein, G.Zorinyants and P. Borri Correlative fluorescence and label-free optical microscopy of model lipid membranes. Oral presentation. Photon 12, Durham University, UK, 3-6 September 2012.
2. **C.McPhee**, W. Langbein, G.Zorinyants and P. Borri. Lipid Phase domains in model membrane systems studied by CARS, Fluorescence and quantitative DIC microscopy. Oral presentation. Photon 14, Imperial College London, UK, 1-4 September 2014.
3. **C.McPhee**, W. Langbein, G.Zorinyants and P. Borri. Lipid Rafts in Giant Unilamellar Vesicles studied by Fluorescence, CARS and quantitative DIC microscopy. Oral Presentation. Econos 2013, University of Exeter, UK, 21-24th April 2013.
4. **C.McPhee**, W. Langbein, G.Zorinyants and P. Borri. Measuring the lamellarity of giant lipid vesicles with DIC microscopy. Poster Presentation. Focus on Microscopy 2013, Maastricht, Netherlands, 24-27 March 2013.

### Academic Achievements

*PUBLICATIONS, ACHIEVEMENTS AND CONFERENCE PROCEEDINGS*264

1. Received Microcors competitive funding of 500 euros to attend FOM 2013 conference in Maastricht.
2. Winner of the second year Ph.D poster and presentation prizes for the Molecular Biosciences research division. May 2013.

**Publications**

Elements of this work have been published in peer reviewed journals:

1. CI McPhee, G Zorinians, W Langbein, and Paola Borri. Measuring the lamellarity of giant lipid vesicles with differential interference contrast microscopy. *Biophysical Journal*, 105(6):1414-1420, 2013.

## Measuring the Lamellarity of Giant Lipid Vesicles with Differential Interference Contrast Microscopy

C. I. McPhee, G. Zorinants,\* W. Langbein, and P. Borri

School of Biosciences and School of Physics and Astronomy, Cardiff University, Cardiff, United Kingdom

**ABSTRACT** Giant unilamellar vesicles are a widely utilized model membrane system, providing free-standing bilayers unaffected by support-induced artifacts. To measure the lamellarity of such vesicles, fluorescence microscopy is one commonly utilized technique, but it has the inherent disadvantages of requiring lipid staining, thereby affecting the intrinsic physical and chemical properties of the vesicles, and it requires a calibration by statistical analysis of a vesicle ensemble. Herein we present what we believe to be a novel label-free optical method to determine the lamellarity of giant vesicles based on quantitative differential interference contrast (qDIC) microscopy. The method is validated by comparison with fluorescence microscopy on a statistically significant number of vesicles, showing correlated quantization of the lamellarity. Importantly, qDIC requires neither sample-dependent calibration nor sample staining, and thus can measure the lamellarity of any giant vesicle without additional preparation or interference with subsequent investigations. Furthermore, qDIC requires only a microscope equipped with differential interference contrast and a digital camera.

### INTRODUCTION

To dissect the complexity of cell membranes and to isolate the behavior of lipid bilayers in simple systems under controlled conditions, giant unilamellar vesicles (GUVs) are widely utilized model systems (1). Compared to supported planar lipid bilayers, GUVs have the advantage of being free-standing, hence free from support-induced artifacts, yet with sufficiently low curvature to well mimic cellular membranes. GUVs have been instrumental in studying fundamental questions in lipid biology, such as the existence of glycosphingolipid- and cholesterol-enriched domains (rafts) in natural membranes and their formation by lipid-lipid interactions (2).

In many studies, where a liposome serves as model system (3) it is preferable that the giant vesicle (GV) should consist of a single lipid bilayer, i.e., be unilamellar, such as an actual cellular membrane. However, formation techniques produce vesicles with a variety of sizes and lamellarities (4). Moreover, vesicles often display inclusions of smaller vesicles, lipid tethers, and membrane fragments, and/or droplets of bulk lipids. It is therefore necessary to be able to measure the membrane thickness of a GV over its entire surface, to identify uniform GUVs.

Optical imaging techniques appear ideally suited to nondestructively assess the shape, size, and uniformity of GVs. Because the thickness of a membrane bilayer (~4 nm) is well below the spatial resolution of optical microscopy ( $\geq 200$  nm), fluorescence intensity measurements have been used (5) to quantify the membrane thick-

ness. However, fluorescence lipid staining can alter the intrinsic physical and chemical properties of the lipid bilayer and is prone to photobleaching (6). It is also limited to measuring the relative lamellarity within an ensemble of GVs under the same staining, excitation, and detection conditions, because the absolute intensity depends on the fluorophore concentration, which is difficult to accurately reproduce between different sample preparations. Furthermore, the assumption that the fluorescence intensity is proportional to the lamellarity requires a homogeneous distribution of the fluorophores in the membranes. In more complex GVs involving lipid mixtures with phase coexistence (2,7), changes in fluorophore concentration between the different phases thus severely complicate lamellarity assessments.

To overcome these limitations, we have developed a believed-novel method for quantitative determination of GV lamellarity based on label-free differential interference contrast (DIC) microscopy. DIC microscopy (8) is a wide-spread tool for observing transparent objects such as living cells and tissues. It measures the difference of the optical phase between two points in the sample plane, spatially separated by an amount typically comparable with the optical resolution. These changes in the optical phase are associated to changes in sample thickness and refractive index. Based on this principle, we have developed a quantitative DIC (qDIC) image acquisition and analysis procedure that enables the measurement of GV lamellarity in a rapid, noninvasive and reproducible way.

A population of GVs was produced using the electroformation method. Their lamellarity was quantified with qDIC on a statistically significant number of GVs ( $n = 77$ ) and exhibited thickness quantization. For direct validation, the

Submitted April 16, 2013, and accepted for publication July 23, 2013.

\*Correspondence: zorinantsg@cardiff.ac.uk

This is an open access article under the CC BY license (<http://creativecommons.org/licenses/by/3.0/>).

Editor: Reinhard Lipowsky.

© 2013 The Authors

0006-3495/13/09/1414/7 \$2.00

<http://dx.doi.org/10.1016/j.bpj.2013.07.048>



lamellarity on the same GVs was measured with fluorescence microscopy and agreement of the quantized lamellarity between the two methods on every investigated GV was found.

## MATERIALS AND METHODS

### Commercial reagents

DOPC (1,2, dioleoyl-3-*sn*-glycero phosphatidylcholine) was purchased from Sigma-Aldrich (Dorset, UK) and used without further purification. A headgroup-modified, fluorescent lipid analog of DOPE (1,2, dioleoyl-3-*sn*-glycero phosphatidyl-ethanolamine) with the fluorophore ATTO-488 was purchased from ATTO TEC (Siegen, Germany). All other chemicals used were from Sigma-Aldrich and were of HPLC grade. Degassed Milli-Q grade water (18.5 MOhm, S. A. S., Molsheim, France) was utilized throughout.

### Electroformation of GUVs

Giant thin-walled vesicles were created using an electroformation protocol based on the initial articles (9,10), which has been modified to increase the GUV yield (see Section S1 in the Supporting Material). A solution of DOPC containing 0.15 mol % ATTO-488 DOPE was applied onto the surface of two tantalum electrodes and dried. The electrodes were then suspended in water and an AC field sequence was applied, leading to formation of GUVs. For the optical microscopy, a 10 $\times$  dilution of the resultant vesicle suspension in Milli-Q grade water (Millipore) was used.

### DIC and fluorescence microscopy

Optical microscopy was performed using an Eclipse Ti-U microscope (Nikon UK Ltd, Kingston upon Thames, UK) and an objective (CFI plan Apochromat  $\lambda$ -series 20 $\times$ , NA 0.75; Nikon). The 1.5 $\times$  magnification multiplier of the Ti-U stand was used. For DIC, illumination was provided by a halogen tungsten lamp (V2-A LL 100 W; Nikon), followed by a blue-green filter (BG40; Galvoptics Ltd, Basildon, UK) to block near-infrared light for which the DIC polarizers do not have sufficient extinction, and a green filter (GIF, transmission band 550  $\pm$  20 nm; Nikon) defining the wavelength range for the qDIC analysis and avoiding fluorophore excitation. A de-Sénarmont compensator was used for offset phase adjustment (a rotatable linear polarizer followed by a fixed  $\lambda/4$  wave-plate, T-P2 DIC Polarizer HT; Nikon), followed by a Wollaston prism (T-C DIC Module High NA N2 Dry; Nikon) in the condenser unit, a Nomarski prism after the objective (D-C DIC Slider 20 $\times$ ; Nikon), and a linear polarizer (Ti-A-E DIC Analyzer Block; Nikon) in the filter turret. Epi-fluorescence microscopy was performed using a metal-halide lamp (Lumen L200/D; Prior Scientific, Rockland, MA) and an exciter/emitter/dichroic filter cube (GFP-A-Basic; Semrock, Rochester, NY) suitable for the ATTO-488 dye.

The vesicle suspension was pipetted into imaging chambers of 500- $\mu$ m height and 20-mm diameter, formed by a microscope slide, an imaging gasket (Grace Bio-Labs, Bend, OR), and a No. 1 24  $\times$  24-mm square coverslip. After mounting onto the microscope, the sample was equilibrated for a minimum of 30 min to reduce convection.

DIC and fluorescence images were acquired using a charge-coupled device camera (Orca 285; Hamamatsu, Hamamatsu City, Japan) with 1344  $\times$  1024 pixels of 6.45- $\mu$ m size. Considering 30 $\times$  magnification, the pixel size corresponds to 0.215  $\mu$ m at the sample plane, which was confirmed by a calibration sample within 0.5% accuracy. The camera has a 12-bit A/D converter, and the images were converted to 16-bit grayscale tiff files. An exposure time of 0.1 s was used for each frame in DIC images, limited by the readout speed, and the illumination intensity was adjusted to provide an average of  $\sim$ 75% of digitizer range, corresponding to  $\sim$ 3.8  $\times$  10<sup>4</sup>

photoelectrons per pixel (at the lowest gain setting of the camera), and a relative shot noise of 0.5%. Whereas the camera has a specified full-well capacity of 18 ke, we found a linear response in the whole range of the camera up to  $\sim$ 50 ke. Fluorescence images were acquired with an exposure time of 2.5 s, resulting in a maximum of  $\sim$ 10<sup>4</sup> photons/pixel for GUVs, leaving dynamic range for higher lamellarities. For each GV, 128 DIC images were acquired for opposite offset phases to analyze noise and movement. qDIC and fluorescence images were focused at the equatorial plane of the GVs. A typical single fluorescence image is shown in Fig. 1 *a*, and a single DIC image is shown in Fig. 1 *c*. Importantly, by performing DIC at 550  $\pm$  20-nm wavelength where the absorption of the ATTO-488 fluorophore label is insignificant (see Section S2 in the Supporting Material), DIC and epi-fluorescence could be applied on exactly the same vesicle without mutual influence.

In general, qDIC requires equipment that is commercially available, affordable, and wide-spread. The essential parts are an optical microscope with DIC, a digital camera with a signal/noise > 100, and a computer to perform the image processing.

### Fluorescence image processing

To quantify the vesicle lamellarity from fluorescence images, we calculated the average intensity in an annulus covering the edge of the vesicle with inner (outer) radius  $R_0 - \rho/2$  ( $R_0 + \rho/2$ ), where  $R_0$  is the vesicle radius and  $\rho = 0.67$   $\mu$ m is given by the optical spatial resolution. We also calculate the average intensity within an inner circle of radius  $R_0 - 4\rho$  and the average intensity outside the vesicle (the background). In this way, we could quantify the average intensity at the edge of the vesicle and the average intensity of the step inside the GV, as shown in Fig. 1 *b*. When fluorescence images contained inclusions and/or stained lipid fragments that were out of focus but were still contributing to the measured signal, we used user-assigned regions to exclude those areas in the image analysis. The averaging procedure and all the following calculations were implemented in MATLAB ver. 2012a (The MathWorks, Natick, MA).

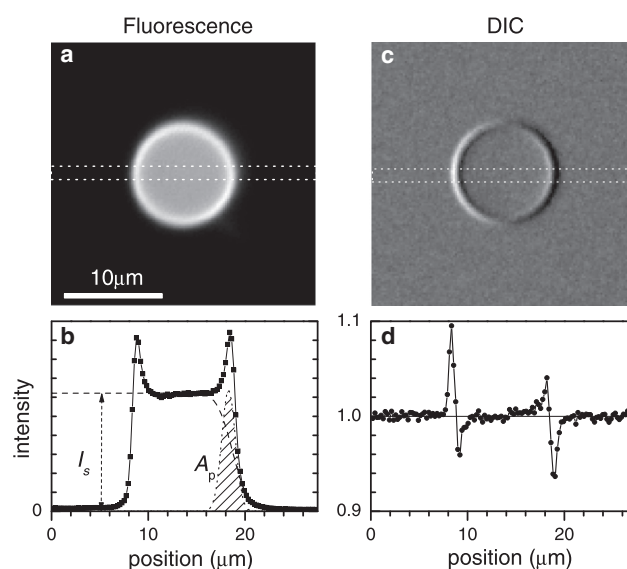


FIGURE 1 Images of a typical GUV made of DOPC labeled with 0.15 mol % DOPE-Atto488: (a) Fluorescence intensity image on a linear grayscale from zero (solid). (b) Fluorescence intensity along the cross-section indicated by the dotted rectangle in panel a. The intensity step  $I_s$  and the edge area  $A_p$  are indicated. (c) DIC image on a linear gray scale from 0.90 $I_0$  (solid) to 1.16 $I_0$  (open), where  $I_0$  is the average intensity outside the GV. (d) DIC profile  $I/I_0$  along the cross-section indicated by the dotted rectangle in panel c.

## DIC CONTRAST IMAGE FORMATION

We start by introducing the DIC contrast and the notations used in the image analysis. The sample is considered as a nonabsorbing object with phase retardation at each point in plane  $\mathbf{r} = (x, y)$  given by the function  $\varphi(\mathbf{r})$ . We use DIC with a de-Sénarmont compensator consisting of a polarizer and a quarter-wave plate in the illumination beam path. The angle  $\theta$  of the polarizer with respect to the fast axis of the  $\lambda/4$  plate is adjustable, resulting in elliptically polarized light after the  $\lambda/4$  plate described as a field vector

$$\mathbf{E}_{\text{in}} = E_0 \frac{1}{\sqrt{2}} \begin{pmatrix} 1 \\ e^{i\psi} \end{pmatrix} \quad (1)$$

with a phase  $\psi = 2\theta$  in the range from  $-\pi$  to  $\pi$ . The Wollaston prism in the back-focal plane of the condenser lens splits the two polarization components in direction, resulting in a shift of the illumination in the sample plane, such that one component passes through the point  $\mathbf{r} + \mathbf{s}/2$ , and the other through the point  $\mathbf{r} - \mathbf{s}/2$ , where  $\mathbf{s}$  is the shear vector and  $\mathbf{r}$  is the DIC image coordinate. We call the phases accumulated by the two beams in the sample  $\varphi_+(\mathbf{r}) = \varphi(\mathbf{r} + \mathbf{s}/2)$  and  $\varphi_-(\mathbf{r}) = \varphi(\mathbf{r} - \mathbf{s}/2)$ . After propagation through the objective lens, the two beams are recombined by a Nomarski prism on the DIC slider, and pass through an analyzer oriented at  $-\pi/4$  so that the final electric field is given by the Jones matrix expression

$$\mathbf{E}_{\text{out}} = \frac{E_0}{2\sqrt{2}} \begin{pmatrix} 1 & -1 \\ -1 & 1 \end{pmatrix} \begin{pmatrix} e^{i\varphi_+} & 0 \\ 0 & e^{i\varphi_-} \end{pmatrix} \begin{pmatrix} 1 \\ e^{i\psi} \end{pmatrix}. \quad (2)$$

The output intensity is thus given by

$$I_{\text{out}}(\mathbf{r}, \psi) = \frac{I_{\text{ex}}}{2} [1 - \cos(\psi - \delta(\mathbf{r}))], \quad (3)$$

with the phase difference  $\delta = \varphi_+ - \varphi_-$  and the excitation intensity  $I_{\text{ex}} \propto E_0^2$ . To reduce the influence of a possible spatial dependence of  $I_{\text{ex}}(\mathbf{r})$ , we acquire two images at opposite angles of the polarizer  $\pm\theta$  resulting in the output intensities  $I_{\pm} = I_{\text{out}}(\mathbf{r}, \pm 2\theta)$ . The contrast image is then defined as  $I_c = (I_+ - I_-)/(I_+ + I_-)$ . If the phase retardation by the sample  $\delta$  is small, as it is the case for GUVs, Eq. 3 can be linearized in  $\delta$ , and for  $\delta \ll \psi < \pi$  the contrast image can be approximated as

$$I_c(\mathbf{r}) = \frac{\sin(\psi)}{1 - \cos(\psi)} \delta(\mathbf{r}) \equiv K(\psi) \delta(\mathbf{r}), \quad (4)$$

with the transduction factor  $K$ . We note that  $K(\pi/2) = 1$  such that for  $\psi = \pi/2$  the contrast is equal to the phase difference. Decreasing  $\psi$  leads to an increase in  $K$ , thus enhancing the measured contrast at the expense of a smaller linear range in  $\delta$ . Choosing  $\psi$  such that  $I_{\text{out}} = \eta I_e$ , i.e., reduced to a fraction  $\eta$  compared to the maximum  $I_e$  reached for  $\psi = \pi$ , we find  $K = \sqrt{1/\eta - 1}$ . In the data shown here, we used

$\eta = 0.05$ , which corresponds to  $K = 4.36$  and a polarizer rotation angle of  $\theta = 12.9^\circ$ , requiring  $\delta < 0.45$  for the validity of Eq. 4, which is fulfilled for the measured GUVs having  $\delta < 0.02$  as visible in Fig. 1 *d*.

## DIC IMAGE ANALYSIS

The image processing was divided into two major parts. In the first part, GVs were identified, centered, and the images were cropped to produce smaller images each containing only one GV (see Section S3 in the [Supporting Material](#)). Rigid GV movements during the acquisition of 128 images for each orientation of the polarizer were corrected by image registration. Averaging over 128 images was performed for noise reduction (see comparison between single acquisition in Fig. 2 *a* and averaging in Fig. 2 *b*) and the contrast image calculated according to Eq. 4. An analysis of the noise showed that a single DIC image with an acquisition time of 100 ms is sufficient to determine the quantized GV lamellarity. In the subsequent image processing, the contrast images were fitted to quantify vesicle lamellarity as detailed in the following subsections.

### DIC model images of giant vesicles

To extract a quantitative measure of the GV lamellarity, we used the simple and rather well-defined geometry of the

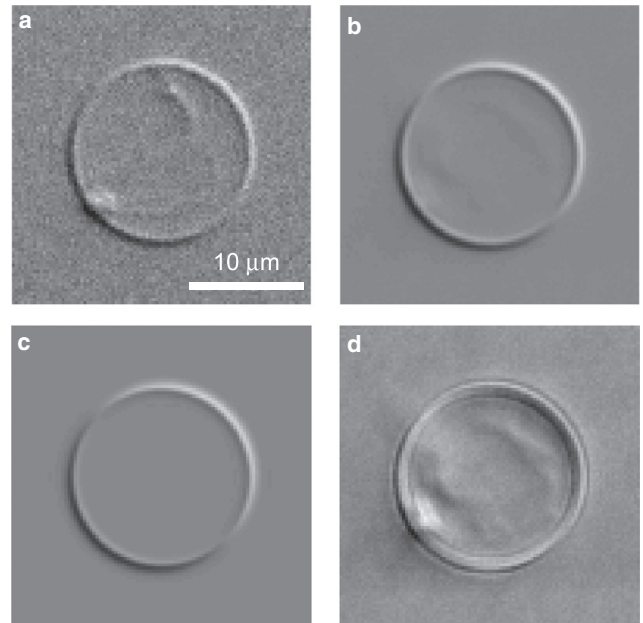


FIGURE 2 (a) Measured DIC of a GUV with a single acquisition. Displayed is the background subtracted and normalized image  $I_+/I_0 - 1$ . (b) Measured DIC contrast image  $I_c$  averaged over 128 acquisitions for each polarizer angle. (c) Simulated DIC image  $I_p$  computed with the best fit parameters. (d) Difference between the measured contrast image *b* and the simulated image *c*. Linear grayscale, solid to open, from  $-0.1$  to  $0.1$  (*a-c*), and from  $-0.02$  to  $0.02$  (*d*).

GVs, being thin, nearly spherical shells. We created a model of the DIC images of GVs and optimized the model parameters to minimize the residuals of the fit. To inform this model, we use the measured epi-fluorescence intensity, which is averaged for each image point over the same light cone as DIC with matched objective and condenser NA, and therefore should be proportional to the phase shift assuming a homogeneously distributed fluorophore in the GV. We have thus modeled the optical phase retardation induced by a GV as

$$\varphi(\mathbf{r}) = \frac{A_p}{w_p \sqrt{\pi}} \exp \left[ - \left( \frac{|\mathbf{r} - \mathbf{R}_c| - R_0}{w_p} \right)^2 \right] + \frac{I_s}{2} \left[ \operatorname{erf} \left( \frac{|\mathbf{r} - \mathbf{R}_c| - R_0}{w_s} \right) + 1 \right], \quad (5)$$

resembling the fluorescence image in Fig. 1 *b*, with an area  $A_p$  under the peak at the vesicle rim and a step height  $I_s$  from the outside to the inside of the GV.  $\mathbf{R}_c$  is the center of the GV,  $R_0$  is its radius, and  $w_p$  and  $w_s$  are the widths of the rim and the step, respectively.

The choice of  $A_p$ , the area of the phase peak at the rim of the vesicle, is aimed at minimizing the effect of distortions of GV. The translational motion of the vesicles as a whole is compensated by the registration procedure (see Section S3.2 in the Supporting Material). A temporally modulated distortion of the membrane shape by a distance less than the optical resolution will, in first-order, lead to an averaging of the phase over the motion, which retains the peak area. GV. showing larger motion are not reproduced by the fit and are discarded by the fit quality cutoff, as discussed in Section S3.2 in the Supporting Material. The step amplitude  $I_s$  is chosen as a fit parameter because it is not affected by small shape fluctuations of the GV. To account for distortions of the vesicles, we introduced an ellipticity in the model using  $|\mathbf{U}(\mathbf{r} - \mathbf{R}_c)|$  in Eq. 5 instead of  $|\mathbf{r} - \mathbf{R}_c|$ , with a matrix  $\mathbf{U}$  given by the ellipticity and its semimajor axis orientation. We found, however, that introducing the ellipticity was not improving the fit, such that we disregarded it in the following.

To model a DIC contrast image, Eq. 5 was used to calculate  $\delta$ . We performed this operation in Fourier domain using the translation property of the Fourier transform  $\mathcal{F}$ ,

$$\mathcal{F}[\delta] = 2i \sin \left( \frac{\mathbf{s} \cdot \mathbf{k}}{2} \right) \mathcal{F}[\varphi]. \quad (6)$$

We used the fast Fourier transform algorithm to reduce the computation time. An example of the resulting model contrast image is shown in Fig. 2 *c*. Adding an elliptical shape of the GV in the model function was evaluated, but did not lead to a better description of the measurements. The model contrast therefore uses a parameter vector  $\mathbf{p}$  with 12 dimensions: the center  $\mathbf{R}_c$ , the mean radius  $R_0$ , the ellipse orientation and eccentricity, the width  $w_p$  and area

$A_p$  of the rim, the width  $w_s$  and height  $I_s$  of the step, the shear vector  $\mathbf{s}$ , and additionally a uniform offset.

### Nonlinear least-squares fitting

For each parameter set  $\mathbf{p}$ , the model contrast image  $I_p = K\delta$  was calculated and the norm of the difference  $\Delta = \|I_c - I_p\|$  to the measured image  $I_c$  was determined. The norm was defined as the sum of the squares of the elements in the two-dimensional image matrix divided by the total number of elements, i.e., the average of the squared elements. The value  $\Delta$  was then minimized over  $\mathbf{p}$  using a downhill simplex method, available as `fminsearch` in MATLAB. This locates a local minimum of an unconstrained multivariable function in a derivative-free algorithm (11). As discussed later, only a subset of parameters was free to vary. A typical residual image  $I_c - I_p$  is shown in Fig. 2 *d* on a scale stretched by a factor of 5 compared to Fig. 2, *a-c*, showing that the residual is small compared to  $I_c$ .

This procedure was applied automatically to measured images of a set of 145 different GV. Some images were not fitted well due to the presence of defects such as inclusions or tethers. The fit was considered successful if  $\|I_c - I_p\|/\|I_c\| < q$ . The fit quality cutoff was chosen to be  $q = 0.5$ , resulting in ~50% successful fits.

## RESULTS AND DISCUSSION

### Lamellarity determined by fluorescence

Fluorescence images were acquired for every GV before DIC as described in Fluorescence Image Processing. The average fluorescence intensity at the vesicle ring, in the inner part (step), and the background outside the GV, are shown in Fig. 3 *a*. The background is virtually constant for all the images, and both the intensity at the ring and in the inner part show clear quantization. The azimuthal intensity at the GV perimeter, within equatorial sections, shows a monotonic increase with vesicle radius consistent with Akashi et al. (5), whereas the intensity in the center relating to the out-of focus polar regions is independent of the radius. This can be attributed to the geometry of the GV and the three-dimensional point-spread function (PSF) of the wide-field fluorescence microscope. When focusing in the sphere center, the area of GV surface within the lateral extension of the PSF grows quadratically with the GV radius. Simultaneously the PSF decays quadratically with the distance from the focus, providing an intensity independent of the GV radius. This is related to the missing sectioning capability of wide-field fluorescence. At the rim instead, the curvature of the GV determines how much GV surface lies within the PSF. We find that the data are consistent with a  $\sqrt{R_0}$  radius dependence, as shown by the dotted lines in Fig. 3 *a*.

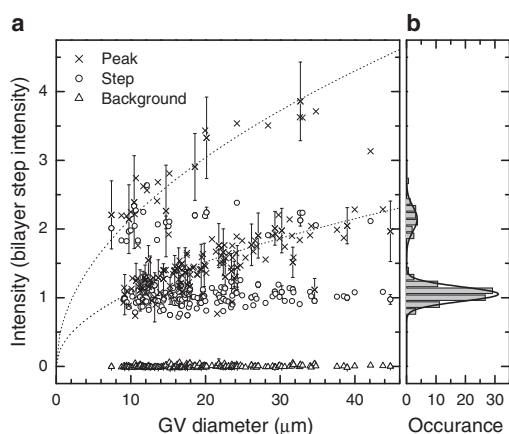


FIGURE 3 Fluorescence of ATTO-488 labeled GV. (a) Intensities of the background, the center, and the peak at the rim of the GV, as labeled; error bars are standard deviations of intensity within the appropriate areas. (b) Histogram of the center intensity with Gaussian fits.

The histogram of the fluorescence intensity at the GV center shown in Fig. 3 *b* reveals a 2:1 ratio of the two observed peaks, indicating the presence of double and single bilayers. The standard error of mean for the single bilayer distribution is  $\sim 1\%$  of the mean value, and its standard deviation is 17%. Using a bilayer thickness of 4 nm, this corresponds to a thickness fluctuation of 0.7 nm. The distinct quantization shown by this fluorescence analysis demonstrates that the electroformation method used allowed us to produce predominantly GUVs and serves as reference to validate our qDIC method.

### Lamellarity quantification using qDIC

To determine the lamellarity from qDIC contrast images  $I_c$ , the fit procedure described in Section S3.2 in the Supporting Material was applied. To achieve convergence, the parameters were initialized, and then sequentially added to the fitted parameters using the following procedure: The GV center  $\mathbf{R}_c$  and radius  $R_0$  were initialized using moments of  $I_c$  as described in Section S3.1 in the Supporting Material. The initial amplitudes  $A_p$  and  $I_s$  were taken to be  $A_p = I_{c,pp} \cdot 0.215 \mu\text{m}$  and  $I_s = 0.3I_{c,pp}$  using the peak-to-peak variation  $I_{c,pp}$  of  $I_c$  over the image. The values  $w_s$  and  $w_p$  were set to the image resolution  $w_s = \lambda/(2NA) \approx 350$  nm and  $w_p = \lambda/(NA) \approx 700$  nm.

The shear vector magnitude was set to  $|\mathbf{s}| = 0.24 \mu\text{m}$ , which was independently determined as described in Section S3.7 in the Supporting Material. The shear vector direction was initially set to  $135^\circ$ , according to the microscope specification. Then, all other model parameters including the shear vector direction were set free, and the fitting was performed for the whole ensemble of the GUVs. The average shear vector direction of  $135.7 \pm 1.1^\circ$  was determined. Fits, the shear vector direction was fixed at  $135.7^\circ$ .

The resulting distribution of  $A_p$  and  $I_s$  showed two branches versus  $R_0$  similar to Fig. 3 *a*, with the radial dependencies of  $A_p \propto \sqrt{R_0}$  and  $I_s$  being constant. Considering the lower branch as corresponding to unilamellar vesicles, we fitted the lower branch data using  $I_s = I_{su}$  and  $A_p = A_{pu}\sqrt{R_0}$ , yielding  $I_{su} = 0.058$  and  $A_{pu} = 0.55/\sqrt{\text{nm}}$  (see Section S3.4 in the Supporting Material). The value of  $I_{su} = 0.058$  corresponds to a phase shift of  $\varphi_u = I_{su}/K = 0.013$ . The phase shift created by a DOPC bilayer is given by  $\varphi_{bl} = 2\pi d(n_{bl} - n_w)/\lambda \approx 0.0064$ , using the thickness (12)  $d = 4$  nm and the refractive indices of a DOPC bilayer for in-plane polarization (12)  $n_{bl} = 1.47$ , and of water  $n_w = 1.333$  at  $\lambda = 550$  nm. We would expect  $\varphi_u = 2\varphi_{bl} = 0.0128$  because the illumination passes through both surfaces of the GUV, which is in agreement with the measured value. We introduce the lamellarity parameter  $L$  giving the number of bilayers as

$$I_s = LI_{su} \text{ and } A_p = LA_{pu}\sqrt{R_0}, \quad (7)$$

because  $A_p$  and  $I_s$  are expected to scale proportional to  $L$ . We then refit the data having now only  $\mathbf{R}_c$ ,  $R_0$ ,  $w_p$ ,  $w_s$ , and  $L$  as free parameters. The result of this fit is given in Fig. 4 and shows quantization of the lamellarity  $L$ . The fit values of  $w_s$  and  $w_p$  were found to be uncorrelated to the other parameters, which we attribute to them being dominated by motion artifacts (blurring) due to dynamical GV distortion by thermal excitation. We note that the above procedure only needs to be done once to determine the instrument parameters  $\mathbf{s}$ ,  $I_{su}$ , and  $A_{pu}$  for a given DIC module, condenser, and objective NA. Once determined, we can measure the lamellarity of any GV repeating only the last fitting step.

The variation of the lamellarity within the two separate groups of points, corresponding to single and double bilayers, was estimated using a Gaussian fit to the histogram shown in Fig. 4 *b*. The standard deviation of  $0.28 \pm 0.02$  in the subset of unilamellar vesicles corresponds to  $\sim 1.1$  nm, well below the thickness of a lipid bilayer, showing

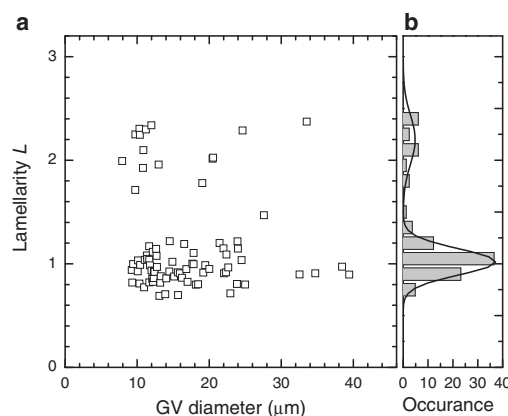


FIGURE 4 Vesicle lamellarity measured by qDIC. (a) Lamellarity as a function of GV diameter. (b) Histogram of the lamellarity; (solid lines) Gaussian fits.

that qDIC is able to identify GUVs. Furthermore, we note that this variation is much larger than the measurement error of  $<0.01$ . It is thus dominated either by systematic errors such as the influence of out-of-focus perturbations, or a non-integer lamellarity of the GVs, i.e., a measured membrane density not consistent with an integer multiple of lipid bilayers. This might arise from membranes incorporating additional lipid or other hydrophobic molecules, or having different order, being stretched, or having subresolution-sized domains of different lamellarities.

The lamellarity obtained by qDIC is correlated in Fig. 5 with the lamellarity obtained using fluorescence given by the fluorescence step intensity normalized to the mean value of the unilamellar distribution (see Fig. 3 b). We find a complete correlation between the lamellarities measured by the two techniques, verifying the validity and accuracy of the qDIC method.

The noise analysis (see Section S3.6 in the Supporting Material) shows that a single DIC image and a shorter exposure down to 1 ms is sufficient to determine the lamellarity, once the microscope has been calibrated. This reduces the sensitivity to drift and allows the measurement of the dynamics of objects, such as motion, vibrations, etc., from which important physical parameters such as membrane stiffness can be retrieved. The fitting model, Eq. 5, presently suited for spherical and elliptical geometries, can be adapted to other geometries. We are currently working on including phase-segregated domains in the membrane into the fit, motivated by the observation of such domains in measured data on GUVs of ternary lipid mixtures (DOPC/Porcine Sphingomyelin/cholesterol with 2:1:1 molar ratio) which showed domains with a 20% higher  $\varphi_u$  of the ordered domains. Even without a specific fitting model, the quantitative analysis can be done using the integration based on Wiener deconvolution (see Section S3.5 in the Supporting

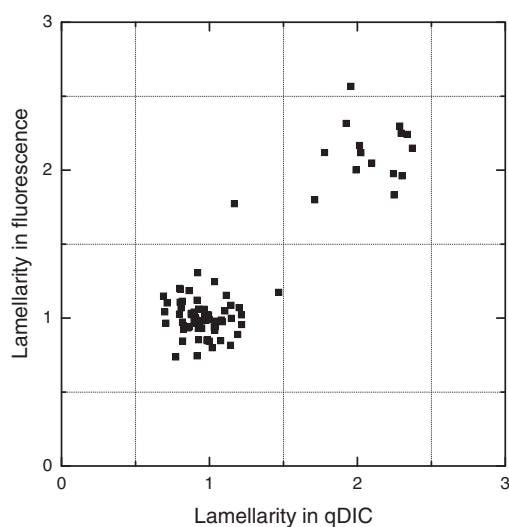


FIGURE 5 GV lamellarity measured by qDIC versus lamellarity measured by fluorescence.

Material). This can be relevant for complex geometries like living cells.

GV systems are often not embedded in pure water, but in aqueous solutions of other substances such as buffers and sugars. The DIC contrast is determined by the refractive index difference between the bilayer and the inside and outside liquid. For equal refractive indices inside and outside, we discuss as example the specific case of a sucrose solution, which has a refractive index of  $n = n_w + kc$ , with the refractive index coefficient  $k = 0.049/\text{M}$  and the molarity  $c$ . Using a 100-mM solution instead of water results in a relative refractive index contrast change of  $-kc/(n_{bl} - n_w) = -4\%$ . Accordingly, the qDIC parameters  $I_{su}$  and  $A_{pu}$  have to be reduced by 4%. We have measured GVs in 100-mM sucrose solution, and the qDIC analysis using the adjusted parameters results in a lamellarity quantization similar to the results in pure water, with GUVs having a lamellarity of  $L = 1.01 \pm 0.15$ . This verifies that qDIC is able to determine the lamellarity of GVs also in homogeneous solutions.

In case inside and outside liquids have different refractive indices, an additional phase contrast component is created which is not considered in our fitting model, Eq. 5. The model can be modified to take such a difference into account, which would allow us to measure both the lamellarity and the refractive index difference. We note that a refractive index difference created by a molarity difference leads also to an osmotic pressure difference. The typical tensile strength of lipid bilayers of  $\tau_{lys} \sim 2 \text{ mN/m}$  (13) allows for a maximum pressure  $p = 2\tau_{lys}/R_0 \sim 400 \text{ Pa}$  (for  $R_0 = 10 \mu\text{m}$ ) before rupture. Although generally osmolarity and molarity are different, we assume in the following discussion that they are equal. This is a good approximation for glucose and sucrose at low concentration, because they do not dissociate in aqueous solution and have an osmotic coefficient equal to unity within a few percent. Using the Morse equation for the osmotic pressure, we find the corresponding excess molarity inside the vesicle as  $\delta_M = 2\tau_{lys}/(TR_A R_0)$  with the gas constant  $R_A$ , yielding, for room temperature  $T = 300 \text{ K}$  and  $R_0 = 10 \mu\text{m}$ , the upper limit of  $\delta_M \sim 0.16 \text{ mM}$ . The resulting additional phase shift across the GV is  $\delta_\varphi = 4\pi R_0 k \delta_M / \lambda$ , which for sucrose yields  $\delta_\varphi = 0.0018$ , much smaller than  $\varphi_u$  and thus negligible, i.e., tolerable osmotic pressure differences do not lead to significant phase shifts. Significant refractive index differences between inside and outside can, however, be created using different solutes with equal osmotic pressure. As example, we consider glucose and sucrose. Assuming equal molarity  $c$  as dictated by the osmotic pressure, the corresponding phase shift is  $\delta_\varphi = 4\pi R_0 \delta_k c / \lambda$  with the refractive index coefficient difference  $\delta_k = 0.024/\text{M}$  between sucrose and glucose. We reach  $\delta_\varphi = \varphi_u$  for a molarity of  $c = \varphi_u \lambda / (4\pi R_0 \delta_k) = 2.4 \text{ mM}$ . We can conclude that for this system we need to take into account  $\delta_\varphi$  in the fit for  $c > 0.5 \text{ mM}$ . We also expect that for  $\delta_\varphi \gg \varphi_u$ , i.e.,  $c > 20 \text{ mM}$ , the error

in the lamellarity determination would be significantly increased, possibly hindering the identification of GUVs.

## CONCLUSIONS

We have demonstrated what we believe to be a novel method (qDIC) to quantify the lamellarity of giant vesicles based on differential interference contrast. We presented an experimental procedure to form a DIC contrast image proportional to the spatial change of the phase retardation at the sample. Fitting a model to the DIC contrast image provides the vesicle lamellarity. The method was validated by comparison with epi-fluorescence microscopy on an ensemble of fluorescently labeled vesicles. Importantly, qDIC is intrinsically label-free, overcoming the inherent drawbacks of fluorescent labeling such as sample modification and photobleaching. Particularly in the context of novel microscopy techniques that have recently emerged to image lipids in a label-free manner, such as coherent anti-Stokes Raman scattering (14,15), the method offers a platform for characterization of vesicle lamellarity compatible with subsequent label-free studies of GUVs. The method is capable to determine the lamellarity from a single DIC image, avoiding motion artifacts and opening up the study of vesicle dynamics. The method is also capable of label-free studies of phase-segregated domains in GUVs of lipid mixtures.

## SUPPORTING MATERIAL

Three sections, references (16–20), and four figures are available at [http://www.biophysj.org/biophysj/supplemental/S0006-3495\(13\)00871-0](http://www.biophysj.org/biophysj/supplemental/S0006-3495(13)00871-0).

The authors acknowledge discussions with John Harwood, and support in setting up the DIC microscopy instrumentation from Iestyn Pope. C.I.M. acknowledges Peter Petrov and co-workers at Exeter University for advice on the electroformation preparation method of GUVs.

This work was funded by the UK Engineering and Physical Sciences Research Council (grant No. EP/I005072/1) and by the UK Biotechnology and Biological Sciences Research Council (grant No. BB/H006575/1).

## REFERENCES

- Chan, Y.-H. M., and S. G. Boxer. 2007. Model membrane systems and their applications. *Curr. Opin. Chem. Biol.* 11:581–587.
- Dietrich, C., L. A. Bagatolli, ..., E. Gratton. 2001. Lipid rafts reconstituted in model membranes. *Biophys. J.* 80:1417–1428.
- Wesołowska, O., K. Michalak, ..., A. B. Hendrich. 2009. Giant unilamellar vesicles—a perfect tool to visualize phase separation and lipid rafts in model systems. *Acta Biochim. Pol.* 56:33–39.
- van Swaay, D., and A. deMello. 2013. Microfluidic methods for forming liposomes. *Lab Chip.* 13:752–767.
- Akashi, K., H. Miyata, ..., K. Kinoshita, Jr. 1996. Preparation of giant liposomes in physiological conditions and their characterization under an optical microscope. *Biophys. J.* 71:3242–3250.
- Satsoura, D., B. Leber, ..., C. Fradin. 2007. Circumvention of fluorophore photobleaching in fluorescence fluctuation experiments: a beam scanning approach. *ChemPhysChem.* 8:834–848.
- Parasassi, T., G. De Stasio, ..., E. Gratton. 1990. Phase fluctuation in phospholipid membranes revealed by Laurdan fluorescence. *Biophys. J.* 57:1179–1186.
- Murphy, D. B. 2002. *Fundamentals of Light Microscopy and Electronic Imaging.* Wiley, New York.
- Dimitrov, D. S., and M. I. Angelova. 1986. Swelling and electroswellling of lipids—theory and experiment. *Studies Biophys.* 113:15–20.
- Angelova, M., S. Soleau, ..., P. Bothorel. 1992. Preparation of giant vesicles by external AC electric fields. Kinetics and applications. *In Trends in Colloid and Interface Science, Vol. VI.* Springer, New York, pp. 127–131.
- Lagarias, J. C., J. A. Reeds, ..., P. E. Wright. 1998. Convergence properties of the Nelder-Mead simplex method in low dimensions. *SIAM J. Optimiz.* 9:112–147.
- Mashaghi, A., M. Swann, ..., E. Reimhult. 2008. Optical anisotropy of supported lipid structures probed by waveguide spectroscopy and its application to study of supported lipid bilayer formation kinetics. *Anal. Chem.* 80:3666–3676.
- Sackmann, E. 1995. Physical basis of self-organization and function of membranes: physics of vesicles. *In Handbook of Biological Physics, Vol. 1.* Elsevier Science, Garching, Germany, pp. 213–304.
- Müller, M., and A. Zumbusch. 2007. Coherent anti-Stokes Raman scattering (CARS) microscopy. *ChemPhysChem.* 8:2156–2170.
- Di Napoli, C., F. Masia, ..., P. Borri. 2012. Chemically specific dual/differential CARS micro-spectroscopy of saturated and unsaturated lipid droplets. *J. Biophotonics.* 10.1002/jbio.201200197.
- Schneider, M., J. Jenkins, and W. Webb. 1984. Thermal fluctuations of large quasi-spherical bimolecular phospholipid vesicles. *J. Phys.* 45:1457–1472.
- Engelhardt, H., H. Duwe, and E. Sackmann. 1985. Bilayer bending elasticity measured by Fourier analysis of thermally excited surface undulations of flaccid vesicles. *J. Phys. Lett. (Fr).* 46:395–400.
- Bracewell, R. 2000. *The Fourier Transform and its Applications*, 3rd Ed. McGraw-Hill Science/Engineering/Math, New York.
- Legarda-Saenz, R., and A. Espinosa-Romero. 2011. Wavefront reconstruction using multiple directional derivatives and Fourier transform. *Opt. Eng.* 50:040501.
- Payne, L. M., W. Langbein, and P. Borri. 2013. Polarization-resolved extinction and scattering cross-section of individual gold nanoparticles measured by wide-field microscopy on a large ensemble. *Appl. Phys. Lett.* 102: 131107–1.

## Supplementary Material

C. I. McPhee, G. Zorinians<sup>1</sup>, W. Langbein\*, P. Borri  
School of Biosciences and  
\*School of Physics and Astronomy,  
Cardiff University, Cardiff CF10 3AX, United Kingdom

<sup>1</sup>Corresponding author. Email: [zorinyantsg@cardiff.ac.uk](mailto:zorinyantsg@cardiff.ac.uk)

## 1 Electroformation of GUVs

Stock lipids were dissolved in 2:1 (v/v) Chloroform:Methanol at 10 g/l except ATTO-488 DOPE which was dissolved at 1 g/l. Stock solutions were stored sealed under Nitrogen at  $-20^{\circ}\text{C}$  until use. For electroformation, 10  $\mu\text{l}$  of a 1 g/l DOPC solution containing 0.15 mol% ATTO-488 DOPE was applied directly onto the surface of two 0.5 mm diameter 2 cm long tantalum electrodes held 3 mm apart by a dielectric spacer. The electrodes were then pre-dried under a stream of nitrogen for approximately 1 minute before evaporation of the organic solvent was completed by placement of the sample under high vacuum for 1 hour. The dried electrodes were then suspended in millipore (18.5 M $\Omega$ ) grade water preheated to  $60^{\circ}\text{C}$  degrees within a 0.5 ml Eppendorf tube. An AC field sequence as given in Table 1) was applied leading to electroformation of GUVs. For the optical microscopy, a  $10\times$  dilution of the resultant vesicle suspension in millipore grade water was used.

$N$	shape	$V_{\text{pp}}$ (V)	$f$ (Hz)	$t$ (mins)
1	square	1.2	10	60
2	sine	1.5	5	30
3	sine	1.5	2	15
4	sine	1.5	1	15

Table 1: Electric voltage sequence for electroformation of GUVs. AC waveforms of given shape, peak to peak voltage  $V_{\text{pp}}$  and frequency  $f$  were applied for a duration  $t$  in the temporal order given by  $N$ .

## 2 Absorption of Atto-488 in DIC

In the present study the GUVs were labeled by 0.15 mol% of fluorescent dye ATTO-488 to determine the lamellarity of the GUVs by both the established fluorescence method and the novel qDIC method. In order to avoid a significant influence of the labeling on the DIC results, we have chosen a dye with weak absorption in the DIC wavelength range 530 – 570 nm. We estimate the residual absorption of the dye in the DIC data as follows. The peak absorption of ATTO-488 is  $\epsilon_{\text{max}} = 90000 \text{ cm}^{-1}\text{M}^{-1} = 9000 \text{ m}^2/\text{mol}$ . The average absorption in the DIC range is 1.3% of the peak value, so that  $\epsilon_{\text{DIC}} = 117 \text{ m}^2/\text{mol}$ , and the resulting absorption cross-section per molecule is  $\sigma = \ln(10)\epsilon_{\text{DIC}}/N_{\text{A}} = 4.48 \times 10^{-4} \text{ nm}^2$ . The density of DOPC bilayers is  $\rho = 780 \text{ kg/m}^3$  (1), and the molecular weight of DOPC is  $\mu = 786D$ , as speci-

fied by the manufacturer (Avanti Polar Lipids, Inc.). Thus, the areal density of DOPC molecules in a  $t = 4.5$  nm thick bilayer is  $\rho t N_A / \mu = 2.69/\text{nm}^2$ , such that the areal density of the 0.15% molar fraction of ATT0-488 fluorophores is  $\rho = 4.03 \times 10^{-3}/\text{nm}^2$ . Taking into account that in DIC the light passes through two bilayers, we arrive at an absorption fraction of  $2\rho\sigma = 3.6 \times 10^{-6}$ . This value is three orders of magnitude below the shot noise in our DIC data (see Sec. 3.6) and thus negligible.

### 3 DIC Image analysis

#### 3.1 Identification of Vesicles

In this study, we measured 145 giant vesicles (GVs). Each DIC image has a size of  $289 \times 220 \mu\text{m}^2$  at the sample, and the GV diameter ranged from 8 to  $45 \mu\text{m}$ . To reduce computer memory usage and to isolate regions containing a single vesicle, all images were re-centred and cropped. The centre of the crop was chosen to be in the centre of the vesicle at the first of the 128 acquisitions, and the size of the square crop was chosen to fully contain the vesicle with one diameter margin to allow for GV drift.

To find the position of the vesicle centre and its radius, a user guided or a fully automated procedure was used. In the user-guided procedure, a Matlab script sequentially shows single DIC images taken at one polarization angle, and the user selects three different points at the GV rim, from which the script determines the GV radius  $R_0$  and center  $\mathbf{R}_c$ .

In the fully automated procedure, the GV centre  $\mathbf{R}_c$  was determined by the first moment of the square of the smoothed intensity  $I_{+\text{sm}}$  which is the first DIC image of the acquisition series smoothed by a low-pass filter (in spatial frequencies) to remove features spatially varying on a scale lower than the resolution (e.g. spikes), and a high-pass filter to eliminate slowly varying background offsets. The center was then determined by

$$\mathbf{R}_c = \frac{\sum \mathbf{r} I_{+\text{sm}}^2}{\sum I_{+\text{sm}}^2}. \quad (1)$$

The radius  $R_0$  was subsequently determined similarly by

$$R_0 = \frac{\sum |\mathbf{r} - \mathbf{R}_c| I_{+\text{sm}}^2}{\sum I_{+\text{sm}}^2}. \quad (2)$$

The size of the cropped image was chosen as  $4R_0$ , increased to reach a pixel number in each dimension being an integer power of two, since array sizes

given by a power of two (typically 128, 256 or 512) are more efficient when performing FFT compared to arbitrary sizes.

### 3.2 Image registration

At room temperature, GVs in aqueous environment are subject to thermal fluctuations (Brownian motion) and drift. The drift is mainly due to convection and was reduced by thermally equilibrating the samples on the microscope and using thin imaging chambers (see methods in main paper Sec. 1.3). The average displacement due to Brownian motion is given by  $\langle x^2 \rangle = 2Dt$  with the observation time of  $t \sim 13$  s from 128 acquisitions at 100 ms. The diffusion constant is given by  $D = (k_B T)/(6\pi R_0 \eta)$  with the Boltzmann constant  $k_B$ , the absolute temperature  $T$ , and the viscosity of water  $\eta$ . Using these expressions we calculate for the GVs investigated in our work an average diffusional displacement of  $0.5 - 1 \mu\text{m}$ . Thermal fluctuations can also cause vibrations, or changes of membrane shape, making it non-spherical. We find that non-sphericity of the investigated GVs negligible when fitting the contrast images, possibly due to the averaging time 13 s being longer than the slowest vibrational dynamics. Vibrational dynamics of the membrane has been studied in literature (2, 3) and is beyond the scope of this paper.

To reduce the effect of GV motion in the subsequent analysis of 128 acquired images (at each phase offset), we performed image registration and averaging. It is important to point out that after developing the qDIC fitting procedure and fixing the instrument dependent parameters, the fit is capable of determining the quantized lamellarity from a single image with an exposure time of only 100 ms (see noise analysis in subsection 3.6), effectively eliminating motion artifacts and the need for image registration.

The registration procedure uses the cross-correlation between the first image and the remaining 127 images. To reduce the influence of shot noise and offsets, the images were low-pass and a high-pass filtered, respectively (4). The filtering was performed in the Fourier domain using the factors  $\exp(-k^2/k_l^2)$  and  $[1 - \exp(-k^2/k_h^2)]$ , for the low- and high-pass filters, respectively. The low-pass edge  $k_l$  was set to the inverse resolution of the microscope  $k_l = 2\pi\text{NA}/\lambda \approx 9 \mu\text{m}^{-1}$  to reduce shot noise, and the a high-pass edge  $k_h$  was set to a value 10 times lower, to reject slowly varying gradients and constant offsets in the background. The cross-correlation was performed using FFT(4). For each cross-correlation, a peak was observed with a size given by the image resolution and the membrane shape. The position of the peak was found by a non-linear least squares fit. The fit

function was empirically chosen to be a two-dimensional Gaussian profile. Using this fitting approach, we found the displacement of the vesicle between the two images with sub-pixel resolution. For all 128 images, the displacement vectors  $\mathbf{d}_i$  ( $i = 1..128$ ) were computed, and the average displacement  $\langle \mathbf{d} \rangle = \langle \mathbf{d}_i \rangle_i$  was calculated. Subsequently, the original images were shifted by  $\langle \mathbf{d} \rangle - \mathbf{d}_i$ , centering the GV in all images to its average center position in the original images. The shift with subpixel precision was done using two-dimensional FFT and the Fourier multiplier  $\exp[i\mathbf{k} \cdot (\langle \mathbf{d} \rangle - \mathbf{d}_i)]$ .

After registration, the 128 images (for the two equal and opposite angles of the polariser) were averaged to yield  $\bar{I}_{\pm}$ . Due to GV membrane distortion dynamics which is not corrected by a rigid shift registration, these average images contain a broadening of the vesicle edge. The fitting parameters in the model of the DIC contrast image describing the edge width  $w_p$  and  $w_s$  were therefore kept free, accounting for this random broadening without influencing the deduced lamellarity.

### 3.3 Contrast image

The two registered averaged images  $\bar{I}_{\pm}$  obtained for the two equal and opposite angles of the polariser  $\pm\theta$  are used to calculate the contrast image  $I_c$ . Since the acquisition of a series of 128 images at one polarizer angle was typically taking  $\sim 13$  s, there was a significant drift during that time, and the two images  $\bar{I}_+$  and  $\bar{I}_-$  showed a displacement, which was corrected using the registration procedure outlined in Sec. 3.2 on  $\bar{I}_{\pm}$ , before the contrast  $I_c$  was calculated. The resulting contrast image is shown in Fig. 2(b). It can be seen that the averaging reduces the stochastic noise significantly compared to a single acquisition shown in Fig. 2(a). Additionally, the contributions of inclusions that can be seen in Fig. 2(a) are blurred due to their movement relative to the GV, reducing their influence in the subsequent analysis.

### 3.4 Lamellarity from peak area and step parameters

The model of the GUV has two adjustable amplitude parameters, the phase step  $I_s$  and the area  $A_p$  under the peak at the edge of the vesicle. Both are expected to be proportional to the lamellarity since they are proportional to the phase change. The radial dependence of  $I_s$  and  $A_p$  is given in Fig. S1, together with fits to the data for the unilamellar branch using  $I_s = I_{su}$  and  $A_p = A_{pu}\sqrt{R_0}$  yielding  $I_{su} = 0.058$  and  $A_{pu} = 0.55\sqrt{\text{nm}}$ . These fits allow us to define a lamellarity from the peak area as  $L_p = A_p/(A_{pu}\sqrt{R_0})$ , and a lamellarity from the step as  $L_s = I_s/I_{su}$ , which are plotted against

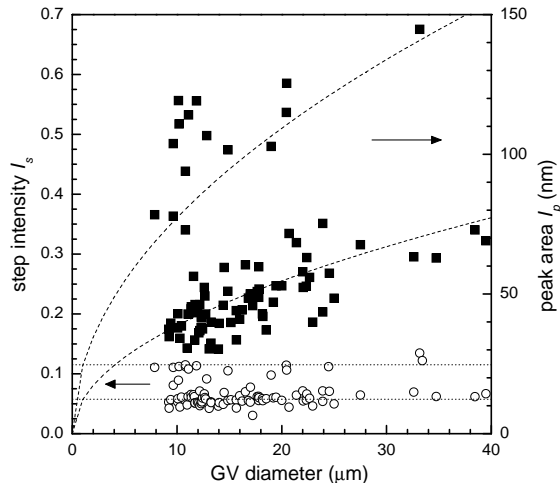


Figure S1: Area  $A_p$  under the peak at the vesicle rim and step amplitude  $I_s$  as obtained from the qDIC analysis of the contrast images in the investigated GVs, plotted versus GV radius  $R_0$ . Fits of the radial dependence are shown as dotted lines.

each other in Fig. S2. They show a significant correlation, supporting our expectation that both are measuring one common lamellarity  $L = L_p = L_s$ , and justifying the use of a single parameter  $L$  in the paper in Eq.(7).

We have fitted the amplitude parameters to the unilamellar vesicles as shown in Fig. S1. The comparison of the predicted bilamellar behavior is thus not a fit, but a prediction. Fitting the amplitude parameter using the bilamellar data would result in a amplitude parameter which is about 10% larger. We attribute this to a small non-linearity of the DIC measurement which was optimized for high contrast for the unilamellar GVs using the phase offset of  $\theta = 12.9^\circ$ . A better linearity would be observed for  $\theta = 45^\circ$ , but this would reduce the contrast by a factor of 4.36, as discussed in the paper, Sec. 2.

### 3.5 Integration in the Fourier-domain

Complementary to fitting the DIC contrast, we performed digital "integration" of the DIC contrast images to obtain the absolute phase of the images. More precisely, we performed a transformation, inverse to the DIC-like transform, see Eq.(6) in the main paper. The Fourier multiplier of the DIC-like

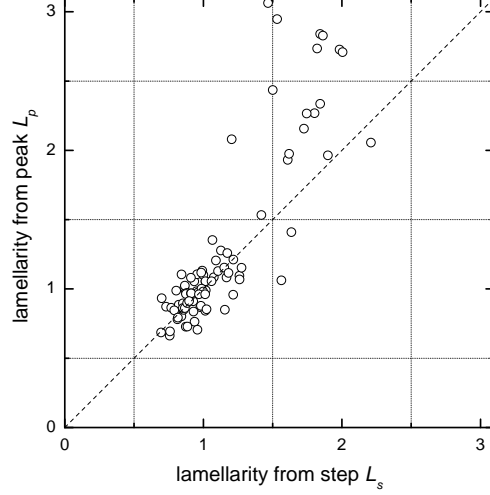


Figure S2: Vesicle lamellarity  $L_p$  and  $L_s$  obtained in the qDIC fit.

transform is

$$\xi = 2i \sin\left(\frac{\mathbf{s} \cdot \mathbf{k}}{2}\right). \quad (3)$$

To do the inverse transformation, we performed a Wiener deconvolution by applying the Fourier multiplier

$$G(\mathbf{k}) = \frac{1}{\xi + \frac{1}{\kappa \xi^*}}. \quad (4)$$

Wiener deconvolution minimizes the RMS deviation of the deconvolved image for a given signal to noise ratio  $\kappa$ , which we assume to be independent of  $\mathbf{k}$ . An example of a resulting integrated phase image of a GUV is shown in Fig. S3, reproducing the fluorescence image of Fig. 1. When the signal-to-noise ratio is relatively small,  $\kappa = 100$ , see Fig. 1(a), the integrated image shows very few integration artefacts (diagonal stripes), but the deconvolution procedure reduces the long-term Fourier components of the image, i.e. it works as a high-pass filter. Therefore, the step-wise shape of the GV is not reproduced. Assuming a significantly higher  $\kappa = 10^4$ , it is possible to demonstrate the stepwise increase of phase at the edge of the GV, but this comes at the expense of long-term stripes parallel to the shear vector (see Fig. 1(b)). Due to the missing information orthogonal to the shear, the phase reconstruction is bound to have artifacts, as is known from other

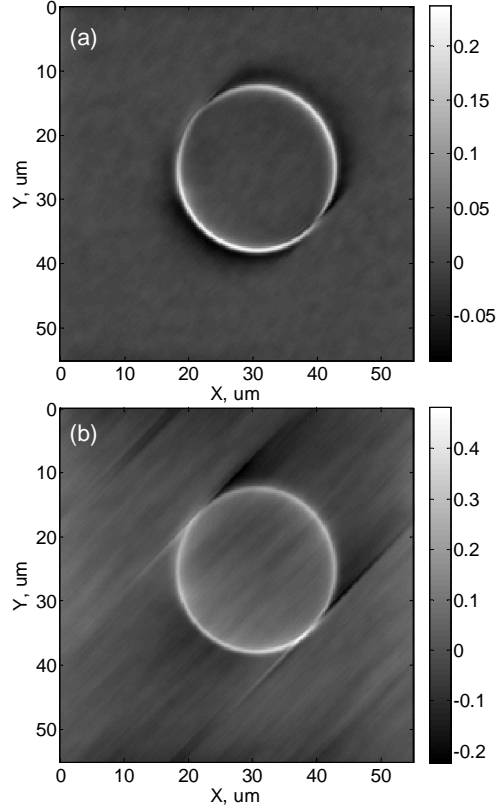


Figure S3: Integrated DIC image of a typical GUV. The signal-to-noise parameter  $\kappa$  is 100 (a) and  $10^4$ (b).

works on DIC phase retrieval (5). A direct fit of the DIC contrast with a specific model function is therefore a more reliable approach which we have chosen for the determination of the lamellarity.

### 3.6 Noise analysis

In the qDIC analysis we used an average over 128 images for each polarizer angle in order to reduce shot noise. To analyze the errors in the lamellarity as function of the number of images averaged, we have divided the 128 images into  $2^{7-n}$  subsets of  $N_n = 2^n$  sequential images each, for different integers  $n$  between 0 and 5. For each subset, we performed registration,

averaging, and qDIC fitting, resulting in  $2^{7-n}$  values of the lamellarity  $L$ . The standard deviation  $\sigma_n$  of this ensemble of lamellarities is shown versus  $n$  in Fig. S4.

If the noise in the individual images would be independent and uncorrelated, as for example shot noise, we would find  $\sigma_n = \sigma_u/\sqrt{N_n}$  (see dotted line in Fig. S4), which is not consistent with the measurements. This shows the presence of fluctuations which are correlated between the subsets, for example due to slow vesicle distortions, giving a drift during the measurement time. Analysis of all fitting parameters as a function of time shows that the position of the particle does drift, even after being compensated for by the registration procedure. The overall image offset also drifts within the experiment time; this is associated with the thermal instability of the light source. However, the lamellarity parameter shows stochastic behaviour very close to the normal distribution. The kurtosis of the particular set of 128 fitted lamellarities is  $-0.3$ , the histogram is well fitted by a Gaussian profile, and the Kolmogorov-Smirnov test implemented by the Matlab function `kstest` shows that the lamellarity distribution is normal at 95% significance level.

We can phenomenologically model this additional contribution as  $\sigma_c$  independent of the averaging, yielding  $\sigma_n = \sqrt{\sigma_c^2 + \sigma_u^2/N_n}$ . The data are reproduced for a shot-noise related  $\sigma_u = 10^{-2}$  of a single exposure, and a drift related  $\sigma_c = 6.5 \times 10^{-3}$  for the given example. The shot noise contribution to the lamellarity of a single image pair is thus 0.01, corresponding to a thickness error of 0.04 nm. This allows for a distinction between the unilamellar GVs and thicker membranes even with a single acquisition.

### 3.7 Shear vector magnitude calibration

For quantitative integration of the DIC images the shear  $\mathbf{s}$  need to be known. The direction of the shear is typically diagonal in the images and is obvious from the DIC contrast. The magnitude  $|\mathbf{s}|$  instead is not obvious, and a specification was not obtainable from the manufacturer Nikon. We have therefore measured  $|\mathbf{s}|$ . We used a calibration sample consisting of 100 nm diameter colloidal gold nanoparticles (GNPs), covalently bound to a glass coverslip and immersed in an index-matching fluid. These GNPs have a large extinction cross-section of about  $30000 \text{ nm}^2$  in the green wavelength range (6), such that they produce diffraction-limited dark spots in the transmission image of more than 10% contrast. The sample was installed in the DIC microscope.

We removed the De Senarmont compensator and the DIC Module from the condenser and inserted a linear polariser in the illumination beam, while

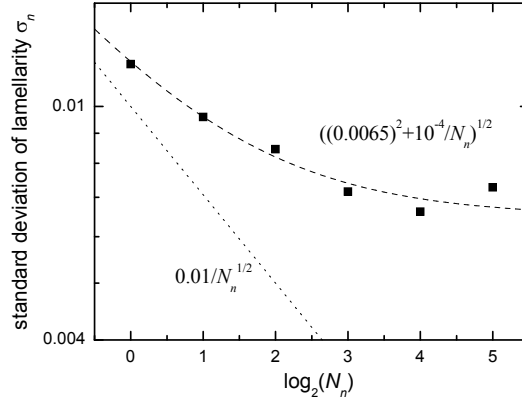


Figure S4: Standard deviation of the lamellarity  $\sigma_n$  as a function of the number of averaged images  $N_n = 2^n$ . Squares: Measurements. Dashed line: expected dependence from shot noise. Dotted line: combination of shot noise and drift. Corresponding formulas are given.

we kept the DIC slider and the analyzer in the detection path. Polarizing the illumination along or orthogonal to the optical axis of the DIC slider, we select the two differently deflected beam paths, leading to an image shift equal to the shear. The shift between the two images of the same GNP was then analyzed using cross-correlation. In detail, a small area of about  $3 \mu\text{m}$  size around each GNP was cropped, and the position of the cross-correlation maximum of this area was found by fitting with a two-dimensional circular symmetric Gaussian profile. In the fitting, the zero-shift value was disregarded as it contains static pixel to pixel variations, and the shear vector direction was fixed to  $135^\circ$ . This procedure was performed for a set of 32 individual single GNPs randomly spread over the field of view, and the shear magnitude was averaged, yielding a value of  $|\mathbf{s}| = (0.24 \pm 0.01) \mu\text{m}$ .

## References

1. Reviakine, I., F. F. Rossetti, A. N. Morozov, and M. Textor, 2005. Investigating the properties of supported vesicular layers on titanium dioxide by quartz crystal microbalance with dissipation measurements. *The Journal of chemical physics* 122:204711.
2. Schneider, M., J. Jenkins, and W. Webb, 1984. Thermal fluctuations

- of large quasi-spherical bimolecular phospholipid vesicles. *Journal de Physique* 45:1457–1472.
3. Engelhardt, H., H. Duwe, and E. Sackmann, 1985. Bilayer bending elasticity measured by Fourier analysis of thermally excited surface undulations of flaccid vesicles. *Journal de Physique Lettres* 46:395–400.
  4. Bracewell, R., 2000. The Fourier transform & its applications. McGraw-Hill Science/Engineering/Math, 3 edition.
  5. Legarda-Saenz, R., and A. Espinosa-Romero, 2011. Wavefront reconstruction using multiple directional derivatives and Fourier transform. *Optical Engineering* 50:040501.
  6. Payne, L. M., W. Langbein, and P. Borri, 2013. Polarization-resolved extinction and scattering cross-section of individual gold nanoparticles measured by wide-field microscopy on a large ensemble. *Appl. Phys. Lett.* 102:131107–1.

# Measuring the lamellarity of Giant lipid vesicles with DIC microscopy

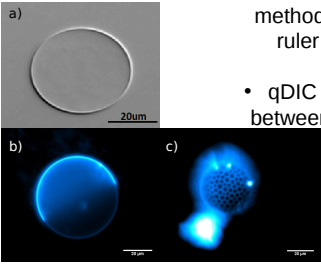
Craig McPhee<sup>1</sup>, George Zorinians<sup>1</sup>, Wolfgang Langbein<sup>2</sup> & Paola Borri<sup>1</sup>

<sup>1</sup>School of Biosciences, <sup>2</sup>School of Physics and Astronomy, Cardiff University, United Kingdom

E-mail: McPheeci1@cf.ac.uk

## Introduction

- Giant Unilamellar vesicles comprise an excellent model with which to study the thermodynamic properties of cellular lipid membranes.
- Conventional techniques for establishing giant vesicle (GV) lamellarity are either invasive and / or perturbative.



- We demonstrate a novel label-free microscopy method functioning as a molecular level optical ruler : **quantitative differential interference microscopy (qDIC)**.
- qDIC determines axial thickness differences between GV samples to a nm level of precision.

Giant unilamellar vesicles incorporating the fluorescent lipid analogue ATTO-488 DOPE, imaged under : a) DIC, b) and c) Epi-Fluorescence

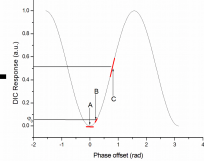
## Implementation

Using standard De Senarmont compensated DIC optics; images captured at equal and opposite initial phase offsets are combined to yield qDIC contrast images with high contrast, low noise & encoding a linear phase response.

Non-linear DIC response:

$$I = \left\{ \sin \left( \frac{\partial \varphi}{\partial x} \frac{\Delta}{2} + \frac{\varphi_0}{2} \right) \right\}^2$$

Where:  
Δ = Shear displacement  
φ = Object phase distribution  
φ<sub>0</sub> = Initial phase offset



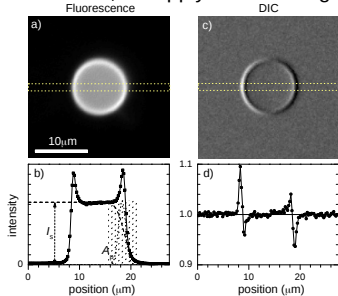
Under our qDIC regime two sets of images are acquired at B (±12.9°, 1, & 1).

Nascent linear qDIC response:

$$C = \frac{I_+ - I_-}{I_+ + I_-} = \frac{\sin \varphi_0}{1 - \cos \varphi_0} \cdot \frac{\partial \varphi}{\partial x} \cdot \Delta$$

A qDIC contrast image is then formed, it possesses zero mean offset and linear phase response.

In order to minimise noise effects and to accurately extract object phase information; we apply automated global fitting and optimisation procedures.



System responses for same vesicle imaged under:

- EPI-Fluorescence,
- DIC contrast image,
- Fluorescence profile,
- qDIC response profile.

Image c) is used for direct lamellarity extraction via fitting of an empirically determined model function.

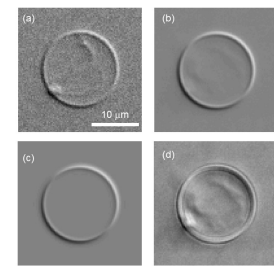


Image analysis methods:

- Single DIC image,
- Mean DIC image (n=128),
- DIC model,
- Residual after optimisation (Data-model)<sup>2</sup>

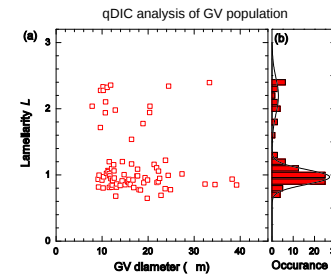
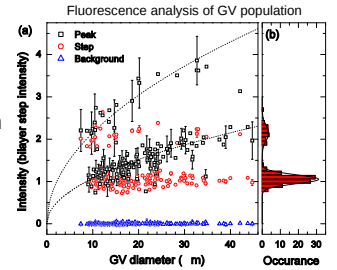
Model (c) is fitted to mean image (b) and the difference taken.

Model fitting returns two parameters which are representative of the vesicle lamellarity:

- The peak area (Focussed profile region)
- The step height (Defocussed region)

## Results

Firstly, the same fitting techniques are applied to Epi-fluorescence images of vesicle populations. Lamellarity is then extracted from this information to act as a conventional, independent and simultaneous correlative metric

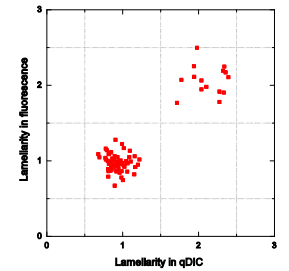


qDIC techniques replicate the distribution of membrane thicknesses seen in typical polydisperse vesicle populations under Epi-Fluorescence.

Precision is sufficient that < 4nm of additional material can be detected and quantified. Differences equivalent to layers just two molecules thick

Direct comparison of the two techniques applied to the same vesicles proves the efficacy of the new method.

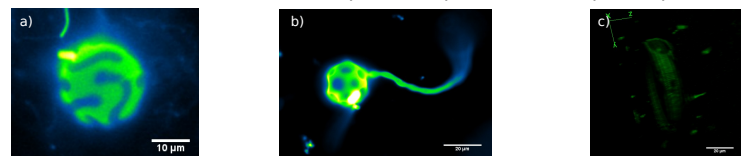
Unlike fluorescence, qDIC requires no sample specific calibration and provides quantitative information regarding optical path length difference.



Correlative qDIC vs Fluorescence analysis upon the same vesicles

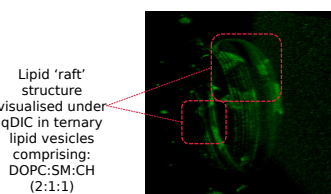
## Conclusions

- qDIC provides an excellent methodology with which to quantitatively measure optically thin samples. Crucially, qDIC is intrinsically compatible with emerging label-free techniques such as CARS / SRS.
- qDIC can be operated without sample specific calibration.
- Systems with known refractive index distributions can be topographically reconstructed with sub-nm precision (see outlook & c) below).



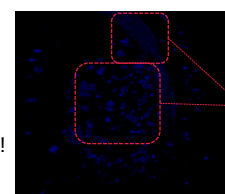
Lipid thermodynamic phase partitioning in ternary GUV visualised under: a) & b) Epi-Fluorescence: Atto-488 DOPE. c) 3d qDIC

## Outlook & Future directions



Lipid 'raft' structure visualised under qDIC in ternary lipid vesicles comprising: DOPC:SM:CH (2:1:1)

- qDIC as stated above is linearly proportional to the derivative of the object phase distribution; image integration recovers φ.
- a priori knowledge of the refractive indices involved permits direct recovery of the object axial topography.
  - Initial results from 3d stacks of ternary lipid vesicles appear to show thermodynamic phase partitioning due to sub-nm thickness variations (~0.6nm)!
- Integration techniques enhance DIC sectioning: Label-free 3d reconstructions for live cell biological applications.



Mouse secondary Oocyte imaged under 3d qDIC, highlighted are the interior of the Zona Pellucida & clustering of cytoplasmic structures in nucleolus region.